Synthesis and Physical Properties of Hetero-substituted-HATNs and their Cu(I) and Re(I) Complexes

A thesis presented in partial fulfilment of the requirements for the degree of Doctor of Philosophy in Chemistry at Massey University, Palmerston North

Nyree Dawn Parker

2013

“An expert is a person who has made all the mistakes that can be made in a very narrow field.”
— Niels Bohr

Acknowledgements

First and foremost I would like to thank my supervisors Associate Professor Eric Ainscough and Associate Professor Ashton Partridge who were friendly and supportive throughout my study. A/Prof Ainscough took this project on half-way through which was no easy task and for that I am especially grateful. Additionally, I would like to thank Dr Ross Davidson for his supervisor-like role, wealth of knowledge and support throughout this time.

I would like to acknowledge Massey University and the MacDiarmid Institute for providing financial support.

I wish to thank Dr Wayne Campbell for his support initially on this project, Graham Freeman for the synthesised copper starting materials and general help, Professor Geoff Jameson for his help with crystallography and Professor Keith Gordon (and his group) for running my Raman samples, running some calculations and providing advice. Finally I would like to thank Massey University, Albany Campus, for allowing me to run my calculations on their computers.

Lastly, I wish to thank my family and Paul for supporting my efforts to pursue a PhD.

Abstract

The electron deficient hexaazatrinaphthalene compounds are of interest for photovoltaic (PV) and molecular devices. These molecules contain multi phenazine (a common dye chromophore) centres that allow coordination of metals, forming complexes that have been shown to have photophysical properties that could be commercially valuable. HATNAs have been investigated for use in molecular devices; including liquid crystals (LCs), light emitting diodes (LEDs), PVs, and field effect transistors (FETs) by a variety of groups.

The initial goal of this thesis was the synthesis of mixed or 'hetero'-HATNs. Preliminary investigations leading into the synthesis of HATNAs showed a number of problems associated with solubility, purification, and stability of these compounds, however a method was established and six hetero-HATNs, HATN-4Me, HATN-4Br, HATN-2Me, HATN4Br2Me HATN-2Br and HATN-4Me2Br, were synthesised and carried throughout the thesis. The rhodizonic acid route and its reactions with the appropriate diaminobenzenes followed by oxidation with nitric acid and then further reactions with diaminobenzene was considered the best.

The crystal structure of one of the possible intermediates for HATN production, PTK-2Me which is based on a 1,2,3,4-phenazinetetrone displays the presence of a gem-diol equilibrium on one of the rings which is no longer aromatic. The crystal structure of PKH-2Me (PKH = 2,3-dihydroxyphenzine-1,4-dione) which is a precursor to the PTK-2Me intermediate shows the C-OH bonds are shortened due to the partial double bond character due to a shifting of the equilibrium between a ketone and a hydroxyl group. The crystal structure of HATN-4Me shows all of the aromatic rings to be mostly planar with slight distortion. The MALDI mass spectra for each of the electron deficient HATNs displays a band due to $[M+2]^+$ cations which is unusual and possibly formed by a $[M+2H^+ + e^-]$ species.

Physical properties of the six HATNs were investigated using UV/Vis, Raman and IR spectroscopies. They were tested as the electron-transport-material in a field effect transistor. It was found that HATN-4Br had the highest electron mobility of 8.13 x 10^4 $cm^2V^{-1}s^{-1}$ and this was obtained after vacuum deposition onto a substrate rather than a solution processed deposition. However as it has a high resistance it is not suitable for a FET device.

The HATNs all display first reduction potentials at -0.9 V with a second at about -1.4 V. They are all quite close and do not appear to follow the expected trend according to the nature of the functional groups.

The HATNs coordinate to rhenium to form A and S isomers which are difficult to isolate. The HATN-1Re complexes display similar physical properties. When two rhenium atoms are added (HATN-2Re) there is a noticeable red-shift in their absorption spectra (100 nm). Crystal structures of HATN-4Me-1ReA and HATN-4Me-1ReS and HATN-2Me-2ReS were obtained and these show twisting of the HATN core up to 13˚. These structures showed the π-π stacking ability of the HATN complexes ranging from 1 to 3 ring overlaps as well as solvent interactions.

Copper willingly binds to all three bidentate hetero-HATN sites and has the unusual property of a colour change between the solvents acetonitrile and chloroform. The reason for this colour change is discussed and found possibly to be due to copper dissociation.

Table of Contents

List of Figures

Chapter 1

Chapter 2

Chapter 5

Tables

Chapter 2

Chapter 3

Chapter 4

Chapter 5

Chapter 1

An introduction to HATNs

1.0 Abbreviations used in Chapter 1

HATN	5,6,11,12,17,18-hexaazatrinaphthalene
CHK	Hexaketocyclohexane
LC	Liquid crystal
FET	Field effect transistor
DAB	1,2-diaminobenzene
QXD	Quinoxalino[2,3-a]phenazine-6,7-dione
PIM	Polymer of intrinsic microporosity
PTK	1,2,3,4-phenazinetetrone
DCM	Dichloromethane

1.1 Introduction

Pyrazino[*2,3-b*:*5,6-b*']diquinoxaline also referred to as 5,6,11,12,17,18-hexaazatrinapthalene, or HATN (Figure 1), contains three pyrazine rings positioned to provide three bidentate sites that allow coordination of metals, forming complexes that have been shown to have photophysical properties that could be commercially valuable.[1-5] HATNs have been investigated for use in molecular devices; including liquid crystals (LCs),[1,2] light emitting diodes (LEDs),[3,4] photovoltaics PVs,[1,5] and field effect transistors (FETs)[1,4] by a variety of groups.

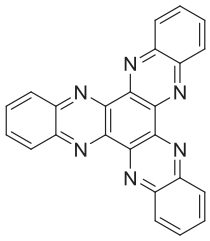

Figure 1 Structure of HATN.

Study in the area of HATNs has been aimed at the synthesis of homo-substituted HATNs, i.e. HATNs where the same functional group occurs on each branch of the molecule. The most common method for synthesis of HATNs is by Schiff-base condensation of hexaketocyclohexane (CHK) with 1,2-diaminobenzene (DAB) (Figure 2).[6-12] This route is preferred when possible as the starting materials can be obtained easily. Both CHK and analogues of DAB where R can be various functional groups are commercially available.

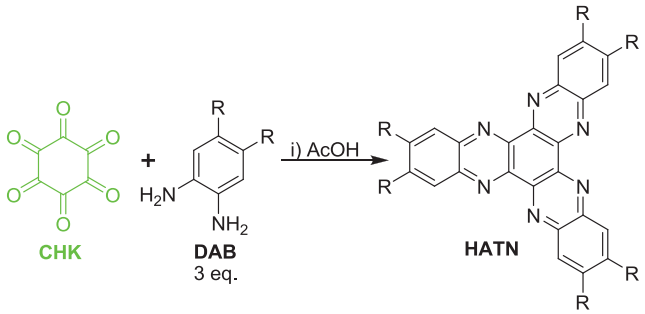

Figure 2 Standard synthetic route for the formation of HATN.

The second procedure used is given in Figure 3, where the ketone and amino groups on DAB and CHK are simply swapped so that 3,5-cyclohexadiene-1,2-dione (DKB) and hexaaminobenzene (HAB) are used. This is unfavourable as the starting materials are not readily available as functionalised DKBs but have to be synthesised. Other problems with this route are that HAB has an explosive intermediate for formation,[13] and HAB decomposes in air.[14]

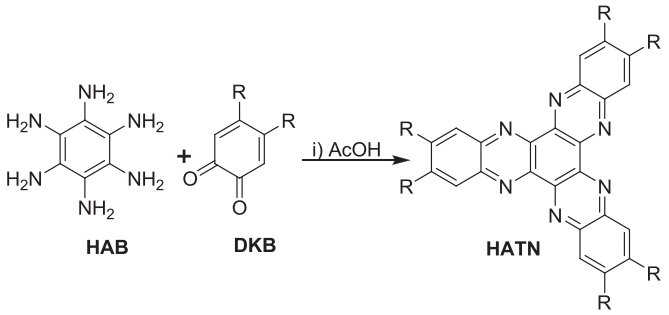

Figure 3 Alternate synthesis to HATN.

The Schiff-base condensation of the ketone and amine is one of the most significant reactions in this thesis. As such, the mechanism (Figure 4) is important as insight into how the reaction can be controlled will be invaluable. It is not known whether both amino groups on DAB attack the adjacent ketones on CHK simultaneously or consecutively, but steric hindrance would ensure only three DAB molecules attach themselves to the CHK. Also the production of quinoxalino[2,3-*b*]phenazine-6,13-dione (QXD) seems unfavourable (as it is not given as a side product in the synthesis of HATNs). This may be due to the fact that the consecutive addition of the 1,2-diaminobenzene enables the adjacent ketones to an occupied site to become more activated and therefore the next amino group will preferentially add there. As can be seen in the mechanism (Figure 4) a weak acid is needed and this is usually acetic acid, which is used as the solvent or a few drops in ethanol.

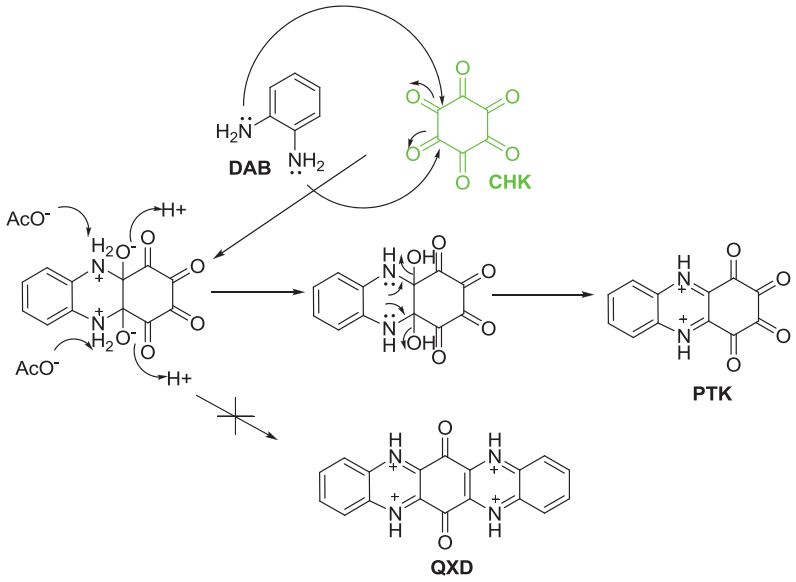

Figure 4 Mechanism for Schiff-base condensation.

The literature provides more 'interesting' synthetic strategies for the production of HATN, the Piglosiewicz et al.[15] method is shown below where metal chelation is used for the synthesis of HATNs (Figure 5). It was found that reacting a quinoxaline (1) with the titanocene acetylene complex, $Cp_2Ti\{\eta^2\text{-}C_2(SiMe_3)_2\}$, leads to the formation of the HATN titanium complex **2** (Figure 5, route (i)). Releasing the titanium with iodine gives HATN (route iii). The yield from this method was reported to be higher than making it directly with the Schiff-base condensation shown in Figure 2. HATN can also be formed by dehydrogenative coupling of 2,3-(2',2'')-diquinoxalylquinoxaline **3** with $Cp_2Ti\{\eta^2\text{-}C_2(SiMe_3)_2\}$ (Fig. 5, route (ii)).

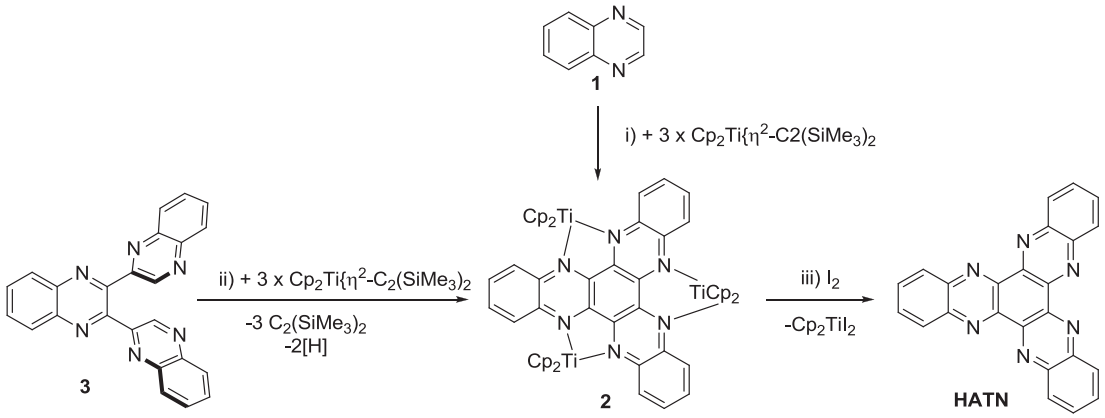

Figure 5 Synthesis of HATN via a titanium metal complex 2.[15]

1.2 Metal coordination

HATNs are attractive supra-molecular building blocks, because of their following attributes:

i) The ligands have three chelating sites to the metal ions, which are useful for the construction of the metal-assembled system. On top of these binding sites it is also possible to add further binding sites to the peripheral branches on HATN.

ii) The ligands afford characteristic electron-deficient π-systems, which exhibit metal-to-ligand charge transfer and/or readily undergo reduction to form paramagnetic radical ligands.

iii) The ligands have a C_3 symmetry axis, leading to degenerate π* orbitals and octupole moment in essence.

iv) Finally, the ligands afford a variety of interesting chemical/physical properties based on their electronic structures which can readily be modified by their six substituent groups.[16]

Oligo- and polynuclear complexes with HATN and its derivatives afford intriguing crystal structures depending on the coordination modes, i.e. single, double, and triple metal-chelating, and range from discrete complexes to infinite coordination polymers. Although discrete complexes or one-dimensional coordination polymers cover most of the oligo- and polynuclear complexes, hydrogen bonding and π–π stacking can also cause supra-molecular assembly to construct higher-dimensional structures.

1.2.1 Discrete complexes

A few examples of discrete HATN-complexes with various transition metals exist in literature. Two HATN zinc complexes have been studied and are shown below (Figure 6). The first is $[Cl_2Zn)(\mu_1\text{-HATN})]$ which is formed by the reaction of three equivalents of zinc chloride. The fact that only the mononuclear product was formed could be explained by the ability of THF to coordinate zinc chloride competing with HATN. Furthermore, the basicity of the N-atoms of the HATN molecule is reduced by coordination of zinc chloride which leads to a mononuclear complex. The reaction of diethyl zinc and HATN leads to the trinuclear complex $[(Et_2Zn)_3(\mu_3\text{-HATN})]$ because zinc appears in diethyl zinc less positive due to the covalency of the Zn-C bond.[17]

Figure 6 Left: $[Cl_2Zn)(\mu_1\text{-HATN})]$ Right: $[(Et_2Zn)_3(\mu_3\text{-HATN})]$.[17]

1.2.2 Extended coordination sites

Ruthenium(II) bipyridyl and palladium(II) chloride complexes have been found to coordinate to PHAT, that is HATN with 1,10-phenanthroline at the peripheral branches (Figure 7). These 1,10-phenanthroline extensions afford HATN three extra coordinating sites which have been found to bind ruthenium in single, bi and tri nuclear discrete complexes. Hetero-nuclear PHAT complexes containing ruthenium and palladium in 2:1 or 1:2 ratios were also synthesised.[18]

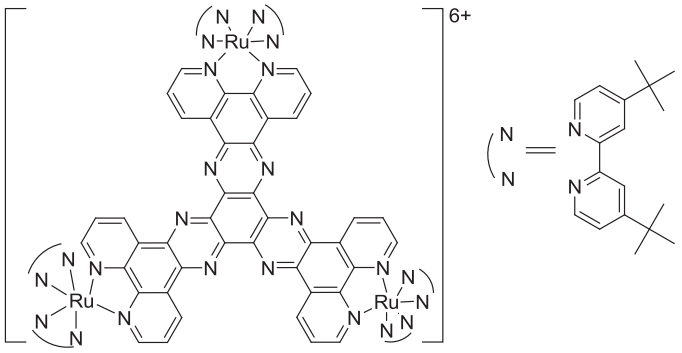

Figure 7 PHAT with three coordinated ruthenium complexes.

1.2.3 Coordination network

The complexation of HATN with silver provides a 3D polymer, the only HATN-metallo-network in the literature. Crystals of $[(Ag_3(HATN)_2)(NO_3)_3 \cdot solvent]$ (HATN-3Ag) was obtained by layering silver nitrate in acetonitrile on top of HATN in dichloromethane. Each silver center in HATN-3Ag acts as a two-connecting node by connecting two ligands of HATN. HATN-3Ag exhibits two fold interpenetrating networks with the two-connected (Ag^I) and three-connected (HATN) nodes.[19]

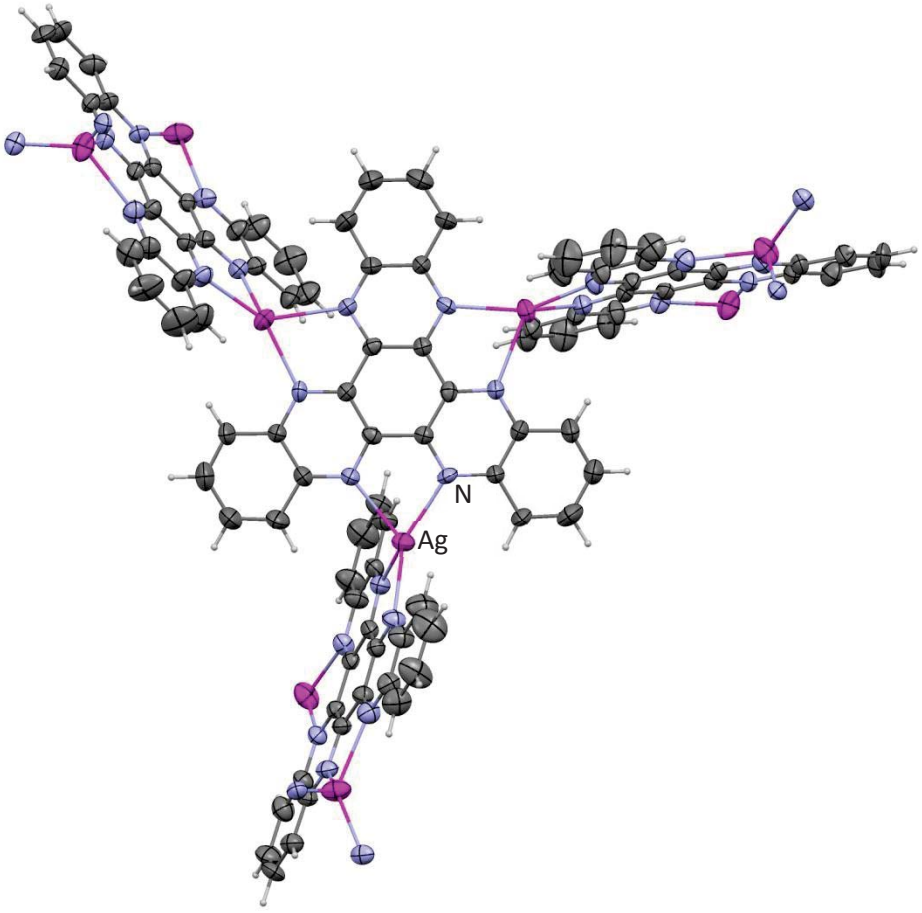

Figure 8 Crystal structure of $[(Ag_3(HATN)_2)(NO_3)_3]$ with solvent removed.[20]

1.3 Applications

Due to the scarcity of n-type materials (i.e. materials that are able to transport electrons) HATNs have been investigated for use in molecular devices; including liquid crystals (LCs),[1,2] light emitting diodes (LEDs),[3,4] photovoltaics PVs,[1,5] and field effect transistors (FETs)[1,4] by a variety of groups.

1.3.1 Liquid crystals

Discotic liquid crystals (DLC) have attracted more and more attention due to their potential in electro-optic and photonic applications where efficient unidirectional charge transport is desired. In the oriented columnar stack of discotic molecules, there is a preferential direction for charge carrier transportation, and thus a well aligned DLC exhibits highly mono-dimensional carrier mobility along the column direction.

N-type mesogens are scarce, and HATN derivatives are one of the few which have this in-demand property.[21-24] HATN-6($OC_{10}H_{21}$) was found to favour π-π stacking which formed a hexagonal columnar mesophase (Figure 9, Left). The photomicrograph of this HATN LC once cooled reflects a typical hexagonal symmetry of the columnar phase (Figure 9, Right).[25]

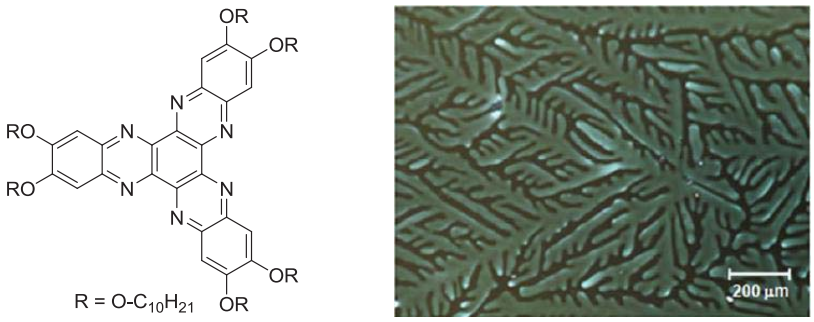

Figure 9 Left: HATN-6(O-$C_{10}H_{21}$) Right: HATN-6(O-$C_{10}H_{21}$) in a confined cell made using glass plates. The pattern reflects a hexagonal symmetry of the columnar structure with face-on molecular anchoring.[25]

This π-π stacking ability of HATN can be further exploited to form one-dimensional nanostructures. Helical superstructures are formed for the achiral HATN-6($OC_{12}H_{25}$) through a surface assisted assembly process. Careful analysis of a single fibre revealed a coiled-coil helical morphology with the expected equal distribution of left and right helices observed.[26]

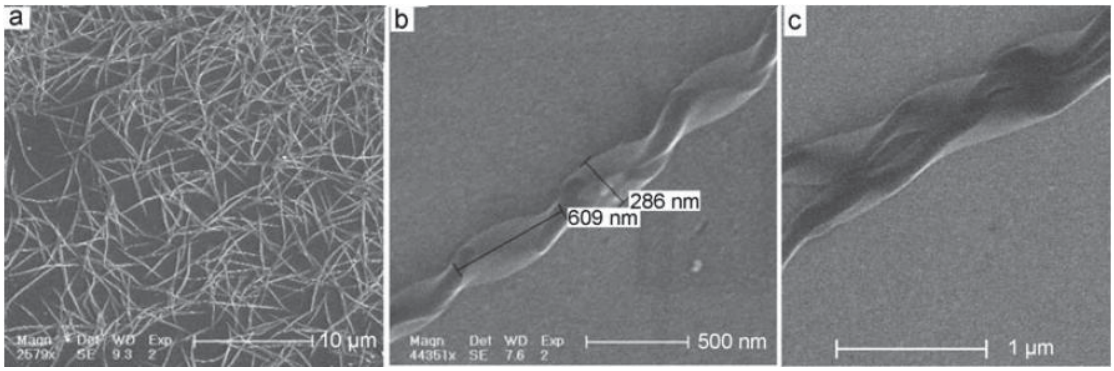

Figure 10 SEM images of HATN on a Si substrate. a) SEM image of a sample prepared by dropping a dilute solution of DCM onto a silicon substrate, followed by solvent evaporation in a closed chamber saturated with the appropriate solvent vapour. b,c) Magnification of the helical structure.[26]

1.3.2 Charge carrier

HATN derivatives with their electron deficient core substituted by six electron-donating alkylsulfanyl chains at the periphery have been designed to efficiently transport electrons (Figure 11). Mesogens with the shortest chains (hexyl and octyl) show only one mesophase at high temperatures and those with longer chains (decyl and dodecyl) form columnar mesophases of lower symmetry at lower temperatures. There is a significant variability of the measured LC phase electron-mobilities (from 0.02 to 0.32 $cm^2V^{-1}s^{-1}$) with changes in the side-chain length. This indicates the side chains have a strong influence in the intra-columnar ordering of the molecules.[24]

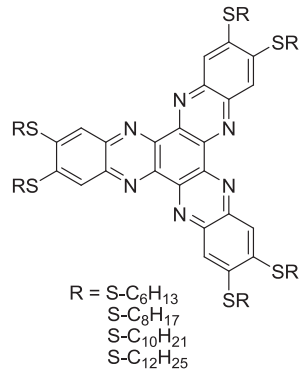

Figure 11 HATN alkylsulfanyl derivatives used in charge transport.[24]

This work has been extended to amorphous HATN derivatives. Two isomers of HATN-3($CO_2CH_2C_6F_5$) exist and are shown in Figure 12. It was found that a mixture of the isomers gave a electron-mobility of 0.02 $cm^2V^{-1}s^{-1}$ while the pure C_{3h} isomer increased the electron-mobility to 0.07 $cm^2V^{-1}s^{-1}$. The C_s isomer was not obtained due to the strong tendency of the films to crystallise and delaminate from the electrodes.[27]

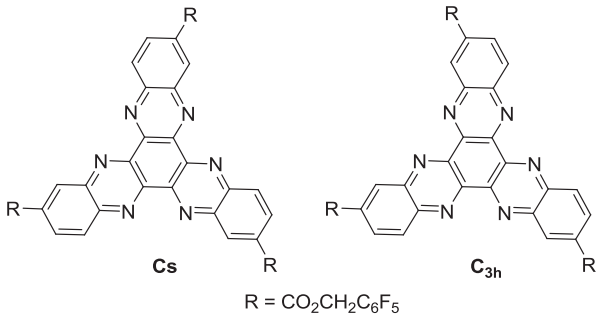

Figure 12 HATN isomers used for electron transport.[27]

1.3.3 Hydrogen storage

The challenge of storing hydrogen at high volumetric and gravimetric density for automotive applications has prompted investigations into the potential of cryo-adsoption on the internal surface area of microporous organic polymers of intrinsic microporosity (PIM). HATN-PIM (Figure 13) was found to have surface area of 590 m^2g^{-1} (based on Langmuir H_2 sorption) where it is thought that a viable hydrogen storage solutions would have a surface area of 2400 m^2g^{-1}.[28]

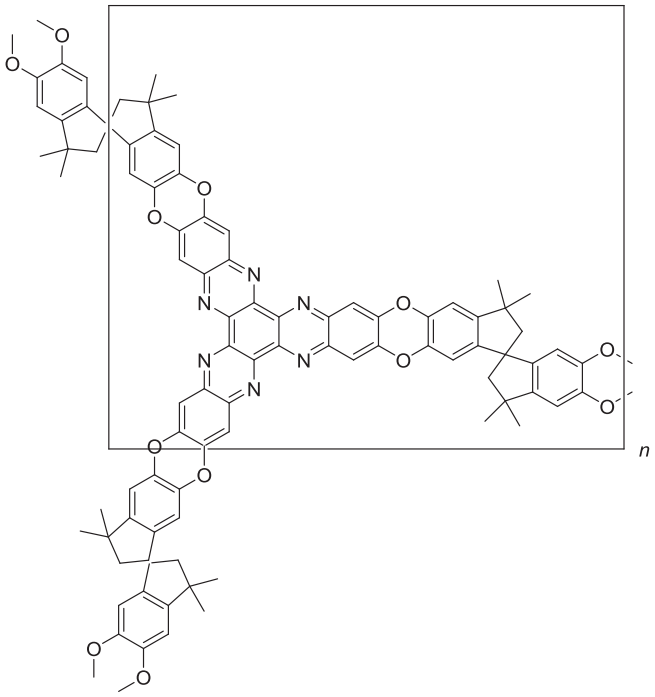

Figure 13 HATN-PIM used for N_2 and H_2 sorption.

1.4 References

1 Marder, S.; Kaafarani, B.; Barlow, S.; Kippelen, B.; Domercq, B.; Zhang, Q.; Kondo, T., **2005,** 2005-US20998 2005123737.

2 Zheng, W.; Chiang, C.-Y.; Ong, C. W.; Liao, S.-C.; Huang, J.-Y. *Proceedings of SPIE-The International Society for Optical Engineering* **2007**, *6587*, 658719/1.

3 Liao, L.-S.; Slusarek, W. K.; Ricks, M. L.; Young, R. H.; Comfort, D. L., **2007,** 2006-US17555 WO2007130047.

4 Uehara, M., **2006,** 2006-JP300407 WO2006075723.

5 Uehara, M., **2006,** 2006-JP312452 WO2006137462.

6 Du, M.; Bu, X. H.; Biradha, K. *Acta Crystallographica Section C* **2001**, *C57*, 199.

7 Ong, C. W.; Liao, S.-C.; Chang, T. H.; Hsu, H.-F. *Journal of Organic Chemistry* **2004**, *69*, 3181.

8 Bock, H.; Babeau, A.; Seguy, I.; Jolinat, P.; Destruel, P. *ChemPhysChem* **2002**, *3*, 532.

9 Barlow, S.; Zhang, Q.; Kaafarani, B. R.; Risko, C.; Amy, F.; Chan, C. K.; Domercq, B.; Starikova, Z. A.; Antipin, M. Y.; Timofeeva, T. V.; Kippelen, B.; Brédas, J.-L.; Kahn, A.; Marder, S. R. *Chemistry – A European Journal* **2007**, *13*, 3537.

10 Gao, B.; Xia, D.; Geng, Y.; Cheng, Y.; Wang, L. *Tetrahedron Letters* **2010**, *51*, 1919.

11 Catalano, V. J.; Larson, W. E.; Olmstead, M. M.; Gray, H. B. *Inorganic Chemistry* **1994**, *33*, 4502.

12 Gao, B.; Liu, Y.; Geng, Y.; Cheng, Y.; Wang, L.; Jing, X.; Wang, F. *Tetrahedron Letters* **2009**, *50*, 1649.

13 Brill, T. B.; James, K. J. *Chemical Reviews* **1993**, *93*, 2667.

14 Knaggs, I. E. *Proceedings of the Royal Society of London. Series A, Containing Papers of a Mathematical and Physical Character* **1931**, *131*, 612.

15 Piglosiewicz, I. M.; Beckhaus, R.; Saak, W.; Haase, D. *Journal of the American Chemical Society* **2005**, *127*, 14190.

16 Kitagawa, S.; Masaoka, S. *Coordination Chemistry Reviews* **2003**, *246*, 73.

17 Krahmer, J.; Beckhaus, R.; Saak, W.; Haase, D. *Zeitschrift für anorganische und allgemeine Chemie* **2008**, *634*, 1696.

18 David Pilz, T.; Rockstroh, N.; Rau, S. *Journal of Coordination Chemistry* **2010**, *63*, 2727.

19 Bu, X.-H.; Biradha, K.; Yamaguchi, T.; Nishimura, M.; Ito, T.; Tanaka, K.; Shionoya, M. *Chemical Communications* **2000**, 1953.

20 Bu, X.-H.; Tanaka, K.; Shionoya, M.; Biradha, K.; Yamaguchi, T.; Nishimura, M.; Ito, T. *Chemical Communications* **2000**, 1953.

21 Li, Y.; Zeng, Q.; Wang, Z.; Qi, G.; Guan, L.; Fan, X.; Wang, C. *Chinese Science Bulletin* **2008**, *53*, 1613.

22 Yip, H.-L.; Zhou, J.; Ma, H.; Tian, Y.; Tucker, N. M.; Jen, A. K. Y. *Journal of the American Chemical Society* **2006**, *128*, 13042.

23 Ming-Che Yeh, S.-C. L., Shih-Hua Chao, Chi Wi Ong *Tetrahedron* **2010**, *66*, 8888.

24 Lehmann, M.; Kestemont, G.; Aspe, R. G.; Buess-Herman, C.; Koch, M. H. J.; Debije, M. G.; Piris, J.; de Haas, M. P.; Warman, J. M.; Watson, M. D.; Lemaur, V.; Cornil, J.; Geerts, Y. H.; Gearba, R.; Ivanov, D. A. *Chemistry - A European Journal* **2005**, *11*, 3349.

25 Zheng, W.; Hu, Y.-T.; Chiang, C.-Y.; Ong, C. W. *International Journal of Molecular Sciences* **2010**, *11*, 943.

26 Gao, B.; Li, J.; Li, M.; Cheng, Y.; Wang, L. *ChemPhysChem* **2009**, *10*, 3197.

27 Kaafarani Bilal, R.; Kondo, T.; Yu, J.; Zhang, Q.; Dattilo, D.; Risko, C.; Jones Simon, C.; Barlow, S.; Domercq, B.; Amy, F.; Kahn, A.; Bredas, J.-L.; Kippelen, B.; Marder Seth, R. *Journal of American Chemical Society* **2005**, *127*, 16358.

28 Budd Peter; Butler, A.; Selbie, J.; Mahmood, K.; McKeown Neil; Ghanem, B.; Msayib, K.; Book, D.; Walton, A. *Physical Chemistry Chemical Physics* **2007**, *9*, 1802.

Chapter 2

Synthesis of hetero-HATNs

2.0 Abbreviations used in Chapter 2

HATN	5,6,11,12,17,18-hexaazatrinapthalene
PTK	1,2,3,4-phenazinetetrone
PTH	1,2,3,4-tetrahydroxy-phenazine
PKH	2,3-dihydroxy-phenazine-1,4-dione
QPK	Quinoxalino[2,3-a]phenazine-6,7-dione
THBQ	Tetrahydroxy-p-quinone
DAB	1,2-diaminobenzene
DKB	3,5-cyclohexadiene-1,2-dione
RDA	Rhodizonic acid
MS	Mass spectroscopy
QPH	6,7-dihydroxy-quinoxalino[2,3-a]phenazine
CHK	hexaketocyclohexane (octahydrate)

2.1 Introduction

The body of this research has two aims:

i) To create a general method of synthesis for hetero-HATNs[a] and to use this method to undertake the synthesis of a 'set' of hetero-HATNs with a range of functional groups including bromo, methyl and hydrogen.

ii) Explore the physical properties of the new HATNs and to study their coordination behaviours with transition metals (Re, Cu, Pd) and to study their physical properties.

In order to elucidate possible pathways to develop new hetero-HATNs it is crucial to establish a route where different functionalities can be incorporated and optimal conditions established for their synthesis.

2.1.1 Hetero-HATN synthesis

The focus of this project is to develop the controlled synthesis of hetero substituted HATNs (hetero-HATNs). That is to form HATNs where not all the functional groups around the rings are identical (Figure 1, ii and iii). There is some literature available to guide the synthesis of hetero-HATNs.[1-3] Most is for compounds with high solubility and a more general approach than that is needed. Ideally the controlled addition of 4,5-diA-1,2-diaminobenzene (DAB-2A) onto the hexaketocyclohexane (CHK) core is required to occur in a one to three (Figure 1, left), one to two (Figure 1, centre) or one to one (Figure 1, right) ratio as desired. This then allows the subsequent addition of DAB-2B to the unreacted sites.

[a] Hetero-HATN is a HATN which has different groups on the peripheral branches (see Figure 1).

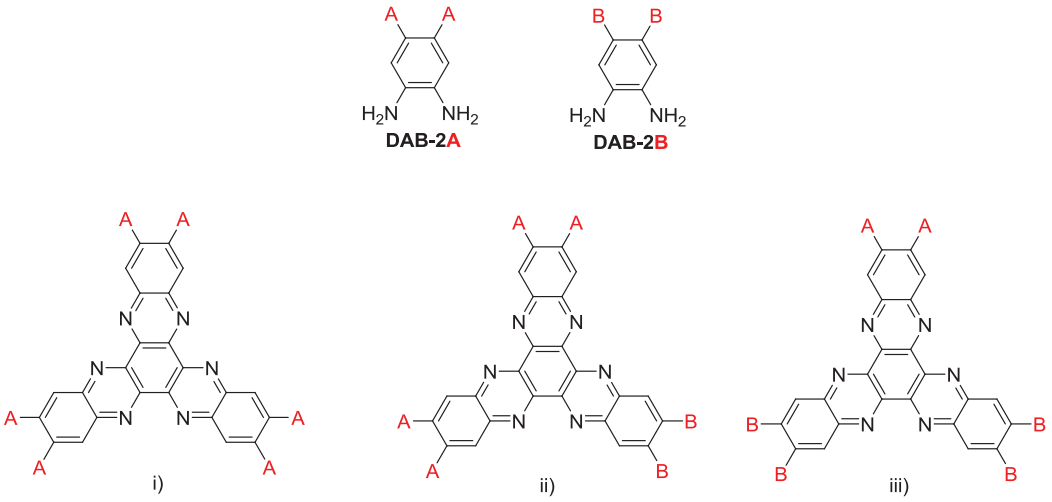

Figure 1 i) homo-HATN HATN-6A ii) and iii) hetero-HATNs HATN-4A2B (ii) and HATN-4B2A (iii).

Hetero-HATNs offer the potential for the incorporation of different functional groups around the HATN core so that certain attributes (e.g. solubility or electronic properties) may be modified and potentially enhanced.

Although not technically a hetero-HATN, HATN-3COOH is the only example of a homo-HATN compound showing selectivity in the isomer formed upon synthesis.[4] The synthesis of HATN-3COOH is expected to produce two isomers, one with C_{3h} symmetry and one with Cs symmetry (Figure 2). However, upon synthesis the product is isomerically pure with only the D_2 isomer present. The reason behind this is a sterically favoured 1:2,3:4-bicondensation intermediate (3,10-dicarboxy-quinoxalino[2,3-a]phenazine-6,7-dione, QPK-2COOH) leading to only one product.

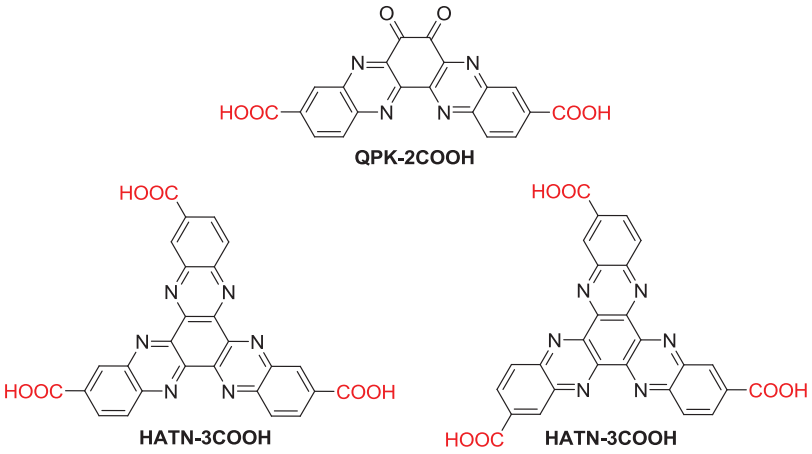

Figure 2 Top: QPK-2COOH Bottom: Possible HATN-3COOH isomers (Left Cs, Right C_{3h})

The focus of this work is the formation of hetero-HATNs where the functional groups on the peripheral rings are different. The first example of a truly controlled hetero-HATN synthesis was described by Yeh et al. where they used hexaketocyclohexane (CHK) to synthesise a selection of hetero-HATN derivatives (Figure 3).[2] They found that the addition of a one to one ratio of CHK and DAB gave the product quinoxalino[2,3-a]phenazine-6,7-dione (QPK), the di-condensation product. Their reasoning behind this was the solubility of the mono and di-condensation products. Once one DAB had reacted to form the mono-condensation product 1,2,3,4-phenazinetetrone (PTK), the increased solubility allowed the molecule to dissolve into the solvent and hence conditions were more favourable for a successive condensation. The change in ratios of the starting materials altered the formation of the PTK and HATN products. Once the reaction was enhanced to form QPK-4R_1 this was further reacted with DAB-2R_2 to give the hetero HATN-4$R_1$2R_2 which was purified by column chromatography and crystallisation.

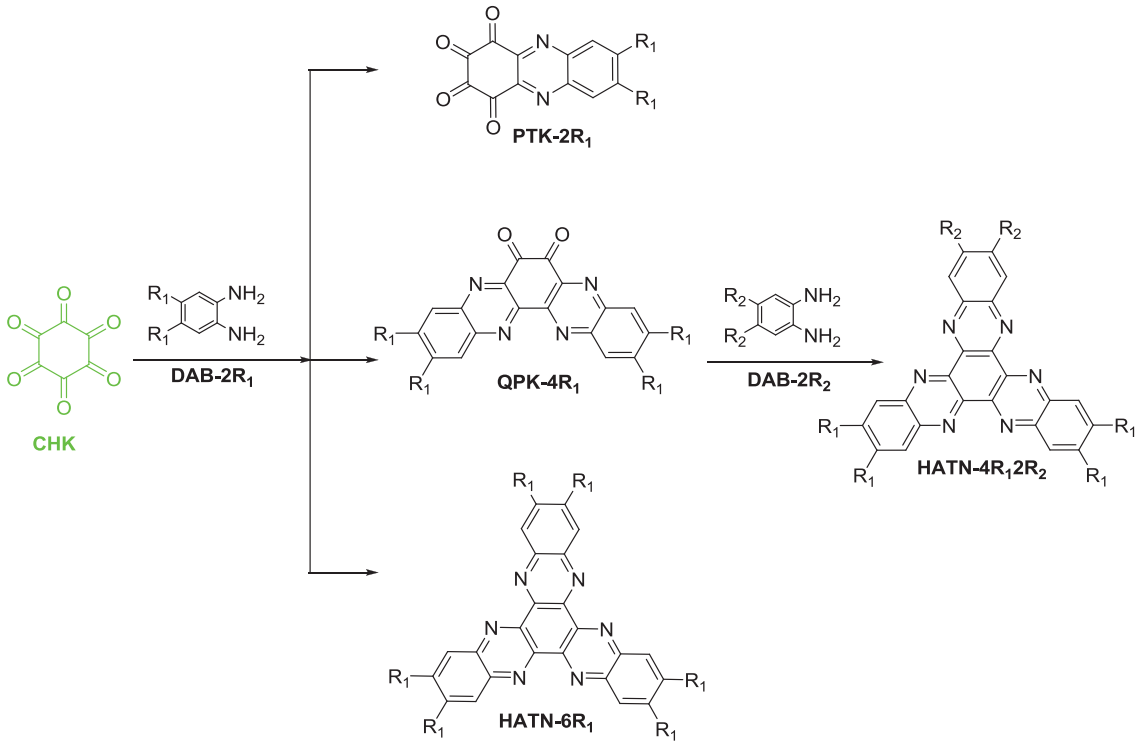

Figure 3 Hetero synthesis of HATN derivatives. R = alkoxy chains of length CnHn+1; n=6, 8, 10, 12 with $R_1 \neq R_2$.

The idea of adding the DAB in a set ratio was extended to the use of tetrahydroxy-p-quinone (THBQ) in forming the PTK which can be further reacted to HATN (Figure 4). Yeh et al. found that when R was an alkoxy chain the tetrahydroxy product could not be oxidised using the traditional nitric acid reagent, nor any other variation which they proposed, but when R was H the oxidation was successful.[2]

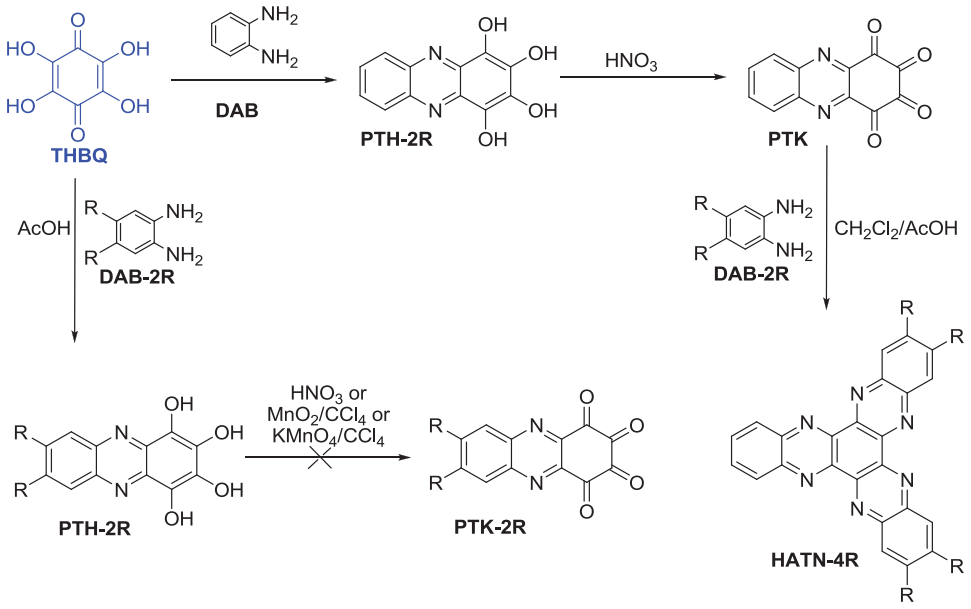

Figure 4 Use of THBQ for formation of HATN-4R.

One of the most significant problems in purification of HATNs in the present study is their lack of solubility, which is mainly limited to chlorinated solvents. Purification has been achieved by crystallisation and column purification in the literature but is generally difficult. Most papers report the formation of pure products, or provide several consecutive methods of purification yielding little product. Marder et al.,[5] however, used sublimation to purify the HATN, HATN-6Cl, and HATN-6Me derivatives. This required low pressures obtained from a diffusion pump which is not practical in all labs.

The hetero-HATNs formed by Yeh's methods had to be rigorously purified by silica gel chromatography followed by recrystallisation. The presence of these alkoxy chains aided purification by enhancing the solubility in solvents, in what would have otherwise been an intractable mixture. This restriction of substitutents has hindered the development of HATN chemistry and this warrants the development of a more general procedure that can be extended to a wide range of functional groups.

2.2 Towards the synthesis of hetero-HATNs in the present study

2.2.1 Exploratory reactions for the preparation of hetero-HATNs

In the study of the feasibility of synthesising hetero-HATNs four different but closely associated methods were investigated. Each required the use of one of the three starting materials shown below (Figure 5).

i) Using CHK and different ratios of DAB for the synthesis of PTK and QPK. These can be further reacted to form hetero-HATNs.

ii) Using THBQ in a one to one ratio with DAB to synthesise PTK. This can be further reacted to form hetero-HATNs.

iii) Using RDA and DAB in a one to one ratio to form PTK, which can be further reacted to form hetero-HATNs.

iv) Using RDA and DAB in a one to two ratio to form QPK, which can be further reacted to form hetero-HATNs.

Without a clean PTK or QPK intermediate to react further, a mixture of compounds would be formed and without groups to aid solubility, the products would be impossible to purify.

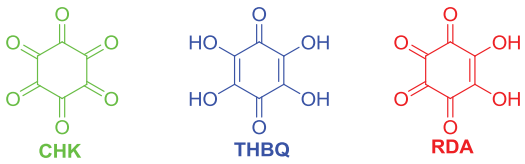

Figure 5 The three starting materials used for the synthesis of hetero-HATNs.

2.2.2 The hexaketocyclohexane method

The hexaketocyclohexane method used three equivalents of CHK to one equivalent of DAB-2R to try to favour the exclusive formation of PTK in ethanol at 70 ^{o}(Figure 6). However, an intractable mixture was obtained from this method. If this reaction is done at room temperature, where CHK is insoluble, HATN itself is cleanly formed. This is thought to be due to increased solubility upon attachment of DAB enabling it to bind more easily with further molecules of DAB in solution.

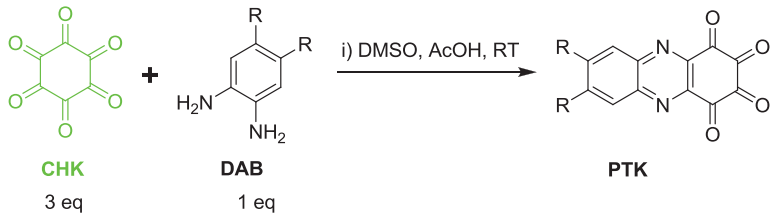

Figure 6 Synthesis of PTK.

The crude reaction mixture was analysed by MALDI-TOF mass spectrometry and shown to contain the desired product PTK as well as HATN. All attempts to purify the mixture by crystallisation were unsuccessful. Column chromatography was unsuccessful and break down products occurred on the column.

2.2.3 The tetrahydroxy-p-quinone method

THBQ has four hydroxyl groups, which is expected to help the formation of a single condensation reaction to form PTH. This procedure required that THBQ and DAB were dissolved in a hot acetic acid/water mixture individually, then mixed (Figure 7). Once cool, the PTH was collected by filtration as a solid. This was then oxidised using nitric acid and once this was complete could be reacted further to form hetero-HATN derivatives.

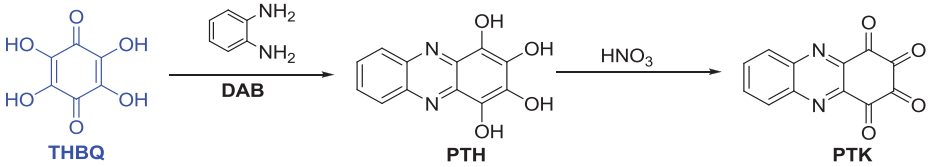

Figure 7 Synthesis of PTK with THBQ.

The advantage of this procedure was in making substituted PTKs where there was only one substituted group on the DAB-1R (i.e. no C_2 symmetry). This is the case for substituting the carboxylic acid functional group (Figure 8).

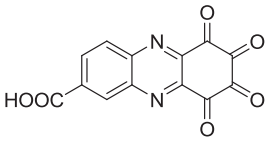

Figure 8 PTK-COOH.

2.2.4 The rhodizonic acid method

RDA provides a more hindered starting material than CHK as it has two hydroxyl groups aiding some limitation to the amount of Schiff-base condensations the molecule can consecutively perform. Although reported in the literature to form homo-HATNs from PTK and PTK-2Me this method has not been exploited to form hetero-HATNs.[1,3] The process is described in Figure 9 by reaction of RDA with DAB-2R in water/acetic acid followed by oxidation using nitric acid giving PTK-2R. The three compounds shown are the ones used in this thesis.

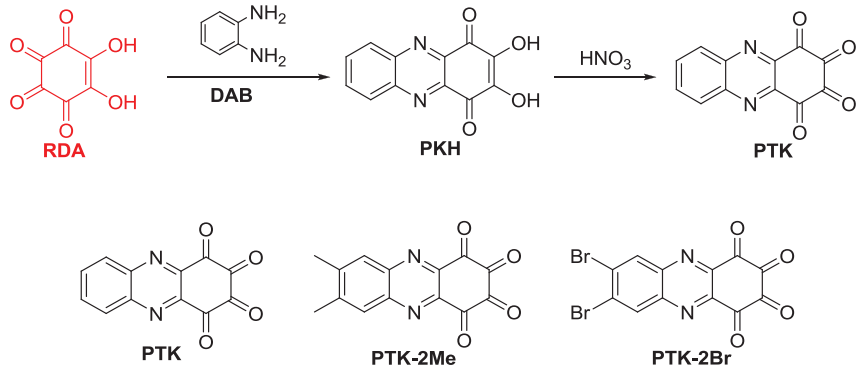

Figure 9 Synthesis of the mono-condensation product synthesised for this project. PTK and PTK-2Me are previously reported in the literature. [1,3]

There was a shift in the NMR spectra of the aromatic protons downfield upon oxidation of the hydroxyl groups as the protons have a reduced electron density in the presence of ketones in the adjacent ring. This was consistent with MS and elemental analysis. It is noted that there are significant water peaks in the 1H NMR spectra with broad bands at ca. 3.5 ppm. All of the phenazine-1,2,3,4-tetrone derivatives are obtained as the hydrates, consequently some of the CO groups may be hydrated to the gem-diol form (Figure 10). This is also evident in the single crystal structure (Figure 12) to be discussed later.

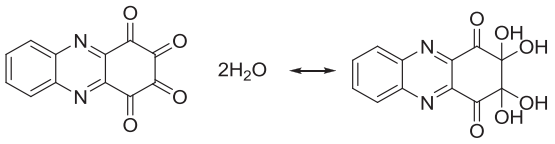

Figure 10 The gem-diol equilibrium for PTK.

2.2.5 Crystallography

The X-ray data for PTK-2Me·CH_2Cl_2·2DMSO and PKH·3DMSO were collected at a reduced temperature with a Rigaku Spider MM007 diffractometer equipped with a microfocus copper rotating anode X-ray source, high-flux Osmic monochromating and focusing multilayer mirror optics and a curved image plate detector. The crystals were mounted in an inert oil, transferred into the cold gas stream of the detector and irradiated with graphite monochromated Cu Ka (λ = 1.54178 Å) X-rays. The data collected by the Crystal Clear[6] program (v.1.4.0) and processed with *FSProcess*[7] to apply Lorentz and polarisation corrections to the diffraction spots (integrated 3 dimensionally).

The structures were solved by direct methods using *SHELXS-97*[8] and *OLEX*[2 9] and refined using SHELXL. Absorption correction was carried out empirically. Hydrogens were calculated at their ideal positions unless otherwise stated. Refinement data for the X-ray crystal structures are given in Table 1.

Table 1 PTK-2Me Crystal data (Left) PKH-2Me Crystal data (right)

Compound	**$C_{14}H_{12}N_2O_6$ ·2(C_2H_6OS)·(CH_2Cl_2)**	**$C_{14}H_{10}N_2O_4$ ·3C_2H_6OS**
Molecular formula	$C_{19}H_{26}C_{l2}N_2O_8S_2$	$C_{20}H_{28}N_2O_7S_3$
M (g mol^{-1})	545.46	504.69
Temperature (K)	153(2)	153(2)
Crystal System	Triclinic	Triclinic
Space group	$P\bar{1}$	$P\bar{1}$
a(Å)	8.5502(5)	6.9333(14)
b(Å)	9.7652(5)	10.513(2)
c(Å)	16.6437(12)	17.708(4)
α(°)	74.373(5)	76.65(3)
β(°)	81.503(6)	81.39(3)
γ(°)	71.763(5)	74.86(3)
V(Å^3)	1268.00(14)	1206.7(4)
Z	2	2
μ(Cu Kα) mm^{-1}	4.247	3.182
ρ_{calc} (g cm^{-1})	1.429	1.389
2θmax(°)	143.6	43.9
Number of unique reflections	4673	2728
Data/restrains/parameters	4673/7/315	2728/174/299
Final R indices [I>2σ(I)]	$R1$ = 0.0509	R=0.0797
	$wR2$ = 0.14522	wR2 = 0.1942
R indices (all data)	$R1$ = 0.0620	R= 0.1202
	$wR2$ = 0.1510	wR2= 0.2327
Goodness-of-fit on F^2	1.081	1.007

2.2.6 Crystal structure of PKH-2Me

Yellow cubes of PKH-2Me·3DMSO were obtained by crystallising in a DMSO gradient. They were found to be triclinic in a $P\bar{1}$ space group with two molecules in the unit cell.

The molecule is planar with aromatic character. The C-C bonds in the dihydroxydiquinone ring (ring 1) are slightly longer (1.439(12)-1.512(11) Å) than the aromatic C-C bonds in the methyl-substituted benzene ring, ring 3 (1.350(12)-1.449(11) Å). However, there is a distinct double bond between C2 and C3 at 1.345(10) Å. For comparison the ethylene C-C bond length is 1.330 Å which is typical for a double bond.[10]

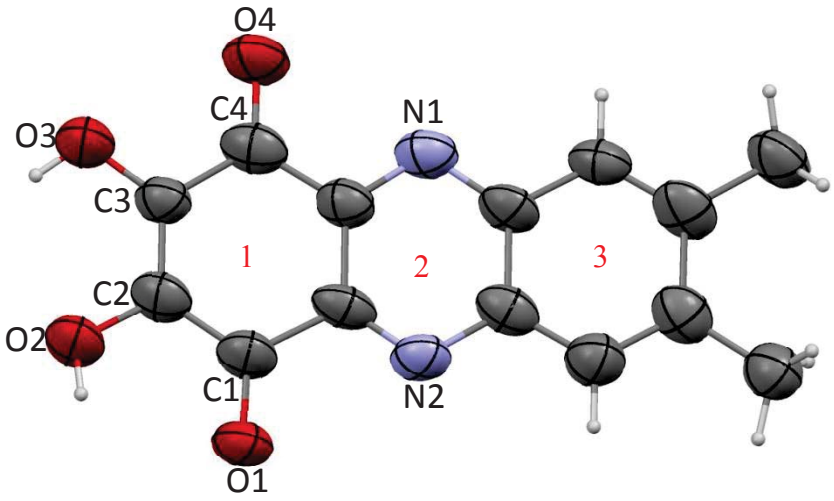

Figure 11 PKH-2Me crystal structure with 50% probability ellipsoids for all atoms excluding hydrogen, and solvent molecules removed for clarity.

The C=O bond lengths range between 1.237(8)-1.240(8) Å showing double bond character, while the C-OH bonds are lengthened with the C2-O2 length of 1.346(9) Å and the C3-O3 with a length of 1.348(9) Å showing partial double bond character. This partial double bond character will be due to the equilibrium in solution between shifting of the ketone and hydroxyl groups. This is similar behaviour to that in tetrahydroxy-p-quinone which has C=O lengths of 1.229(5) Å and C-O lengths of

1.343(5) Å.[11] (see Appendix A for further bond lengths and angles). Typical bond lengths for C=O and C-O bonds are 1.210 and 1.427 Å respectively.[12]

2.2.7 Crystal structure of PTK-2Me

Triclinic PTK-2Me crystallises in the space group $P\bar{1}$ with one molecule of dichloromethane and two molecules of DMSO (one of which is disordered). The cell refines with two molecules per unit cell. The molecule is planar apart from C2 and C3 which lie above and below the plane in a twisted geometry. The gem-diol presence has meant that this ring also has no aromaticity and the lengths of the C-C bonds range between 1.503(3)-1.544(3) Å.

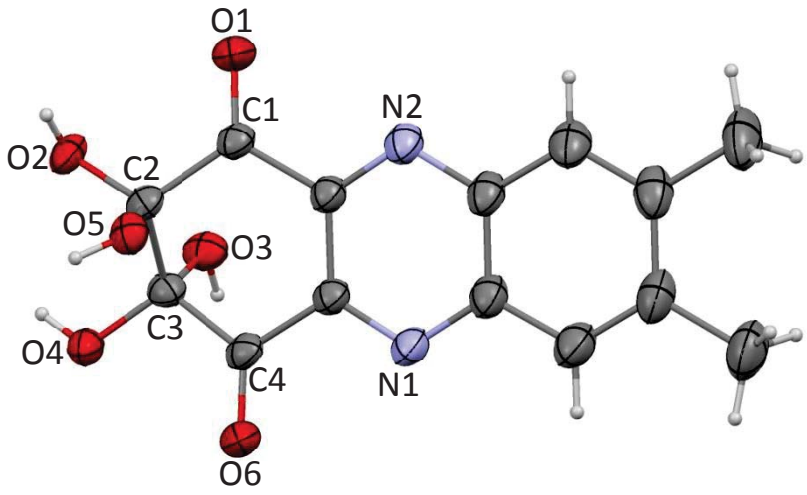

Figure 12 Top: PTK-2Me structure with 50% probability ellipsoids for all atoms excluding hydrogen, solvent molecules removed for clarity.

The C1-O1 and C4-O6 lengths of 1.218(3) Å and 1.216(3) Å indicate that a double bond is present while in the germinal diols the C2-O2, C2-O5, C3-O4, and C3-O3 bond lengths range from 1.380-1.402(3) Å showing partial double bond character. The two hydroxyls in a geminal diol are easily converted to a keto group by loss of one water molecule, thus turning the diol into a ketone. Conversely, ketones tend to combine with water to form the corresponding geminal diols. The equilibrium in water solution may be shifted towards either compound. This explains a noticeable water peak in the NMR spectrum of PTK-2Me. This will be due to the equilibrium in solution between the ketone and the germinal diol. See Appendix A for further bond lengths and angles.

2.2.8 The quinoxalino[2,3-a]phenazine-6,7-dione (QPK) method

As a final approach the synthesis of the di-condensation intermediate (QPK) was investigated.[1] Having the control of adding two DAB molecules on RDA is also investigated (Figure 13). It is important to have both routes available as the oxidation of the hydroxyl groups requires a strong acid and not all functional groups will remain intact. By the controlled addition to give the mono or di-condensation product (PTK and QPK respectively) this can in turn be used to add one or two acid sensitive groups.

The addition of two equivalents of a substituted DAB to RDA was studied at 100°C. It was found that higher temperatures favoured this reaction with predominantly 6,7-dihydroxy-quinoxalino[2,3-a]phenazine (QPH) being formed. The solubility of these compounds is limited to methanol and DMSO. This method was used to synthesise the already reported di-substituted QPH-4R with R=H, and a new compound QPH-4Me. The products were isolated as a mixture of QPH and HATN which can be purified by crystallisation in dioxane. The fact that the R group can be changed means this can potentially be used to make many QPH-4Rs.

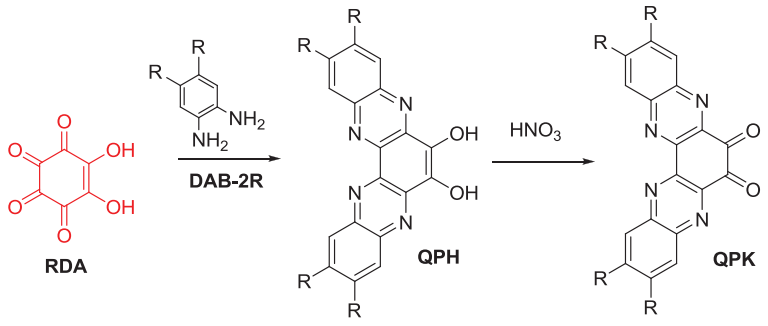

Figure 13 Synthesis of QPK. R=H, Me.

Of the methods explored the use of RDA is the most applicable to a general synthesis of hetero-HATNs. This is due to it being able to form both the QPK and PTK intermediates which can be selected on the basis of the functional groups wanted. If an acid sensitive group is needing to be incorporated into the hetero-HATN, the RDA

method allows the group to be incorporated in either one or two of the peripheral branches after the di or tetrone precursors have formed.

2.3 Synthesis of hetero-HATN

As highlighted in Figure 14 there are two routes available for the synthesis of hetero-HATNs. The first being to create the PTK-2R_1 intermediate followed by addition of two equivalents of DAB-R_2 to form hetero HATN-4$R_2$2R_1. The second is to start with the pre-formed QPK-4R_2 intermediate followed by addition of one equivalent of DAB-2R_2 to give the hetero HATN-4$R_2$2R_1.

As previously discussed in Section 2.2.5 it is preferable to form the tetrone PTK-2R_1 and continue on via that route as this intermediate comes out clean and little purification is needed. This then enables the next step (Route (i)) to proceed quickly without much hassle. On the other hand Route (ii) which involves formation of the dione QPK-4R_2 (see Section 2.2.8) is much more cumbersome and hence only preferred if the addition of a single acid sensitive group was desired.

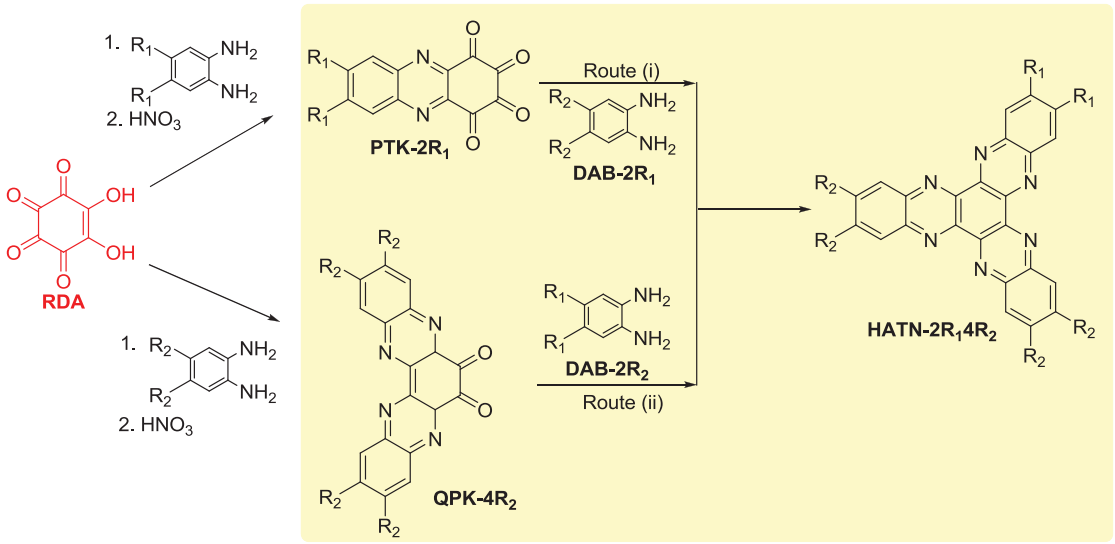

Figure 14 The two routes to hetero-HATN synthesis using rhodizonic acid.

By judicious selection of R_1 the starting materials of the six HATNs, PTK-2R_1 (where R_1 = H, Me, Br) were synthesised. PTK-2R_1 was reacted with the DAB–2R_2 (where R_2 = H, Me, Br and $R_1 \neq R_2$) and heated in a water acetic acid mixture for four hours before impure HATN-2$R_1$4R_2 was filtered off (Figure 14). Purification of the final HATN-

$2R_12R_2$ was done by adding chloroform to the mixture and sonicating for 30 minutes. The mixture was then filtered and the process repeated until all of the impurities had been removed. This gave the products, HATN-4Me, HATN-4Br, HATN-2Me, HATN-4Br2Me, HATN-2Br and HATN-4Me2Br that are investigated in this thesis (Figure 15). In the work-up of these compounds chromatography was not an option as they did not have the required solubility. Crystallisation was tried but successive crystallisations were needed and the sonication provided a faster, albeit more crude, method. The compounds were characterised using ^{1}H NMR and ^{13}C NMR spectroscopies as well as MS. Synthetic details are given in Chapter 7.2.1.

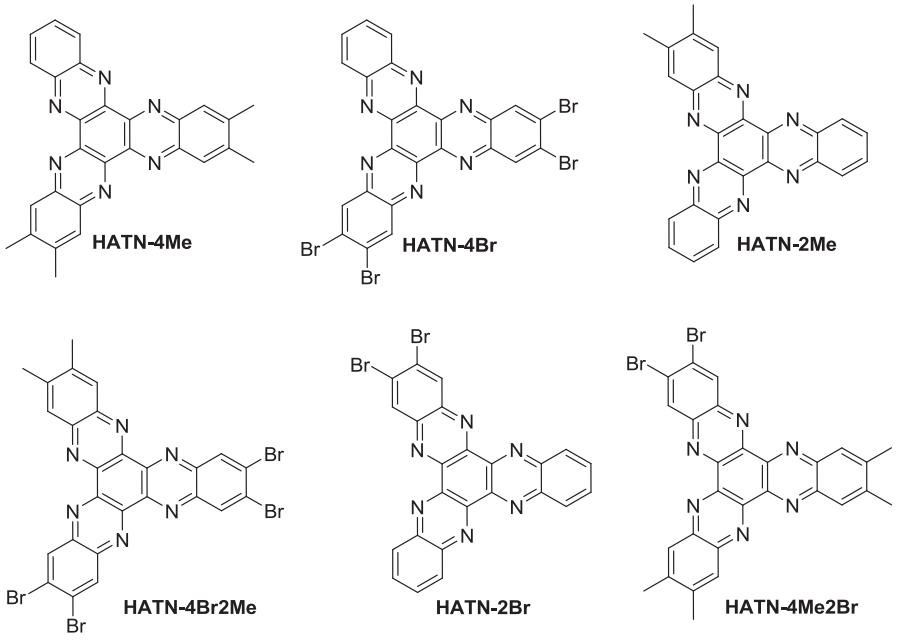

Figure 15 The six HATN compounds synthesised for use in this thesis.

As well as these six HATNs two additional hetero-HATNs were synthesised that contained the carboxylic acid functional group for use in dye-sensitised-solar cells (HATN-4Me1COOH and HATN-1COOH, Figure 16). These were synthesised using the same method as outlined above.

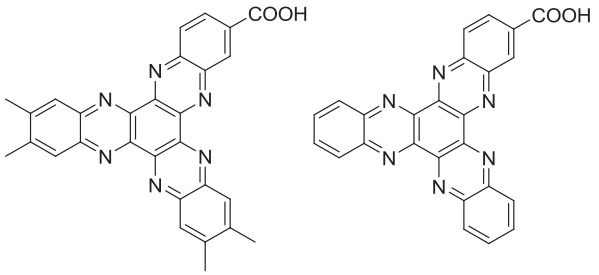

Figure 16 Left: HATN-4Me1COOH Right: HATN-1COOH

The synthesis of HATN-4Me1CN is used to illustrate the alternative preparative route, Route (ii) (Figure 14). Using Route (i) requires oxidation of PTH-1CN with nitric acid and this can occur at either the tetrahydroxy groups to give the tetrone or the CN to give acetamide or carboxylate derivatives, thus inhibiting the cyano incorporation into HATN. However by using Route (ii) QPK-4Me or QPK can be synthesised first followed by reaction with a single DAB-1CN to give HATN-4Me1CN or HATN-1CN respectively.

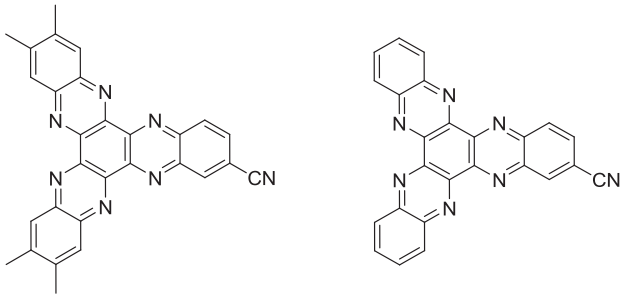

Figure 17 Left: HATN-4Me1CN Right: HATN-1CN

2.3.1 Crystallography of HATN-4Me

Table 2 Crystal data for HATN-4Me

Compound	**$C_{28}H_{20}N_6 \cdot 2CHCl_3$**
Molecular formula	$C_{30}H_{22}Cl_6N_6$
M (g mol^{-1})	679.24
Temperature (K)	163(2)
Crystal System	Monoclinic
Space group	*Cc*
a(Å)	30.116(6)
b(Å)	5.012(1)
c(Å)	26.162(5)
α(°)	90
β(°)	133.02(3)
γ(°)	90
V(Å^3)	2887.1(17)
Z	4
μ(Cu Kα) mm^{-1}	5.707
ρ_{calc} (g cm^{-1})	1.563
2θmax(°)	142.1
Number of unique reflections	4778
Data/restrains/parameters	4778/14/386
Final R indices [I>2σ(I)]	*R*1 = 0.0770
	*wR*2 = 0.2042
R indices (all data)	*R*1 = 0.0851
	*wR*2 = 0.2212
Goodness-of-fit on F^2	1.035

HATN-4Me·2$CHCl_3$ crystallises in the monoclinic system in the space group *Cc*. The structure consists of one molecule of HATN, which is a large, mostly planar, delocalised π-electron system, and two chloroform solvent molecules. Table 2 contains the crystal data which refined to an R value of 7.70 % (see Appendix A for a listing of the bond lengths and angles).

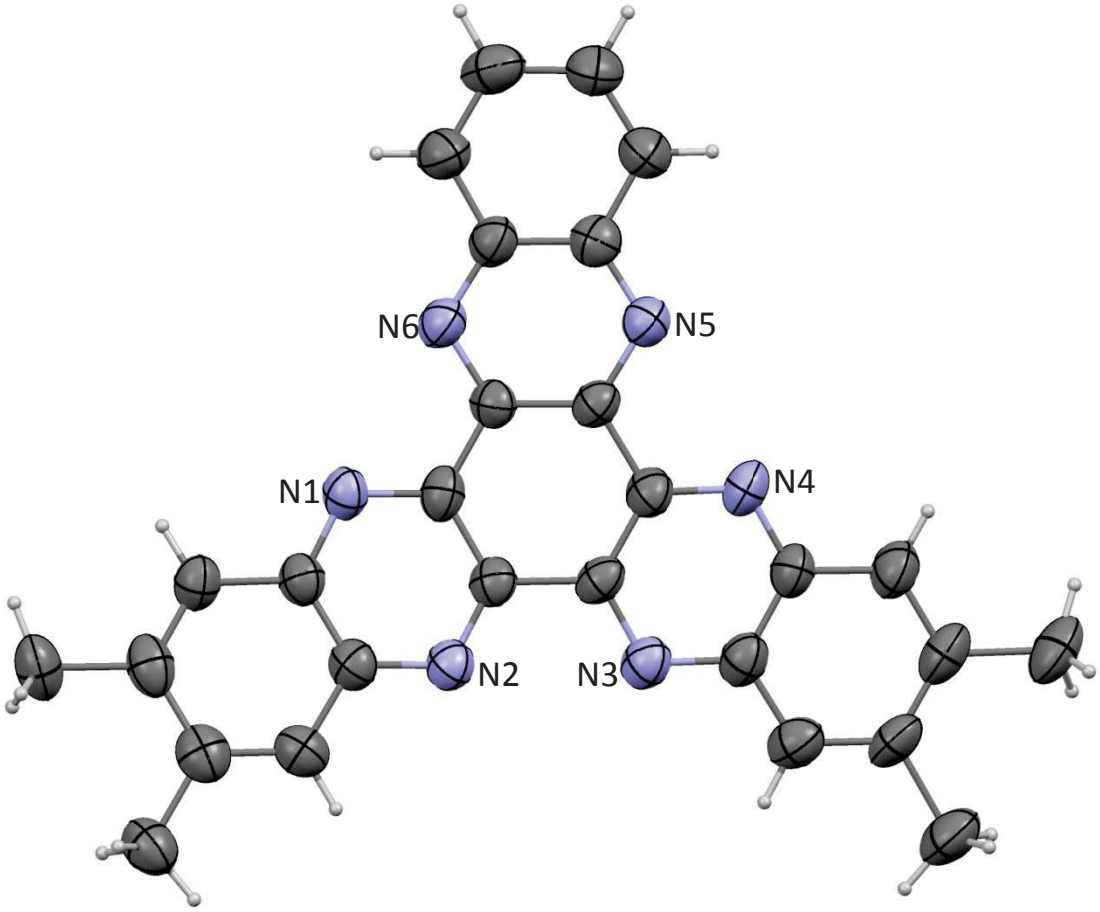

Figure 18 Single crystal structure of HATN-4Me with 50% probability ellipsoids for all atoms excluding hydrogen, and solvent molecules (2$CHCl_3$) removed for clarity.

All non-H atoms lie roughly in a plane where the largest distance of a carbon from the central ring plane is 0.274 Å. The distortion from planarity should have a noticeable effect on the electronic communication provided by this bridging ligand. The main

molecule has C_2 symmetry and the bond distances and angles are quite similar in three different directions. The C-N bond distances lie in the range 1.300(7)-1.363(7) Å, which are shorter than a normal C-N single bond (1.47 Å) and longer than the value of a C=N double bond distance (1.28 Å) due to π-electron repulsion of the bulky system. The aromatic bond distances are in the range of 1.385(10)-1.490(7) Å and all bond angles are about 120˚. These features indicate that HATN has a very large delocalised pi-electron system.

2.4 Mass spectral data of HATNs

In matrix-assisted laser desorption/ionization (MALDI) mass spectrometry, translational energy is passed from the irradiated matrix to the analyte of interest, often through proton or charge transfer resulting in pseudo-molecular ions which are mono-cations or larger molecules exhibiting di- or tri-cationic or charge states. However, there are issues with the analysis of small molecules caused by interference from the matrix compounds, which themselves are small organic molecules.[13]

One class of molecules are the electron deficient small molecules which contain a nitrogen, which when ionized yield the common protonated species $[M+H]^+$, the mass plus one [M+1], (attributed to the presence of 1 ^{13}C) and the mass plus two [M+2], (attributed to the presence of 1 ^{14}C), however with small molecules, the percentage incorporation of ^{14}C is negligible and another possible interpretation may be proton abstraction followed by hydrogen atom incorporation to yield the mass plus two species, which is a mono-cation, or di-protonation followed by electron neutralization of one charge through electron emission from the surface or from the gas plume. Under both scenario's the $[M+2]^+$ cation would be generated.

The essentiality of the matrix can be minimized through use of laser desorption/ionization on engineered surfaces, typically with metal/metal oxides, as a "matrix-free" "MA"LDI. Here the 'MA' component is carried out by the surface, without the limitations imposed by the matrix species and has applications where low mass identification is essential, such as with small molecules (pharmaceuticals or metabolites). In order to develop more efficient surfaces, investigation of the physicochemical properties of these molecules is important.

HATNs have the ability to be detected in MALDI with and without the use of a matrix. They also exhibit the $[M+2]^+$ cation (Table 3). This unusual occurrence has been passed on to another group to investigate using high level DFT calculations. The use of an

Ultra High Resolution Field Desorption Ionization Fourier Transform Ion Cyclotron Resonance Mass Spectrometer will be required to further these studies.

Table 3 HATN MALDI experimental results compared with the calculated results for the 100% peaks.

Ligand	100% peak experimental	100% peak calculated for $[M]^+$
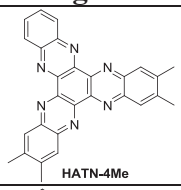 HATN-4Me	442.361	440.17
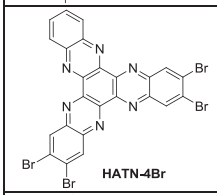 HATN-4Br	702.003	699.75
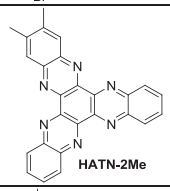 HATN-2Me	414.364	412.14
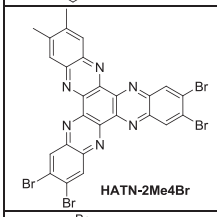 HATN-2Me4Br	729.092	727.78
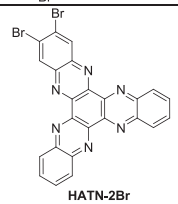 HATN-2Br	543.550	541.93
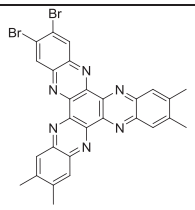 HATN-2Br4Me	600.265	597.99

2.5 Conclusion

Four methods were explored to form hetero-HATNs, but only two provided general procedures to their synthesis. Both start with rhodizonic acid (RDA), with the first reacting with one equivalent of the diaminobenzene (DAB-2R_1) to give PKH-2R_1. This can then be oxidised using nitric acid and further reacted with substituted 1,2-diaminobenzenes to form hetero-HATNs (Figure 19, Route (i)). The second was to use RDA and add two equivalents of DAB-2R_1 to give QPK-4R_2. This was then oxidised using nitric acid and further reacted with substituted DAB to form hetero HATN-4$R_2$2R_1 (Figure 19, route ii).

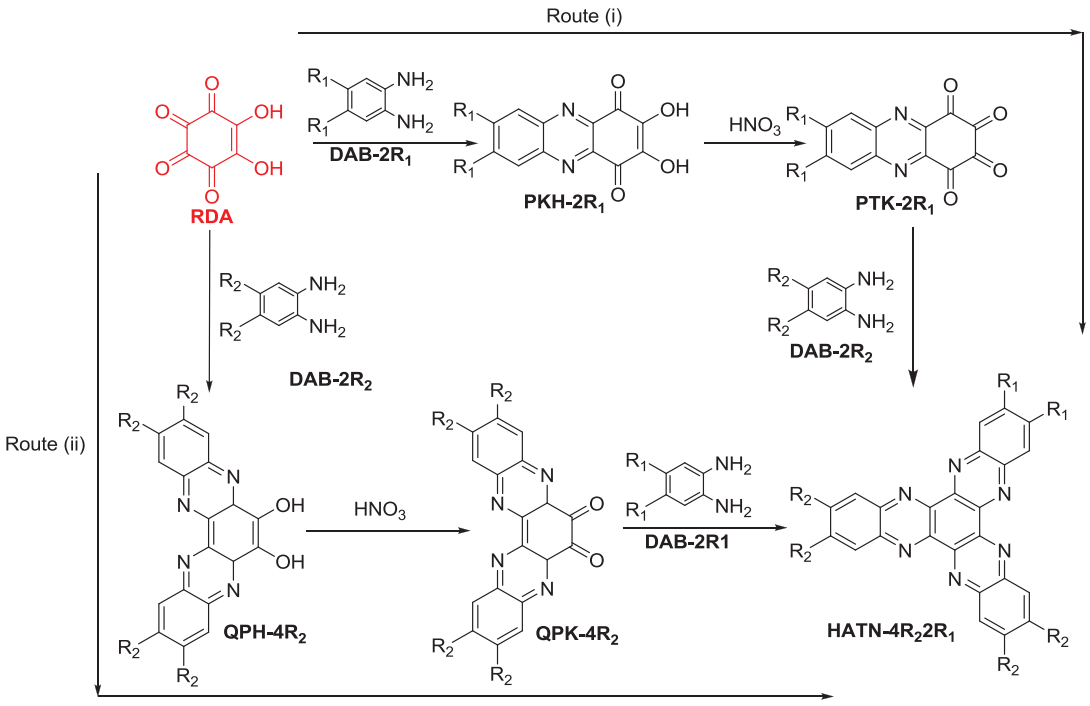

Figure 19 Synthetic routes to forming hetero-HATNs

Of these two routes, Route (i) is preferred due to the intermediates precipitating cleanly so no purification is needed in those steps. Route (ii) requires purification by recrystallisation of QPK using dioxane (see Chapter 7.2.1). This reduces yields and makes this a more tedious route. Both methods are successful at forming hetero-HATNs.

Ten hetero-HATN ligands were successfully synthesised and characterised (HATN-4Me, HATN-4Br, HATN-2Me, HATN-4Br2Me, HATN-2Br, HATN-4Me2Br, HATN-4Me1COOH, HATN-1COOH, HATN-4Me1CN, and HATN-1CN). They contained a range of groups ranging from electron-withdrawing bromo to the weakly electron-donating methyl.

Three crystal structures were obtained for PKH-2Me, PTK-2Me and HATN-4Me. The crystal structure for HATN-4Me showed that it was a large delocalised aromatic system therefore it is safe to assume that all the other hetero-HATNs would have the same delocalised structure. The crystal structure of PTK-2Me shows a gem-diol presence in the ring containing the two keto moieties, and this ring has no aromaticity.

2.6 References

1 Eistert, B.; Fink, H.; Werner, H. K. *Justus Liebigs Annalen der Chemie* **1962**, *657*, 131.

2 Ming-Che Yeh, S.-C. L., Shih-Hua Chao, Chi Wi Ong *Tetrahedron* **2010**, *66*, 8888.

3 Skujins, S. W., G. *Tetrahedron* **1969**, *25*, 3935.

4 Ong, C. W.; Liao, S.-C.; Chang, T. H.; Hsu, H.-F. *Journal of Organic Chemistry* **2004**, *69*, 3181.

5 Marder, S.; Kaafarani, B.; Barlow, S.; Kippelen, B.; Domercq, B.; Zhang, Q.; Kondo, T., **2005,** 2005-US20998 2005123737.

6 Rigaku; Woodlands, R. A. C. T., Ed. 2007; Vol. Version 1.4.0 ed.

7 Rigaku; Rigaku Corporation: Matsubara: 1998.

8 Sheldrick, G. *Acta Crystallographica Section A* **2008**, *64*, 112.

9 Colip, L. A.; Koppisch, A. T.; Broene, R. D.; Berger, J. A.; Baldwin, S. M.; Harris, M. N.; Peterson, L. J.; Warner, B. P.; Birnbaum, E. R. *Journal of Applied Crystallography* **2009**, *42*, 329.

10 Craig, N. C.; Groner, P.; McKean, D. C. *The Journal of Physical Chemistry A* **2006**, *110*, 7461.

11 Klug, A. *Acta Crystallographica* **1965**, *19*, 983.

12 Glockler, G. *The Journal of Physical Chemistry* **1958**, *62*, 1049.

13 Soltzberg, L. J.; Patel, P. *Rapid Communications in Mass Spectrometry* **2004**, *18*, 1455.

Chapter 3

Physical properties of HATN

3.0 Abbreviations

FET	Field Effect Transistor
PV	Photovoltaic
ETM	Electron Transport Material
V_{DS}	Drain-Source Voltage
V_G	Gate Voltage
V_T	Threshold Voltage
ITO	Indium Tin Oxide
DSSC	Dye-sensitised Solar Cell
HJSC	Hetero-junction Solar Cell
IPCE	Incident Photon to Current Efficiency
FF	Fill Factor
J_{SC}	Short Circuit Current
P_S	Input solar radiance
V_{OC}	Open-circuit Voltage
P_{max}	Maximum Power Point Voltage
J_{mp}	Maximum Current Point
I_D	Drain Current

3.1 Introduction

An organic semiconductor is an organic material with semiconductor properties, i.e. having electrical conductivity intermediate in magnitude between that of a conductor and an insulator. Almost all organic solids are insulators, but when their constituent molecules have π-conjugate systems, an electron can move via π-electron cloud overlaps. For this reason semiconductors play an important role in electronic technologies such as organic light emitting diodes (OLEDs),[1] field-effect transistors (FETs)[2] and photovoltaics (PVs).[3]

Organic materials are an attractive area of study due to their potentially low cost, light weight, ability to be manufactured into large-area structures, and chemical flexibility enabling a tuneable band gap.[4] In the past two decades, the vast majority of research in the field has been devoted to hole transporters (p-type) organic semiconductors. Now the focus has leaned towards finding more suitable electron transporters (n-type).[5]

The unique properties of organic semiconductors are based on the versatility to synthesise multifunctional conjugated materials by judicious molecular design. Tailoring the energy band gap of conjugated materials allows variation in emission wavelength, absorptive colours in electrochromic devices, and conductivity in the neutral state.[6] Changes in energy levels also allow optimisation of interfacial energy level alignment between the materials and electrode contacts in organic electronics. Band gap control may potentially be achieved by simply altering substituents around a core, for example introduction of halogen groups can increase electron-withdrawing properties and electron-transporting properties.[7]

At the moment there is interest in π-conjugated electron deficient molecules based on nitrogen heterocycles, for example pyrazine and quinoxaline (Figure 1) because they generally have low LUMO levels and less negative reduction potential than their non-nitrogen analogues.[8] This has made them attractive for molecular devices such as FETs and PVs.[9]

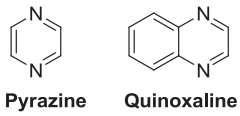

Figure 1 Nitrogen containing π-conjugated heterocycles

3.1.1 Field effect transistor background

A field-effect transistor (FET) is a transistor that uses an electric field to control the conductivity of a channel of one type of charge carrier in a semiconductor material so as to act as an amplifier or switch. It took almost six decades until 1987 when Koezuka and co-workers[10] reported the first organic field-effect transistor based on a polymer of thiophene molecules. Since then many organic-FETs (OFET) employing many aromatic and conjugated materials as the active semiconducting layer have been reported. OFETs have been developed to realize low-cost, large-area electronic products and/or biodegradable electronics.[11] A schematic of mobility (how quickly an electron/hole can move through a semiconductor, when pulled by an electric field.) versus discovery is plotted below (Figure 2).

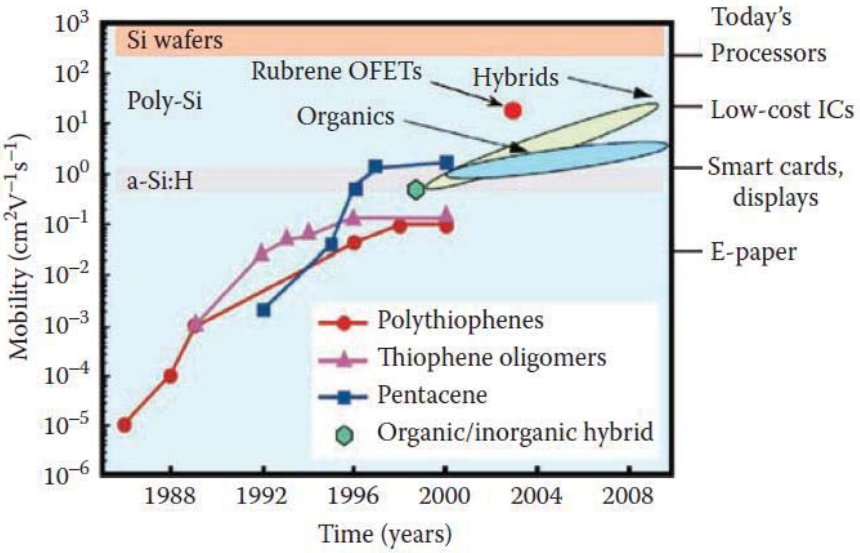

Figure 2 Comparison of mobility versus year for different charge carriers.[12]

The performance of OFETs can compete with that of amorphous silicon (a-Si) thin-field transistors (TFTs) with field-effect mobilities of 0.5 $cm^2V^{-1}s^{-1}$. Currently, thin-film OFET mobility values of 20 $cm^2V^{-1}s^{-1}$ have been reached in the case of vacuum-deposited small molecules (such as Rubrene at RT).[13] As a result, there is now a greater industrial interest in using OFETs for applications that are currently incompatible with the use of amorphous Si or other inorganic transistor technologies. One of their main technological attractions is that all the layers of an OFET can be deposited and patterned at room temperature by a combination of low-cost solution-processing and direct-write printing, which makes them suited for low-cost, large-area electronic functions on flexible substrates.

3.1.2 Field effect transistor make-up

Three essential components of field-effect transistors are the source, the drain and the gate (Figure 3). A charge induced at the gate controls the amount of current that can flow between the source and the drain. The insulator is often made from SiO_2 and the electron transport material (ETM) is the organic material to be tested.[14-16] There are many different ways in which the ETM can be deposited such as electrospray,[17] solution casting,[18] spin coating,[19] and vacuum deposition.[20] The last two will be investigated in this thesis. In spin coating the introduction of ETM can be done under ambient conditions and the equipment is commonly available. Vacuum deposition is a more controlled method allowing specific ETM film thicknesses.

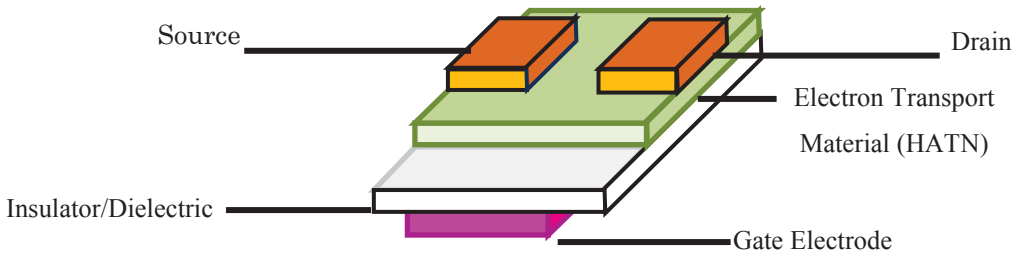

Figure 3 Schematic construction of an OFET

At the molecular level, the OFET works by a process of 'band bending'.[21] If there is zero bias, i.e. no external applied voltage at the gate, the electrons are unable to travel

between the source and the drain. When a positive charge is applied at the gate, the accumulation of holes at the gate interface leads to a build-up of electrons at the ETM, causing the bending of the ETMs HOMO and LUMO bands hence lowering the conduction band with regard to the Fermi-level of the semiconductor (Figure 4, left). Once sufficient 'bending' has been achieved a conductive channel forms at the interface so electrons are able to move from source to the drain (Figure 4). This voltage is also known as the threshold voltage, V_T (Figure 4, right).[22]

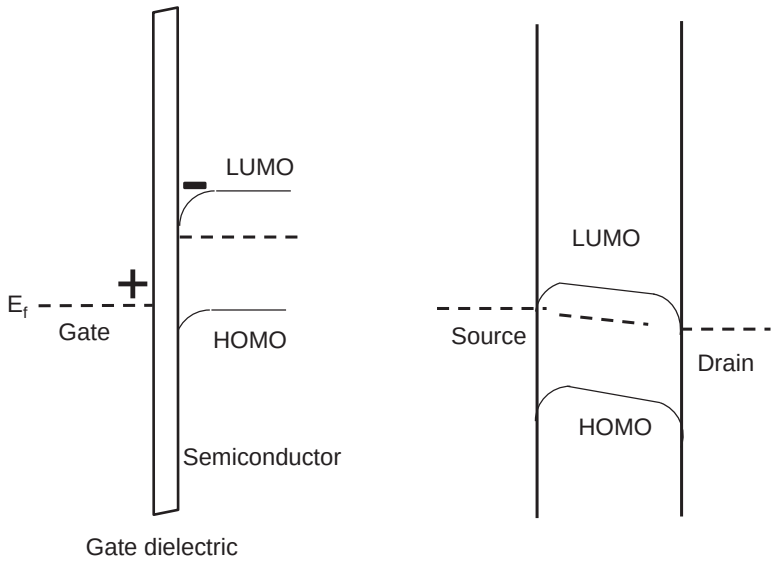

Figure 4 Schematic graphs of band-bending in the OFET. Left: Build-up of holes by a positive bias being placed on the gate leading to a negative charge build-up in the semiconductor. This causes 'band bending'; the lowering of the effective HOMO and LUMO orbitals. Right: The lowered HOMO and LUMO orbitals enable the transfer of electrons between the source and the drain.

Once there is current flow the electron mobility, μ, is obtained. This measurement characterizes how quickly an electron can move through a semiconductor, when pulled by an electric field, E.

$$\mu = \frac{E}{\nu_d} \qquad \textbf{Equation 1}$$

where ν_d is average drift-velocity of the electrons.

3.1.2.1 Measurements

There are two important regions in FET measurements, the linear region and the saturated region. These can clearly be seen in a graph of the drain current (I_D) versus the voltage between the drain and source (V_{DS}). Linear characteristics occur when the transistor is turned on, and a channel has been created which allows current to flow from the source to the drain. This is indicated by the curves on the left hand side of the red dashed line in Figure 5. Saturation then occurs when there is zero slope obtained, this is sometimes called active mode, indicated by the straight line on the right hand side of red dashed line in Figure 5. [22]

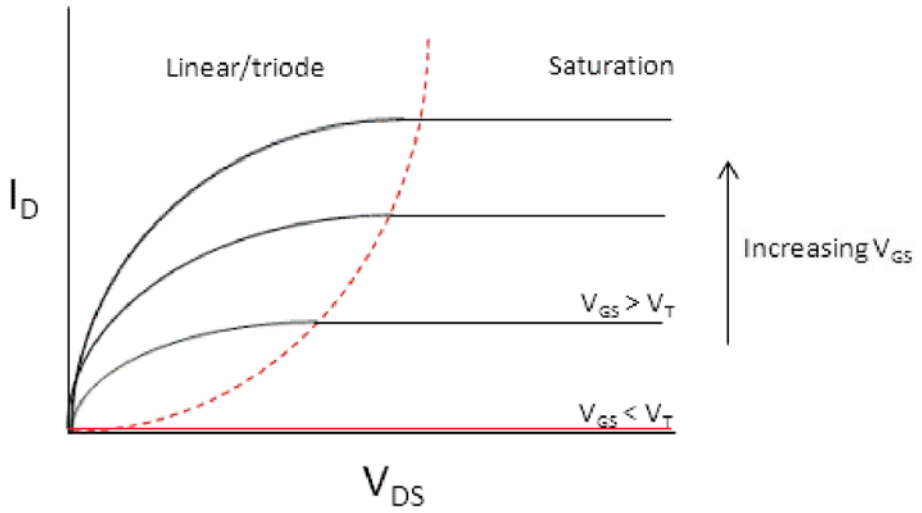

Figure 5 Schematic of current flow in an FET with the regions of operation noted.

Figure 6 is a schematic showing the $I_D^{1/2}$ versus V_{GS} transfer characteristic. The importance of this graph is that the threshold voltage, V_T can be extrapolated.[22]

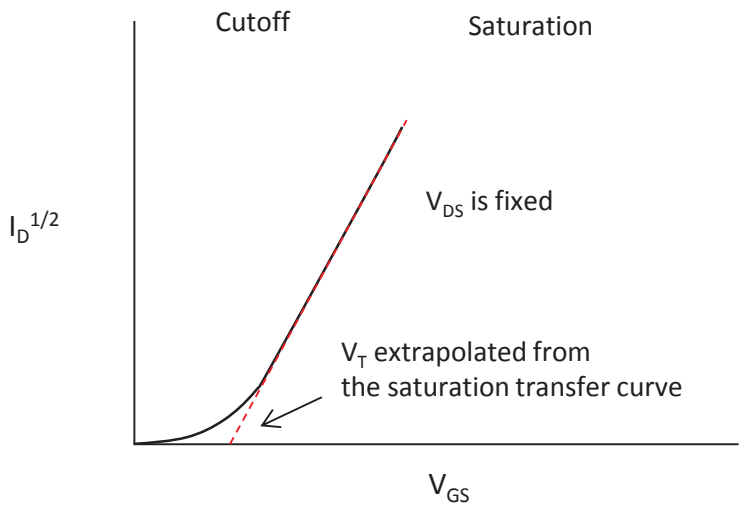

Figure 6 : A figure schematically showing the extrapolation of V_T from $I_D^{1/2}$ – V_{GS} transfer characteristic.

The sub-threshold slope is the inverse slope of the log(I_D) versus V_{GS} measured below the threshold (Figure 7). The threshold voltage can be taken as the point at which the current deviates from the exponential character expected from purely diffusive transport.[22]

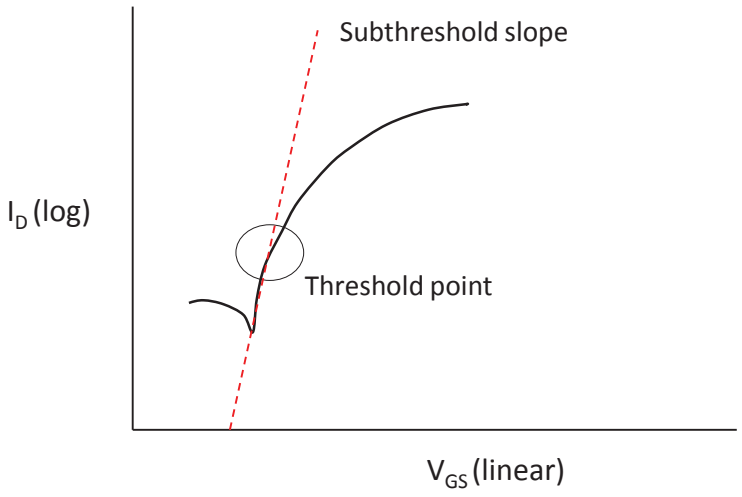

Figure 7 A schematic showing the subthreshold voltage/current characteristic and the subthreshold slope extraction. The threshold voltage can be taken as the point at which the current deviates from the exponential character expected from purely diffusive transport.

The linear regions should be plotted as I_D versus V_{GS}. The saturation region is often plotted with the linear region together in the literature using a split axes.[23-26] Velocity-based charge carrier mobility can be determined from the linear graph when the total charge from capacitance measurements or charge modelling is known. The determination of threshold voltage can be determined by extrapolation.

The linear region measurement should ideally be taken at the lowest value of V_{DS} as possible. For pentacene, the operation value is -20V so the linear curve could be taken at -0.1V.[26] It is only for low values of V_{DS} that the electric field and charge density in the channel is uniform and the measurement of mobility is valid. Mobility varies significantly as a function of gate voltage. It should therefore be measured and reported as a function of V_{GS} by taking the slope tangent at each V_{GS} individually. The saturation curve is given at -20 V for pentacene. From this the threshold voltage can be obtained.

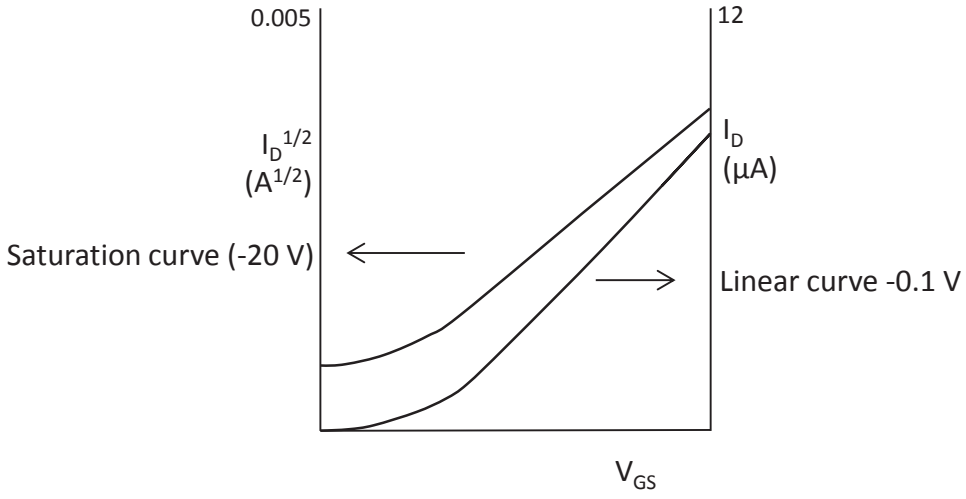

Figure 8 A sample device transfer measurement showing both the saturation and linear characteristics on one graph.

One common feature of OFET materials is the inclusion of an aromatic or otherwise conjugated π-electron system, facilitating the delocalization of orbital wavefunctions. Electron withdrawing groups or donating groups can be attached that facilitate hole or

electron transport. A popular OFET material is pentacene, which has been used since 1980s. However, pentacene has 10 times lower hole mobility than that of rubrene (OFET with highest mobility)(Figure 9).[27] The major problem with pentacene, as well as many other organic conductors, is its rapid oxidation in air.[27]

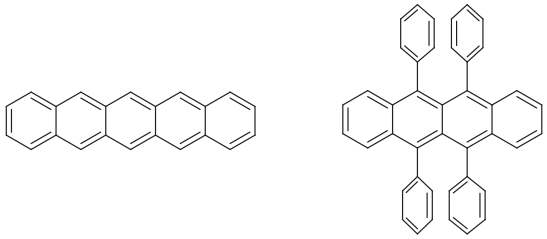

Figure 9 Left: Pentacene. Right: Rubrene.

Yamashita et al.[28] briefly looked into the use of HATN-6Cl and HATN-6F for field effect transistors (Figure 10). They found that they had good electron affinity and moderate field-effect mobility in thin films with electron mobilities of 2.8×10^{-5} $cm^2V^{-1}s^{-1}$ and 9.6×10^{-3} $cm^2V^{-1}s^{-1}$ respectively. The films had a high threshold voltage of around 40 V, too high for use in standard devices.[28]

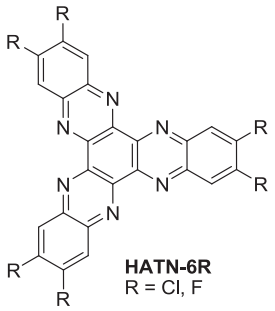

Figure 10 HATN-6R used in OFET studies.

3.1.3 Photovoltaics

Photovoltaics (PVs) are best known as a method for generating electric power by using solar cells to convert energy from the sun into a flow of electrons.[29] The PV effect refers to photons of light exciting electrons into a higher state of energy, allowing them to act as charge carriers for an electric current. PV generation of electricity already supplements society's demand for fossilised fuels, and as demand for electricity grows and supply of fossil fuel decreases the need for alternative energy sources will increase.[30]

PV devices made from purely organic materials have the advantage of being cheap and easy to process. Organic materials can be deposited on flexible substrates and are bendable unlike their inorganic counterparts, although not yet as efficient. There are two main types of photovoltaic devices. The first is a dye-sensitized solar cell (DSSC) and the second a junction cell which will be discussed briefly.

3.1.3.1 Dye-Sensitized Solar Cell

Dye Sensitized Solar Cells (DSSCs), commonly known as Gratzel cells, are of interest as they mimic natural occurring processes from nature. Light is used and converted into energy which can be stored or used directly.

A typical cell is depicted in Figure 11. It consists of a transparent electrode such as glass coated with indium tin oxide (ITO) supporting a layer of nanocrystalline, mesoporous TiO_2. The TiO_2 surface is sensitised with a dye.[31] The circuit is completed with a counter electrode of platinum and a redox-active electrolyte, typically containing an iodide/triiodide redox couple. The whole assembly is hermetically sealed and no other complicated procedures are necessary thus minimising production costs. Due to their simple construction these cells offer hope of a significant reduction in the cost of solar electricity.

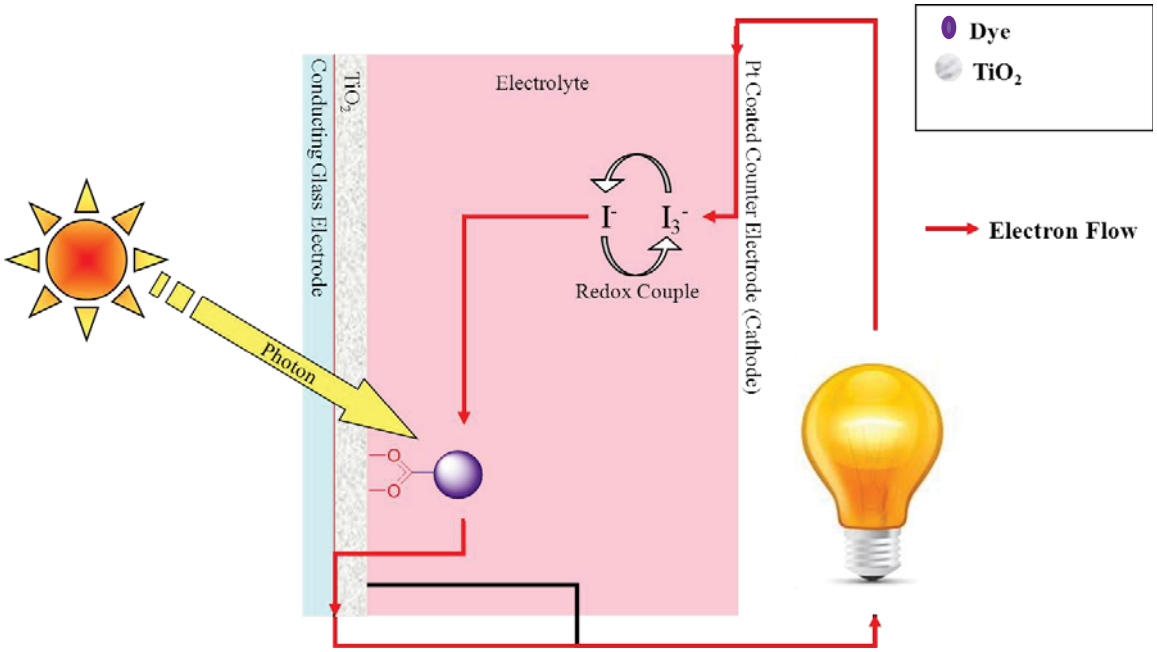

Figure 11 DSSC schematic.

In DSSCs the photosensitizer is one of the most important components influencing solar cell performance as the choice of sensitizer determines the photo-response of the DSSC and initiates the primary steps of photon absorption and subsequent electron transfer process. Polypyridine complexes of Ru have been the first choice of dyes in most of the studies due to their high efficiencies, broad absorption bands, high extinction coefficients and high electron transfer values. Ru-complexes based on carboxy bipyridyls or carboxy terpyridyls such as N3, N719, Z907 and 'black dye' Ru(II) were developed by Gratzel and coworkers and are used worldwide as benchmark reference dyes.[32] Their structures and efficiencies (η, the solar conversion efficiency) are shown in Figure 12.

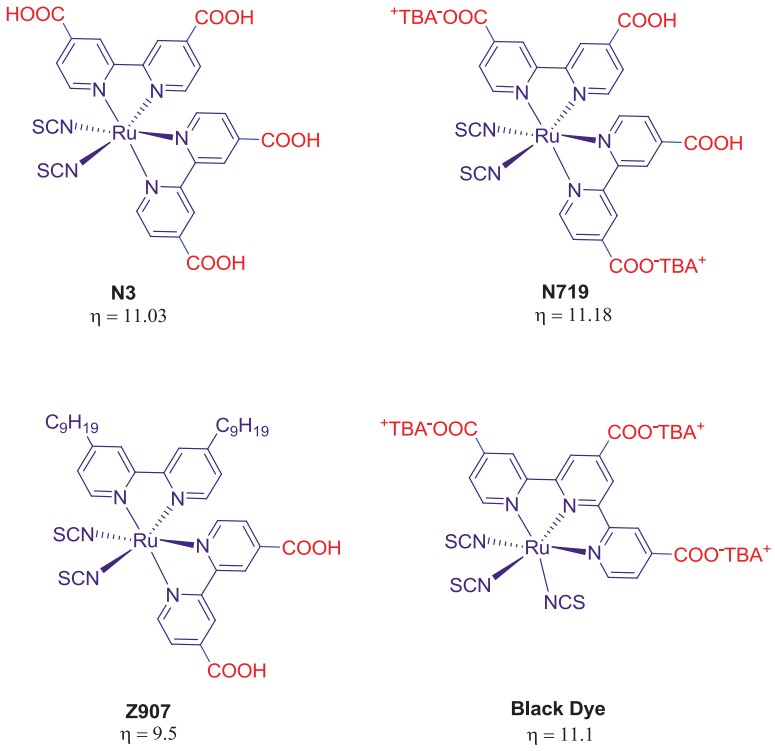

Figure 12 Common dyes used for DSSC work.

Although the N3 dye is highly efficient at converting absorbed photons into free electrons in the TiO_2, only photons absorbed by the dye ultimately produce current. The rate of photon absorption depends upon the absorption spectrum of the sensitized TiO_2 layer and upon the solar spectrum. The overlap between these two spectra determines the maximum possible photocurrent. The dye molecules typically used generally have poorer absorption in the red part of the spectrum compared to silicon, which means that fewer of the photons in sunlight are usable for current generation. These factors limit the current generated by a DSSC, for comparison, a traditional silicon-based solar cell offers about 35 mA cm^{-2}, whereas current DSSCs offer about 20 mA cm^{-2}.[33]

Upon photoexcitation with visible light an electron in the adsorbed dye molecule is excited from the highest occupied molecular orbital (HOMO) to the lowest unoccupied molecular orbital (LUMO). Subsequently charge transfer from the adsorbed molecules to the surface can occur if the LUMO overlaps energetically with the conduction band of the substrate. The non-absorption of photons carrying less energy than the

semiconductor band gap and the excess energy of photons, larger than the band gap, are the two main losses in the energy conversion process using solar cells. Both of these losses are thus related to the spectral mismatch of the energy distribution of photons in the solar spectrum and the band gap of the semiconductor material. Solar cell efficiency is the ratio of the electrical output of a solar cell, to the incident energy, in the form of sunlight. This is the Incident Photon to Charge Carrier Efficiency or IPCE. Figure 13 shows the IPCE for the Black dye and N3 dye.[34]

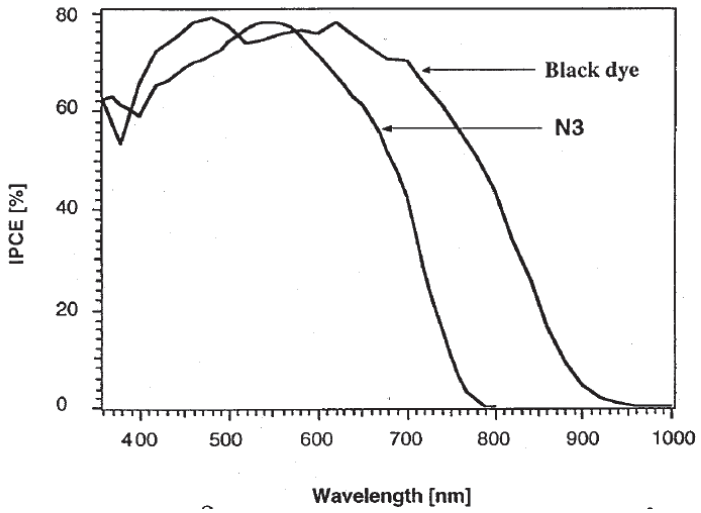

Figure 13 IPCE for N3 dye.[34]

The ideal sensitizer for a single junction photovoltaic cell converting standard global AM 1.5 sunlight to electricity should absorb all light below a threshold wavelength of about 920 nm. In addition, it must also carry attachment groups such as carboxylate or phosphonate to firmly graft it to the semiconductor oxide surface. Upon excitation it should inject electrons into the solid with a quantum yield of unity. The energy level of the excited state should be well matched to the conduction band of the oxide to minimize energetic losses during the electron transfer reaction. Its redox potential should be sufficiently high that it can be regenerated via electron donation from the redox electrolyte or the hole conductor. Finally, it should be stable enough to sustain about 10^8 turnover cycles corresponding to about 20 years of exposure to natural light.[35]

In addition to conventional Ru-complex sensitizers, metal-free analogues in the form of organic dyes have also been investigated in DSSCs.[36,37] The photovoltaic performance of the organic-dye sensitizers has continually improved. Organic dyes have several advantages:

1) There are fewer concerns about limited resources, because they do not contain noble metals such as ruthenium.

2) They have large absorption coefficients due to the intra-molecular π-π* transitions

3) There are a wide variety of structures, each of which is relatively easy to modify.[38]

Uchida and co-workers designed indoline-based dyes for use as sensitizers in DSSCs (Figure 14).[39] An efficiency of 9.5 % was obtained. Even though these indoline compounds have a narrower absorption band than N3, they show high photocurrent because of their large incident photon to charge carrier efficiencies. It was also found to be essential to incorporate a bulky conjugated electron-donating group to prevent stacking and a rigid π conjugative space to harvest solar spectrum effectively.

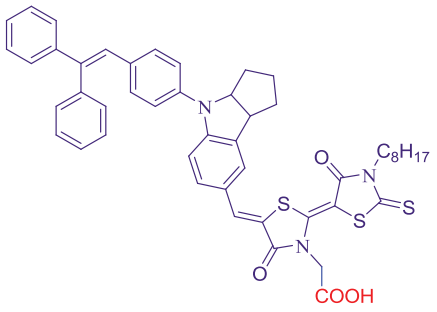

Figure 14 Indoline-based dye for use in DSSC with η = 9.5 %.

However, the performance of DSSCs based on organic dyes has not yet exceeded those based on Ru complexes. To achieve higher performances for solar cells based on organic dyes, comparable to those for solar cells based on Ru complexes, sophisticated molecular design of organic dyes is required.

3.1.3.2 Hetero-junction solar cell

A hetero-junction solar cell (HJSC) consists of an electron donor and an electron acceptor (Figure 15). Light generates excitons in the donor with subsequent separation of charges in the interface between an electron donor and acceptor. These charges then transport to the device's electrodes where these charges flow outside the cell, perform work and then re-enter the device on the opposite side. The cell's efficiency is limited by several factors especially non-geminate recombination.

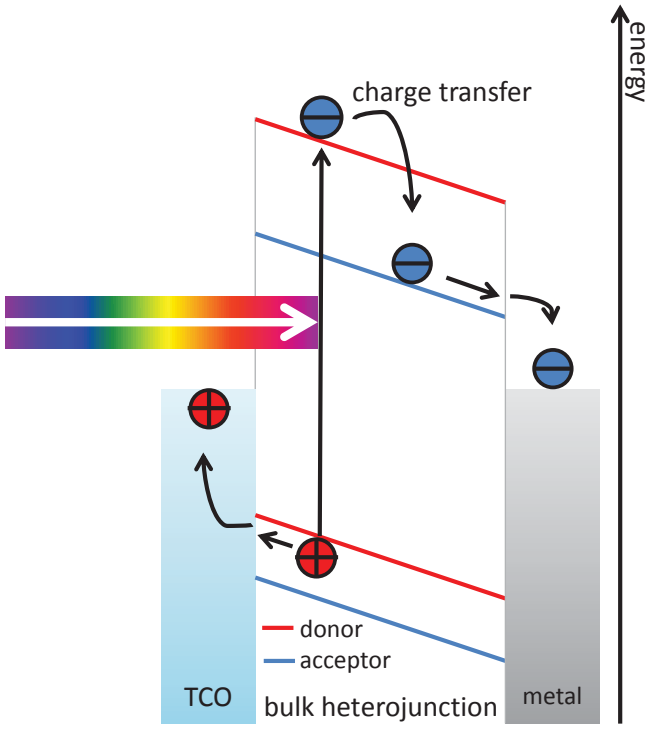

Figure 15 Schematic of HJSC with indication of orbital energy requirements

The molecules forming the electron donor region of organic PV cells, where exciton electron-hole pairs are generated, are generally conjugated polymers possessing delocalized π electrons. These π electrons can be excited by light (in or near the visible part of the spectrum) enabling an electron transition from the molecule's highest occupied molecular orbital (HOMO) to the lowest unoccupied molecular orbital (LUMO), denoted as a π→π* transition.[40]

The main difference between bi-layer hetero-junction and bulk hetero-junction devices is the separation of the donor and acceptor materials. In the bi-layer hetero-junction solar cell the donor and acceptor materials are separated by an interface whereas in the bulk hetero-junction solar cell they are mixed in a single layer increasing the interfacial surface area.

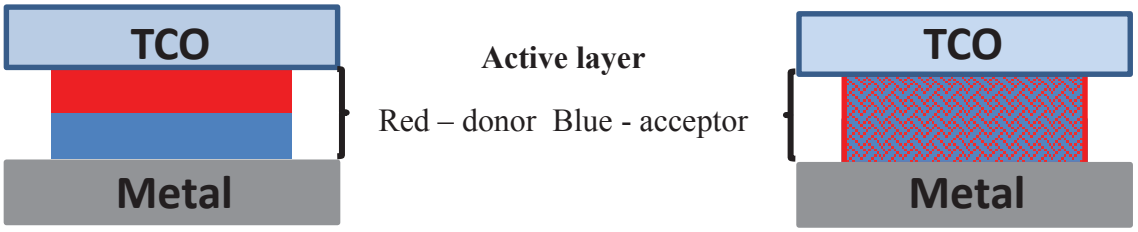

Figure 16 Schematic of the architecture of a bi-layer hetero-junction solar cell (left) and a bulk hetero-junction solar cell (right).

The common design strategy for high performance PV cells is an electron-rich donor and electron-deficient acceptor. A common blend is the donor poly(3-hexylthiophene (P3HT) with the acceptor PCBM.[41-44] The donor should have as small a band gap as possible (with 1.1 eV being the target due to absorption possibility of 77% of solar photons) but still having a high overall extinction coefficient). [45]

The HOMO level of the donor and the LUMO level of the acceptor are also very important, where a method to improve efficiency would be to manipulate the LUMO level of the acceptor.[46] The LUMO level of donor materials has to be at least 0.3-0.8 eV higher than that level of the ETM to guarantee a downhill driving force for the energetically favourable electron transfer.[47]

After exciton dissociation, the electron and hole must be collected at contacts. If charge carrier mobility is insufficient, the carriers will not reach the contacts, and will instead recombine at trap sites or remain in the device as undesirable space charges that oppose the drift of new carriers. The latter problem can occur if electron and hole mobilities are

not matched. In that case, space-charge limited photocurrent hampers device performance.

HATN-6Cl has been previously investigated as an electron transport material (ETM) for p-i-n solar cells (similar to heterojunctions but there is an intrinsic or undoped layer sandwiched between the p and n materials). Because of its large optical energy gap of 2.7 eV and has well suited energy level positions, the material can be implemented as a semi-transparent spacer layer between the reflecting metal contact and the photoactive C_{60} acceptor layer in p-i-n type solar cells. Applying HATN-6Cl instead of the reference ETM, C_{60}, results in a considerably improved photocurrent density and accordingly in a higher efficiency. The power conversion efficiency is more than doubled from 100 nm C_{60} (0.5%) to 100 nm HATN-6Cl (1.1%).[48]

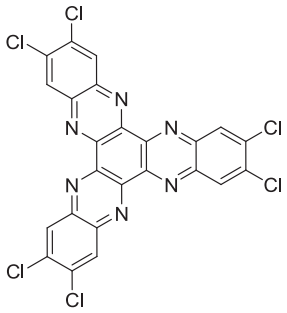

Figure 17 HATN-6Cl used in hetero-junction solar cell studies.

3.1.3.3 Data Acquisition

The performance of a solar cell can be determined by several values, the fill factor (FF) or efficiency (η). Both are determined using a current-voltage curve which yields important operational parameters (Figure 18).

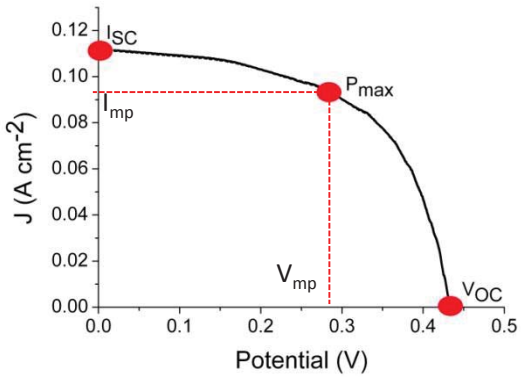

Figure 18 Sample J-V curve.

Among which are the short-circuit current I_{SC}, the open-circuit voltage V_{OC}, the current, I_{mp}, voltage, V_{mp}, and J is the current density; the current per unit area of cross section. At the maximum power point, P_{max} these are used to determine the fill factor, or FF (see Equation 2).[49]

$$FF = \frac{P_{\max}}{V_{OC} I_{SC}}$$ **Equation 2**

The fill factor does not depend on the area of the device. For practical Si photovoltaic cells, the fill factor ranges from approximately 0.70 to 0.85. Most practical applications would require more power. Fortunately one can increase the voltage by adding more cells in series, and one can increase the current by wiring more cells in parallel. This is how PV modules are produced.[49]

A more conventional measure of solar cell performance is by calculating the solar conversion efficiency, which is given by

$$\eta = \frac{FF \cdot V_{OC} J_{SC}}{P_S}$$ **Equation 3**

Where P_s is the input solar irradiance (e.g., Wm^{-2} or $mWcm^{-2}$). This quantity is best measured with a broadband pyranometer (sensitive to all wavelengths), or in our case, using a calibrated detector with similar spectral sensitivity as the device (solar cell) under test.[49]

3.1.3.4 Design and Fabrication of Test Equipment

Campbell et al. developed a quick and efficient method and apparatus to test the efficiency of a solar cell dye.[50] This consists of a light source designed to emit a broad spectrum white light similar to that of the sun with an adjustable stage for cell placement (Figure 19, left). The cell is a circuit completed by the introduction of the dye absorbed on TiO_2 upon an ITO covered glass slide (Figure 19, right cell Bottom: Dye absorption schematic).

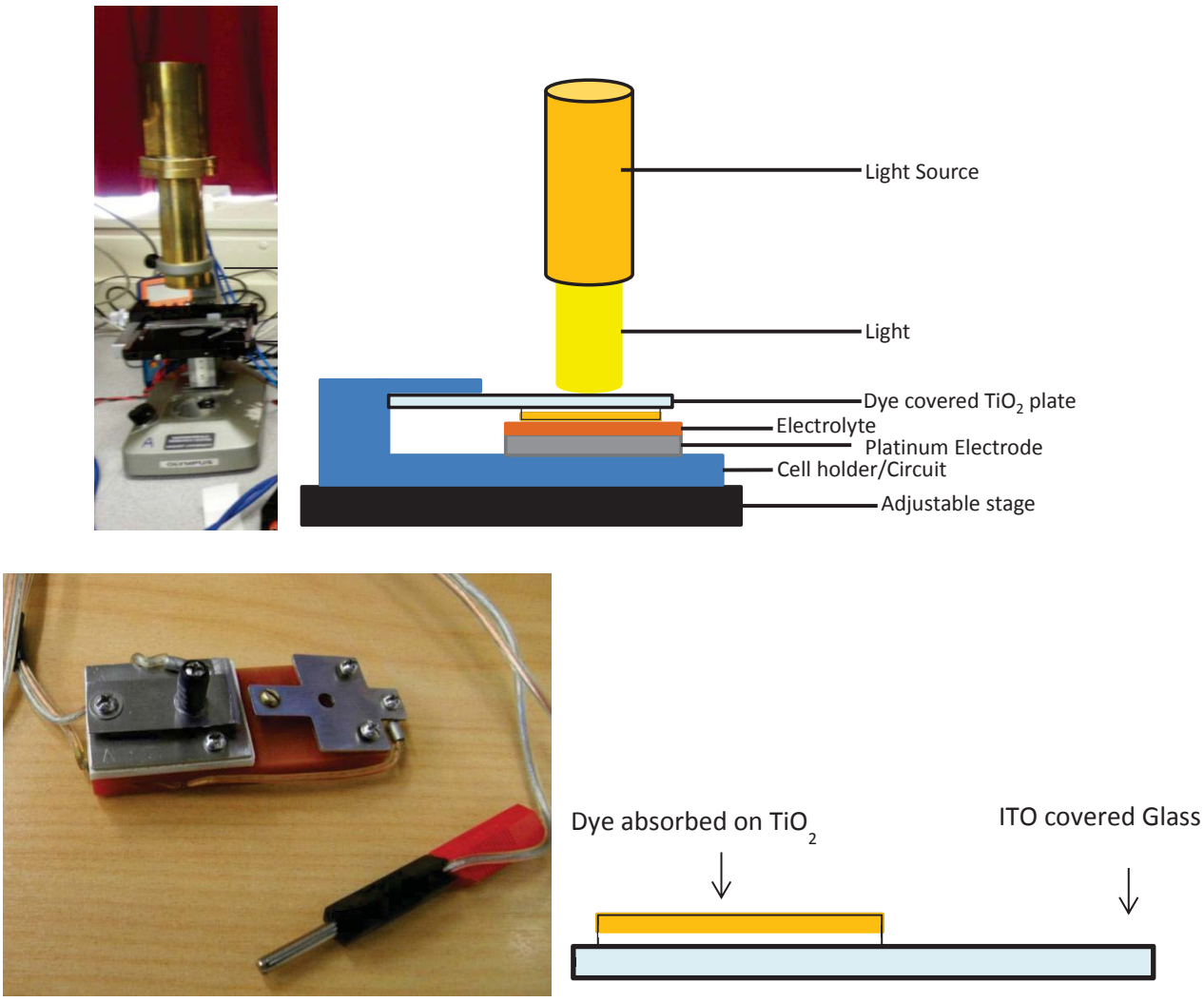

Figure 19 Left Top: Light source with adjustable stage for calibration. Right Top: Schematic of DSSC set up. Left Bottom: Cell holder used for testing DSSCs. Right bottom: Dye covered plate.

As this system is very modular it is possible to rapidly test a range of cell variations such as the type of TiO_2 used (rutile, anatase, brookite) or the electrolyte. Although this testing rig does not accurately reproduce the solar spectrum, at best, it provides an in-house way of comparing the efficiency values of devices which it typically under-estimates by 0.5% relative to a hermetically sealed cell.

3.2 Current Research

This chapter focuses on the photophysical and electrochemical properties of the hetero-substituted HATNs synthesised in Chapter 2 (Figure 20). These measurements were used to determine the suitability of these ligands for use in molecular devices such as PV and FETs.

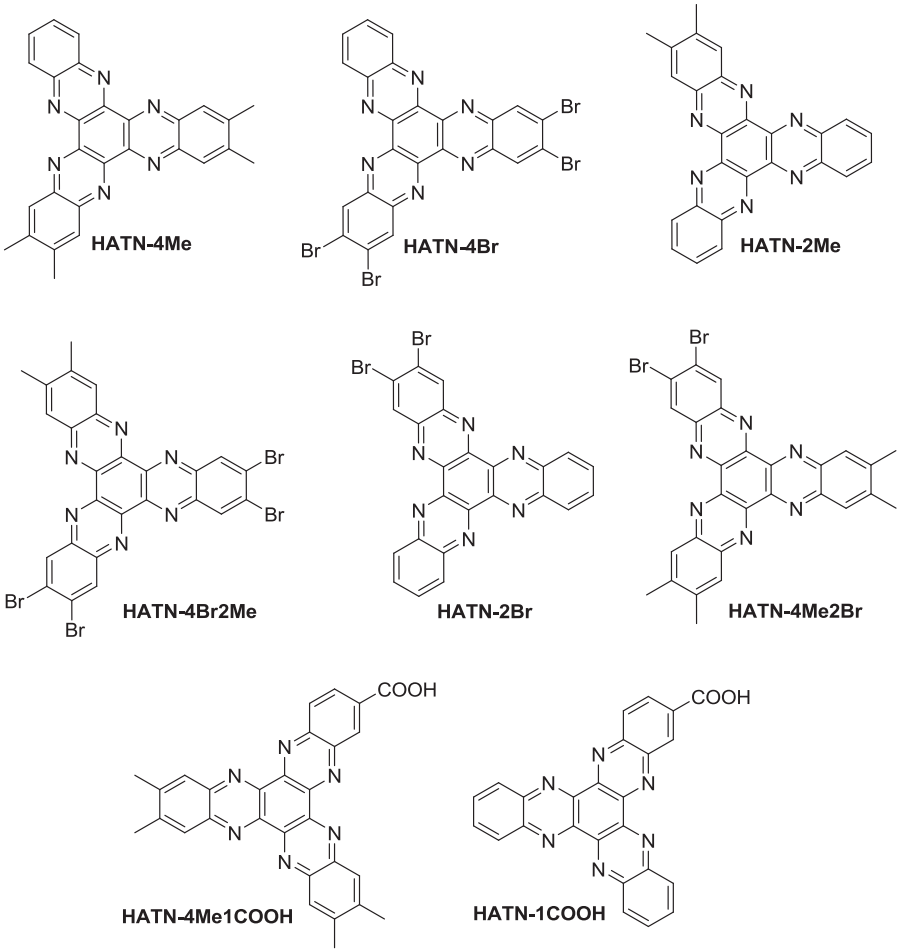

Figure 20 Hetero-HATNs used in Chapter 3.

Electronic absorbance and electrochemical data were recorded in chloroform for these ligands. Density functional theory (DFT) calculations were carried out using the Gaussian 09 package (Gaussian, Inc).[51] Frequency and time-dependent-DFT (TD-DFT) calculations were performed on optimised ground-state structures, all results were displayed using GaussView 5.[52] All calculations used the 6-31G(d) basis set employing the B3LYP level. An unambiguous assignment of vibrational modes from visual

comparison of IR and FT-Raman spectra was possible for most peaks (calculated frequencies were scaled by 0.96). TD-DFT calculations were carried out in an chloroform solvent field using the SCRF-PCM method which creates the solvent cavity via a set of overlapping spheres.[53] Geometry optimisations were not carried out in a solvent field, due to computational expense; however, correlation is found to be better than for calculations where solvent contributions have been completely neglected.

As a means of determining the accuracy of these models, the calculated N—C bond lengths were compared to those obtained from crystallographic data (see Appendix B). This gave a mean absolute deviation (MAD) of 0.025 Å.

In addition to structural accuracy, the electronic accuracy of the models was measured by comparison of the calculated vibrational frequencies to the IR and FT-Raman (example Figure 21); the output frequencies were scaled by 0.96. As these ligands did not contain unique vibrational modes, the mean average deviation values were calculated using all the assigned vibrational modes. This gave a range of MAD values of 5.9 cm^{-1} (HATN-4Me) to 17.0 cm^{-1} (HATN-2Br) (See Appendix B).

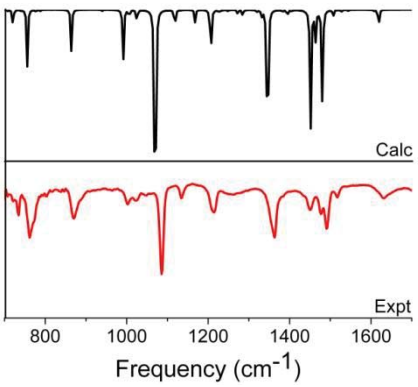

Figure 21 Comparison between calculated and experimental IR spectrum for HATN-4Me.

3.2.1 Electronic absorbance

The electronic spectra of HATNs (HATN-4Br, HATN-2Br, HATN-4Me, HATN-2Me) displayed two $\pi \rightarrow \pi^*$ transitions, the first at 413.5-418 nm with a second less distinguished band at 389-396 nm (as well as other $\pi \rightarrow \pi^*$ and $n \rightarrow \pi^*$ transitions below 350 nm) (see Figure 22).

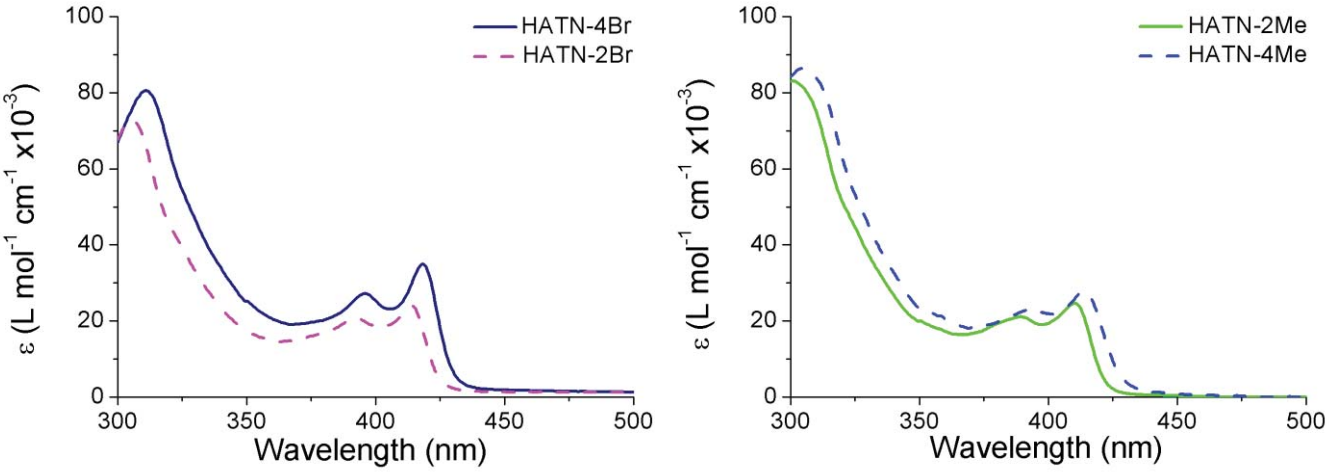

Figure 22 Electronic absorbance spectra of, left: HATN-2Br and HATN-4Br, right: HATN-2Me and HATN-4Me

A comparison of HATN-2Br and HATN-4Br demonstrated that as the bromine substitution was increased a very slight red-shift of ~4 nm occurred for the two lowest absorption bands (see Table 1). This behaviour is consistent with bromine acting as an electron withdrawing group and further explained using TD-DFT calculations (see Appendix B for full assignment). They show that the lowest energy transition consists of a simple $\pi \rightarrow \pi^*$ transition involving only the HOMO and LUMO orbitals (see Figure 23). As bromine substitution was increased, that is HATN-2Br to HATN-4Br, the HOMO energy was only lowered by 0.07 eV (-6.53 eV to -6.60 eV) while the LUMO was lowered by 0.15 eV (-2.93 eV to -3.08 eV).

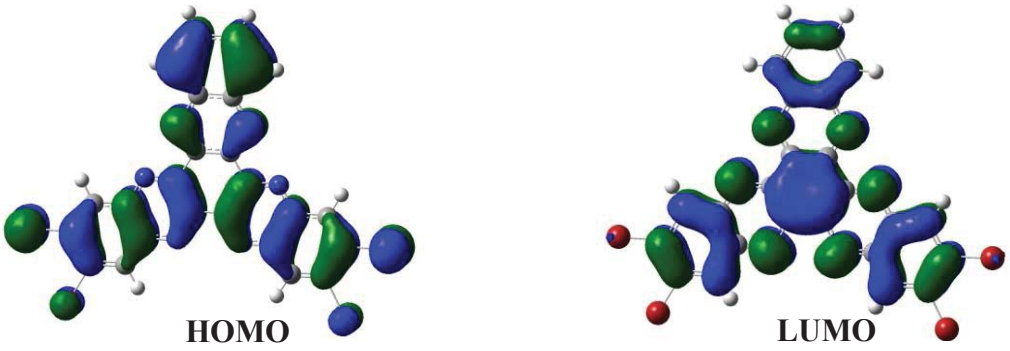

Figure 23 HOMO and LUMO orbitals of HATN-4Br.

Table 1 λ_{max} and absorption coefficients of selected HATNs.

HATN	λ / nm (ε / 10^3 L $mol^{-1}cm^{-1}$)
HATN-2Br	414 (24.1), 392.5 (20.8)
HATN-4Br	418 (37.1), 396 (29.3)
HATN-2Me	410 (24.6), 389 (21.1)
HATN-4Me	413.5 (27.7), 393 (23.1)
HATN-6Me[a]	413 (30.6) , 391 (20.6)

[a]UV/Vis measured in DCM, values from the literature.[54]

HATN-2Me and HATN-4Me also demonstrated that as the methyl substitution was increased a very slight red-shift of ~4 nm occurred for the two lowest absorption bands (see Figure 22). HATN-6Me did not follow this pattern, having its lowest energy transition at 413 nm. This red-shift is not what is expected with an electron donating group but can be rationalised using TD-DFT calculations. They show that the lowest energy transition consists of more than a HOMO to LUMO transition with HOMO-2→LUMO+1 in HATN2Me, HOMO-2→LUMO+2 in HATN-4Me and HATN-6Me. As methyl substitution increased from (2Me to 4Me) the HOMO was increased by 0.09 eV (-6.35 eV to -6.26 eV) while the LUMO increased by 0.05 eV (-2.69 eV to -2.64 eV), while HATN-4Me to HATN-6Me had a change of 0.07 eV HOMO (-6.26 eV to -6.19 eV) and 0.03 eV (-2.64 eV to -2.61 eV) for the LUMO.

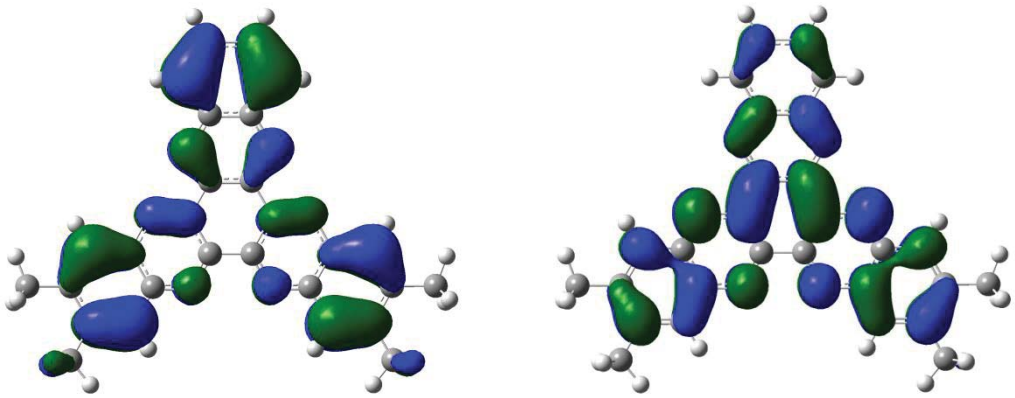

HOMO-2 **LUMO+2**

Figure 24 Orbital diagrams for HATN-4Me

HATNs (HATN-4Me2Br, HATN-4Br2Me, HATN-4Me1COOH, HATN-1COOH) electronic spectra displayed two π→π* transitions, the first at 405-422 nm with a second less distinguished band at 384-400 nm (as well as other π→π* and n→π* transitions below 350 nm) (see Figure 25).

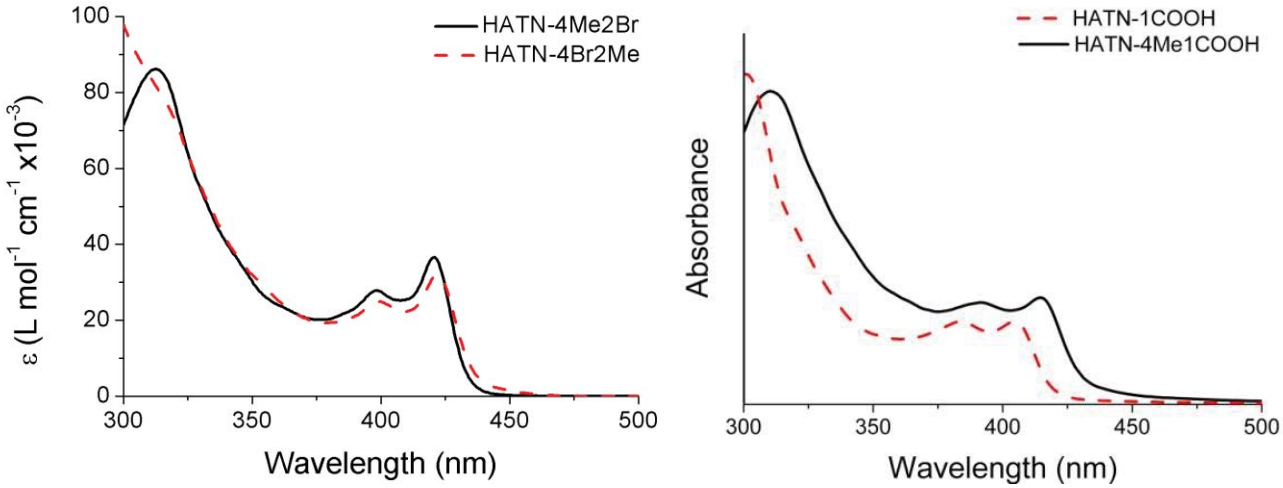

Figure 25 Electronic absorbance spectra of, left: HATN-4Me2Br and HATN-4Br2Me, right: HATN-4Me1COOH and HATN-1COOH

HATN-4Me2Br and HATN-4Br2Me showed only a negligible red-shift of ~2nm (see Table 2 and Table 1) for the two lowest absorption bands as the bromine substitution increased. Although very weak, this behaviour follows on from the transitions for HATN-2Br and HATN-4Br and is rationalised in that bromine is acting as an electron

withdrawing group, which is supported by TD-DFT calculations that show the lowest energy transition consists of only HOMO → LUMO, the same as for HATN-2Br and HATN-4Br.

HATN-1COOH and HATN-4Me1COOH show a similar trend to the methyl HATNs in that as the methyl substitution was increased and a red-shift (of 10 nm) was observed for the two lowest absorption bands (Figure 25, Table 2). Excitation from a HOMO to LUMO orbital accounted for the low energy transition. This is different in that the non-COOH equivalents (HATN-4Me and HATN) involved different orbitals (HOMO-2, LUMO+1, LUMO+2) for their low energy transition. The COOH addition red-shifts the spectrum by 2-5 nm from HATN and HATN-4Me. It is also interesting that the LUMO orbital has electron density over the COOH functionality (Figure 25) as this could lead to promising electron transfer in DSSC devices.

Table 2 λ_{max} (nm) and absorption coefficients (ε / 10^3 L $mol^{-1}cm^{-1}$) of selected HATNs.

	λ / nm (ε / 10^3 L $mol^{-1}cm^{-1}$)
HATN-1COOH[a]	405, 384
HATN-4Me1COOH[a]	415, 391
HATN-4Br2Me	420.5 (36.6), 398 (27.8)
HATN-4Me2Br	422 (32.1), 400 (24.9)

[a] ε could not be calculated as the compounds were not very soluble.

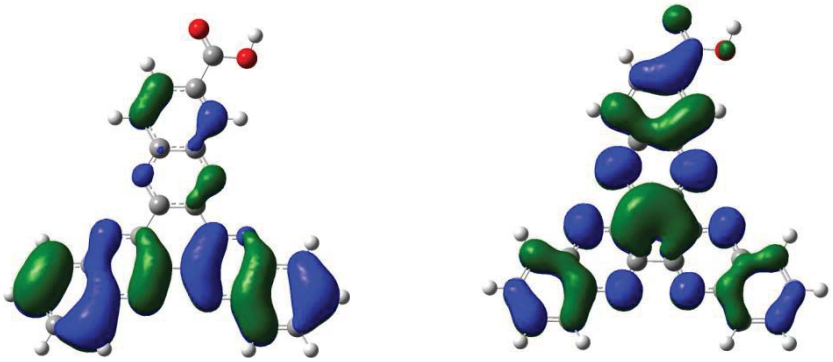

HOMO **LUMO**

Figure 26 Orbital diagrams for HATN-1COOH

3.3 Dye-sensitised solar-cell (DSSC)

Initially we attempted to prepare Ru(II) dyes similar to those in Figure 12, but with dyes containing HATN-1COOH, the presence of a carboxylate group being required for attachment to TiO_2. After exhaustive attempts we were not able to obtain pure Ru(II) species instead mixtures of Ru(II) and Ru(III) compounds were present as evidenced in NMR spectra. Studies on the ligand HATN-1COOH were then performed. The electronic absorbance spectra of HATN-1COOH and HATN-4Me1COOH show limited absorbance in the visible region of the electromagnetic spectrum. The observed peaks in this region do however, possess reasonable extinction coefficients. This, along with their stability and the presence of the carboxy functional group (to anchor the compound to TiO_2) directed the study of their performance as solar cell dyes with the prospect of further insight into their photochemical properties. The cells were prepared using a solution of either HATN-1COOH or HATN-4Me1COOH in ethanol using both E-Zn (LiI, I_2, BMII, BHT in valeronitrile:glutaronitrile see Appendix B) and E-Th (LiI, I_2, BMII in glutaronitrile see Appendix B) as the electrolyte and subsequently tested using the Campbell et al.[50] equipment, described in Section 3.3.1 (specific cell preparation details are given in Appendix B). See Section 3.3.2 for discussion of current-voltage curves.

3.3.1 Electrochemistry

Before we discuss the current-voltage curves for HATN-1COOH and HATN-4Me1COOH the use of cyclic voltammetry studies in DSSCs will be given. Cyclic voltammetry is a useful tool for estimating the HOMO and LUMO energies and giving an indication as to a compound's ability to be used as a dye in a dye-sensitised-solar cells. The cyclic voltammograms of the ligands HATN-4Me, HATN-4Br, HATN-2Me, HATN-2Br, HATN-4Me2Br and HATN-4Br2Me were measured in DCM using 0.1 M $^{t}Bu_4NBr$ as supporting electrolyte. The solubilities of HATN-1COOH and HATN-4Me-1COOH in DCM precluded these studies. Data are tabulated in Table 3. The cyclic voltammetry of these compounds in the range 1 V to -2V reveals two reversible one-electron waves, assigned to adding two successive electrons to the π^*(HATN).

Table 3 HATN-1Re first reduction potentials (vs. Fc/Fc^+ in DCM)

HATN	$HATN/HATN^{-1}$ (V)	$HATN^{-1}/HATN^{-2}$ (V)
HATN-2Me	-0.89	-1.34
HATN-4Me	-0.92	-1.38
HATN-4Me2Br	-0.86	-1.31
HATN-4Br	-0.96	-1.52
HATN-4Br2Me	-0.97	-1.58
HATN-2Br	-0.86	-1.22

Reversible ligand reduction processes attributed to $HATN/HATN^-$ are observed at -0.92, -0.96, -0.89, -0.86 and -0.86 and -0.97 V (vs. Fc/Fc^+) for HATN-4Me, HATN-4Br, HATN-2Me, HATN-2Br, HATN-4Me2Br and HATN-4Br2Me respectively. Comparison with the HATN-6Me (-1.09 V) and HATN (-1.55 V) (for the $HATN/HATN^{-1}$ reduction potential) showed similar reduction potential values.[55]

The electron-withdrawing bromo group on the HATN is expected to provide more electron density therefore the reduction of the ligand is expected to occur at a more anodic value. The opposite effect occurs when electron-donating groups such as methyl are added to the ring. The reduction potentials are all very close. The HATNs do not seem to follow the trend expected in the reduction potentials according to the nature of the functional groups, e.g. HATN-4Me2Br and HATN-2Br have the less negative reduction potential (-0.86 V), whereas HATN-4Br2Me has the most negative reduction potential (-0.97 V).

LUMO levels and the band gap was calculated using the physical data from electrochemistry and their absorption spectra and are given in Table 4.

Table 4 Summary of the energy levels obtained from cyclic voltammetry.

HATN	E_{onset}^{red} (V vs Fc/Fc^{+})	λ (nm)	E_{gap}[a]	HOMO[b] (V)
HATN-4Me	-0.898	431	2.884	1.986
HATN-4Br	-0.952	432	2.877	1.925
HATN-2Me	-0.777	424	2.932	2.155
HATN-2Br	-0.761	427	2.911	2.15
HATN-4Br2Me	-0.956	444	2.800	1.844
HATN-4Me2Br	-0.761	438	2.838	2.077

[a] Band gap (eV) = $\frac{1243}{\lambda_{onset}(nm)}$

[b] HOMO (eV) = LUMO (V) + band gap (eV)

Now we have these fundamental results we can predict what is likely to occur for their use in dye-sensitised solar cells. The HOMO and LUMO results were used to form a HOMO-LUMO diagram for the HATN complexes (Figure 27). The addition of I^-/I_3^- redox couple HOMO level is shown as well as the conduction band of TiO_2. When a dye gets excited the electron moves from the LUMO of the complex into the TiO_2 and this would only be possible for half of the dyes (with anchoring groups such as COOH). Practically, it has been found that cell efficiency requires approximately 0.2 V of over-potential between the TiO_2 conduction band and the dye LUMO level, and 0.3 V of over-potential between the dye HOMO level and redox potential for sufficient driving forces of electron injection from the dye to the CB of TiO_2 and the regeneration of oxidized dye, respectively.[56,57] HATN reduction potentials are too negative for this to occur and hence would not be expected to be suitable as a DSSC-dye candidate and presumably for the HATN-1COOH and HATN-4Me1COOH too.

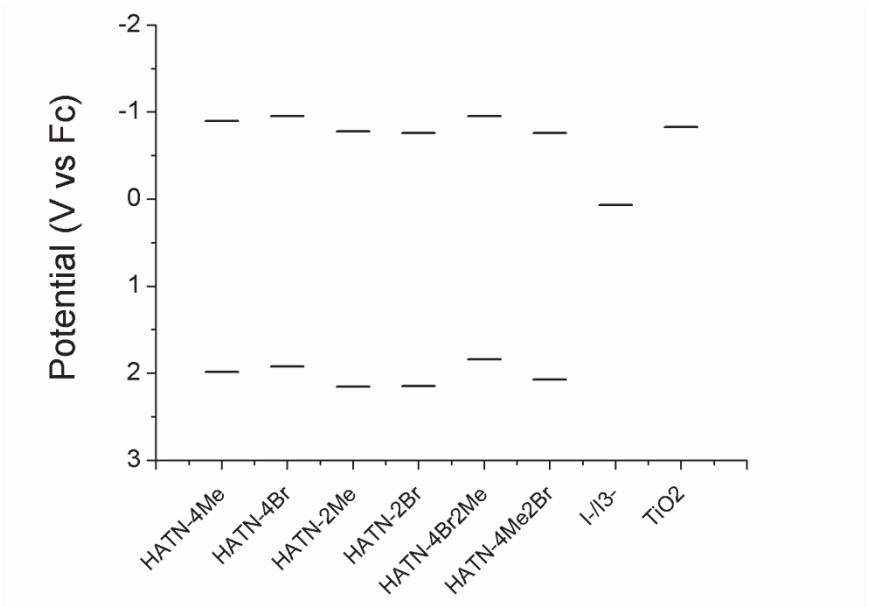

Figure 27 HOMO and LUMO levels of HATN compounds as well as redox potential for I^-/I_3^- and conduction band for TiO_2

3.3.2 HATN measurements

The current-voltage curves of HATN-1COOH (with electrolyte E-Th) and HATN-4MeCOOH (with electrolyte E-Zn) are given below (Figure 28). Differing electrolytes were chosen as they gave the highest efficiency for these cells. These give fill factors (see Section 3.1.3.3) of 0.396 and 0.322 for HATN-4Me1COOH and HATN-1COOH respectively. Their efficiencies are 0.003 and 0.001%, both very low and negligible.

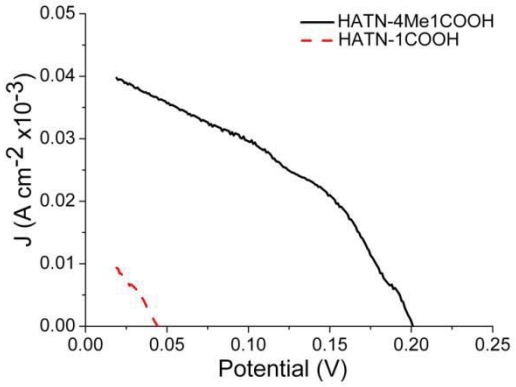

Figure 28 Current potential graph for HATN-4Me1COOH and HATN-1COOH

The lack of efficiency of these dyes may be attributed to their relatively weak absorption in the visible region, as well as their unfavourable HOMO and LUMO energies.

Although these HATNs are not ideal DSSC-dye candidates, HATN-6Cl has been successfully incorporated as the electron transport material (ETM) in a hetero-junction solar cell, and calculations suggest that selected HATNs from this work may also be used as ETMs in hetero-junction solar cells. A comparison is given in Table 5 between C_{60}, a standard ETM for vacuum deposited organic PVs, and PCBM ([6,6]-phenyl-C61-butyric acid methyl ester), a standard ETM for solution-deposited organic PVs and two bromo substituted HATN compounds. It can be seen that both C_{60} and PCBM have lower LUMO levels than HATN-2Br and HATN-4Br, though PCBM and HATN-4Br are 1.1 eV apart. This difference may lead to unfavourable transfer properties, but if the HATNs match up more favourably with the donor molecules this could provide a better ETM. This will require future studies.

Table 5 Comparison of HOMO LUMO energy levels of typical ETM and HATNs

ETM	HOMO (eV)	LUMO (eV)	Δ HOMO-LUMO (eV)
C_{60}[58]	-6.1	-4.5	1.6
PCBM[59]	-6.1	-3.7	2.4
HATN-2Br	-5.3	-2.4	2.9
HATN-4Br	-5.5	-2.6	2.9

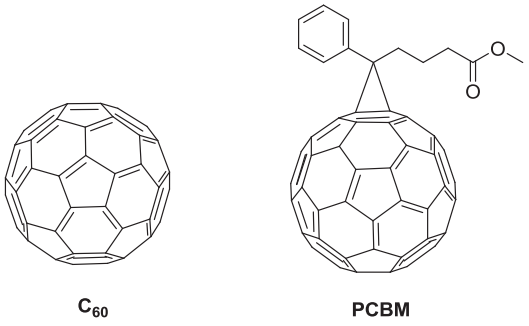

Figure 29 Standard electron-transporters, left: C60 and right: PCBM

3.4 Field Effect Transistor

As previously described in Section 3.1.2 a transistor consists of source, drain and gate electrodes. For these experiments, the gate was a highly doped p-type silicon wafer, on which a silicon oxide layer has been thermally grown to give the dielectric. For the purpose of testing the FET behaviour of HATNs, they were deposited on the insulating layer using two different techniques, solution processing and vacuum deposition. This is followed by electrodeposition of the gold electrodes.

3.4.1 Solution-Processed Deposition

For solution-processed deposition the HATNs were dissolved in chloroform to make a saturated solution and any solids filtered off. This solution was then deposited on top of the gate/dielectric using a spin-coater to give a thin film. When the technique is well handled, it allows the production of very homogeneous films with perfect control of their thickness over relatively large areas. Electrodeposition was used to place the gold contacts onto the surface using masks to ensure correct placement. This gave a chip with multiple devices that can be analysed (Figure 30, for details see Appendix B).

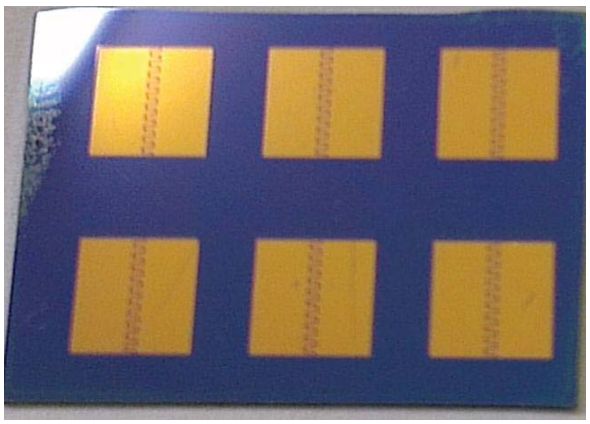

Figure 30 Six HATN-4Me FET devices

3.4.2 Solution Processed FET testing

HATN-4Me2Br and HATN-4Me were the only compounds to show any activity. HATN-4Me2Br responses have been plotted at three different V_{DS} values (30, 40 and 60 V, Figure 31). As the V_{DS} is increased the I_{DS} also increases. The currents here are low and the device is acting as a resistor. There is very little change at varying gate voltage indicating this material does not exhibit FET behaviours. Resistances have been calculated to range between 43 and 54 MΩ. This changing resistance may be due to different film thickness throughout the devices.

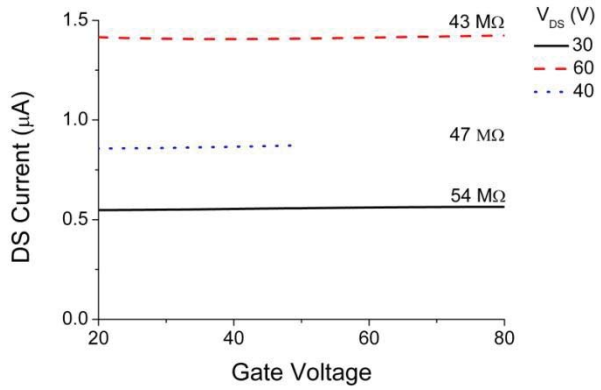

Figure 31 Current Voltage graphs of HATN-4Me2Br at a range of drain source voltages

The same linear type of graph was achieved using HATN-4Me (Figure 32), but at a much higher current, or more correctly there was a significant decrease in resistance. This sample was annealed after the introduction of the HATN-4Me at 145 ˚C. HATN-4Me has less resistance than HATN-4Me2Br. This increased current could not be repeated with a new set of FETs. The uniformity of the resistance may be due to a more regular thickness of the ETM film in these HATN-4Me2Br devices.

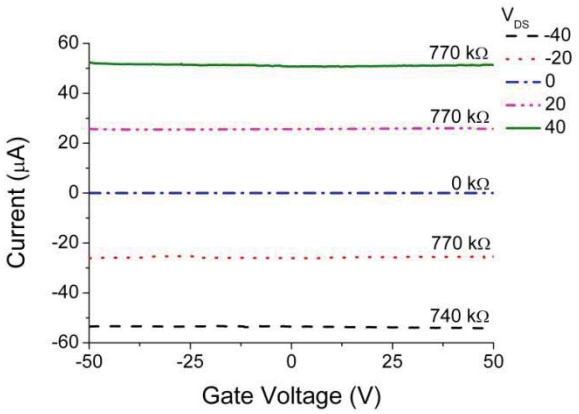

Figure 32 Current voltage graph for HATN-4Me at varying V_{DS}.

As repeated procedures did not reproduce similar results it can be said that spin-coating didn't have reliable reproducibility in the case of HATNs. A requirement for this technique is solubility and as HATNs have relatively poor solubility this may have been an issue. Also HATNs have strong π-π stacking ability, and this may also have led to problems with surface reproduction.

3.4.3 FET with Vacuum Deposition

The second method used was vacuum deposition, which consists of heating the material under reduced pressure which then allows the deposition of layers molecule-by-molecule on to the substrate. Its main advantages are the easy control of the thickness and purity of the film, and the fact that highly ordered films can be generated by monitoring the deposition rate and the temperature of the substrate.

The high temperatures required in this technique mean the stability of the compounds at these temperatures is paramount. Hence, thermogravimetric analyses (TGA) for the HATNs were performed and are given in Table 6. It is interesting to note the variation in decomposition temperatures between the various substituents. The bromo substituted HATNs decompose at the highest temperatures whereas the mixed HATNs decompose at the lowest with a range of over 150 ˚C between them.

Table 6 Decomposition temperatures found by TGA.

HATN	Decomposition Temperature (˚C)
HATN-2Me	425
HATN-4Me	440
HATN-2Br	480
HATN-4Br	494
HATN-4Me2Br	310
HATN-4Br2Me	320

HATN-4Me and HATN-4Br FET devices were prepared according to the literature[60] method at Prof. Zhang's laboratory at Lanzhou University, China and the transfer characteristics for HATN-4Me are given in Figure 33. On the left hand ordinate axis $|I_{DS}|^{\frac{1}{2}}$ is plotted against the gate voltage V_G while the right hand axis plots I_{DS} against V_G (data obtained with thin film deposited at 60 ˚C). It can be seen that there is a very small change in current during the 100 V gate range. From the data it is calculated that the FET electron mobility is 5.38 x10^{-5} $cm^2V^{-1}s^{-1}$ which is poor. To try and improve this result different variables such as substrate temperature and film thickness were altered. The resistance varied with gate voltage and the lowest resistance (at highest current) was calculated to be 1.23 GΩ.

Substrate temperatures for thermal evaporation were carried out, at 60℃, 80℃ and 110℃. The AFM image of the thin film at T_{sub}=60 ˚C is shown in Figure 34. The crystals were small and the film was not continuous. This was tested but no OFET signal was obtained. At 80℃ and 110 ˚C, the results were the same. Additionally, different thicknesses of the thin film were investigated. At both 30 nm and 60 nm no OFET signals were observed. Lastly, the deposition speed was changed and again there was no improvement in the results.

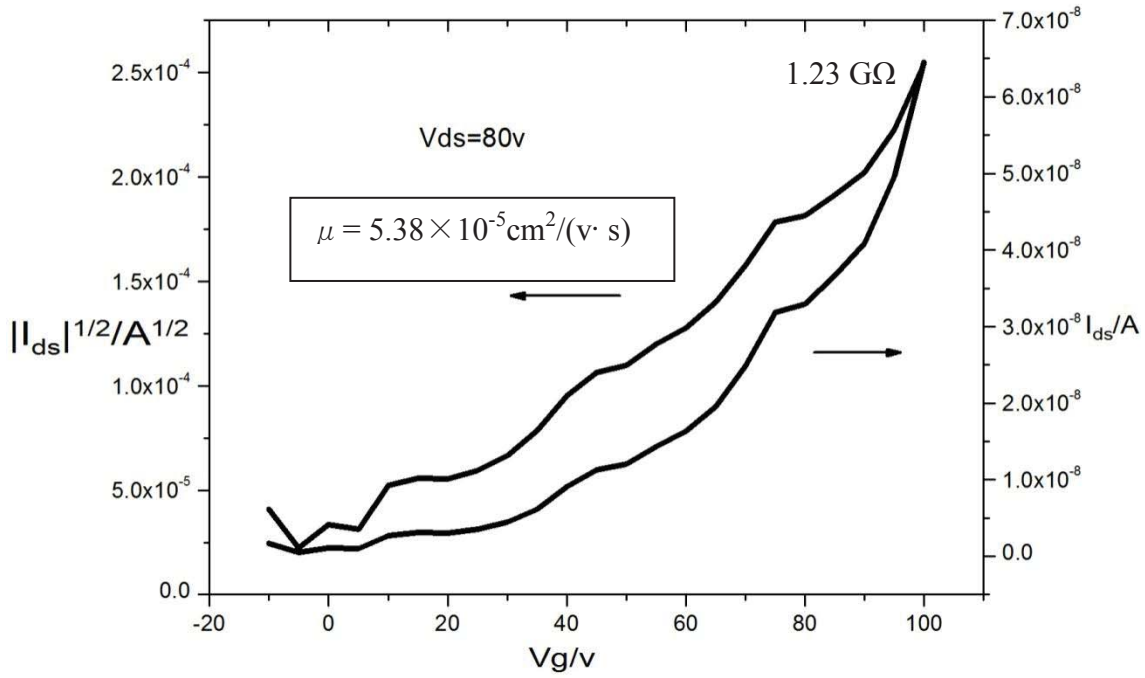

Figure 33 Transfer curves of HATN-4Me with 30 nm film thickness.

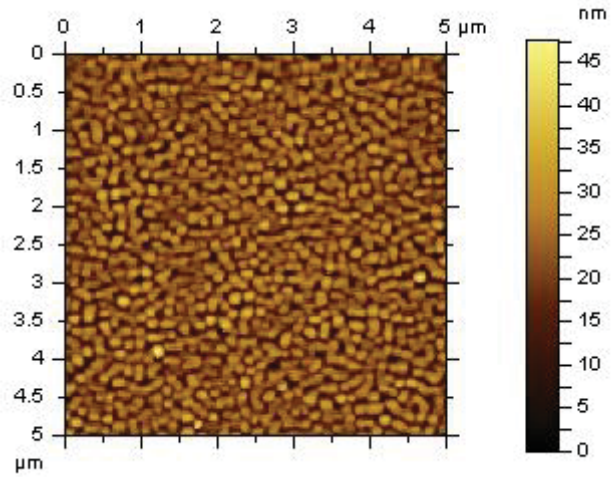

Figure 34 AFM image of HATN-4Me deposited on octadecyltrimethoxysilane modified SiO_2 substrate at T_{sub}=60℃.

For HATN-4Br, poor OFET results were obtained as shown in Figure 35. In comparison with HATN-4Me there was a more significant current change over the 100 V gate

change. This led to an increased FET electron mobility of 8.13 x10^{-4} $cm^2V^{-1}s^{-1}$. The resistance varied with gate voltage but the lowest resistance (at highest current) was calculated to be 107 MΩ which is a lot less than for HATN-4Me. Less resistance invariably leads to higher mobility.

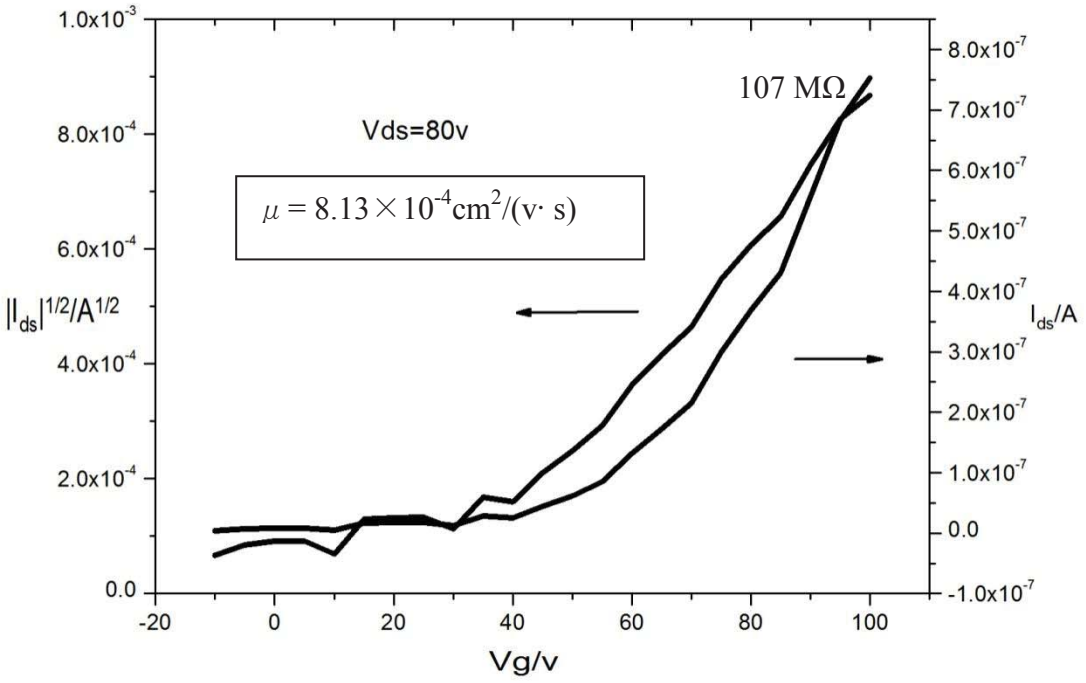

Figure 35 Transfer curves of HATN-4Br with 30 nm film thickness.

Thin films were obtained for HATN-4Me and HATN-4Br. The results for HATN-4Me and HATN-4Br are similar to that in the literature for HATN-6Cl and HATN-6F (with mobilities of 2.8x10^{-5} $cm^2V^{-1}s^{-1}$ for HATN-6Cl and 9.6x10^{-3} $cm^2V^{-1}s^{-1}$ for HATN-6F). HATN-4Me has the lowest mobility as is expected due to the higher LUMO orbital energy (-2.57 eV) with the methyl groups. The mobility of HATN-4Br is higher than that of the methyl functionality due to its lower LUMO level (-2.63 eV). HATN-4Br is intermediate in mobility to that of HATN-6F and HATN-6Cl. This is somewhat unexpected as chlorine is expected to have a more electron-withdrawing ability than that of bromine.[61]

3.5 Conclusions

UV/Vis spectra were employed to gain understanding of HATN orbitals showing $\pi \rightarrow \pi^*$ transitions in the range of 405-422 nm and another transition at 384-400 nm. This was similar to what was observed with the homo-substituted HATNs. These were successfully compared with calculated values so the orbitals could be assigned to particular transitions throughout the spectrum indicating energy transitions involved in the various HATN excitations and patterns in their orbital level energies formed by the various functional substitutions. It was found that the bromine inclusion decreased the HATNs' HOMO and LUMO levels while the introduction of methyl groups increased these levels as expected. The levels of the hetero-HATNs were also non-degenerate indicating that the symmetry of the molecule has been broken by the different functional groups around the rings.

Two ligands (HATN-4Me1COOH and HATN-1COOH) were tested for use as dyes in dye-sensitised solar cells. HOMO and LUMO orbital diagrams suggest charge moves from the ring to the carboxyl functional group upon excitation indicating electron transfer is possible. However, it was found that both HATNs had low efficiencies (<0.1%). This was attributed to their weak absorption spectra in the visible and near IR regions and their expected reduction potentials being too negative.

Six ligands (HATN-4Me, HATN-4Br, HATN-2Me, HATN-4Br2Me, HATN-2Br, HATN-4Me2Br) were tested for use in Field Effect Transistors. It was found that only two, HATN-4Me and HATN-4Br, had a FET-like response. These results showed that HATN-4Br had an electron mobility of 8.13 $x10^{-4}$ $cm^2V^{-1}s^{-1}$ while HATN-4Me had an electron mobility of 5.38 $x10^{-5}$ $cm^2V^{-1}s^{-1}$. This shows that the electron withdrawing group increased the electron mobility in these devices. Also as they have strong resistances of 107 MΩ and 1.23 GΩ, respectively, they are not suitable for FET devices. The solution processed FETs also had high resistances ranging between 740 kΩ and 54 MΩ and do not exhibit FET behaviour.

3.6 Acknowledgements

Professor Keith Gordon and his student Holly van der Salm from Otago University for running and collecting the Raman spectra on equipment at Otago University. Also, for use of their computers in computational models.

Professor Haoli Zhang, the Deputy Director of State Key Laboratory of Applied Organic Chemistry at Lanzhou University, China for fabricating and running the vacuum deposited FETs.

Dr. Natalie Plank from Victoria University for use of their equipment for fabrication of FETs using the spin-coating deposition method.

3.7 References

1 Knapp, E.; Häusermann, R.; Schwarzenbach, H. U.; Ruhstaller, B. *Journal of Applied Physics* **2010**, *108*, 054504.

2 Yoshiro, Y. *Science and Technology of Advanced Materials* **2009**, *10*, 024313.

3 Coffey, D. C.; Ferguson, A. J.; Kopidakis, N.; Rumbles, G. *ACS Nano* **2010**, *4*, 5437.

4 Leng, S.; Chan, L. H.; Jing, J.; Hu, J.; Moustafa, R. M.; Van Horn, R. M.; Graham, M. J.; Sun, B.; Zhu, M.; Jeong, K.-U.; Kaafarani, B. R.; Zhang, W.; Harris, F. W.; Cheng, S. Z. D. *Soft Matter* **2010**, *6*, 100.

5 Jiang, H. *Macromolecular Rapid Communications* **2010**, *31*, 2007.

6 Thomas, C. A.; Zong, K.; Abboud, K. A.; Steel, P. J.; Reynolds, J. R. *Journal of the American Chemical Society* **2004**, *126*, 16440.

7 Roncali, J. *Macromolecular Rapid Communications* **2007**, *28*, 1761.

8 Winkler, M.; Houk, K. N. *Journal of the American Chemical Society* **2007**, *129*, 1805.

9 Naka, S.; Okada, H.; Onnagawa, H.; Tsutsui, T. *Applied Physics Letters* **2000**, *76*, 197.

10 Koezuka, H.; Tsumura, A.; Ando, T. *Synthetic Metals* **1987**, *18*, 699.

11 Preedy, V. R. P., V. *Biosensors and Environmental Health*; CRC Press, 2012.

12 Shaw, J. M.; Seidler, P. F. *IBM Journal of Research and Development* **2001**, *45*, 3.

13 Stassen, A. F.; Boer, R. W. I. d.; Iosad, N. N.; Morpurgo, A. F. *Applied Physics Letters* **2004**, *85*, 3899.

14 Romero, H. E.; Shen, N.; Joshi, P.; Gutierrez, H. R.; Tadigadapa, S. A.; Sofo, J. O.; Eklund, P. C. *ACS Nano* **2008**, *2*, 2037.

15 Takagi, S.; Toriumi, A.; Iwase, M.; Tango, H. *IEEE Transactions on Electron Devices* **1994**, *41*, 2357.

16 Liu, Z.; Zhang, D.; Han, S.; Li, C.; Tang, T.; Jin, W.; Liu, X.; Lei, B.; Zhou, C. *Advanced Materials* **2003**, *15*, 1754.

17 Ju, J.; Yamagata, Y.; Higuchi, T. *Advanced Materials* **2009**, *21*, 4343.

18 Ling, M. M.; Bao, Z. *Chemistry of Materials* **2004**, *16*, 4824.

19 Mitzi, D.; Kosbar, L.; Murray, C.; Copel, M. *Nature* **2004**, *428*, 299.

20 Takimiya, K.; Ebata, H.; Sakamoto, K.; Izawa, T.; Otsubo, T.; Kunugi, Y. *Journal of the American Chemical Society* **2006**, *128*, 12604.

21 Zhang, Z.; Yates, J. T. *Chemical Reviews* **2012**.

22 Kymissis, I. *Organic Field Effect Transistors; Theory, Fabrication and Characterization*; Springer: New York, 2009.

23 Qiao, Y.; Guo, Y.; Yu, C.; Zhang, F.; Xu, W.; Liu, Y.; Zhu, D. *Journal of the American Chemical Society* **2012**, *134*, 4084.

24 Lei, T.; Cao, Y.; Fan, Y.; Liu, C.; Yuan, S.; Pei, J. *Journal of the American Chemical Society* **2011**, *133*, 6099.

25 Di, C.; Yu, G.; Liu, Y.; Xu, X.; Wei, D.; Song, Y.; Sun, Y.; Wang, Y.; Zhu, D.; Liu, J.; Liu, X.; Wu, D. *Journal of the American Chemical Society* **2006**, *128*, 16418.

26 Dimitrakopoulos, C. D.; Brown, A. R.; Pomp, A. *Journal of Applied Physics* **1996**, *80*, 2501.

27 Yamashita, Y. *Science and Technology of Advanced Materials* **2009**, *10*, 024313.

28 Nishida, J.; Amada, A.; Murakami, S.; Yamashita, Y. *Journal of Photopolymer Science and Technology* **2009**, *22*, 675.

29 Brabec, C. J. *Solar Energy Materials and Solar Cells* **2004**, *83*, 273.

30 Dresselhaus, M. S.; Thomas, I. L. *Nature* **2001**, *414*, 332.

31 Yu, Q.; Wang, Y.; Yi, Z.; Zu, N.; Zhang, J.; Zhang, M.; Wang, P. *ACS Nano* **2010**, *4*, 6032.

32 Gratzel, M. *Philosophical Transactions of the Royal Society, A: Mathematical, Physical & Engineering Sciences* **2007**, *365*, 993.

33 Hardin, B. E.; Snaith, H. J.; McGehee, M. D. *Nature Photonics* **2012**, *6*, 162.

34 Grätzel, M. *Current Opinion in Colloid & Interface Science* **1999**, *4*, 314.

35 Hagfeldt, A.; Grätzel, M. *Accounts of Chemical Research* **2000**, *33*, 269.

36 Ito, S.; Miura, H.; Uchida, S.; Takata, M.; Sumioka, K.; Liska, P.; Comte, P.; Pechy, P.; Gratzel, M. *Chemical Communications* **2008**, 5194.

37 Zhang, G.; Bala, H.; Cheng, Y.; Shi, D.; Lv, X.; Yu, Q.; Wang, P. *Chemical Communications* **2009**, 2198.

38 Hara, K. K., N *Material Matters* **2009**, *4*, 92.

39 Mishra, A.; Fischer, M. K. R.; Bäuerle, P. *Angewandte Chemie International Edition* **2009**, *48*, 2474.

40 Pivrikas, A.; Sariciftci, N. S.; Juška, G.; Österbacka, R. *Progress in Photovoltaics: Research and Applications* **2007**, *15*, 677.

41 Jo, J.; Kim, S.-S.; Na, S.-I.; Yu, B.-K.; Kim, D.-Y. *Advanced Functional Materials* **2009**, *19*, 866.

42 Kozub, D. R.; Vakhshouri, K.; Orme, L. M.; Wang, C.; Hexemer, A.; Gomez, E. D. *Macromolecules* **2011**, *44*, 5722.

43 Treat, N. D.; Brady, M. A.; Smith, G.; Toney, M. F.; Kramer, E. J.; Hawker, C. J.; Chabinyc, M. L. *Advanced Energy Materials* **2011**, *1*, 82.

44 Treat, N. D.; Brady, M. A.; Smith, G.; Toney, M. F.; Kramer, E. J.; Hawker, C. J.; Chabinyc, M. L. *Advanced Energy Materials* **2011**, *1*, 145.

45 Cheng, Y.-J.; Yang, S.-H.; Hsu, C.-S. *Chemical Reviews* **2009**, *109*, 5868.

46 Silvestri, F.; Marrocchi, A. *International Journal of Molecular Sciences* **2010**, *11*, 1471.

47 Mayukh, M.; Jung, I. H.; He, F.; Yu, L. *Journal of Polymer Science Part B: Polymer Physics* **2012**, *50*, 1057.

48 Falkenberg, C.; Leo, K.; Riede, M. K. *Journal of Applied Physics* **2011**, *110*, 124509.

49 Smestad, G. *Optoelectronics of Solar Cells* Washington, 2002.

50 Campbell, W., Massey University, 2001.

51 Frisch, M. J. G. W. T., B.; Schlegel, H.B.; Scuseria, G. E.; Robb, M. A.; Cheeseman, J. R.; Scalmani, G.; Barone, V.; Pattersson; A.1 ed ed.; Gaussian, Inc: Wallingford CT: 2009.

52 Dennington, R. K., T.; Millam, J.; *Semichem Inc.: Sawnee Mission KS*, 2009; Vol. Version 5 ed.

53 Colip, L. A.; Koppisch, A. T.; Broene, R. D.; Berger, J. A.; Baldwin, S. M.; Harris, M. N.; Peterson, L. J.; Warner, B. P.; Birnbaum, E. R. *Journal of Applied Crystallography* **2009**, *42*, 329.

54 Gao, B.; Liu, Y.; Geng, Y.; Cheng, Y.; Wang, L.; Jing, X.; Wang, F. *Tetrahedron Letters* **2009**, *50*, 1649.

55 Roy, S.; Kubiak, C. P. *Dalton Transactions* **2010**, *39*, 10937.

56 Oskam, G.; Bergeron, B. V.; Meyer, G. J.; Searson, P. C. *The Journal of Physical Chemistry B* **2001**, *105*, 6867.

57 Daeneke, T.; Mozer, A. J.; Uemura, Y.; Makuta, S.; Fekete, M.; Tachibana, Y.; Koumura, N.; Bach, U.; Spiccia, L. *Journal of the American Chemical Society* **2012**, *134*, 16925.

58 Nanditha, D. M.; Dissanayake, M.; Hatton, R. A.; Curry, R. J.; Silva, S. R. P. *Applied Physics Letters* **2007**, *90*, 113505.

59 Sigma-Aldrich (2012). "Sigma-Aldrich." from www.sigmaaldrich.com.

60 Song, C.-L.; Ma, C.-B.; Yang, F.; Zeng, W.-J.; Zhang, H.-L.; Gong, X. *Organic Letters* **2011**, *13*, 2880.

61 Smith, M.; March, J. *March's Advanced Organic Chemistry: Reactions, Mechanism, and Structure*; 5 ed.; Wiley: Canada, 2001.

Chapter 4

Reactions of HATN ligands with selected transition metals

4.0 Abbreviations used in Chapter 4

HATN	Hexaazatrinaphthalene
HAT	Hexaazatriphenylene
MeOH	Methanol
THF	Tetrahydrofuran
$CHCl_3$	Chloroform
CH_2Cl_2/DCM	Dichloromethane
h	Hours
BF_4^-	Tetrafluoroborate anion
ClO_4^-	Perchlorate anion
Ar	Aromatic
EtOAc	Ethylacetate
CaH_2	Calcium hydride
NMR	Nuclear Magnetic Resonance
DMSO	Dimethylsulfoxide
TMS	Tetramethylsilane
DCM	Dichloromethane

4.1 Introduction and applications

Hexaazatriphenylene (HAT, Figure 1 (i)) is an interesting ligand system; with its three sites for bidentate coordination it can serve as a ligand in mononuclear complexes and as a bridging di-bidentate and tri-bidentate ligand in di-, tri- and polynuclear compounds. In addition to these sites there is also the possibility to have control in adding metal coordinating functionality to the peripheral positions in HAT[1] (Figure 1, (ii)), thus increasing the binding sites by as many as three (but only one shown).[2] The advantage of adding functional groups to particular areas of a molecule is that this allows control of the electronic properties which can be beneficial to applications such as photovoltaics. All these possible coordination sites have made HAT a well-studied complex system. HAT has formed complexes with many transition metals including Re(I),[3] Cr(0),[4] Ir(III),[5] Rh(III),[5] Ru(II),[6] and Cu(II).[7]

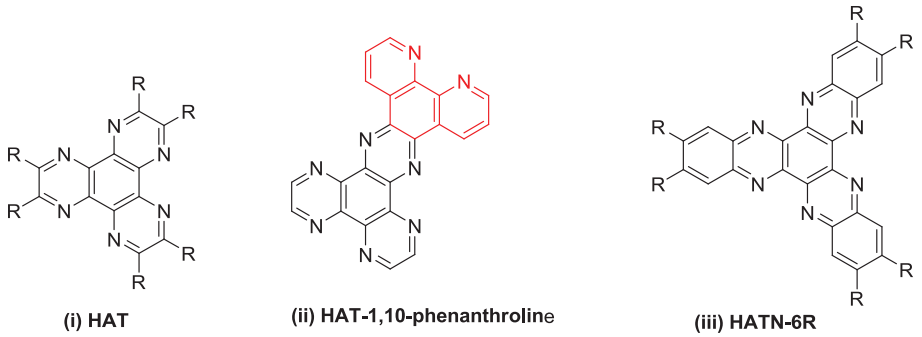

Figure 1(i) HAT (ii) HAT with peripheral binding site (iii) HATN

It is surprising that the coordination chemistry of hexaazatrinaphthalene, HATN (Figure 1, (iii)), is relatively unexplored in view of its obvious similarity to HAT. HATN has been substituted with only a small selection of transition metals including Ru(II),[8] Zn(II),[9] Cu(I),[10]and Re(I)[11] to give discrete complexes and with Ag(I)[12] forming a coordination network (see Figure 8 Chapter 1). The relative lack of interest in the metal coordination of HATN to date – despite the relative ease of synthesis of suitable derivatives – may be due to perceived steric and solubility problems. One particular example of the solubility issue is given by Gray and co-workers[13] who reported that HATN forms mono- and bi-nuclear complexes with palladium cations, but a lack of solubility in the latter prevented the isolation and characterisation of the symmetrical tri-nuclear complex.

Gray's initial work into palladium HATN complexes was further extended by using HATN with benzdioan extended onto the core structure.[14] This has increased solubility, due to the long alkyl chains, which allowed the mono- di- and tri- palladium complexed HATN-like compounds to be formed *in situ* through NMR titration (Figure 2).

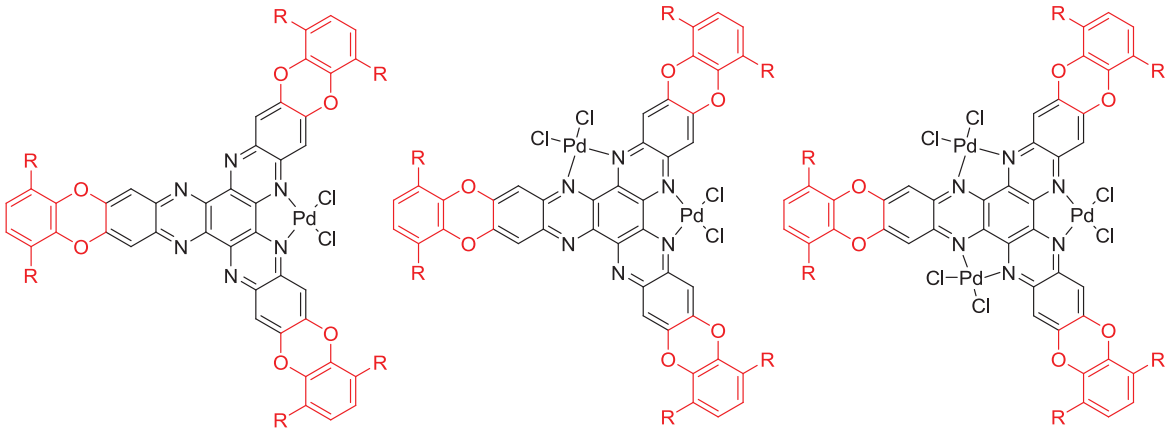

Figure 2 A group of isolated HATN complexes with mono, bi, and tri- palladium coordination (R = *n*-$C_{12}H_{25}$).

Analysis of structural fragments of three iron metals coordinated to one HAT (Figure 3) reveals that the coordination environment around the metal atoms is distorted in the case of octahedral coordinated 3d (first row transition) metals with the N-Fe-N angles in the range 73.3(4) – 78.6(3)°.[15] This distortion introduces excessive strain and renders them rather unstable (in comparison 1,10-phenanthroline has a bite angle of 75.5(6)°,[16] while a mono-chelating ligand such as bipyridine (bpy) is larger and usually exceeds 80° [15]). One way to stabilise metal-HAT interactions is to use 4d and 5d metals, whose larger atomic radii should lead to less distorted N-M-N angles.[17] The other possibility is to use 3d metal ions that exhibit lower coordination numbers.

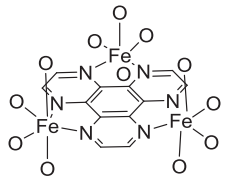

Figure 3 $[Fe_3(HAT)(H_2O)_{12}](SO_4)_3 \cdot 3H_2O$ without H atoms or anions shown. This complex gives a distorted coordination environment for the Fe atoms.

4.1.1 Copper HATN complexes

Copper(I) is a 3d metal ion that has a low coordination number and is known to form complexes with HAT so is a logical choice for HATN coordination complexes. Baxter et al.[18] reported several complexes in which three Cu(I) atoms are coordinated to one HAT molecule. The resulting compounds contain Cu(I) ions in a tetrahedral geometry and the interlinked fragments appear to be less strained as compared to other metals such as Fe(II).[17] This type of chemistry has been extended to HATN where three Cu(I) phosphine metal compounds have been coordinated to HATN-Me_6 (Figure 4, left).[10]

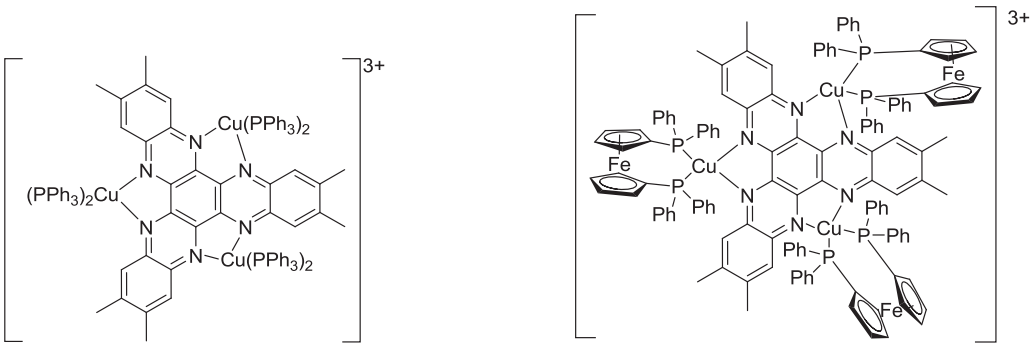

Figure 4 Left: HATN-Me_6 copper phosphine complex. Right: HATN-Me_6 copper ferrocene phosphine complex.

However, the first HATN copper complex reported in the literature was much more complex, containing three copper-ferrocene moieties[19] (Figure 4, right). Ferrocene is a well-known redox active compound; linked to copper and incorporated into the electronegative HATN structure its electronic characteristics were observed. It was

found that there was splitting of the three ferrocene-based oxidations indicating metal communication, which could not be resolved for the HAT-CN_6 analogue.[20]

4.1.2 Rhenium HATN complexes

Rhenium(I) polypyridyl complexes are a well-studied class of compounds because of their rich photo-physical properties.These properties are comparable to isoelectronic Ru(II)-diamines.[21] They often show similar photo- and electro-catalytic behaviour towards various oxidation and reduction process. These properties have led to the investigation for their use in molecular devices such as field effect transistors[22,23] and photovoltaics.[22,24]

Incorporating rhenium into HATN is interesting as it provides a system where control over the number of coordinated atoms in sterically hindered bidentate sites can be executed. The first HATN-Re complex was formed in 1994 by Gray et al.[13] who based their synthesis on similar chemistry occurring with HAT. They found that HATN was able to be coordinated to rhenium(I) pentacarbonyl chloride in a single bidentate site (Figure 5). From this they were then able to coordinate palladium dichloride to give a Re, Pd heteronuclear complex. This is the only heteronuclear HATN in the literature. What is interesting to note is that the HATN-1Pd is still soluble in chloroform but the HATN-2Pd complex (Figure 5) is insoluble hence the HATN-3Pd complex was unable to be isolated.

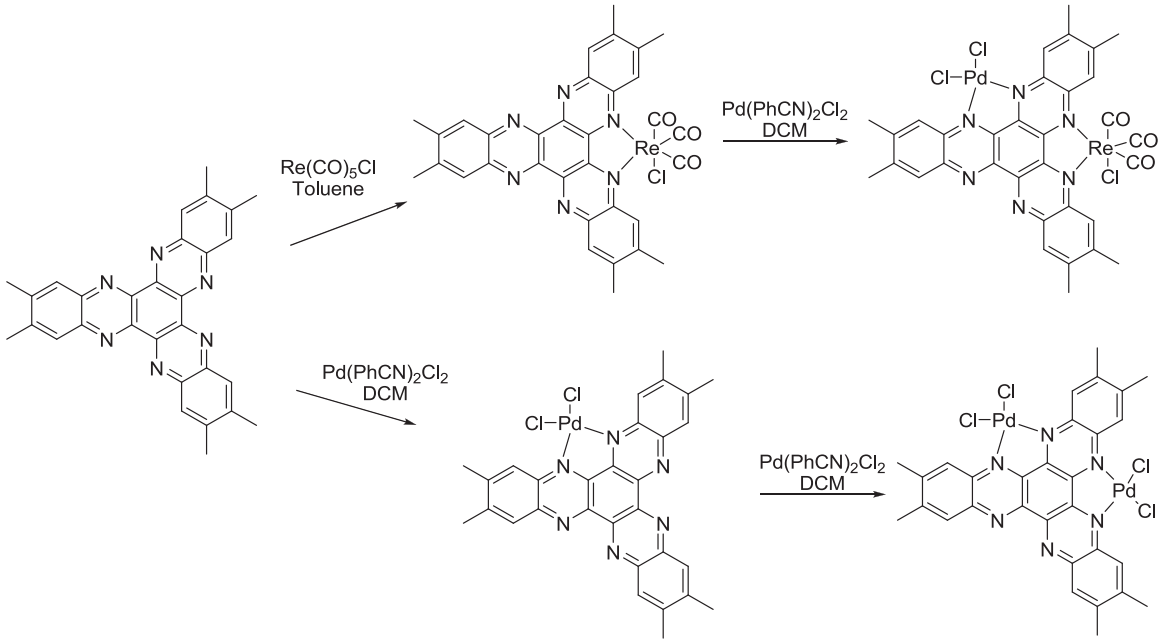

Figure 5 The first and only synthesis of a heteronuclear HATN complex containing rhenium and palladium along with a HATN-2Pd complex.

In a more recent rhenium study, Kubiak et al.[21] reported the synthesis and characterization of the mononuclear complex [(HATN-6Me)($Re(CO)_3Cl$)], as well as the binuclear complex [(HATN-6Me)($Re(CO)_3Cl)_2$], where the two chloro atoms were found to lie on the same side of the ligand plane, i.e. the *syn* isomer. The number of occupied sites is altered simply by changing the ratio of rhenium complex to HATN material. Gordon et al.[11] expanded upon this and found that for the complex [(HATN-6Me)($Re(CO)_3Cl)_2$] *syn* and *anti* (the two chlorines on the opposite side of the ligand plane) isomers could be isolated in a 1:1 ratio using chloroform as solvent. For the HATN-3Re complex, isomers could be manipulated by synthesising the 3Re complexes in two steps. The first was by preparing the HATN-2Re complex, and separating the *anti* and *syn* isomers. This step resulted in a statistically likely 1:1 mixture of the *syn* to *anti* isomers. The *syn* isomer could then be taken and depending on the solvent, toluene or chloroform, the near exclusive formation of the *syn* or *anti* HATN-3Re complex was achieved (see Figure 6).[11]

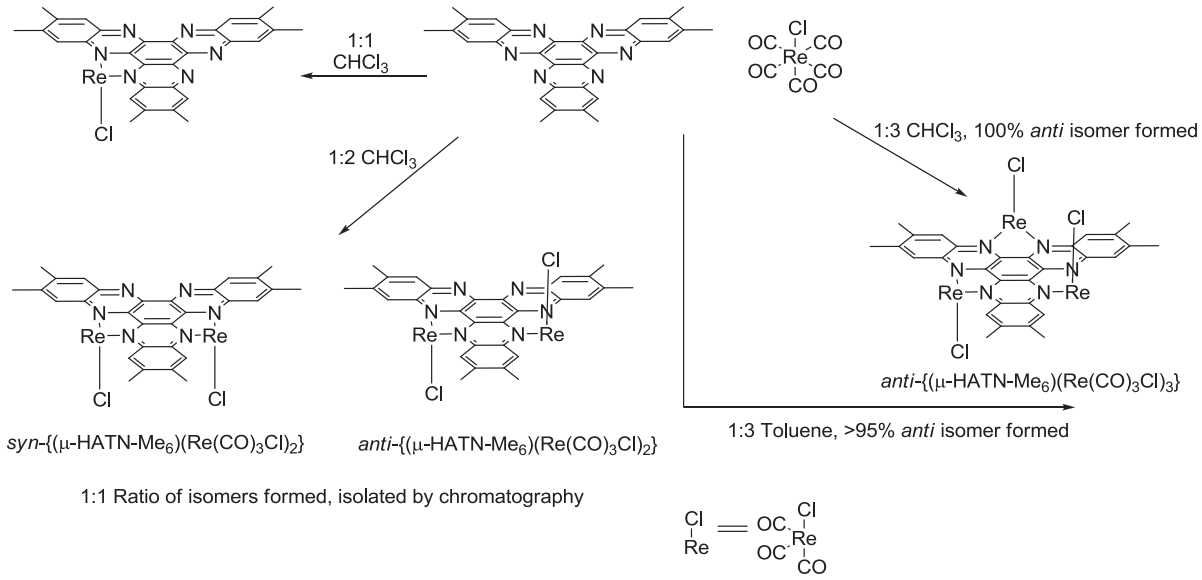

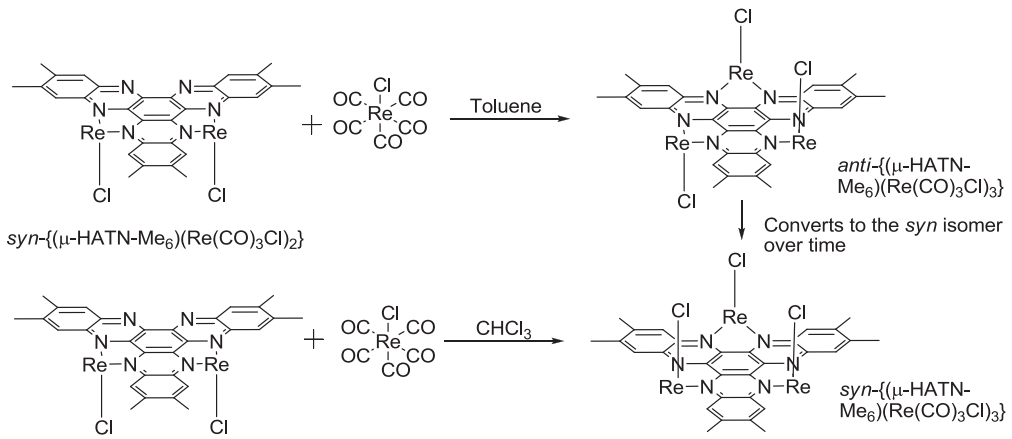

Figure 6 Detailed synthetic steps to form mono- bi and tri- rhenium HATN complexes as well as the controlled synthesis of the *syn* and *anti* isomers of HATN-2Re complexes.

4.2 Reactions of hetero-HATNs

The HATNs are electron deficient with low-lying π^* orbitals. Electron-rich metals in low oxidation states such as Cu(I) ($3d^{10}$) and Re(I) ($5d^6$) are able to donate electron density into them. Hence this study will explore the coordination behaviour of HATN with Cu(I) and Re(I). In this chapter the ligands produced in Chapter 2 (HATN-4Me, HATN-4Br, HATN-2Me, HATN-4Br2Me, HATN-2Br, HATN-4Me2Br), see Figure 7, were reacted with $[Re(CO)_5Br]$ and $[Cu(MeCN)_2(PPh_3)_2]BF_4$ to give their associated complexes. HATN-4Me was also reacted with $[PdCl_2(C_6H_5CN)_2]$ to produce its respective complex. Hence this investigation was performed in order to elucidate the coordination behaviour of the HATN ligands with a selection of transition metals and to study the physical properties of the complexes formed.

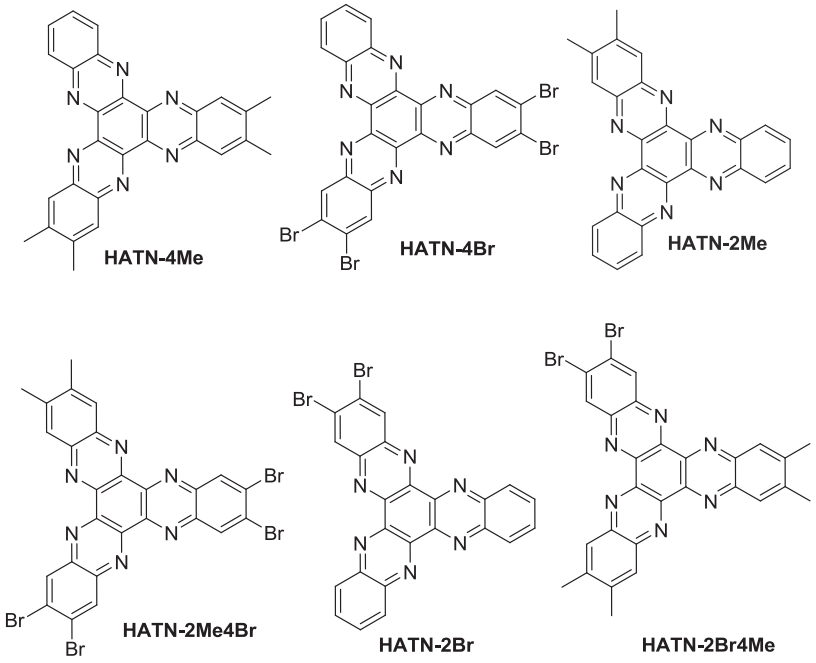

Figure 7 Six HATN ligands with varying donating and withdrawing groups used in the synthesis of complexes.

4.2.1 Labelling compounds

Due to the possibility of adding varying ratios of rhenium to the tridentate HATN it is possible for many isomers to be formed, thus the separation and identification of products becomes a lot more time consuming. Figure 8 shows the possible structural isomers that can, for example, be formed with HATN-4Me

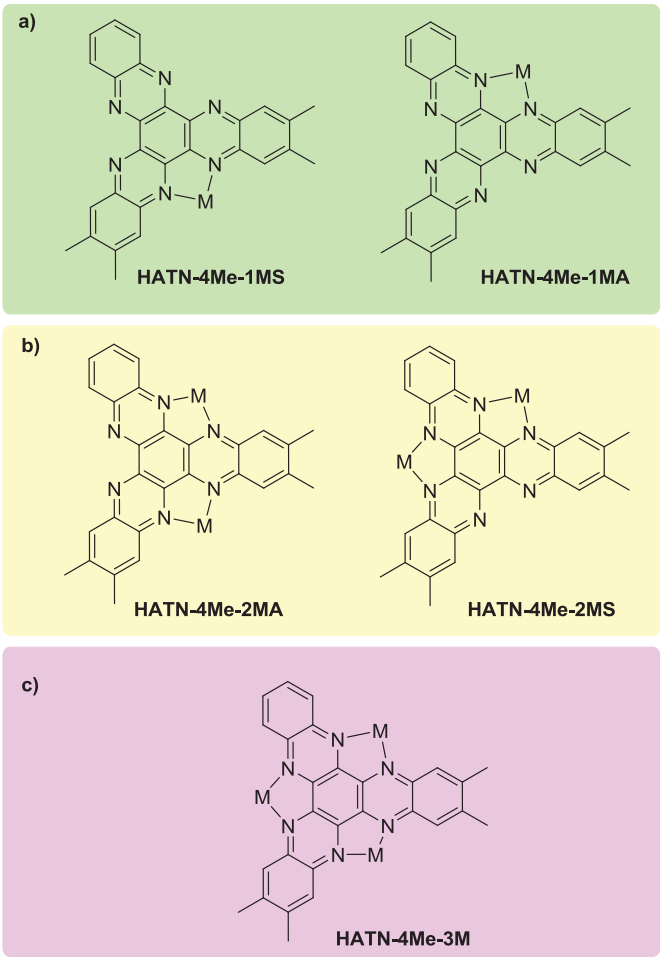

Figure 8 Labelling of various coordination compounds of HATN-4Me and their isomers. (a) the isomers formed when the metal:HATN-4Me ratio is 1:1 (b) the isomers formed with the metal:HATN-4Me ratio is 2:1 (c) the isomer formed with the metal:HATN-4Me ratio is 3:1.

Comments about the labelling convention used are now given. The first part of the name indicates the HATN and its functional groups, i.e. HATN-4Me. The next indicates what metal and how many have been added, i.e. HATN-4Me-2M for the addition of two

metals to HATN. The last letter is A or S indicating when it is possible which structural isomer is present, i.e. that asymmetric (no C_2 symmetry) or symmetric (C_2 symmetry) isomer.

4.2.2 Synthesis of rhenium complexes

4.2.2.1 Mono-rhenium complexes

The addition of bromopentacarbonylrhenium to the appropriate HATN in a 1:1 ratio with each of the six ligands (Figure 9) resulted in the detection and characterisation of seven 1Re complexes and four 2Re complexes (Figure 10, and see Chapter 7.2.2 for full details of their isolation). Unlike previous studies on homo-HATNs the coordination sites were not equivalent resulting in the formation of asymmetric (A) and symmetric (S) sites. It is interesting to note that one site is not preferred over the other and that these isomers were formed in uncontrollable ratios in the synthesis. Many products can be formed in the reaction of $Re(CO)_5Br$ with the hetero-HATNs in a 1:1 ratio. These include the S and A isomers of the mono-rhenium complexes and the *syn* and *anti* isomers of the S and A isomers of the di-rhenium complexes. It was not possible to isolate each of the isomers from the complex mixture, instead two complexes were obtained after consecutive chromatography for each reaction.

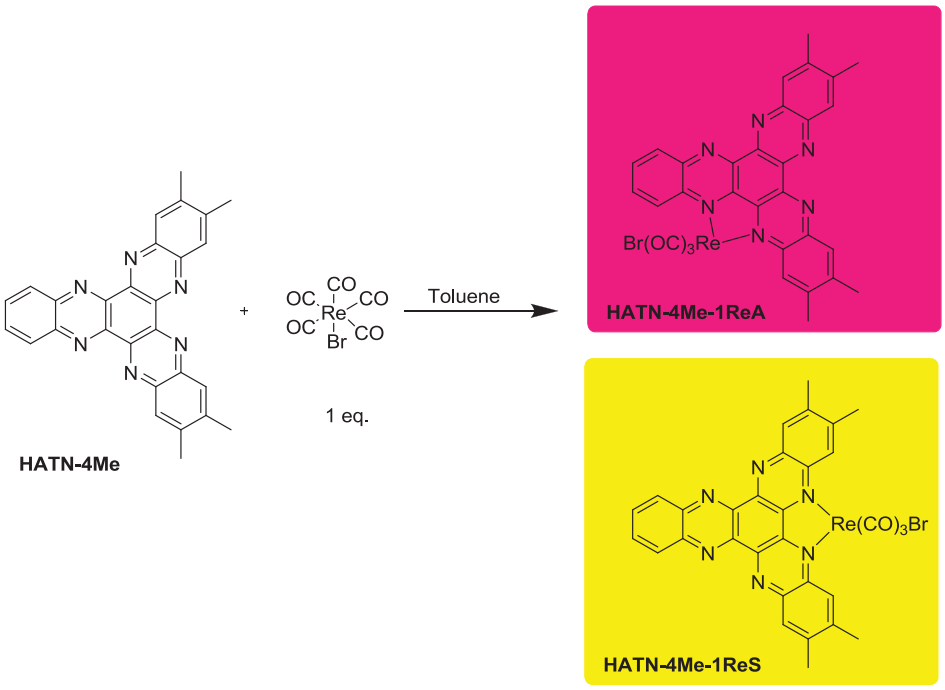

Figure 9 A representative rhenium HATN-4Me reaction to give the A and S isomers.

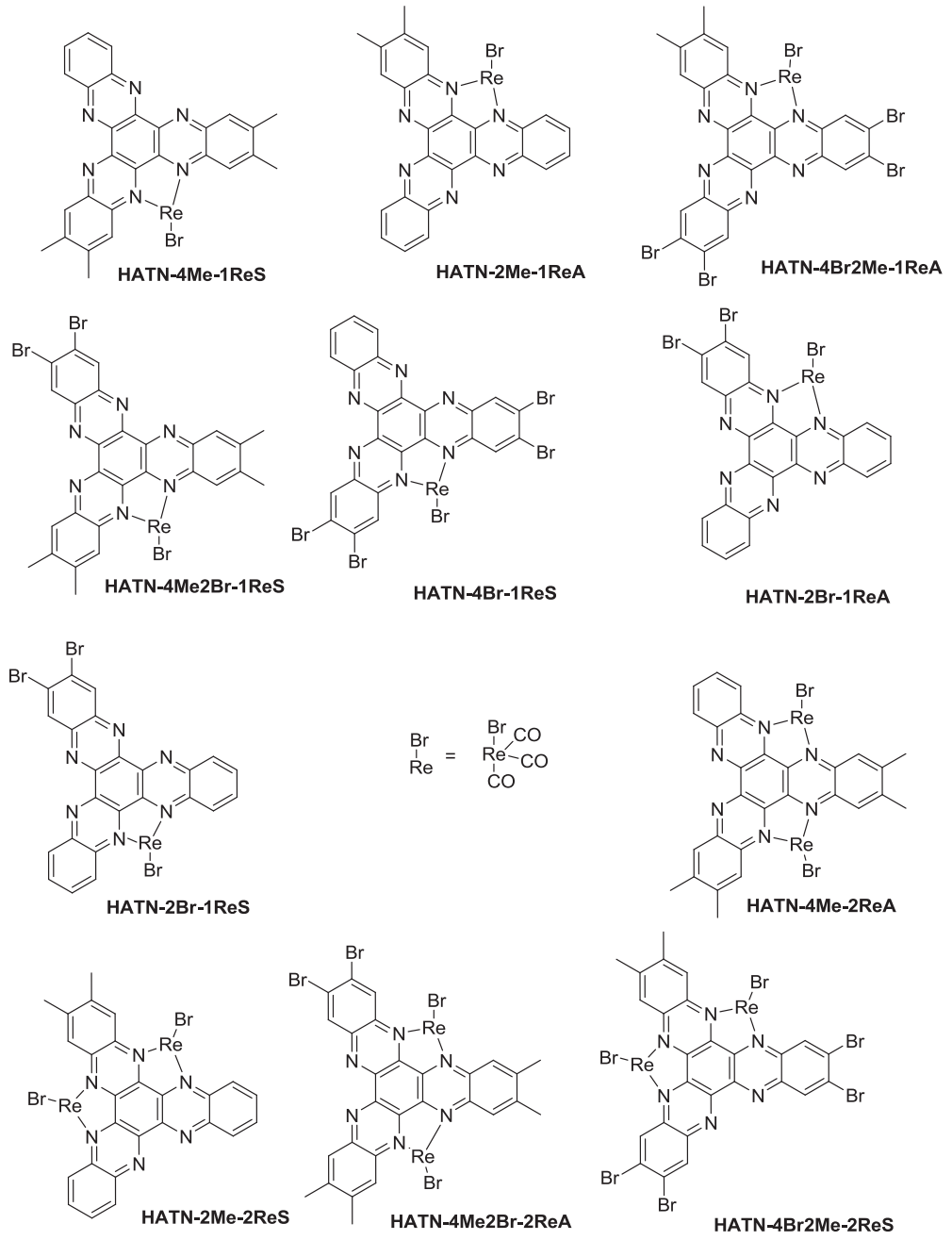

Figure 10 The seven HATN-1Re and four HATN-2Re complexes identified.

Each of the HATN complexes was synthesised similarly to literature procedures and described in the Chapter 7.2.2. A 1:1 ratio of the HATN and bromopentacarbonyl rhenium(I) was mixed overnight in toluene to produce the complexes. $[Re(CO)_5Br]$ was used as this was easier to synthesise in the laboratory than the chloro analogue most often used in the literature. Purification of the complexes was done using silica gel

chromatography as several side products were formed. It was found that the compound which had substituted more than one rhenium eluted faster and this allowed the separation of the HATN-2Re from the HATN-1Re materials. The different isomers of the HATN-1Re also gave overlapping bands on column chromatography so required multiple columns to purify. However, eventually the columns were unable to separate impurities from the HATN-Re materials and the latter began to degrade. This produced more complex side products after consecutive columns. Nuclear magnetic resonance (NMR) was able to give the isomer formed, A or S of the HATN-1Re and HATN-2Re complexes. UV/Vis was a much more useful tool as it made it possible to specify the rhenium number on HATN without waiting for elemental analysis.

The A and S positions in the HATN-1Re complexes formed in different ratios as shown in Figure 11 (this has been calibrated for the doubling up of protons in the symmetric isomers with both the aromatic and methyl protons checked and the 2Re complexes have also been dismissed). Statistically the A isomer should be favoured as there are two A coordination positions compared with one S, hence a 2:1 ratio should occur if there is no effect of the functional groups within the HATNs. It is found that in half the cases the S isomer was favoured. The two cases in which the A isomer formed in an equal yield are HATN-4Br2Me and HATN-2Br respectively, while HATN-4Br favours the asymmetric isomer. The bromines in this case may draw significant electron density away from the coordinating nitrogens making complexation at those sites less favoured. Whereas the S position in the HATNs may be more thermodynamically favoured generally.

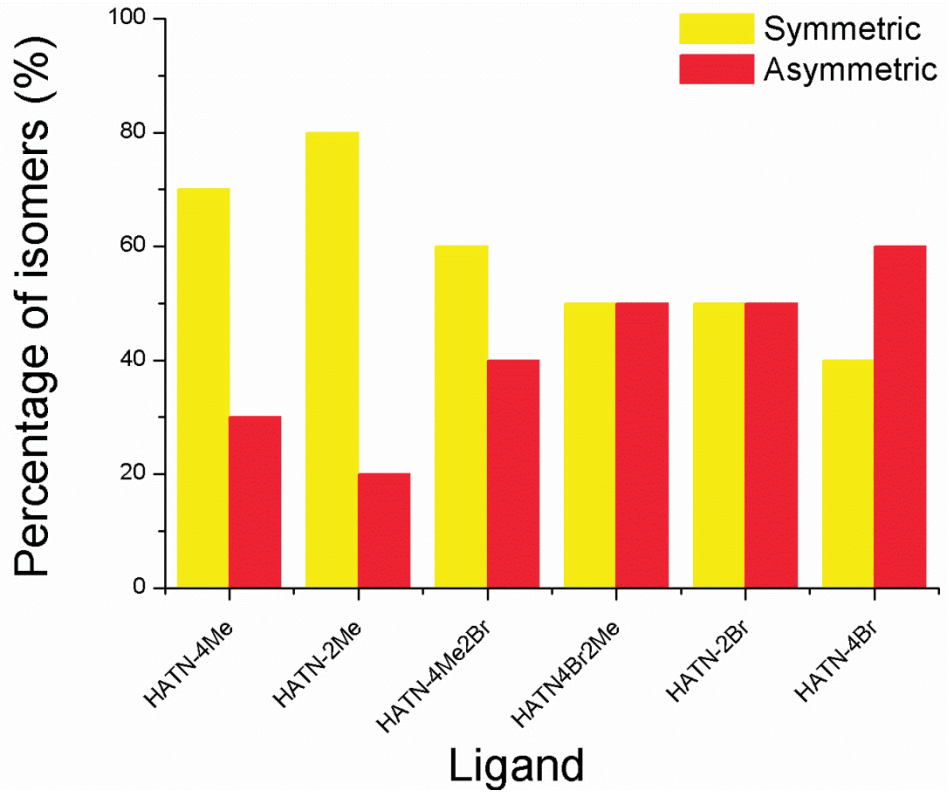

Figure 11 Percentage of hetero-HATN-1Re A and S isomers formed during synthesis. This has been calibrated for the doubling up of protons in the symmetric isomers.

Additionally upon coordination of one rhenium or two rhenium atoms results in a colour change shown in Table 1.

Table 1 Colours of HATN-1Re and HATN-2Re complexes. G=green complex, O=orange complex, blank = isomer wasn't isolated.

Complex	Asymmetric	Symmetric
HATN-4Me-1Re		O
HATN-2Me-1Re	O	
HATN-4Br-1Re	G	
HATN-2Br-1Re	O/G	O
HATN-4Me2Br-1Re		O
HATN-4Br2Me-1Re	O/G	
HATN-4Me-2Re	G	
HATN-2Me-2Re		G
HATN-4Me2Br-2Re	G	
HATN-4Br2Me-2Re		G

4.2.2.2 Multi-rhenium HATN complexes

HATN di-rhenium complexes were obtained in small yield as a side product in the 1:1 mixing of HATN ligands and rhenium pentacarbonyl bromide. Although it was possible to form a library of HATN-2Re complexes and extend this to HATN-3Re complexes directly this was not a focal point of this project with its attendant DFT calculations as well. Instead Figure 12 suggests possible isomers that may be expected.

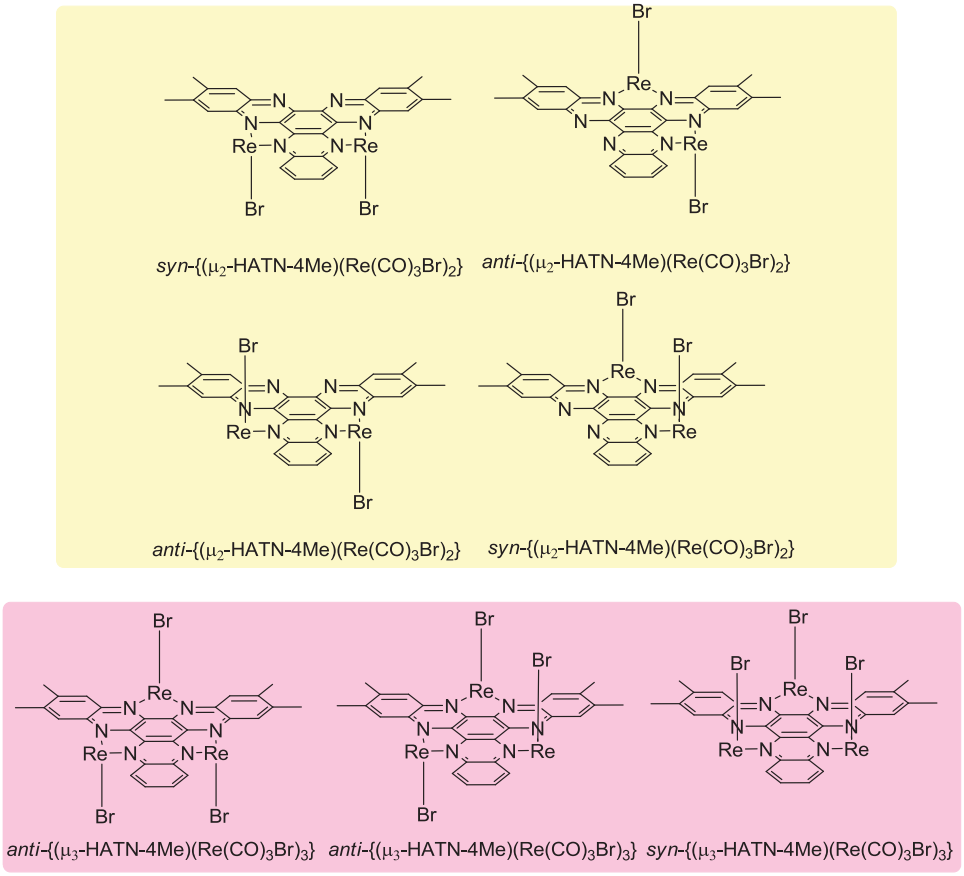

Figure 12 Possible isomers for multi-rhenium complexes illustrated with HATN-4Me.

4.2.3 Crystallography

The X-ray data for HATN-4Me-1ReA·H_2O and HATN-4Me-1ReS·$CHCl_3$·H_2O and HATN-2Me-2ReS were collected at a reduced temperature (-110 ˚C) with a Rigaku Spider MM007 diffractometer equipped with a microfocus copper rotating anode X-ray source, high-flux Osmic monochromating and focusing multilayer mirror optics and a curved image plate detector. The crystals were mounted in an inert oil, transferred into the cold gas stream of the detector and irradiated with graphite monochromated Cu Kα (k = 1.54178 A) X-rays. The data was collected by the Crystal Clear[25] program (v.1.4.0) and processed with *FSProcess*[26] to apply Lorentz and polarisation corrections to the diffraction spots (integrated three dimensionally).

The structures were determined by direct methods using *SHELXS-97*[27] and *OLEX*[2] [28] and refined using the same programs. Absorption correction was carried out empirically. Hydrogens were calculated at their ideal positions unless otherwise stated. Refinement data for the X-ray crystal structures are given in Table 2.

Table 2 HATN-4Me-1ReA·H_2O left and HATN-4Me-1ReS·$CHCl_3$·H_2O

Compound	**HATN-4Me-1ReA**	**HATN-4Me-1ReS ·$CHCl_3$·H_2O**
Molecular formula	$C_{31}H_{20}BrN_6O_3Re$	$C_{32}H_{23}BrCl_3N_6O_4Re$
M (g mol^{-1})	790.64	928.02
Temperature (K)	154	153
Crystal System	Triclinic	Triclinic
Space group	$P\bar{1}$	$P\bar{1}$
a(Å)	7.2876(15)	9.2240(3)
b(Å)	18.967(4)	11.4445(3)
c(Å)	21.881(4)	15.6900(11)
α(°)	99.73(3)	76.274(5)
β(°)	93.46(3)	88.169(6)
γ(°)	90.08(3)	81.406(6)
V(Å^3)	2975.3(11)	1590.92(14)
Z	4	2
μ(Cu Kα) mm^{-1}	9.956	11.674
ρ_{calc} (g cm^{-1})	1.805	1.937
2θmax(°)	117.84	130.160
Number of unique reflections	6925	5296
Data/restrains/parameters	6925/1002/681	5296/40/434
Final R indices [I>2σ(I)]	*wR*2 = 0.3253	*wR*2 = 0.0858
	R = 0.1432	*R* = 0.0368
R indices (all data)	*wR*2 = 0.3575	*wR*2 = 0.1071
	R = 0.1670	*R* =0.0435
Goodness-of-fit on F^2	1.109	1.146

Table 2 shows the refinement data for the isomers HATN-4Me-1ReA and HATN-4Me-1ReS. CIF files are included on the accompanying disc for reference. On conducting an online CIF check, all significant alerts have been explained in the CIF file.

Table 3 HATN-2Me-2ReS

Compound	**HATN-2Me-2ReS**
Molecular formula	$C_{32}H_{16}Br_2N_6O_6Re_2$
M (g mol^{-1})	1112.73
Temperature (K)	154
Crystal System	Monoclinic
Space group	*C*2/*c*
a(Å)	41.981 (8)
b(Å)	7.0230(14)
c(Å)	22.001(4)
α(°)	90.00
β(°)	99.81(3)
γ(°)	90.00
V(Å^3)	6392(2)
Z	8
μ(Cu Kα) mm^{-1}	17.991
ρ_{calc} (g cm^{-1})	2.313
2θmax(°)	144.14
Number of unique reflections	6169
Data/restrains/parameters	6169/10/455
Final R indices [I>2σ(I)]	*wR*2 = 0.0767 *R* = 0.0320
R indices (all data)	*wR*2 = 0.0770 *R* = 0.0326
Goodness-of-fit on F^2	1.275

Table 3 shows the refinement data for HATN-2Me-2ReS. CIF files are included on the accompanying disc for reference. On conducting an online CIF check, all significant alerts have been explained in the CIF file.

4.2.4 Crystal structure of HATN-4Me-1ReA

Green needles of HATN-4Me-1ReA were obtained by slow evaporation of the pure solid dissolved as a saturated solution with chloroform. The structure is consistent with the data obtained by NMR. The crystal exhibits a facial (*fac*) arrangement of the tricarbonylrhenium(I) moiety as expected from literature.[11] Bond lengths and angles are discussed in detail in section 4.2.6.

Triclinic HATN-4Me-1ReA crystallizes in the space group $P\bar{1}$ with two HATN-4Me ligands each coordinated to a single bromotricarbonylrhenium in the asymmetric position. The rhenium is 0.733 Å out of plane of the HATN. The R-factor is high, 14.32 %, this is due to multiple crystals being present on the goniometer. There was also significant residual electron density present indicating disordered solvent so this was squeezed using PLATON.[29,30]

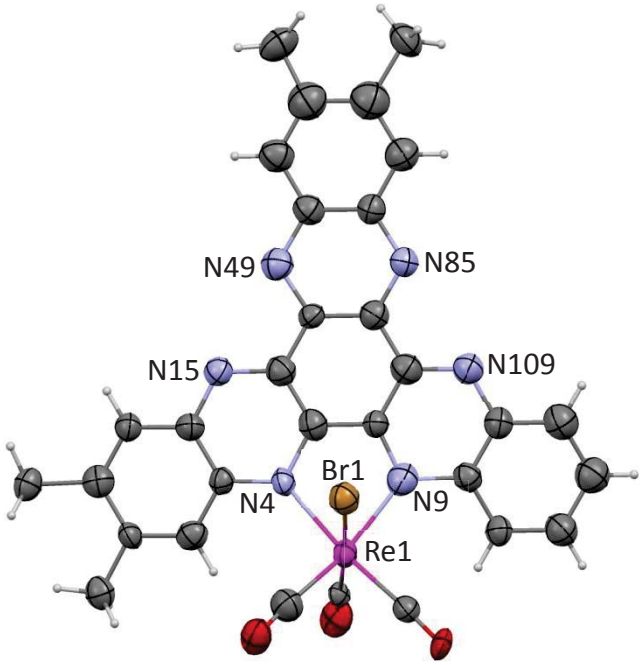

Figure 13 Crystal structure for HATN-4Me-1ReA with 50% probability ellipsoids for all atoms excluding hydrogen, solvent molecule removed for clarity.

4.2.5 Crystal structure of HATN-4Me-1ReS·$CHCl_3$·H_2O

Reddish needles of HATN-4Me-1ReS were obtained by slow evaporation of a saturated solution in chloroform. The crystal exhibits a *fac* arrangement of the tricarbonylrhenium(I) similar to the A isomer. This is consistent with the data obtained by MS, IR and NMR spectroscopies and elemental analysis. The structure refined well with an R-factor of 3.68 %. Bond lengths and angles are discussed in detail in Section 4.2.6.

Triclinic HATN-4Me-1ReS crystallises in the space group $P\bar{1}$ with 1 molecule of water and 1 molecule of chloroform per asymmetric unit. The cell refines with two ligand molecules per unit cell. The rhenium is 0.400 Å out of plane of the HATN.

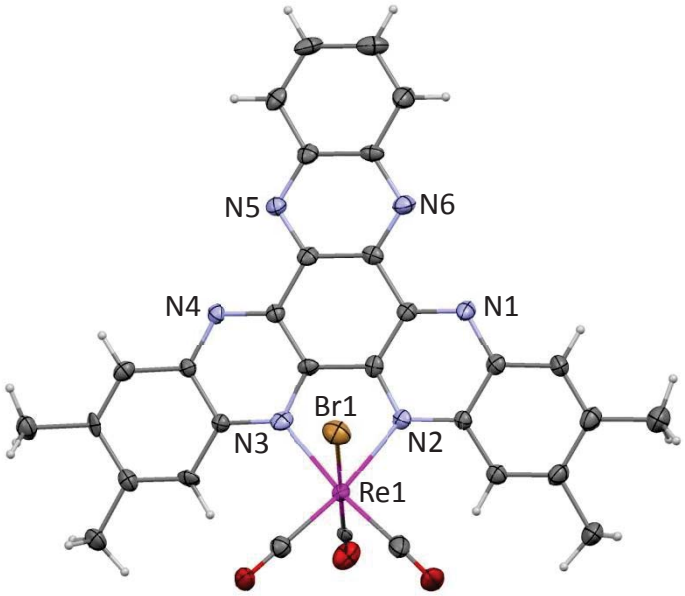

Figure 14 Crystal structure of HATN-4Me-1ReS with 50% probability ellipsoids for all atoms excluding hydrogen, solvent removed for clarity.

4.2.6 Crystal structure of HATN-2Me-2ReS

Dark red crystals of HATN-2Me-2ReS were obtained by slow evaporation of the carrier solution from the column obtained, which in this case was 5% methanol in chloroform. The structure shows the chelation of two bromotricarbonylrhenium(I) units by the HATN-2Me ligand in positions such that the molecule is still symmetric (Figure 15). The crystal exhibits a *fac* arrangement of the tricarbonylrhenium(I) moieties and the bromo groups crystallize as the *anti* isomer. Two bromine ligands are disordered with a minor occupancy component trans to the major with complementary carbonyl disordering. Bond lengths and angles are discussed in detail in Section 4.2.6.

Monoclinic HATN-2Me-2ReS crystallizes in the space group C2/c with one molecule of water and one molecule of chloroform per asymmetric unit. The rhenium atoms are 0.803 Å and 0.810 Å out of plane of the HATN. Syn and anti di-rhenium isomers have been synthesised with homo-HATNs in the literature from the reactions of HATNs with [Re(CO)5Br] in a 1:1 ratio. However, in the present work the data showed only the presence of the *anti* isomer in the material collected (Figure 15). This could be because only this isomer was isolated during chromatography as a side product whereas the *syn* isomer may have been formed but not collected.

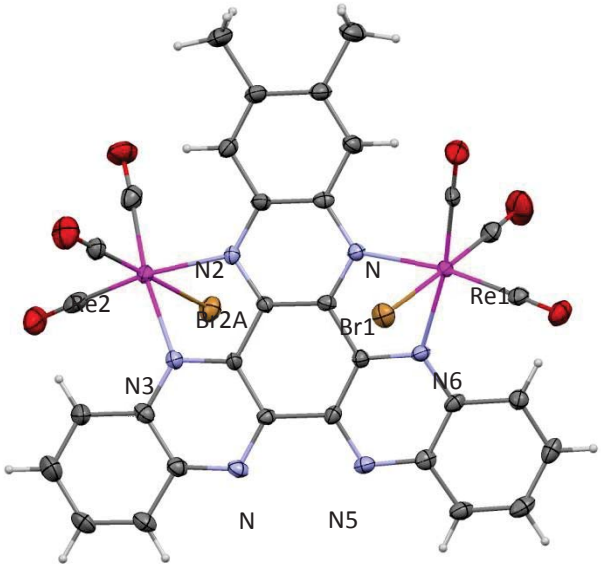

Figure 15 Crystal structure of HATN-2Me-2ReS with 50% probability ellipsoids for all atoms excluding hydrogen.

4.2.7 Crystallography discussion

For all three rhenium compounds the coordination geometry at the rhenium atom is a distorted octahedron with three carbonyl ligands arranged in the *fac* fashion. There is a significant contraction in the N-Re-N bond angle to 74.9(2)-75.7(10)°, significantly smaller than the ideal 90°. This is a result of the small bite angle of the ligand (1,10-phenanthroline has a bond angle of 75.8(2)°.[31]

All the ligands are distorted from planarity by steric interactions between the HATN ligands and the metal centre. The peripheral aromatic rings are twisted from the central ring by 7° -13°. In HATN-4Me-1ReA and S the steric strain is evenly distributed between those rings in contact with the rhenium.

In HATN-4Me-1ReA the Re is located between one unsubstituted ring (ring 1, Figure 16) and the methyl substituted ring (ring 2, Figure 16). The unsubstituted ring, ring 1, twists more than the methyl ring, ring 2; this may be due to π-π stacking of these unsubstituted rings on top of one another.

In HATN-4Me-1ReS the Re is located between the two methyl rings (ring 2 and 3, Figure 16). The unsubstituted ring, ring 1, stays in plane with the two rings closest to the rhenium twisting out of plane. The twisting of ring 2 and 3 is very similar with both around 8.4°. The intermolecular stacking occurs between ring 1 on the molecules which may be a reason why they are in plane.

HATN-2Me-2ReS also has significant twisting in two of its unsubstituted branches (rings 2 and 3, Figure 16). The methyl substituted branch (ring 1) doesn't seem to twist as it is locked in plane by being in between two Re atoms. One unsubstituted phenazine branch twists more than the other due to π-π T-shape stacking of only one branch stabilising this extra strain. These key parameters are given in Table 4.

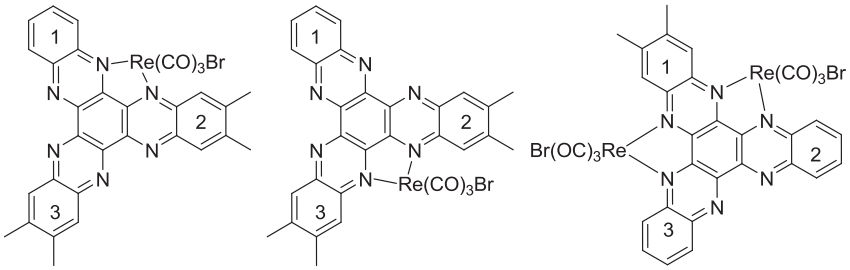

Figure 16 Left: HATN-4Me-1ReA Middle: HATN-4Me-1ReS Right: HATN-4Me-2ReS and their ring numbers to help aid description

Table 4 Table of important HATN-Re crystallography information

Measurements	HATN-4Me-1ReA	HATN-4Me-1ReS	HATN-2Me-2ReS
N-Re-N angle (°)	75.7(10)	74.9(2)	Re1 74.92(17) Re2 75.08(16)
Plane twisting (°)	10.50 (ring 1) 7.05 (ring 2)	8.45 (ring 2) 8.38 (ring 3)	12.98 (ring 2) 8.03 (ring 3)
Re-N (Å)	Re-N4 2.18(2) Re2-N9 2.202(5)	Re1-N3 2.192(5) Re1-N2 2.194(5)	Re1-N6 2.191(4) Re1-N1 2.185(4) Re2-N2 2.182(4) Re2-N3 2.202(5)

The Re-N bond lengths range from 2.18(2) to 2.21(3) Å with the deviations attributable to differences in the π-back-bonding. The Re-CO bond lengths range from 1.91(4)-2.08(4) Å do not show any significant differences These are typical of tricarbonylrhenium(I)-diimine systems. The rhenium–nitrogen bond lengths are typical of rhenium(I) and are consistent with those observed in similar complexes.[32,33]

Further bond lengths and angles for HATN-4Me-1Re A and S are found in Appendix C.

4.2.8 Packing in the rhenium complexes

Based on the crystal structure the packing of the rhenium HATNs is largely determined by the π-π stacking with H-bonding between solvent molecules and the ligand. The π-π stacking provides stability for extra twist obtained in the HATN branches.

HATN-4Me-1ReA·H_2O has π-π stacking between the unsubstituted rings (3.58 Å Figure 17). This stacking allows an increase in the twist of the overlapping unsubstituted rings. The water molecules sit near the free nitrogens at a distance of 3.5-3.8 Å (O-N). There is an intermolecular distance of 3.3-3.6 Å. There also appears to be H-bonding between the bromo and CO groups on the rhenium to the unsubstituted ring on another HATN.

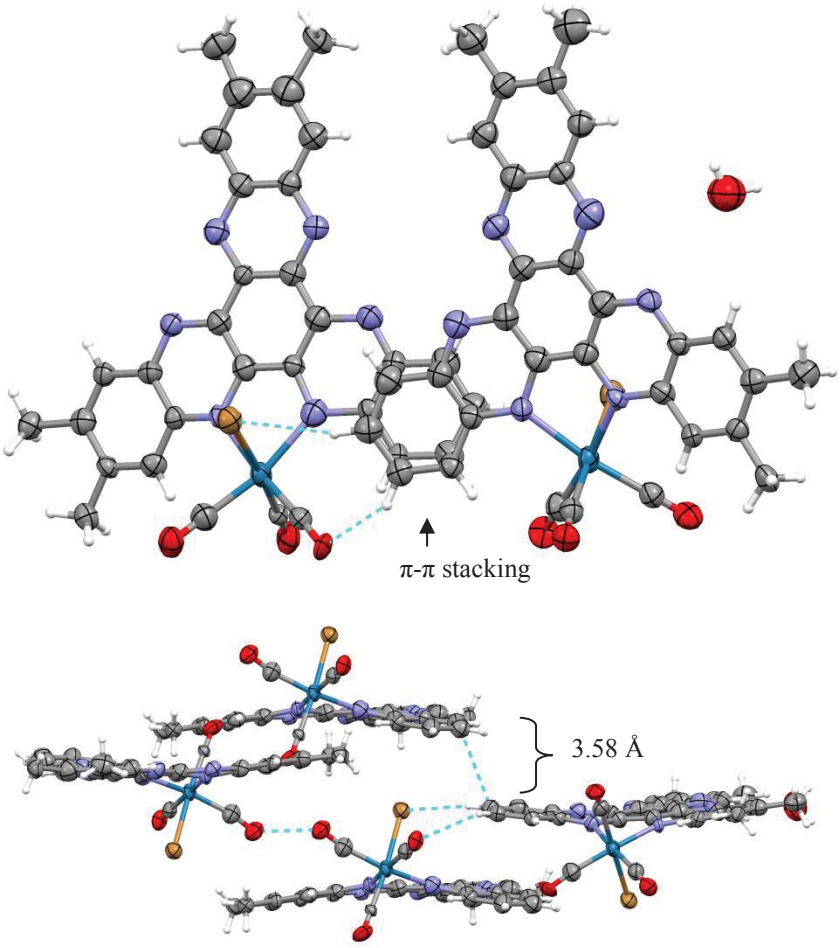

Figure 17 Packing structure for HATN-4Me-1ReA. Blue lines indicate H bonding and H-π bonding.

HATN-4Me-1ReS·$CHCl_3$·H_2O has π-π stacking of three of the rings with an inter-plane distance of 3.41 Å̊ (Figure 18). There appears to be H-bonding between the H of $CHCl_3$ to Br from rhenium. The water H-bonds to the free nitrogen atoms with O-H-N angles of 132.7 – 152.8°.

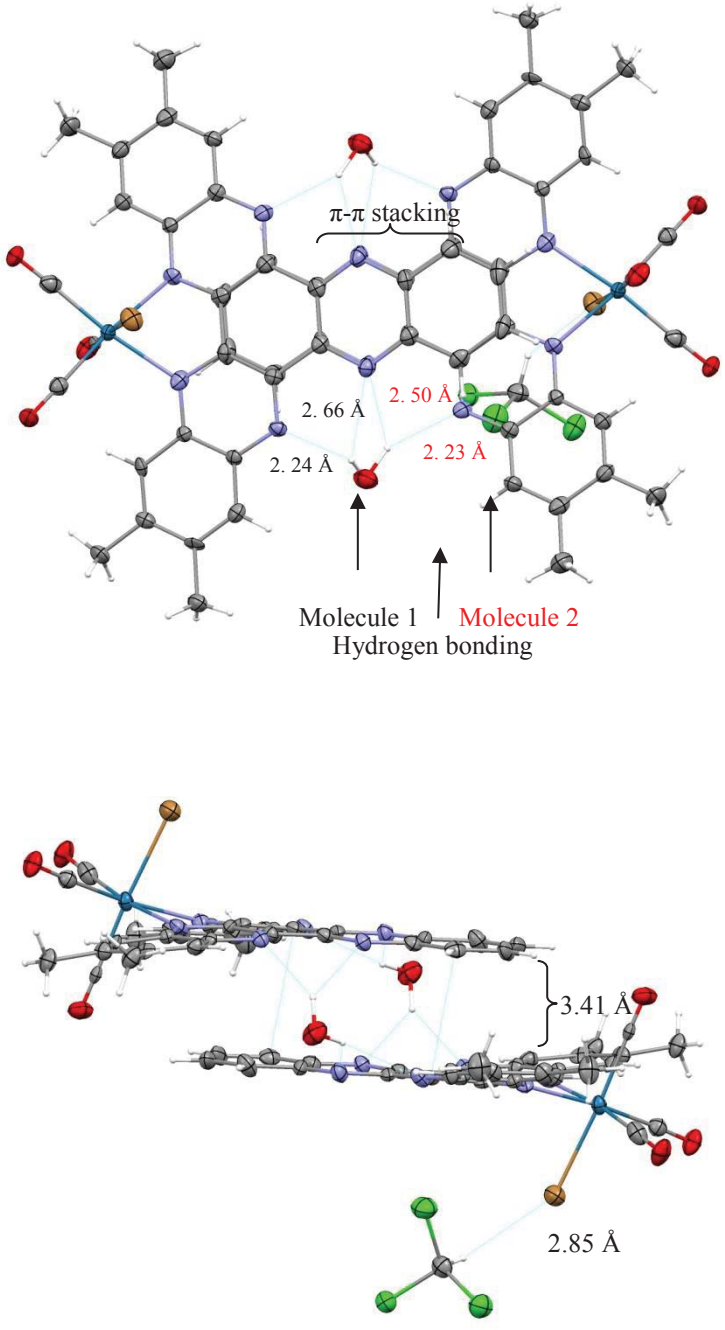

Figure 18 Packing structure for HATN-4Me-1ReS·$CHCl_3$·H_2O, dotted line indicates H-bonding.

HATN-4Me-2ReS packing is largely dictated by the CO bonding from the rhenium to the π electrons of another ligand (Figure 19). There is also some overlap between one unsubstituted ring and a pyrazine ring of another HATN molecule with the rings 4.45 Å apart.

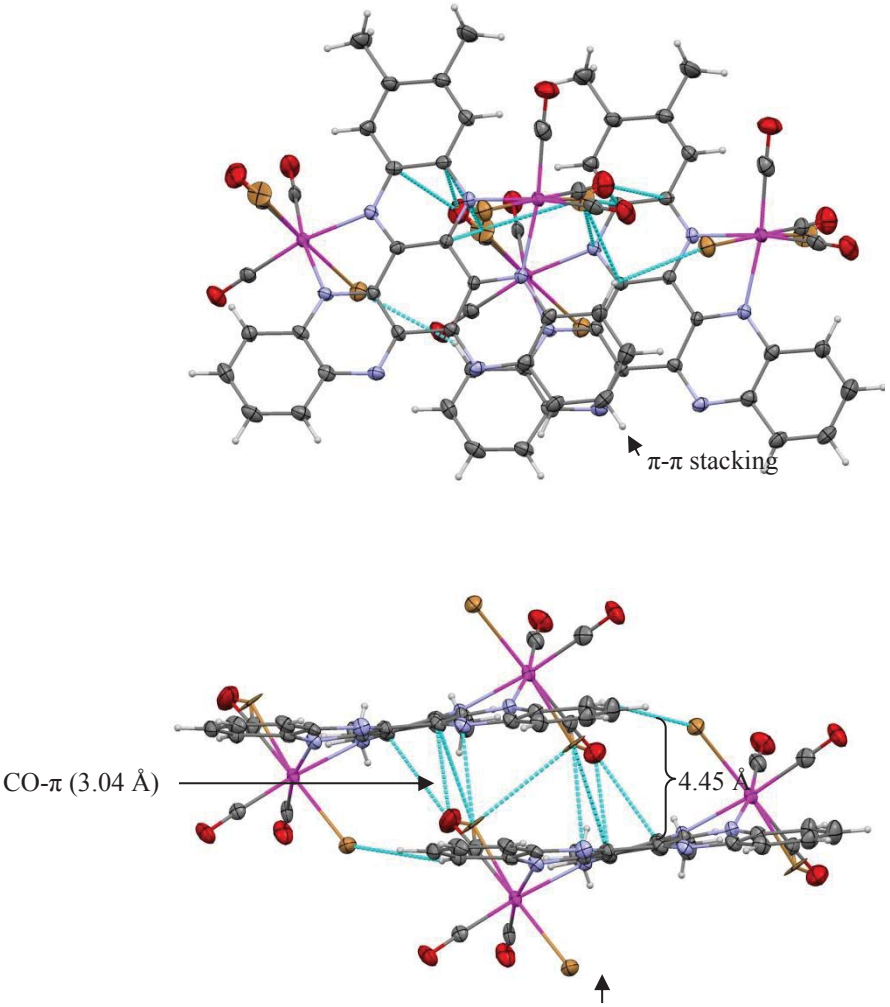

Figure 19 Crystal packing for HATN-2Me-2ReS. Blue lines show H-bonding.

4.3 Copper(I) HATN complexes

The copper complexes were prepared following a literature method[10] whereby bis(acetonitrile)bis(triphenylphosphine)copper(I) tetrafluoroborate was reacted with each of the ligands (HATN-4Me, HATN 4Br, HATN-2Me, HATN-4Br2Me, HATN-2Br, HATN-4Me2Br) in a 3:1 ratio in diethyl ether. The mixture was stirred under argon for 48 h and the resulting green product was filtered off with yields ranging from 70-80%. Six tri-metallic copper complexes were synthesised and characterised (Figure 20). Repeated crystallizations in methanol were required to ensure pure complexes. See Chapter 7.2.2 for experimental details.

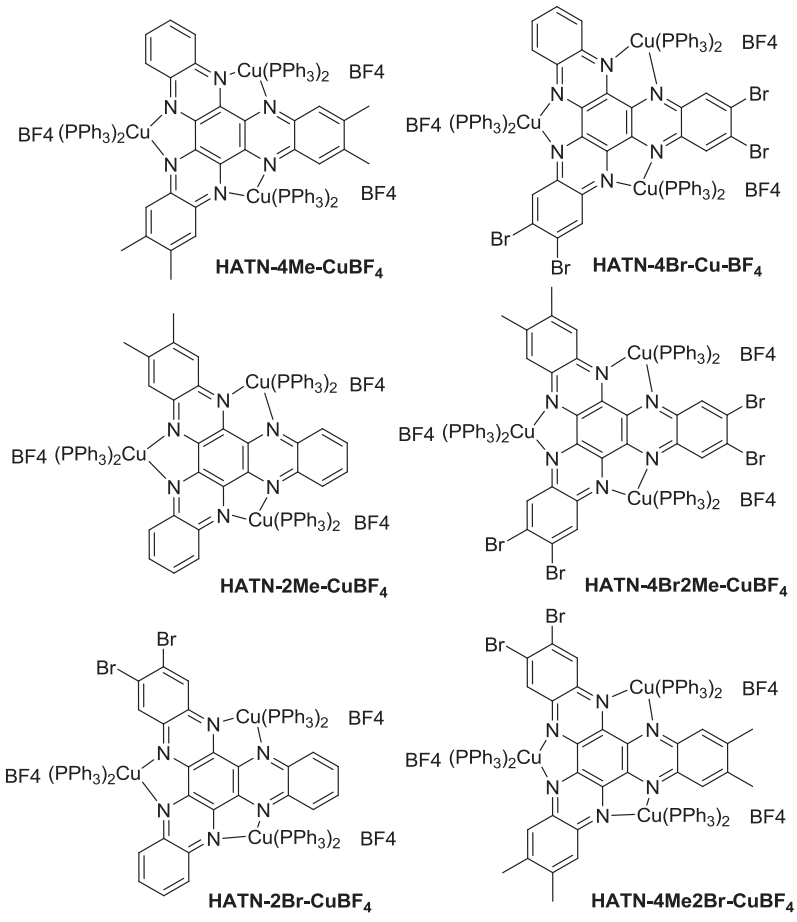

Figure 20 HATN-copper complexes of the HATNs that were characterised.

Due to the significant broadening of the proton peaks in ^{1}H NMR at room temperature, the spectra were not a useful indicator of formation. Lowering the temperature to -50°C

did not help resolve the peaks and the broadening observed was possibly due to rotation of the phenyl groups and exchange reactions occurring with the triphenylphosphine. Elemental analysis and mass spectra were used to verify the stoichiometry of these complexes. Previously, HATN-6Me has been shown to give the similar compound $[(Cu(PPh_3)_2)_3(HATN\text{-}6Me)](BF_4)_3$ but no ^1H NMR spectra were recorded (see Figure 21).[10] Attempts to prepare a 1:1 complex with $[Cu(MeCN)_2(PPh_3)_2]BF_4$ and HATN-4Me failed, instead only the tri-copper complex was isolated. The driving force therefore is in the direction of the formation of the tris-copper complex and this is expected to be enhanced by its insolubility.

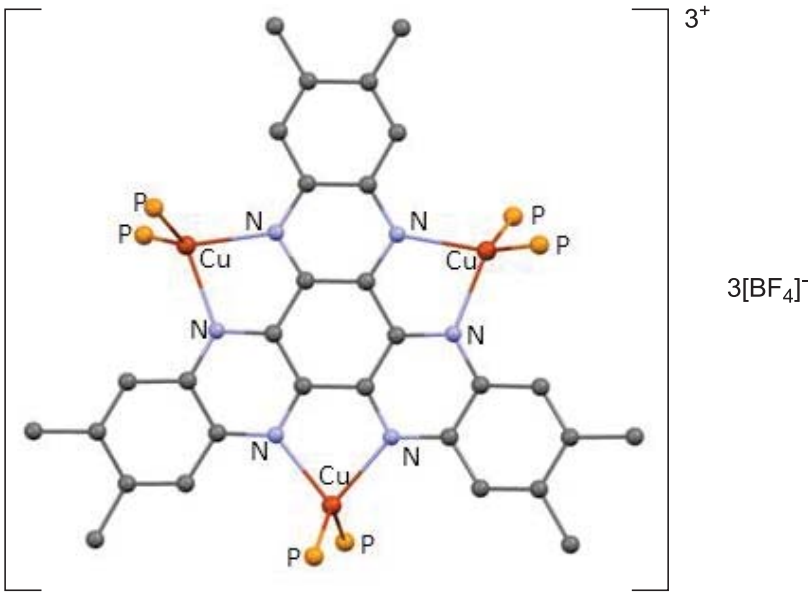

Figure 21 Crystal structure of $[(Cu(PPh_3)_2)_3(HATN\text{-}6Me)]^{3+}$ cation. The phenyl rings of the PPh_3 ligands have been removed for clarity.[10]

Unfortunately as crystals of the BF_4^- salts could not be obtained in the present study, an attempt was made to prepare a perchlorate (ClO_4^-) salt in a selected case. With HATN-4Me and $[Cu(MeCN)_2(PPh_3)_2]ClO_4$ the complex $[Cu(PPh_3)_2(Cu(PPh_3)ClO_4))(HATN\text{-}4Me)](ClO_4)_2$ was isolated where one ClO_4^- anion binds directly to the copper in place of a triphenylphosphine as discussed in Section 4.3.1.

For all HATN copper complexes with the BF_4^- anion it is worth noting that a colour change from green to red was observed on shifting between solvents $CHCl_3$ and MeCN as shown in Table 5. This colour change is discussed in Chapter 5. Upon removal of the MeCN the equilibrium swings back to the green form again.

Table 5 Colour changes of the six HATN copper complexes with BF_4^- anion. G = green, R = red.

Anion	$CHCl_3$	MeCN	THF
BF_4^-	G	R	G

4.3.1 The crystal structure of $[(Cu(PPh_3)_2)_2(Cu(PPh_3)ClO_4)(HATN\text{-}4Me)](ClO_4)_2$ ($HATN\text{-}4Me\text{-}CuClO_4$)

Triclinic HATN-4Me-Cu-ClO_4 crystallises in the space group $P\bar{1}$. The crystal had residual electron density near the HATN and so the data was squeezed giving a final R value of 16.68 %.[29,30] Although the data is too poor to draw conclusions about bond distances and angles the connectivity of the complex has been established.

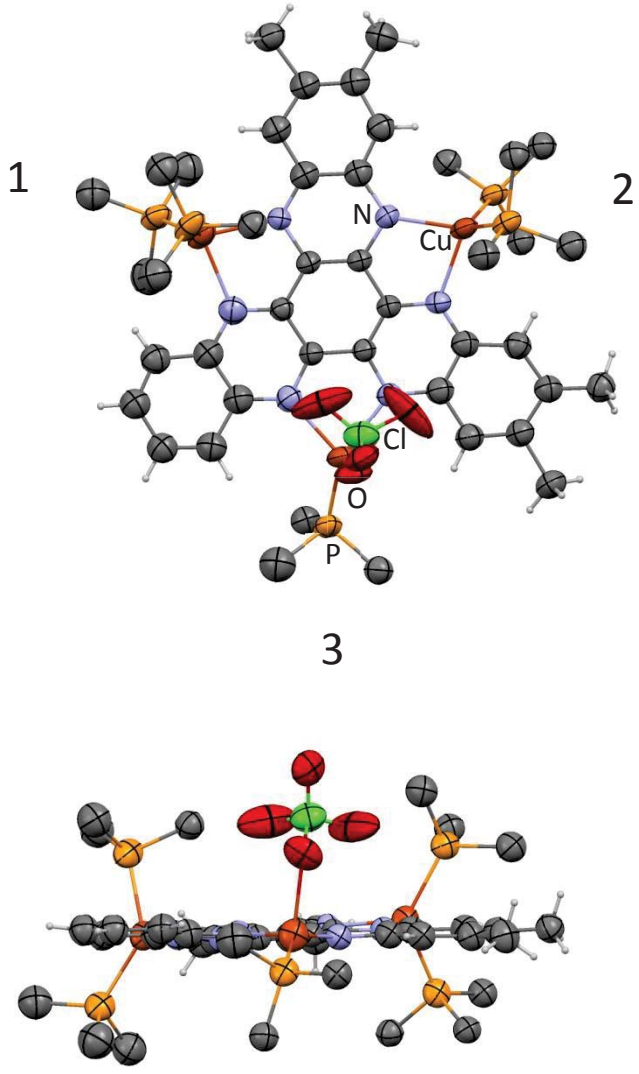

Figure 22 Top: The $HATN\text{-}4Me\text{-}CuClO_4$ crystal structure with phenyl rings, anions and solvent removed for clarity. Copper sites are labelled. Bottom: Side view of $HATN\text{-}4Me\text{-}CuClO_4$ showing the perchlorate ion bound to the copper that has one triphenylphosphine attached to it.

Two of the pseudo-tetrahedral copper sites (1) and (2) have two triphenylphosphine ligands and two HATN nitrogen atoms attached as has been observed in previous structures for the BF_4^- salts but surprisingly for the present ClO_4^- salt a most unusual feature occurs on copper site (3). Here one of the usual two triphenylphosphine has been removed and its position has been replaced with a coordinated monodentate ClO_4^-. The driving force for this is difficult to say, except that after removal of one triphenylphosphine the ClO_4^- slots on to the now ligand deficient copper site which has one triphenylphosphine ligand and the two nitrogen atoms of HATN still bound to give it a pseudo-tetrahedral structure.

This substitution suggests that the Cu—P bonds are dissociating to some extent at room temperature. Coordination of ClO_4^- would be more favourable than BF_4^- due to the higher donor ability of the anion.[34] However, a HATN copper complex has displayed weak BF_4^- association before.[19]

Table 6 HATN-4Me-$CuClO_4$

Compound	$C_{118}H_{95}ClCu_3N_6O_4P_5$, 2($ClO_4$)
Molecular formula*	$C_{118}H_{95}ClCu_3N_6O_4P_5$, 2($ClO_4$)
M (g mol^{-1})	2240.86
Temperature (K)	154
Crystal System	Triclinic
Space group	$P\bar{1}$
a(Å)	17.4062(7)
b(Å)	25.0212(9)
c(Å)	29.280(2)
α(°)	90.017(6)
β(°)	101.766(7)
γ(°)	102.228(7)
V(Å^3)	12188.5(11)
Z	4
μ(Cu Kα) mm^{-1}	2.294
ρ_{calc} (g cm^{-1})	1.221
2θmax(°)	108.48
Number of unique reflections	29286
Data/restrains/parameters	29286/3906/2657
Final R indices [I>2σ(I)]	*wR*2 = 0.3944
	R = 0.1668
R indices (all data)	*wR*2 = 0.4254
	R = 0.2051
Goodness-of-fit on F^2	1.332

*Due to significant residual electron density from disordered solvent the data has been squeezed.[29,30]

Table 6 indicates that the refinement data for each structure. CIF files are included on the accompanying disc for reference. On conducting an online CIF check, all significant alerts have been explained in the CIF file.

4.4 Palladium Complexes

Palladium chemistry was briefly investigated by studying the interaction of $[PdCl_2(benzonitrile)_2)]$ with HATN-4Me in chloroform which produced two complexes (Figure 23), however separation of HATN-4Me-1PdA from the HATN-4Me-1PdS isomer was not possible. The HATNs solubility can sometimes be improved by complexing various metals, however, in this case the resulting isomers were not soluble enough to separate by column chromatography which left few possible approaches. One of these was crystallisation of a favourable isomer in benzene but this was not successful.

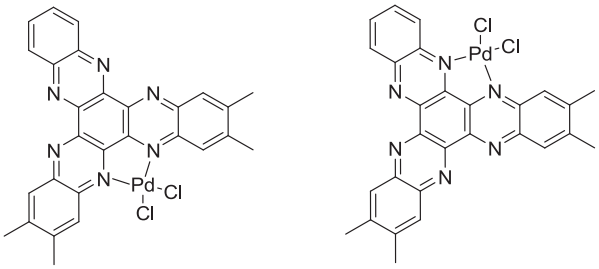

Figure 23 HATN-4Me-1PdS (left) and HATN-4Me-1PdA (right) palladium isomers obtained as a mixture but not separated.

The isomers HATN-4Me-1PdS and HATN-4Me-1PdA were found to form in a ratio of 3:1, as indicated by ^1H NMR integrals (methyl and aromatic protons, which were calibrated according to symmetry), with the symmetric isomer being preferred. Mass spectrometry was used to confirm the formation of these HATN-4Me-1Pd complexes where the $[HATN\text{-}4Me\text{-}1PdH]^+$, $[HATN\text{-}4Me\text{-}1Pd\text{-}Cl+H]^+$ and $[HATN\text{-}4Me\text{-}1Pd\text{-}2Cl+H]^+$ peaks were present. The HATN-4Me ligand does not seem to be strongly attached to the Pd for when the complex is dissolved in DMSO the ligand is easily displaced.

Further physical measurements were not carried out on these palladium compounds as the isomers could not be separated.

4.5 Conclusions

Electron deficient hetero-HATNs have low-lying non-degenerate π* orbitals that low oxidation state transition metals such as Cu(I) ($3d^{10}$), and Re(I) ($5d^6$) can donate electrons into. In this work seven mono-rhenium and four di-rhenium complexes were synthesised by addition of the $[ReBr(CO)_5]$ to each of the ligands (HATN-4Me, HATN-4Br, HATN-2Me, HATN-4Br2Me, HATN-2Br, HATN-4Me2Br) in a 1:1 ratio. Due to the ligands having hetero-substituted groups, this led to the possibility of two isomers, A and S i.e. HATN-1ReA and HATN-1ReS. It was found that for the methyl dominated HATN-1Re complexes (HATN-4Me, HATN-2Me, HATN-4Me2Br) the S isomer formation was preferred, while the bromo analogues had an equal A and S isomer formation (HATN-4Br2Me and HATN-2Br) or the A isomer was preferred (HATN-4Br). This deviates from the statistically expected 2:1 A:S formation purely by site number. The HATN-4Br compounds might be less likely to favour S formation due to these strong electron withdrawing groups affecting the basicity of the nitrogens in HATN. The seven HATN-1Re and four HATN-2Re complexes were successfully characterised using ^1H NMR, elemental analysis and mass spectrometry. Both groups contained various functional groups in a hetero-arrangement, weakly electron-donating methyl and electron withdrawing bromo as well as unsubstituted groups to give a range of results.

Crystal structures of HATN-4Me-1ReA and HATN-4Me-1ReS and HATN-2Me-2ReS were obtained and these gave important structural information about the complexes and starting points for calculations in chapter 5. These structures showed the π-π stacking ability of the HATN complexes ranging from 1 to 3 ring overlaps for the former two compounds as well as solvent interactions.

The copper complexes were prepared by the addition of $[Cu(MeCN)_2(PPh_3)_2]BF_4$ to the HATN ligands in a 3:1 ratio in diethylether. The HATN ligands used were HATN-4Me, HATN-4Br, HATN-2Me, HATN-4Br2Me, HATN-2Br and HATN-4Me2Br. Six copper compounds of general stoichiometry HATN-3$[Cu(PPh_3)_2BF_4]$ were synthesised and

characterised successfully. HATN-4Me was also successfully complexed with $[Cu(MeCN)_2(PPh_3)_2]ClO_4$ and crystallography showed that the perchlorate anion dislodged a triphenylphosphine entity to form $[(Cu(PPh_3)_2)_2Cu(PPh_3)ClO_4$(HATN-4Me)]$2ClO_4$.

Finally, palladium chemistry was briefly investigated by studying the complexation of $[PdCl_2(benzonitrile)_2]$ with HATN-4Me (Figure 23). Similar to the rhenium complexes the HATN-4Me-1PdS isomer was formed in a higher ratio than the HATN-4Me-1PdA isomer, even though statistically the opposite is expected. From this observation it is reasonable to expect that hetero-HATNs seem to favour S isomer formation and this could extend to other metals. Separation of the HATN-4Me-1PdA and HATN-4Me-1PdS isomers was however not possible. The displacement of HATN-4Me from these complexes with DMSO attests to the weaker nature of the complex formation with HATN versus 1,10-phenanthroline.

4.6 References

1 Moucheron, C.; Kirsch-De Mesmaeker, A.; Choua, S. *Inorganic Chemistry* **1997**, *36*, 584.

2 Ishi-I, T.; Yaguma, K.; Kuwahara, R.; Taguri, Y.; Mataka, S. *Organic Letters* **2006**, *8*, 585.

3 Sahai, R.; Rillema, D. P.; Shaver, R.; Van Wallendael, S.; Jackman, D. C.; Boldaji, M. *Inorganic Chemistry* **1989**, *28*, 1022.

4 Nasielski-Hinkens, R.; Benedek-Vamos, M.; Maetens, D.; Nasielski, J. *Journal of Organometallic Chemistry* **1981**, *217*, 179.

5 Ortmans, I.; Didier, P.; Kirsch-De Mesmaeker, A. *Inorganic Chemistry* **1995**, *34*, 3695.

6 Rutherford, T. J.; Van Gijte, O.; Kirsch-De Mesmaeker, A.; Keene, F. R. *Inorganic Chemistry* **1997**, *36*, 4465.

7 Grove, H.; Sletten, J.; Julve, M.; Lloret, F.; Lezama, L.; Carranza, J.; Parsons, S.; Rillema, P. *Journal of Molecular Structure* **2002**, *606*, 253.

8 Ghumaan, S.; Sarkar, B.; Patil, M. P.; Fiedler, J.; Sunoj, R. B.; Kaim, W.; Lahiri, G. K. *Polyhedron* **2007**, *26*, 3409.

9 Krahmer, J.; Beckhaus, R.; Saak, W.; Haase, D. *Zeitschrift für anorganische und allgemeine Chemie* **2008**, *634*, 1696.

10 Lind, S. J.; Walsh, T. J.; Blackman, A. G.; Polson, M. I. J.; Irwin, G. I. S.; Gordon, K. C. *The Journal of Physical Chemistry A* **2009**, *113*, 3566.

11 Fraser, M. G.; Clark, C. A.; Horvath, R.; Lind, S. J.; Blackman, A. G.; Sun, X.-Z.; George, M. W.; Gordon, K. C. *Inorganic Chemistry* **2011**, *50*, 6093.

12 Bu, X.-H.; Tanaka, K.; Shionoya, M.; Biradha, K.; Yamaguchi, T.; Nishimura, M.; Ito, T. *Chemical Communications* **2000**, 1953.

13 Catalano, V. J.; Larson, W. E.; Olmstead, M. M.; Gray, H. B. *Inorganic Chemistry* **1994**, *33*, 4502.

14 Budd, P. M.; Ghanem, B.; Msayib, K.; McKeown, N. B.; Tattershall, C. *Journal of Materials Chemistry* **2003**, *13*, 2721.

15 Shatruk, M.; Chouai, A.; Prosvirin, A. V.; Dunbar, K. R. *Dalton Transactions* **2005**, 1897.

16 Xina, S.; Xiaoming, L.; Junhe, F.; Shuo, W.; Peizhou, L. *Journal of Coordination Chemistry* **2008**, *61*, 1568.

17 Shatruk, M.; Chouai, A.; Dunbar, K. R. *Dalton Transactions* **2006**, 2184.

18 Marquis-Rigault, A.; Dupont-Gervais, A.; Baxter, P. N. W.; Van Dorsselaer, A.; Lehn, J.-M. *Inorganic Chemistry* **1996**, *35*, 2307.

19 Roy, S.; Sarkar, B.; Duboc, C.; Fiedler, J.; Sarper, O.; Lissner, F.; Mobin, S. M.; Lahiri, G. K.; Kaim, W. *Chemistry – A European Journal* **2009**, *15*, 6932.

20 Furukawa, S.; Okubo, T.; Masaoka, S.; Tanaka, D.; Chang, H.-C.; Kitagawa, S. *Angewandte Chemie International Edition* **2005**, *44*, 2700.

21 Roy, S.; Kubiak, C. P. *Dalton Transactions* **2010**, *39*, 10937.

22 Marder, S.; Kaafarani, B.; Barlow, S.; Kippelen, B.; Domercq, B.; Zhang, Q.; Kondo, T., **2005,** 2005-US20998 2005123737.

23 Uehara, M., **2006,** 2006-JP300407 WO2006075723.

24 Uehara, M., **2006,** 2006-JP312452 WO2006137462.

25 Rigaku; Woodlands, R. A. C. T., Ed. 2007; Vol. Version 1.4.0 ed.

26 Rigaku; Rigaku Corporation: Matsubara: 1998.

27 Sheldrick, G. *Acta Crystallographica Section A* **2008**, *64*, 112.

28 Colip, L. A.; Koppisch, A. T.; Broene, R. D.; Berger, J. A.; Baldwin, S. M.; Harris, M. N.; Peterson, L. J.; Warner, B. P.; Birnbaum, E. R. *Journal of Applied Crystallography* **2009**, *42*, 329.

29 van der Sluis, P.; Spek, A. L. *Acta Crystallographica Section A* **1990**, *46*, 194.

30 Spek, A. *Journal of Applied Crystallography* **2003**, *36*, 7.

31 Connick, W. B.; Di Bilio, A. J.; Hill, M. G.; Winkler, J. R.; Gray, H. B. *Inorganica Chimica Acta* **1995**, *240*, 169.

32 Bardwell, D. A.; Barigelletti, F.; Cleary, R. L.; Flamigni, L.; Guardigli, M.; Jeffery, J. C.; Ward, M. D. *Inorganic Chemistry* **1995**, *34*, 2438.

33 Moya, S. A.; Guerrero, J.; Pastene, R.; Sartori, R.; Schmidt, R.; Sariego, R.; Sanz-Aparicio, J.; Fonseca, I.; Martinez-Ripoll, M. *Inorganic Chemistry* **1994**, *33*, 2341.

34 Davies, J. *Synthetic Coordination Chemistry*; World Scientific: London, 1996.

Chapter 5

Physical properties of hetero-substituted HATN complexes

5.0 Abbreviations

LC	Ligand centred
MLCT	Metal-to-ligand charge transfer
BF_4^-	Tetrafluoroborate anion
ClO_4^-	Perchlorate anion
IR	Infrared
DFT	Density functional theory
TD-DFT	Time-Domain density functional theory
FT	Fourier transform
rR	Resonance Raman
MAD	Mean average deviation
HOMO	Highest occupied molecular orbital
LUMO	Lowest unoccupied molecular orbital
Phen	1,10-phenanthroline

5.1 Introduction

Transition metal complexes containing polypyridyl ligands have received much attention because of their rich and diverse electronic, photophysical and photo-chemical properties. Multinuclear systems of this type are very important for applications in supramolecular chemistry, DNA binding studies, light harvesting and molecular devices.[1]

Previously the tri-ruthenium(II) complexes [(μ_3-HATN){Ru(acac)$_2$}$_3$], [(μ_3-HATN-6Me)[Ru(acac)$_2$]$_3$ and (μ_3-HATN-6Cl)[Ru(acac)$_2$]$_3$ (acac = anion of acetylacetone) (Figure 1) were synthesised and their electrochemical properties investigated.[2,3] The two former complexes underwent three well-separated one-electron oxidations and three stepwise one-electron reductions, while the latter underwent analogous reactions but with four electrons. They indicated electron removal from the ruthenium(II) centres on oxidation and the occupation of a largely HATN-based molecular orbital on reduction. However, no obvious intervalence charge transfer bands were detected in the visible, near-infrared and infrared regions in the spectroelectrochemistry, suggesting very weak electronic coupling between the metal centres in the mixed-valent intermediates.[2,3]

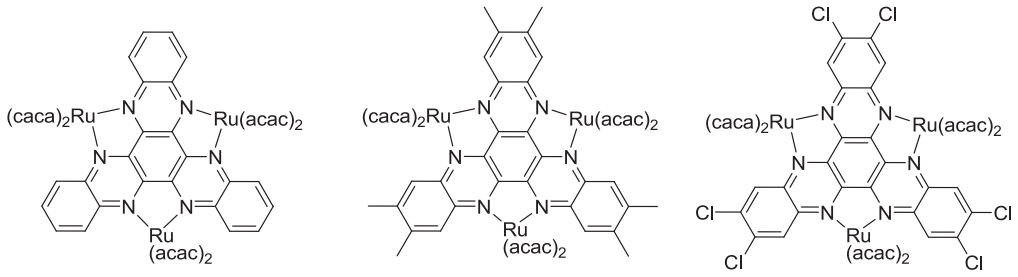

Figure 1 Previous examples of ruthenium HATN derivatives. Left: [(μ_3-HATN){Ru(acac)$_2$}$_3$]. Middle: [(μ_3-HATN-6Me)[Ru(acac)$_2$]$_3$. Right: (μ_3-HATN-6Cl)[Ru(acac)$_2$]$_3$.[2,3]

5.1.1 Rhenium HATN complexes

Over the last two decades many studies have been carried out on polypyridyl-carbonyl complexes of d^6 transitional metals (Re(I)) because of their comparable photo-physical and chemical properties with Ru(II)-diimines.[4] They often show similar photo-and electrocatalytic behaviour towards various oxidation and reduction processes.[5] Re(I)-polypyridyl-carbonyl complexes in particular have been widely studied for applications in photochemical storage devices, multi-electron redox agents and intra-molecular electron and energy transfer processes.[1,3,6,7]

The known mono-nuclear and di-nuclear complexes $[(HATN)Re(CO)_3Cl]$ and $[(\mu_2\text{-}HATN\text{-}6Me)[Re(CO)_3Cl]_2]$ (Figure 12) of highly symmetric ligands HATN and HATN-6Me have been characterised and infrared spectroelectrochemistry experiments confirmed ligand-based reductions.[1] To gain insight into the reduction mechanism the triflate salts, $[(HATN)Re(CO)_3](OTf)$ and $[(HATN\text{-}6Me)(Re(CO)_3)_2](OTf)_2$, were synthesized. Their electrochemical and spectroelectrochemical behaviour also exhibits reduction of the aromatic systems.[1]

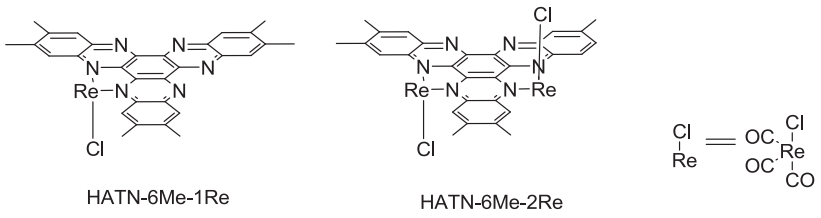

Figure 2 Left: The mono-nuclear HATN complex, $[(HATN)Re(CO)_3Cl]$. Right: The di-nuclear HATN complex $[(\mu_2\text{-}HATN\text{-}6Me)[Re(CO)_3Cl]_2]$

This work has been extended to the *syn*- and *anti*-isomers of the bi- and tri-nuclear $Re(CO)_3Cl$ complexes of HATN-6Me (Figure 3a).[8] The complexes showed intense absorptions in the visible region, comprising strong $\pi \rightarrow \pi^*$ and MLCT transitions, which were modelled using time-dependent density functional theory (TD-DFT). For the bi-nuclear complexes the absorption wavelengths were almost identical for the two

isomers at 600 nm and for the relative tri-nuclear complexes the wavelengths were slightly red-shifted and the absorption intensity increased (~10 fold) in the MLCT region relative to the bi-nuclear complexes, but with both three-rhenium-isomers having almost identical wavelengths. The energy of the MLCT absorption decreases from mono- to bi- to tri-nuclear complexes.[8]

The binuclear isomers showed identical electrochemical behaviour for their first reduction potentials (-0.05 V) but a difference of 0.05 V (vs. SCE) for the second reduction potentials (-0.58 V and -0.63 V for *anti* and *syn* respectively). The first and second reduction potentials for the isomers of the tri-nuclear complexes were virtually identical (0.21 V for first and -0.16 V for second reduction potential).[1,8] This was consistent with the lowering in energy of HATN based LUMOs as suggested by DFT calculations and observed in the UV-Vis absorption spectra, where subsequent binding of {$Re(CO)_3Cl$} moieties resulted in longer wavelength of the MLCT absorption. The first reduction potentials of the complexes became more positive upon binding of subsequent $Re(CO)_3Cl$ fragments, consistent with changes in the energy of the MLCT bands and lowering of the energy of relevant lowest unoccupied molecular orbitals, and this was supported by TD-DFT calculations. The nature of the excited states of all of the complexes was also studied using both resonance Raman and picosecond time-resolved IR spectroscopy, where it was shown that the MLCT excitation resulted in the oxidation of one rhenium centre. The patterns of the shifts in the carbonyl bands upon excitation revealed that the MLCT state is localized on one rhenium centre on the IR time scale.[8]

a)

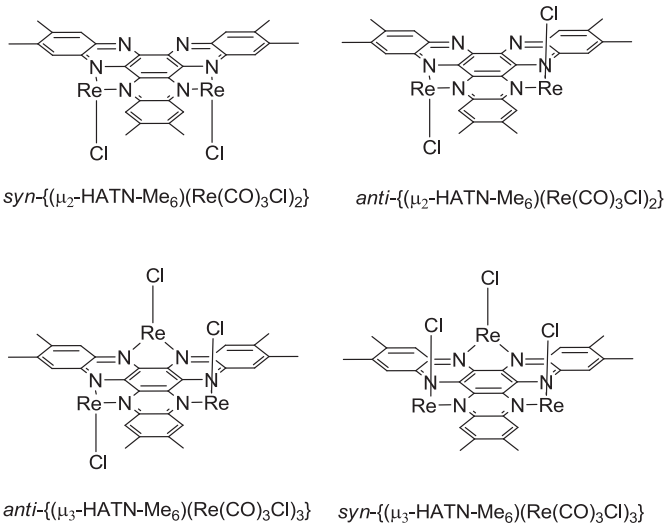

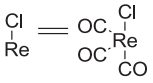

b)

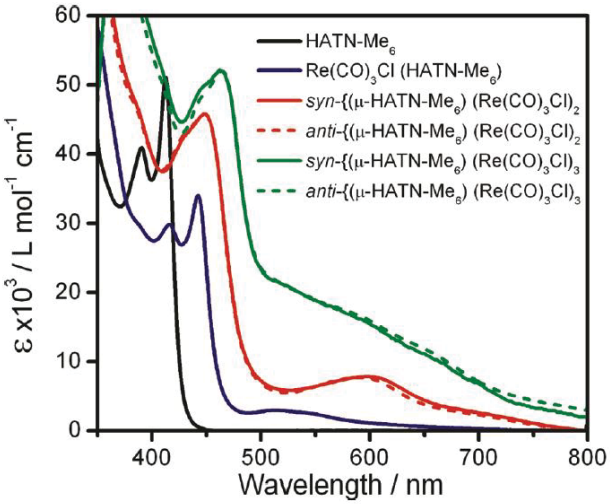

Figure 3 a) Di-nuclear and tri-nuclear HATN rhenium complexes and their isolated isomers. b) UV-Vis absorption spectra for a series of HATN-6Me and its rhenium complexes.

Electrochemistry found that the first reduction potential for HATN-6Me was stabilised by almost 600 mV upon chelation of a single $\{Re(CO)_3Cl\}$ moiety (-1.09 V to -0.42 V). The binding of a second and third metal centre had a diminishing effect, with the first reduction potentials stabilised by 430 mV (-0.05 V) and 260 mV (0.21 V), respectively.[8]

Subsequently this study was broadened to the hetero-nuclear HATN-6Me complexes. The electronic absorption spectra of chloroform solutions of HATN-6Me and the various rhenium and palladium complexes (HATN-6Me-1Pd, HATN-6Me-1Re, HATN-6Me-1Re1Pd and HATN-6Me-2Pd) are shown in Figure 4. The HATN-6Me spectrum

was dominated by intense π→π* absorptions between 300 and 420 nm; these features broadened and red shifted upon coordination with rhenium and palladium. The single rhenium addition to HATN-6Me was not quite as pronounced as it was in the palladium addition, and the spectrum resembled that of the free ligand more closely. Spectral features became poorly resolved upon coordination of a second metal centre.[9]

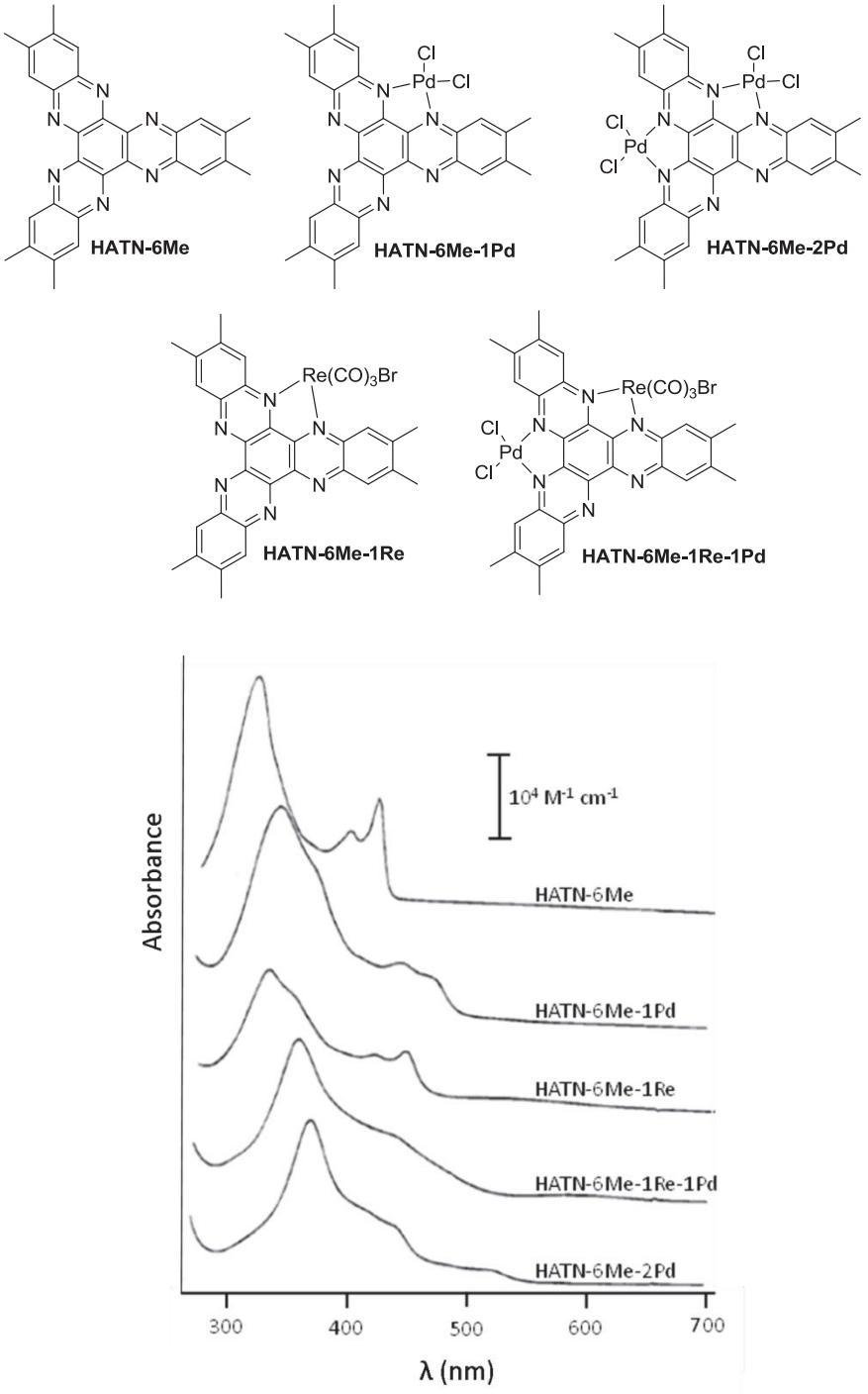

Figure 4 HATN rhenium and palladium complexes and their corresponding UV-Vis absorption spectra.[9]

The HATN-6Me electrochemistry work was expanded[9] and shown to have a reversible first reduction potential at -1.09 V, a quasi-reversible reduction at -1.40 V (second reduction potential), and an irreversible first oxidation potential at 1.52 V vs. Ag/AgCl at room temperature. In HATN-6Me-1Re, the two ligand reductions shifted to less negative values (-0.48 and -0.75 V), and four new irreversible reduction waves were observed out to the solvent limit. An irreversible oxidation was observed toward the positive solvent limit. All the palladium-containing compounds decomposed upon oxidation or reduction as evidenced by their irreversible electrochemistry.[9]

5.1.2 Copper(I) HATN complexes

Oligionuclear metal complexes with multiple redox processes were studied because of their possible use in supramolecular electronics and because of their relation to enzymatic systems. Intra-molecular interaction between two redox-active metal and/or ligand centres is a fundamental requirement for many kinds of potential molecular electronic devices.[10] Copper is attractive for use with HATNs as it provides easy coordination to all three sites.

Previously it was shown that the compound $[(Cu(PPh_3)_2)_3(\mu_3\text{-HATN-6Me})](BF_4)_3$ (Figure 5) had a HATN-6Me core that was slightly twisted with a mean plane angle between the central and outer rings of 6.93°. The electronic absorption spectrum of the complex in chloroform displayed two bands in the visible region attributed to ligand-centred (LC) and metal-to-ligand charge-transfer (MLCT) transition.[11]

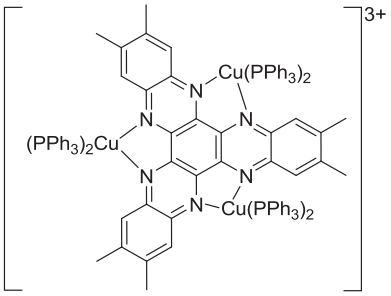

Figure 5 $[(Cu(PPh_3)_2)_3(\mu_3\text{-HATN-6Me})]^{3+}$

Tris(diphenylphosphino-ferrocene) (dppf) compounds $[\{Cu(dppf)\}_3(\mu_3\text{-HATN})][X]_3$, $[\{Cu(dppf)\}_3(\mu_3\text{-HATN-6Me})][X]_3$ and $[\{Cu(dppf)\}_3(\mu_3\text{-HATN-6Cl})][X]_3$ where dppf = 1,1'- (diphenylphosphino-ferrocene), X = BF_4^- or PF_6^-) undergo at least two different, reversible one-electron reductions and three very closely spaced one-electron oxidations (Figure 6 shows the HATN-6Me derivative), with the latter not being attributed to the stepwise ferrocene/ferrocenium conversions. A crystal structure of the compound with un-substituted HATN showed notable deviation from the trigonal symmetry and the close association of two tetrafluoroborate anions with the complex tri-cation along the quasi-trigonal axis to yield $[(\mu_3\text{-HATN})\{Cu(dppf)\}_3(\eta^3\text{-}BF_4)_2]BF_4$.[10]

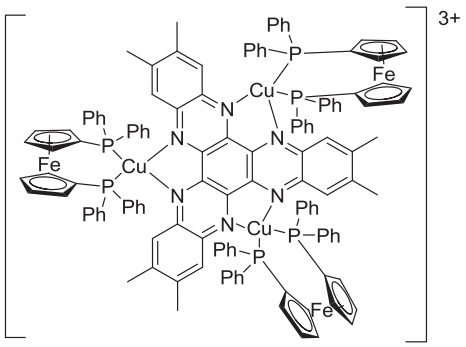

Figure 6 The structure of [{Cu(dppf)}$_3$(μ$_3$-HATN-6Me)]$^{3+}$

The result that both the BF_4^- and the PF_6^- salts of the tri-cation [(Cu(dppf)$_3$)$_3$(μ$_3$-HATN-6Me)]$^{3+}$ displayed virtually identical cyclic voltammetry as well as spectroelectrochemical response in CH_2Cl_2 suggested that the association found for the solid was not retained to the same extent in solution (the absorbance spectra are shown in Figure 7). To study possible anion binding in solution ^{19}F NMR and ^{31}P NMR measurements were carried out at room temperature and low temperature (223 K) on both sets of compounds with both anions. In the ^{31}P NMR spectra, signals from the dppf ligands were observed for all complexes in addition to one septet at about -145 ppm, which was attributed to the PF_6^- counter-ions. In the ^{19}F NMR spectra the complexes showed a doublet around -73 ppm for PF_6^- ions and a singlet around -152 ppm for BF_4^- anions. The NMR results thus confirmed weak binding (fast exchange) or dissociation of the counter-ions, BF_4^- or PF_6^-, on the NMR timescale in solution.[10]

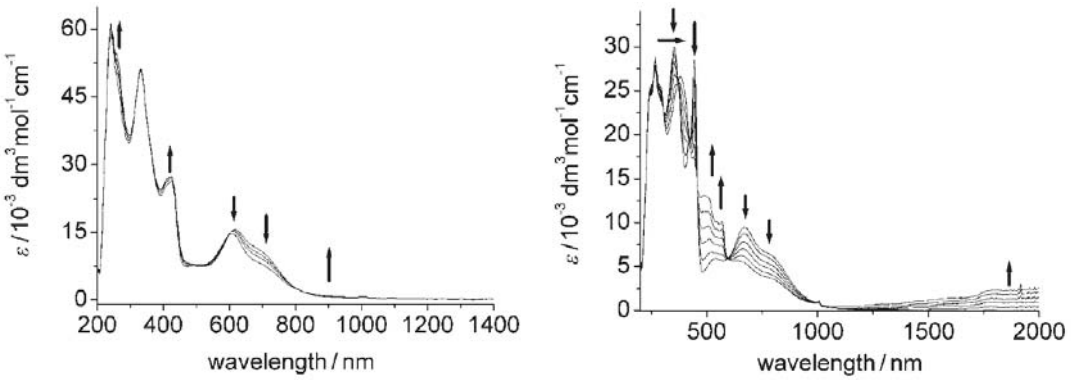

Figure 7 The absorption spectra of [{Cu(dppf)}$_3$(μ$_3$-HATN-6Me)]$^{3+}$ in its oxidised (left hand spectrum) and reduced forms (right hand spectrum) obtained from spectroelectrochemistry.

5.2 Chromism

Chromism is a process that induces a change, often reversible, in the colours of compounds. In most cases, chromism is based on a change in the energy levels of molecules, especially the π- or d-energy levels, so this phenomenon is induced by various external stimuli which can alter the electron density of substances.

Chromism is classified by what kinds of stimuli are used, these are:

- thermochromism: chromism that is induced by heat, that is, a change of temperature. This is the most common chromism of all.
- photochromism: induced by light irradiation. This phenomenon is based on the isomerization between two different molecular structures, light-induced formation of colour centres in crystals, precipitation of metal particles in a glass, or other mechanisms.
- electrochromism: induced by the gain and loss of electrons. This phenomenon occurs in compounds with redox active sites such as metal ions or organic radicals.
- solvatochromism depends on the polarity of the solvent. Most solvatochromic compounds are metal complexes.
- cathodochromism is induced by electron beam irradiation.

Solvatochromism describes the ability of a substance to change colour due to a shift in the polarity of the solvent. This can be observed as either a negative transition or positive transition depending on the relative change of polarity in either direction. This change can then be quantified by measuring the transition dipole moment. Positive and negative solvatochromism depend on the difference between the dipole moment of the ground and excited states of the substance. This phenomenon is explained by the solvatochromic effect, which relates the absorption and emission spectra with the polarity of the solvent.

5.2.1 Solvatochromic effect

The solvatochromic effect refers to the correlation of absorption and emission spectra with the polarity of the solvent. This is caused by the presence of differing polarities of the ground and excited state of a chromophore. Therefore, a change in the solvent polarity will lead to a change in stabilization energy for each of the ground and excited states. This will in turn change the energy gap between these two states. This can be greatly influenced by various polar interactions including: hydrogen bonding, dipole-dipole, cation-dipole, etc.[12]

The nuclear coordinates of the atoms constituting the molecule do not have time to change during the very brief amount of time involved in an electronic transition and this is true for the solvent surrounding the molecule as well. The molecules are dissolved and subsequently surrounded by the solvent, which forms a stabilizing interaction known as solvation. This is particularly true in the case of polar chromophores that are dissolved in polar solvents, as the energy of the interactions is significantly higher. The solvation sphere will constantly change and evolve until it has minimized the total energy of the system (but still remains in a dynamic equilibrium). These interactions include the same ones mentioned previously, including: hydrogen bonding, dipole-dipole, van der Waals, etc. This is significant to solvatochromism when the solvation interactions are different between the ground state and the excited state. The change in dipole moment after the energy transition can change the energetic drive of solvation.[13]

The photophysical properties of the trinuclear copper(I) complex $\{[Cu3,5\text{-}(CF_3)_2Pz]\}_3$ (Pz = pyrazole) (Figure 8), which exhibits multicolour bright phosphorescent emissions that are sensitive to temperature, solvent, and concentration is used as an example to illustrate. The structure shows weak intramolecular (3.221−3.242 Å) and essentially no intermolecular Cu···Cu interactions (3.879; 3.893 Å). [14]

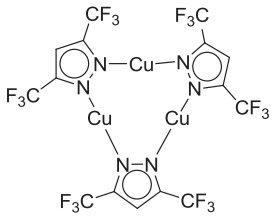

Figure 8 The {Cu[3,5-$(CF_3)_2$Pz] }$_3$ complex that exhibits solvato, thermo and concentration chromism.

The changes in the luminescence energies in different solvents are related to both the extent of excited-state association of {[Cu3,5-$(CF_3)_2$Pz]}$_3$ and the different electronic structures of various {[Cu3,5-$(CF_3)_2$Pz]$_3$·solvent} complexes. What is unusual about the results here is not only the selectivity even for similar solvents (e.g., toluene vs. benzene) and the versatility of solvents in which {[3,5-$(CF_3)_2$Pz]Cu}$_3$ shows luminescence solvatochromism, but also the qualitative changes in the visible emission colours and spectra when the concentration is varied in the same solvent. The most striking changes were seen in dichloromethane, in which the luminescence was tuned to essentially all visible colours between blue and red by varying the concentration (Figure 9).[14]

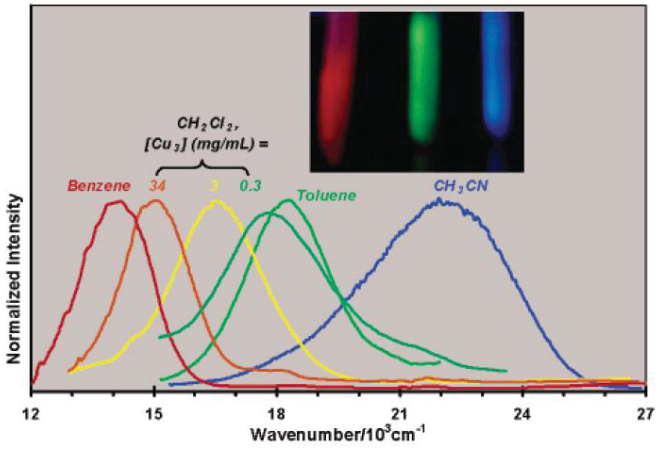

Figure 9 {[3,5-$(CF_3)_2$Pz]Cu}$_3$ luminesence chromism.

5.3 Raman spectroscopy

Raman spectroscopy utilises a single frequency of radiation to irradiate the sample. When light is scattered by matter the photons are scattered in two ways: elastic or inelastic. In elastic scattering, the energy therefore of the wavelength of incident photon is conserved and only direction has changed. This is also known as Rayleigh scattering and accounts for most of the light scattered from molecules. Inelastic scattering occurs when there is a change in energy between the incident photon and the emitted photon. This phenomenon accounts for approximately one in 10^6-10^8 photons. This is known as a Stokes shift and forms the basis for Raman scattering or the Raman Effect (Figure 10). Raman spectroscopy measures the energy difference between the ground and excited vibrational states. [15,16]

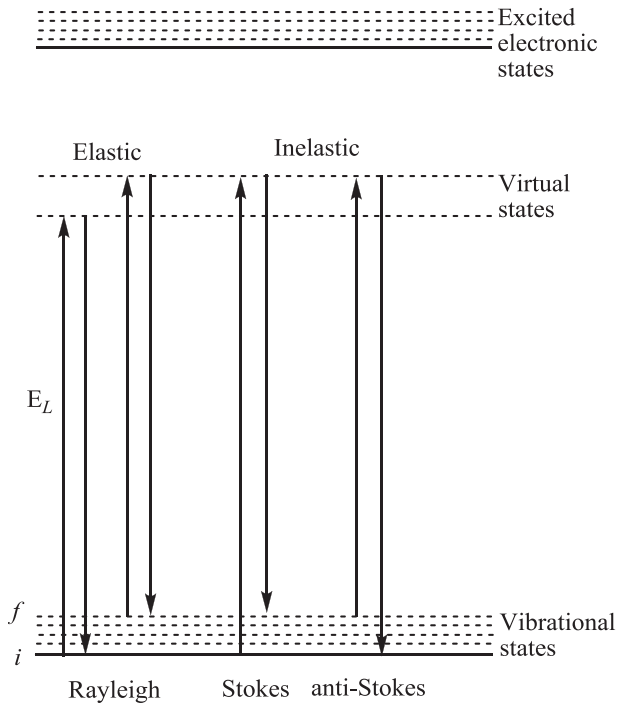

Figure 10 Spectroscopic transitions underlying Raman and Resonance Raman spectroscopy. *i* and *f* represent the ground and excited vibrational states, respectively. The virtual states are not real states of the molecule and are determined by the frequency of the light source used for excitation.

Placzek developed the theory of Rayleigh and Raman spectroscopy by considering ground state polarizability.[17] The classical description of Raman scattering is as follows; an electric dipole is induced, P, when an oscillating incident electric field, E Vm^{-1}, interacts with an electron cloud of a chemical bond. This is given by:

$$P = \alpha E$$ **Equation 1**

where α is the polarizability of the molecule. The incident electric field term is given by:

$$E = E_o \cos 2\pi \nu_o t$$ **Equation 2**

where υ_o is the frequency of the laser and t is time. The molecular vibrations are comprised of normal modes, Q_j, where there are 3N-6 vibrations in a non-linear molecule with N atoms.

$$Q_j = Q_j^{\circ} \cos 2\pi \nu_j t$$ **Equation 3**

υ_j is the characteristic harmonic frequency of the jth normal mode. For a vibrating molecule, the polarizability term is given by the following Taylor series expansion:

$$\alpha = \alpha_0 + \frac{1}{2}\left(\frac{\partial \alpha}{\partial Q_j}\right)_{Q_j=0} Q_j + \ldots$$ **Equation 4**

Substitution of equations Equation 2 to Equation 4 into Equation 1 gives:

$$P = \alpha_0 E_0 \cos 2\pi \nu_0 t + \frac{1}{2}\left(\frac{\partial \alpha}{\partial Q_j}\right)_{Q_j=0} E_0 \, Q_j^0 \left[\cos\left\{2\pi\left(\nu_0 + \nu_j\right)t\right\} + \cos\left\{2\pi\left(\nu_0 - \nu_j\right)t\right\}\right]$$

Equation 5

The first term is the Rayleigh scattering, which has the same frequency as the laser frequency. The second term is the anti-Stokes Raman scattering and occurs at a frequency of $\nu_o + \nu_j$. The third term is Stokes Raman scattering and occurs at a frequency of $\nu_o - \nu_j$.[18]

Raman intensity, I_R, varies with frequency:

$$I_R = \mu(\nu_o \pm \nu_j)^4 \alpha_j^2 Q_j^2$$ **Equation 6**

where μ is a constant. Equation 6 illustrates that the Raman intensity varies with the observed frequency (ν_s where $\nu_s = \nu_o \pm \nu_j$) to the fourth power for normal Raman

scattering, which in turn depends on the laser frequency (ν_o). The ν^4 dependence is derived from the classical treatment of scattering from an oscillating induced dipole.

Equation 6 leads to the major distinction between Raman spectroscopy and infrared spectroscopy. Raman scattering requires a change in the polarizability for an allowed transition.[15] That is, $\frac{\partial \alpha}{\partial Q_j}$ in Equation 5, must be non-zero to observe Raman bands.[19]

Symmetric vibrations usually give the greatest scattering. In comparison, for infrared absorption the most intense peaks are caused by a change in dipole, which results from non-totally symmetric vibrations. Not all vibrations from a molecule are both infrared and Raman active. Therefore the two techniques are complementary methods of investigating the vibrations of a molecule.[15]

5.3.1 Resonance Raman spectroscopy

There are two serious shortcomings of Raman spectroscopy.

1) Raman signals are very weak (1 photon in 10^6-10^8). This puts limits on the detection for low concentrations.

2) Weak fluorescence signals can mask Raman signals.

To overcome the inherent weakness of the Raman effect, there are two possible approaches based on Equation 1:

$$P = \alpha E \qquad \textbf{Equation 1}$$

1) Modify/increase the polarizability (α) of the molecule. This approach is the basis of the resonance Raman spectroscopy.

2) Modify/increase the strength of the electric field (*E (eV)*) that the molecule experiences. This approach is the basis of surface-enhanced Raman spectroscopy. (This was not investigated)

The sensitivity of Raman spectroscopy is greater when the frequency of the excitation is close to that of an electronic transition of the molecule of interest. Resonance Raman occurs when the excitation frequency coincides with an electronic transition of the molecule of interest (Figure 11).[20] Pre-resonance Raman occurs when the excitation frequency is close to the electronic transitions of the molecule of interest. The closer the excitation frequency is to the electronic transition the greater the intensity of the Raman bands. The vibrational modes associated with the electronic transition are selectively enhanced in resonance Raman and give rise to Raman bands with a greater intensity. Resonance Raman scattering leads to up to 10^6 times stronger Raman scattering. The resulting spectrum may also be different. For example, overtones and combinations may be enhanced and bands may be selectively enhanced.[16]

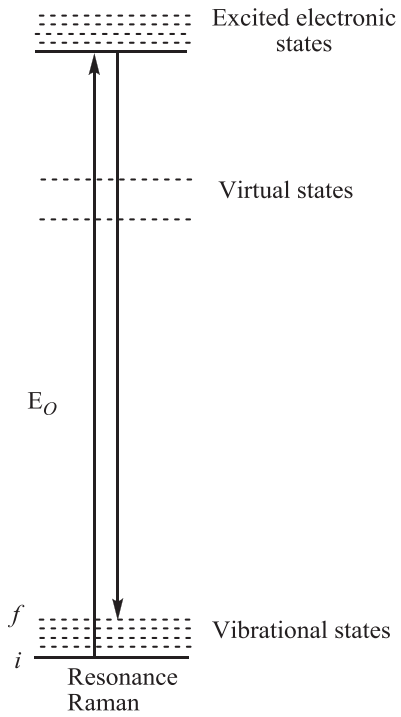

Figure 11 Resonance Raman transition

Raman spectroscopy is commonly used in chemistry, since vibrational information is specific to the chemical bonds and symmetry of molecules. Therefore, it provides a

fingerprint by which the molecule can be identified. The fingerprint region of organic molecules is in the (wavenumber) range 500–1500 cm^{-1}.[21]

Not all fundamental vibrational transitions can be studied by both IR and Raman spectroscopy because they have different selection rules. Selection rules tell us if a transition is allowed or forbidden. An allowed transition has a high probability of occurring and will result in a strong band. Conversely a forbidden transition's probability is so low that the transition will not be observed. If a normal mode has an allowed IR transition, it is IR active. Similarly if a normal mode has an allowed Raman transition, it is Raman active.[22]

If the point group and symmetry labels for the normal modes are known then group theory makes it easy to predict which normal modes will be IR and/or Raman active. The character table for the point group of the molecule can be inspected and if the symmetry label of a normal mode corresponds to x, y, or z, then the fundamental transition for this normal mode will be IR active. If the symmetry label of a normal mode corresponds to products of x, y, or z (such as x^2 or yz) then the fundamental transition for this normal mode will be Raman active.[22]

5.4 Current Research

This Chapter focuses on the photophysical, vibrational and electrochemical properties of the hetero-substituted HATN rhenium(I) (see Section 5.3.1) and copper(I) (see Section 5.5) complexes synthesised in Chapter 4 (Figure 12). These measurements were used to determine how varying hetero-substituents of HATN alters the physical behaviour of the complexes. This provides valuable insight for further development of these systems.

5.4.1 Rhenium

The photophysical, vibrational and electrochemical properties of eleven rhenium HATN complexes synthesised in Chapter 4 (Figure 12) were investigated. Some of these compounds existed as coordination isomers e.g. HATN-2Br-1ReA and HATN-2Br-1ReS, whereas for others just one of the two S or A mono-rhenium isomers was isolated and finally four di-Re complexes. For the ligand HATN-4Br only the HATN-4Br-1ReS isomer was able to be isolated in pure form.

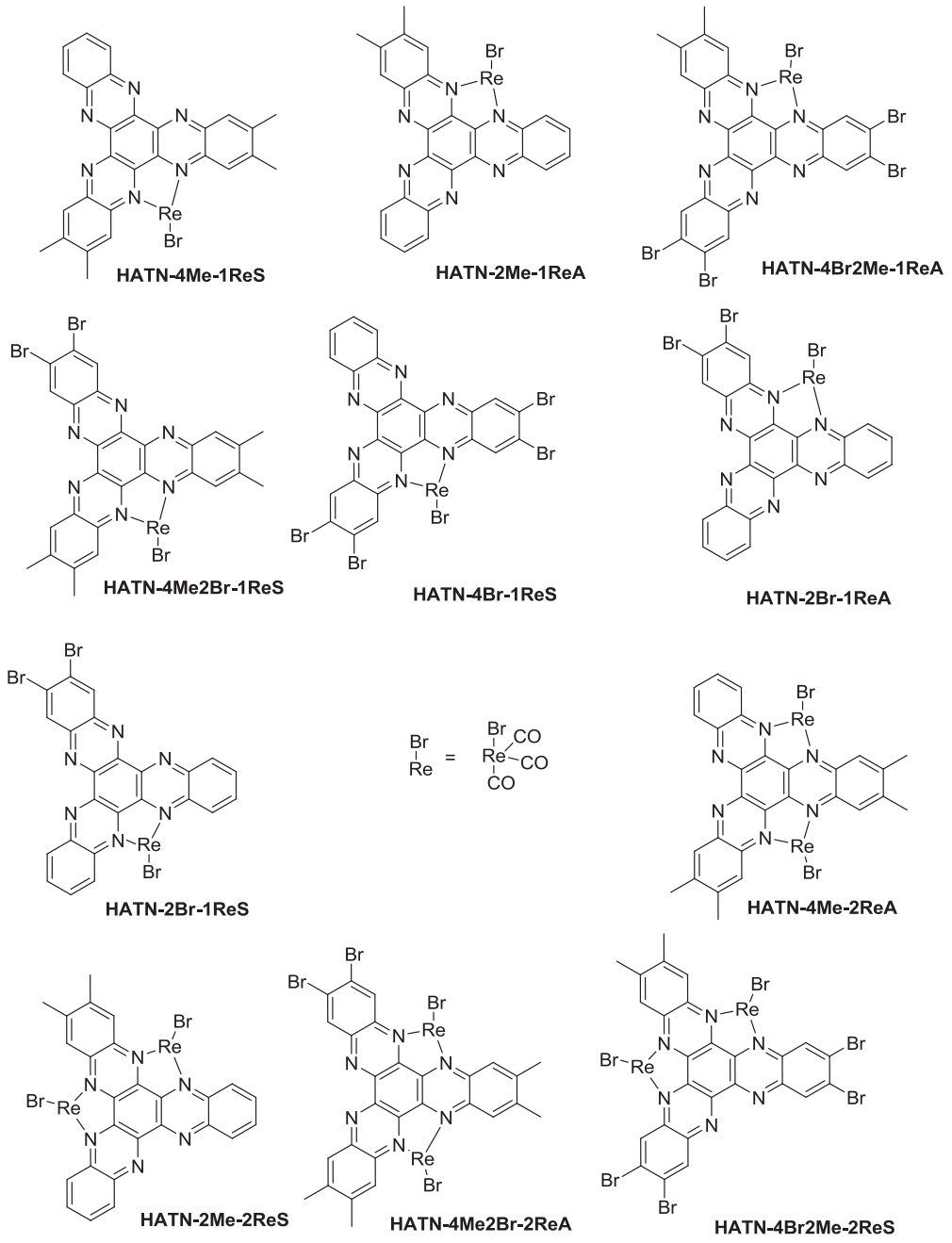

Figure 12 Hetero-HATNs synthesised in Chapter 4.

Electronic absorbance and resonance Raman (rR) spectra were recorded in chloroform and electrochemical data in dichloromethane solutions. FT-IR data was collected at Massey University. FT-Raman data and resonance-Raman were collected by Holly van der Salm of Keith Gordon's group at Otago University. Instrumental details and specific conditions are given in Appendix D.

Computational models of the HATN complexes were employed to aid the assignment of the electronic absorbance and vibrational spectra, using a DFT/B3LYP calculation with LANL2DZ basis set for the rhenium atoms and 6-31G (d) for all the other atoms. The time-dependent calculations were carried out in a chloroform solvent field using the PCM method. All calculations were performed using the Gaussian09/GaussView5 packages.[23,24]

As a means of determining the accuracy of these models, the calculated bond lengths were compared to those obtained from crystallographic data (see Appendix D). This gave a mean absolute deviation (MAD) of 0.077 Å for HATN-4Me-1ReA and 0.029 Å for HATN-4Me-1ReS. In addition to structural accuracy, the electronic accuracy of the models was measured by comparison of the calculated vibrational frequencies to the IR and FT-Raman (example Figure 13, HATN-2Me-1ReA); the output frequencies were scaled by 0.96. Carbonyl stretches required different scaling factors so these were ignored and all assigned ligand based vibrational modes were used to calculate the mean absolute deviation values. This gave a range of MAD values of 9 cm^{-1} for HATN-2Me-1ReA and 14 cm^{-1} for HATN-2Br-1ReS for IR spectra and 12 cm^{-1} for HATN-4Br-1ReS and 18 cm^{-1} for HATN-4Br-1ReS for FT-Raman (See Appendix D).

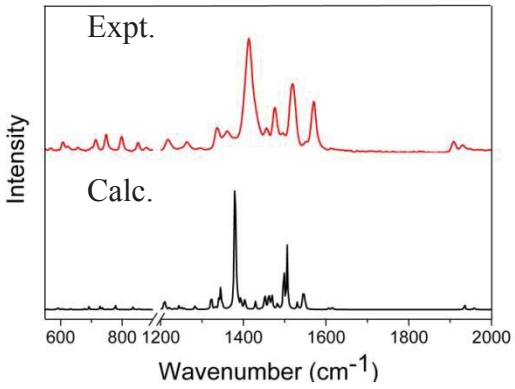

Figure 13 Comparison between calculated (black) and experimental (red) FT-Raman spectra of HATN-2Me-1ReA.

5.4.2 Electronic absorbance spectra

5.4.2.1 Mono-rhenium HATN complexes

The seven HATN-1Re complexes had electronic spectra displaying two distinct $\pi \rightarrow \pi^*$ transitions in the 400-800 nm region. The lowest energy transition was a very broad band between 500-700 nm, this was followed by two or three absorption peaks in the 400-500 nm range (see Figure 14). These peaks were all MLCT in character as determined using TD-DFT calculations (see Appendix D).

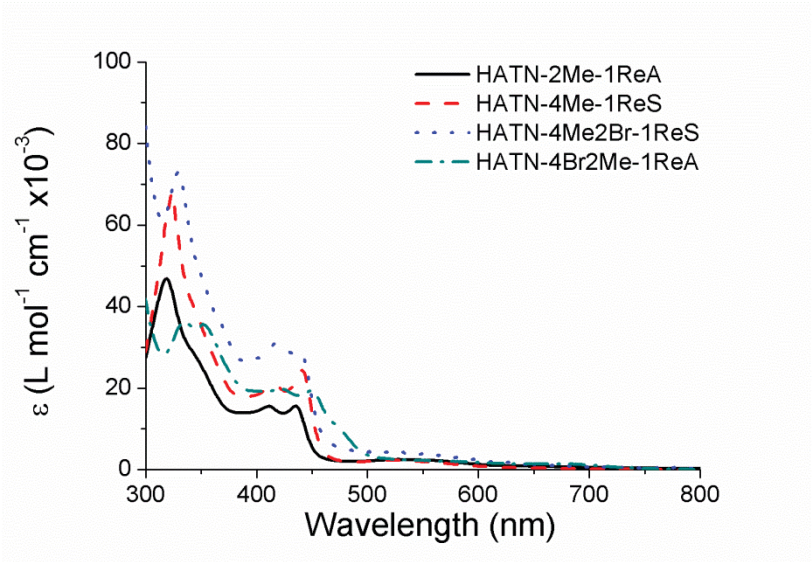

Figure 14 Electronic absorbance spectra of the mono rhenium HATN-2Me and HATN-4Me complexes.

There is a small blue shift of 7 nm between the HATN-2Me-1ReA and the HATN-4Me-1ReS complexes for the lowest energy band and this is associated with the functional groups on the rings. The more electron donating groups causes a higher charge density on the HATN core hence giving a lower wavelength for HATN-4Me-1ReS. This is also seen between the HATN-4Br2Me-1ReA and HATN-4Me2Br-1ReS complexes (Table 1), where the latter compound has the lower wavelength. Alternatively the more electron withdrawing groups present, the longer the wavelength as found for HATN-4Br2Me-1ReA.

Table 1 λ_{max} (nm) and absorption coefficients ($\varepsilon/10^3$ $Lmol^{-1}cm^{-1}$) of selected HATN-1Re complexes.

HATN	λ (nm) / nm (ε / 10^3 L $mol^{-1}cm^{-1}$)
HATN-4Me-1ReS	522 (b, 2.3), 441 (24.4), 416 (20.9)
HATN-2Me-1ReA	529 (b, 2.5), 436 (15.6), 411 (15.5)
HATN-4Br2Me-1ReA	550 (b, 2.2), 450 (19.4), 423 (19.8)
HATN-4Me2Br-1ReS	532 (4.3), 439 (28.6), 419 (31.1)

b = broad absorption

The lowest energy transition for HATN-2Me-1ReA, HATN-4Me-1ReS, HATN-4Br2Me-1ReA and HATN-4Me2Br-1ReS consisted of only HOMO → LUMO while the highest oscillator strength MLCT transition was dominated by HOMO-1 → LUMO. The complexes have HOMO and HOMO-1 rhenium based orbitals with all the electron density around the metal centre. The LUMOs are a ligand based orbital where the density has shifted onto the ligands to the rings closest to the rhenium. For the HATN-1ReA isomers the HOMO and HOMO-1 orbitals have a slightly uneven distribution of electron density over the closest rings, with the functional groups influencing a slight shift in electron density. The calculated HATN-2Me-1ReS LUMO orbital is symmetric with slight electron density reaching the rings furthest from the rhenium centre. The HATN-2Me-1ReA isomer is similar but there is slightly more electron density on the non-functionalised side due to the electron-donating groups pushing it away. The transitions, as calculated by TD-DFT, for HATN-2Me-1ReA are given in Figure 15 (the other HATN-1Re complexes show similar orbitals). The distribution of the electron density in the LUMO orbital is consistent with localised charge distributions which have given rise to a shift in the MLCT bands of the complexes.

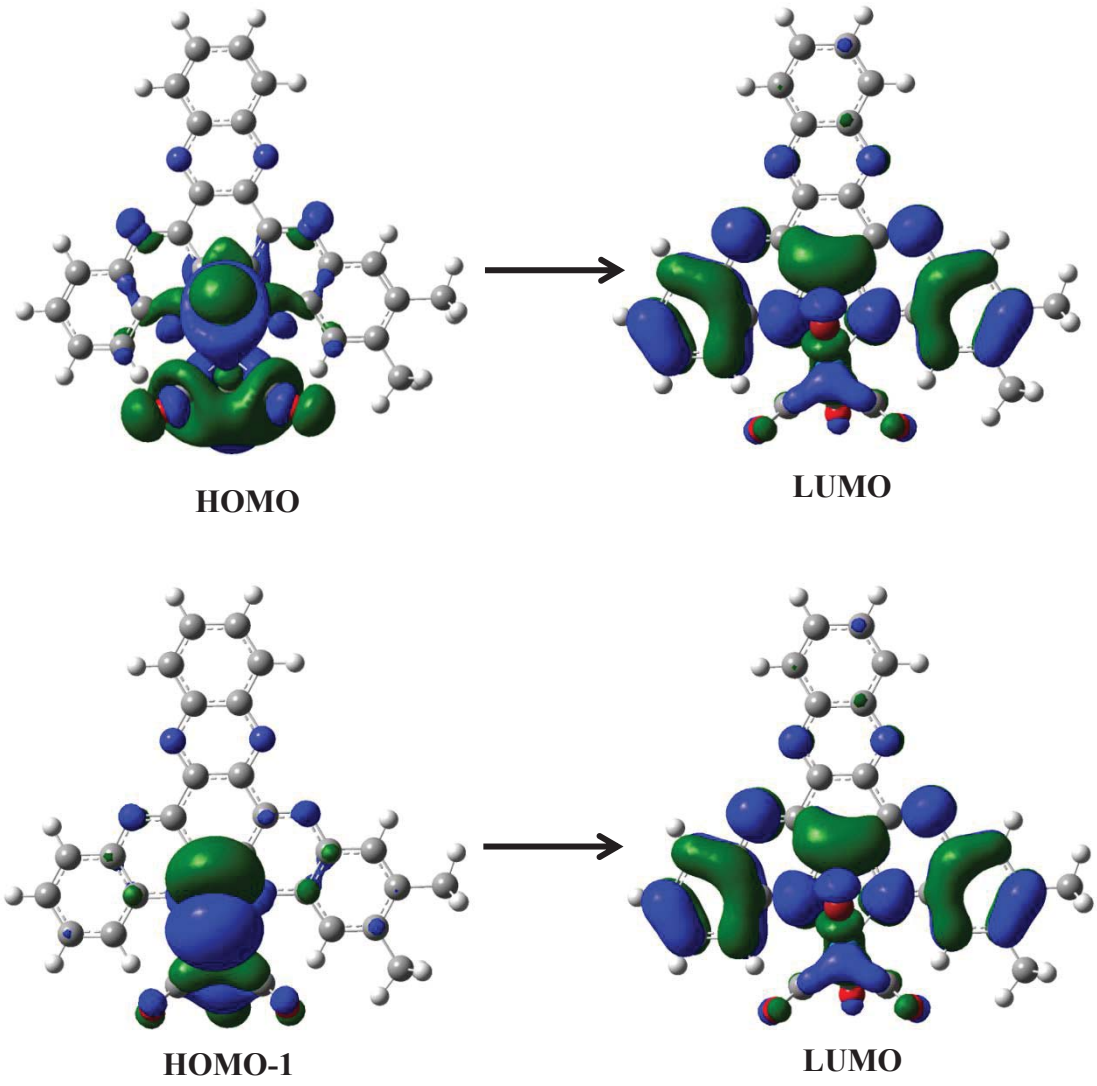

Figure 15 Top: Lowest energy HOMO to LUMO transition orbitals of HATN-2Me-1ReA. Bottom: Highest oscillator strength MLCT HOMO-1 to LUMO transition orbitals for HATN-2Me-1ReA

HATN-2Br-1ReA or S and HATN-4Br-1ReS also had very broad absorption bands ranging from 500-700 nm for the lowest energy transition (HOMO→LUMO) (Figure 16). The higher energy transitions are dominated by MLCT transitions. The lowest energy transitions (553 - 557 nm) are sitting at a longer wavelength than HATN-4Me-1Re and HATN-2Me-1Re complexes (522 – 529 nm) as expected due to the presence of bromo groups.

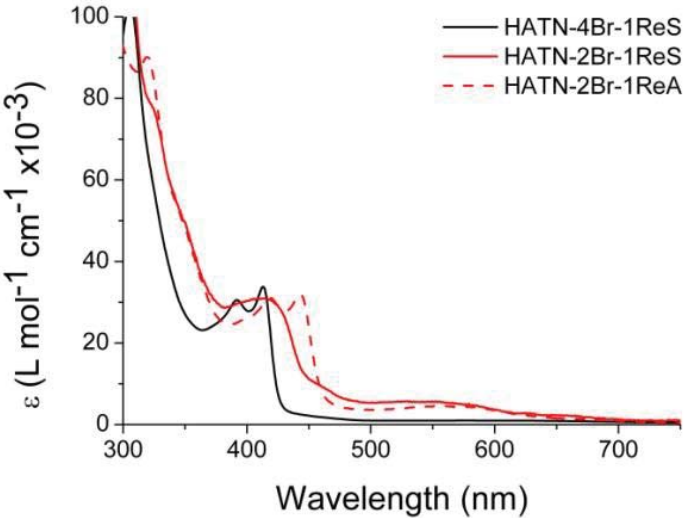

Figure 16 Electronic absorbance spectra of HATN-4Br-1ReS and HATN-2Br-1ReA/S

Table 2 λ_{max} (nm) and absorption coefficients ($\varepsilon/10^3$ $Lmol^{-1}cm^{-1}$) of selected HATN-1Re complexes.

HATN	λ (nm) / nm (ε / 10^3 L $mol^{-1}cm^{-1}$)
HATN-2Br-1ReS	553 (b, 5.7), 462 (s, 9.2), 415 (31.0)
HATN-2Br-1ReA	554 (b, 4.6), 443 (32.1), 418 (31.1)
HATN-4Br-1ReS	577 (b, 1.04), 413 (33.8), 392 (30.5)

b = broad absorption

The attempted synthesis and isolation of the homo-substituted HATN-6Cl rhenium complex can be found in the literature,[1] however it was not successful so this is the first study of the effect of electron withdrawing groups in HATN rhenium complexes. In HATN-2Br-1ReA the rhenium is close to a bromo group whereas in HATN-2Br-1ReS the rhenium is close to no functional groups (Figure 17). If the electron density introduced by the functional groups was localised the position of the rhenium should have an effect on the position of the MLCT band. As bromo groups are electron withdrawing and if this charge was localised near the rhenium it would be expected to decrease the energy in the HATN system and the MLCT band would red-shift, which in this case is not noticeable (see Table 2), so it can be assumed that the functional groups

influence is delocalised around the HATN core. TD-DFT calculations show that the lowest energy transition is a MLCT transition consisting of the HOMO→LUMO while the highest oscillator strength MLCT excitation was HOMO-1→LUMO. The electron density is localised on the rhenium metal for HOMO and HOMO-1, while in the LUMO the electron density is spread to the 1,10-phenanthroline type unit closest to the metal centre with slightly more electron density on the bromo rings but is very similar to the HATN-2Me-1ReA orbitals shown in Figure 15 and this is similar to the other complexes as well.

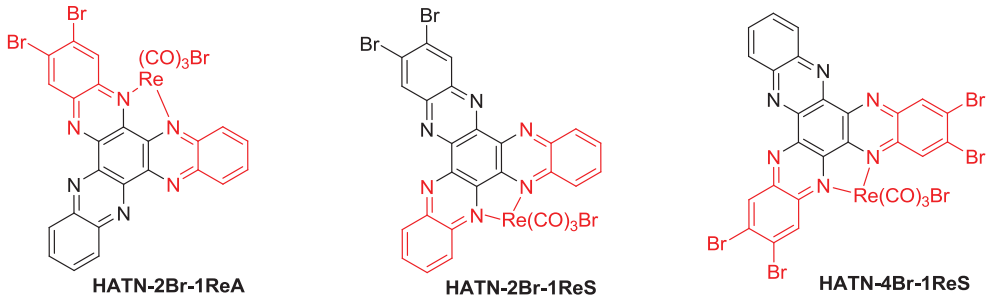

Figure 17 Isomers of HATN-2Br-1Re and HATN-4Br-1Re isomers with red indicating the pyrazine rings and functional groups influenced by binding of rhenium.

5.4.3 Di-rhenium complexes

The four HATN-2Re complexes had electronic spectra displaying one distinct π→π* transition in the 400-457 nm region (Figure 18) as well as a lower energy broad MLCT transition in the 622-640 nm range.

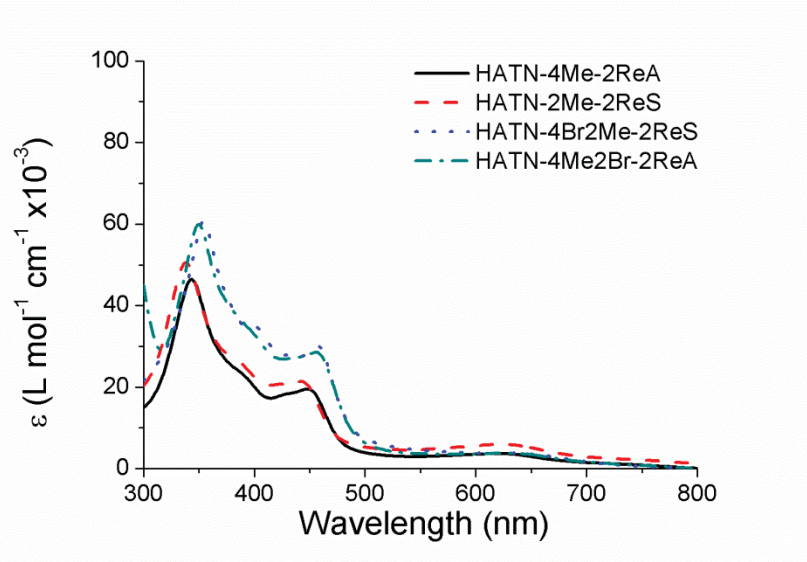

Figure 18 Electronic absorbance spectra of HATN-4Me-2ReA, HATN-2Me-2ReS, HATN-4Br2Me-2ReS and HATN-4Me2Br-2ReA.

The most significant difference between the mono and di-rhenium HATN complexes is the red-shift in the MLCT transitions of the mono-rhenium complex by about 100 nm. The HATN with the most electron-withdrawing groups vis. HATN-4Br2Me-2ReS has the lowest energy MLCT band as expected; while the methyl substituted derivatives have MLCT bands higher in energy (see Table 3).

Table 3 λ_{max} (nm) and absorption coefficients ($\varepsilon/10^3$ $Lmol^{-1}cm^{-1}$) of selected HATN-1Re complexes.

HATN	λ (nm) / nm (ε / 10^3 L $mol^{-1}cm^{-1}$)
HATN-4Me-2Re A	622 (b, 3.8), 448 (19.5), 389 (23.5)
HATN-2Me-2Re S	622 (b, 6.0), 441 (21.3), 381 (27.4)
HATN-4Br2Me-2ReS	640 (b, 3.7), 457 (30.2), 431 (27.8), 400 (34.8)
HATN-4Me2Br-2ReA	624 (b, 3.8), 455 (28.5)

5.4.3 Vibrational spectroscopy

FT-IR and Raman spectroscopy were used to study the vibrational behaviour of the HATN-1Re and HATN-2Re complexes. FT-IR gives an insight into the different orientations of the CO groups attached to the rhenium. The rest of the FT-IR and the FT-R spectra are dominated by the aromatic vibrational modes showing little difference between each complex (< 8 cm^{-1}). Resonance Raman spectra were useful to gauge the delocalisation of the orbitals associated with the MLCT transition.

5.4.3.1 Ground-State FT-IR and FT-Raman vibrational spectroscopy

The IR data are dominated by the rhenium terminal carbonyl peaks (ca. 1900 and 2025 cm^{-1}, Figure 19). The slight shifts in frequencies in the range 1090-1500 cm^{-1} between the HATN-2Br ligand relative to HATN-2Br-1Re A and S complexes are attributed to the presence of rhenium. Slight shifts also occur for the HATN-2Re complexes. Representative examples of the FT-IR spectra of the compounds are illustrated with HATN-2Br, HATN-2Br-1ReS and HATN-2Br-1ReA and are shown in Figure 19.

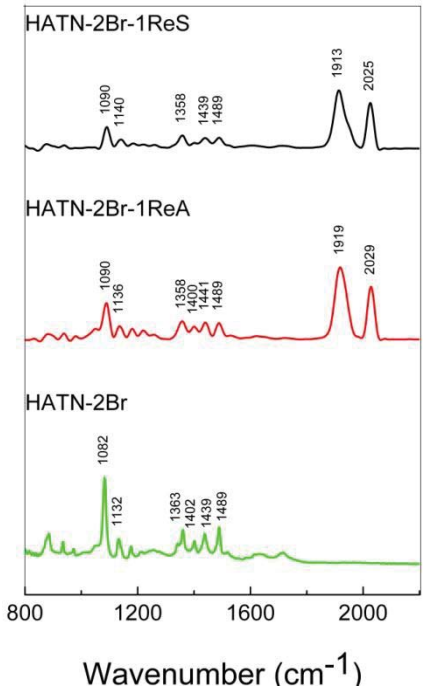

Figure 19 FT-IR spectra of HATN-2Br-1ReS (Black), HATN-2Br-1ReA (Red) and the HATN-2Br ligand (Green) measured without solvent.

The addition of $Re(CO)_3$ into the ring introduced CO stretching frequencies which become the most dominant aspect of the spectra (Figure 19). However, the rest of the spectra are relatively similar in vibration number and intensities to the parent HATN ligand used. The FT-IR spectrum of HATN-2Br-1ReS shows one peak at ca. 1920 cm^{-1}, which was resolved into two peaks using solution IR in dichloromethane (Table 4), however not all peaks could be resolved this way e.g. HATN-2Br-1ReA. These peaks along with the peak at ca. 2030 cm^{-1} are carbonyl bands due to the facial arrangement of the $\{Re(CO)_3Cl\}$ unit with C_s symmetry, corresponding to three modes, as is illustrated in Figure 20. From lowest to highest energy, the vibrations are as follows: a'(2), out-of-phase stretch, a", in-plane anti-symmetric stretch; a'(1), in-phase symmetric stretch. DFT calculations on these systems are in agreement with these observations. The facial arrangement of the 3CO's is consistent with the single crystal X-ray structure of HATN-4Me-1ReA and HATN-4Me-1ReS (Chapter 4, Figures 13 and 14).

Table 4 Solution IR spectra of selected HATN compounds in DCM.

HATN	A'(1)	A"	A"-A'(2)	A'(2)
HATN-2Me-2ReS	2024	1958		1925
HATN-4Me-2ReA	2024		1928	
HATN-4Me-1ReS	2026	1953		1913
HATN-2Br-1ReA	2025		1922	
HATN-2Br-1ReS	2026	1942		1922
HATN-4Br2Me-1ReA	2026	1942		1922
HATN-4Br2Me-2ReS	2025	1942		1923

Since back-bonding from the d-orbitals of rhenium feeds electron density into the carbonyl anti-bonding orbitals, IR carbonyl stretching frequencies can give information about the environment of the metal centre. For example, an increase in the carbon-oxygen stretching frequency indicates an increase in the carbon-oxygen bond strength thus decreased anti-bonding electron-density from the metal. For example the FT-IR solid state spectrum of HATN-2Br-1ReA (Figure 19) shows the A'(1) symmetric carbonyl stretch at a frequency of 2029 cm^{-1}, slightly higher than 2021 cm^{-1} observed for HATN-2Me-1ReA. The decrease of electron density on the rhenium atom would

indicate that the HATN is relatively electron-poor which in the case of HATN-2Br-1ReA could be due to the attachment of two electron withdrawing bromo groups. As can be seen the various substituents placed on the parent HATN do not influence the position of the A'(1) mode to a great extent so their influence is not large.

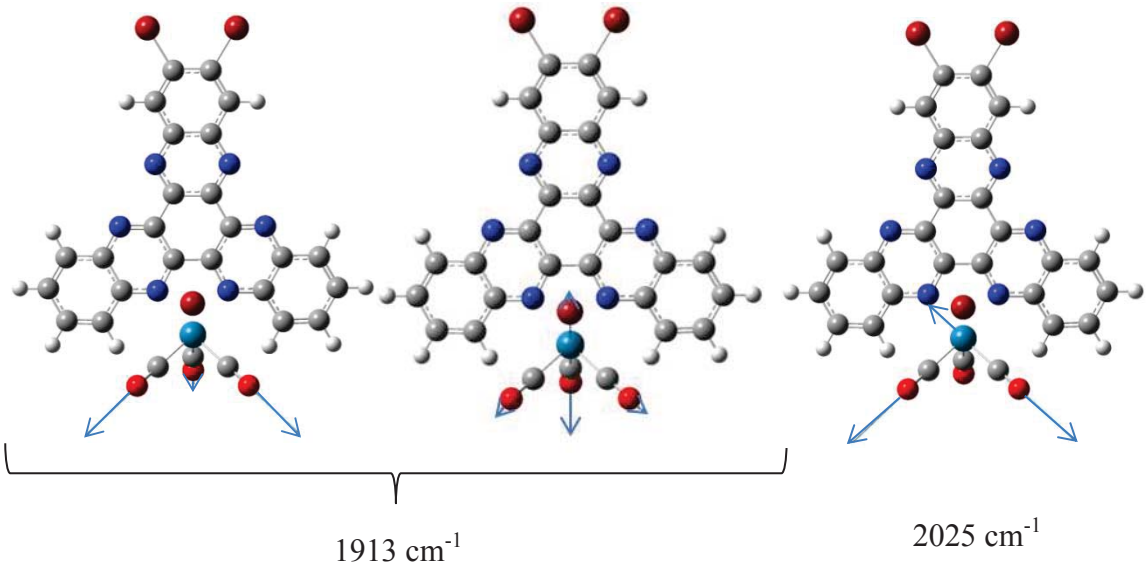

Figure 20 Experimental CO stretching frequencies along with theoretical CO stretching frequency diagrams for HATN-2Br-1ReS (blue arrows indicate vibration direction).

The rest of the bands (1090, 1358, 1402, 1439, 1489 cm^{-1}) are dominated by ring distortions similar to the metal-free HATN ligand (Figure 19), with the variation attributed to the rhenium affecting the vibration frequency. The peaks at 1090 cm^{-1} show delocalised distortions throughout the HATN-2Br ligand as well as the complex, with the shift of 8 cm^{-1} being attributed to the binding of rhenium. The peak at 1358 cm^{-1} is mainly H-wagging while the 1400cm^{-1}, 1440 cm^{-1}, and 1489 cm^{-1} bands have H-wagging as well as ring distortions near the rhenium centre (Figure 21).

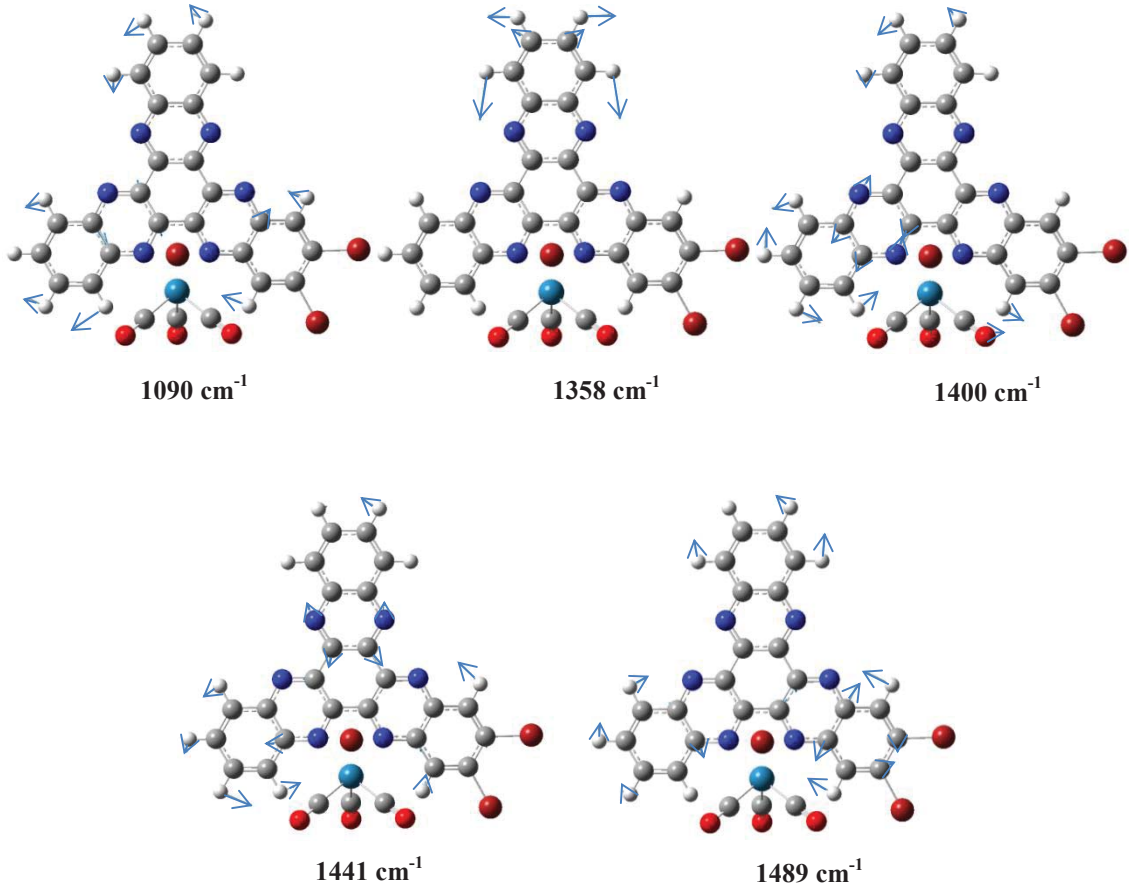

Figure 21 IR vibrational modes of HATN-2Br-1ReA (blue arrows indicate vibration direction).

The FT-Raman spectra of the ligand HATN-2Br as well as its associated complexes HATN-2Br-1ReA and S are shown in Figure 22. Similar peaks are present in the ligand and the complexes but their intensities have altered by the addition of rhenium. The most intense feature is a band around 1410 cm^{-1}, which corresponds to the HATN ring deformations. The peaks ranging from 1340-1580 cm^{-1} all correspond to displacements in the HATN ring around the N bound to the rhenium metal. This will be discussed further in Section 5.4.2.2.

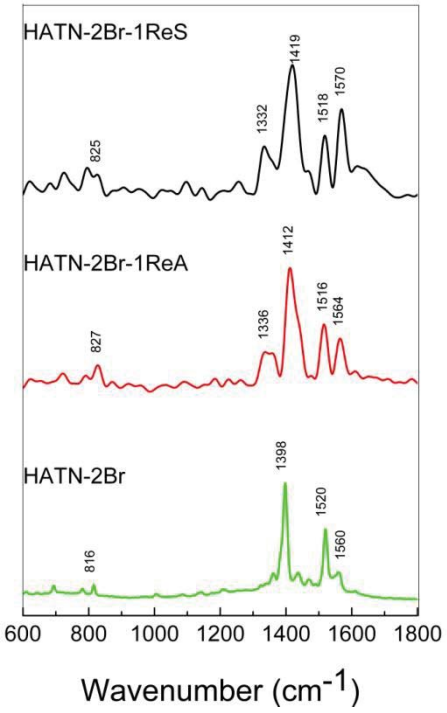

Figure 22 FT-Raman spectra of HATN-2Br-1ReS (Black), HATN-2Br-1ReA (Red) and HATN-2Br (Green) measured without solvent.

5.4.3.2 Resonance Raman spectra

Resonance Raman spectra show selective enhancements of modes within active chromophores, where the excitation wavelength determines which particular chromophores are being probed. Each of the complexes was excited by wavelengths at 488 and 532 nm which correspond to the end of a $\pi \rightarrow \pi^*$ band and the broad MLCT absorption band respectively. The rR spectra of the complexes are shown in Figure 23, while the vibrational modes assignments are in the Appendix D. Some data did not have a sufficient signal to noise ratio and were not considered.

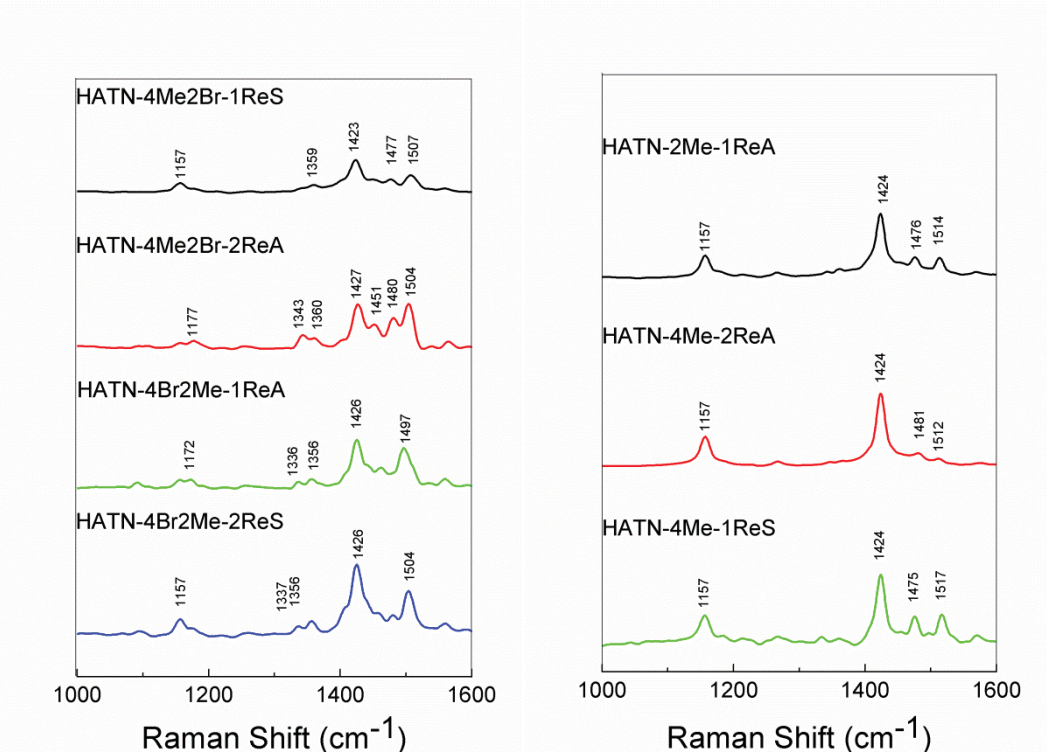

Figure 23 Resonance Raman spectra of HATN complexes collected at 488 nm (left) and 532 nm (right)

The most prominent vibration which appears in all the spectra collected for the HATN-1Re compounds (rR and FT-Raman) is the peak lying at ca. 1410 cm^{-1}. This peak is associated with in plane delocalised HATN ring distortions. In the 488 nm probed spectra a vibrational mode at 1475 cm^{-1} is present for the HATN-4Me-1ReS isomer, this shifts to 1481 cm^{-1} for the HATN-4Me-2ReA isomer. In the 532 nm excited spectra of the HATN-4Br2Me-1ReA and HATN-4Br2Me-2ReA this same peak does not shift even though there is the inclusion of an extra rhenium. However, it shifts 5 cm^{-1} from the HATN-4Me2Br-1ReS and HATN-4Me2Br-2ReA. The normal modes for this vibration at ca. 1475 cm^{-1} are associated with significant bond vibration about but not on the chelating nitrogen atoms; the addition of rhenium centres to these sites results in a change in the HATN environment and thus the energy required for vibration. The increased enhancement of the modes associated with the chelating nitrogen atoms is consistent with a MLCT excitation. Only a small number of distinct bands at 1450 to 1510 cm^{-1} are obtained for these complexes (Figure 24). These arise from the asymmetric ligand breathing mode localised on the aromatic rings closest to the point of

ligation. It can be assumed that for all HATN complexes the rings closest to rhenium will be enhanced showing localisation of the electron density within the complexes.

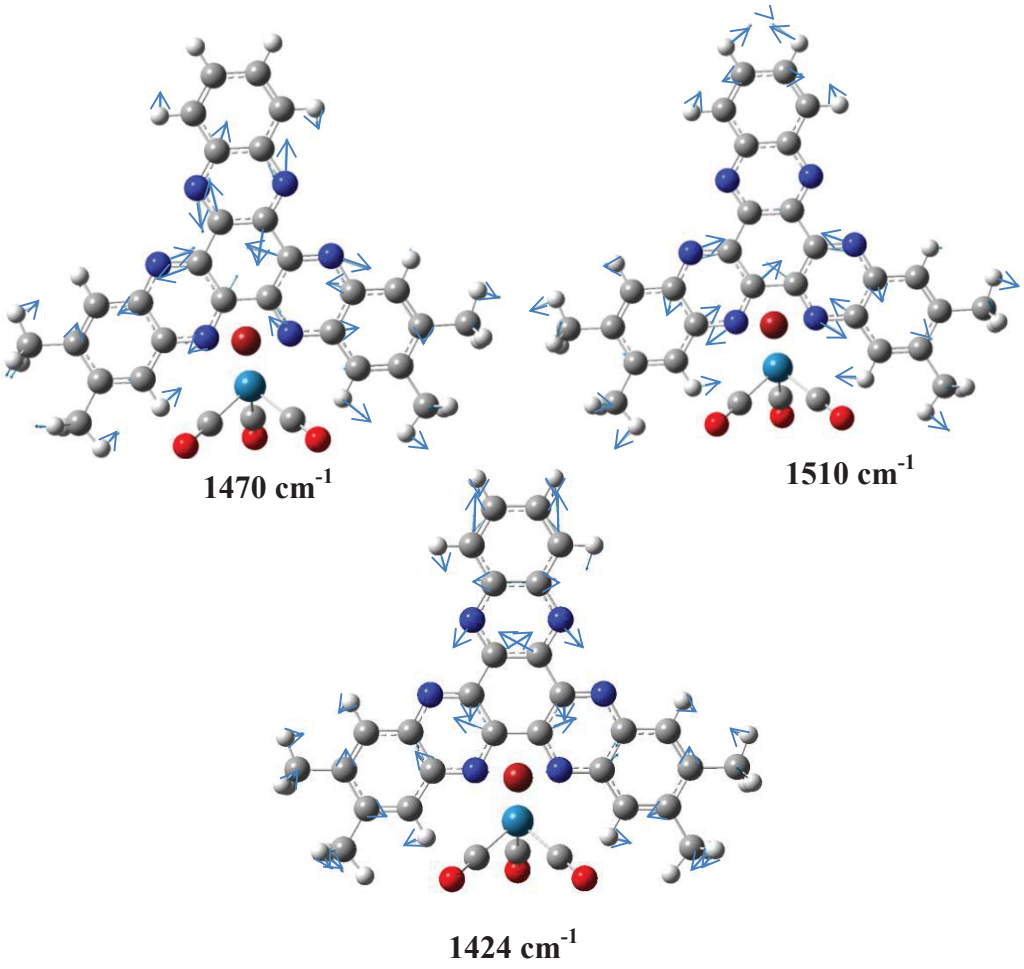

Figure 24 Vibrational modes top left: ca. 1470 cm^{-1} and right: ca. 1510 cm^{-1} of HATN-4Me-1ReS with blue arrows indicating vibration mode. Bottom: 1424 cm^{-1} (blue arrows indicate vibration direction).

5.4.4 Electrochemistry

Cyclic voltammetry is a useful tool for estimating HOMO and LUMO energies. The cyclic voltammograms of HATN-2Me-1ReA HATN-2Br-1ReS HATN-2Br-1ReA HATN-4Br2Me-1ReA and HATN-4Br2Me-1ReS were measured in DCM using 0.1 M $^{t}Bu_4NBr$ as supporting electrolyte. Data are tabulated in Table 5. The cyclic voltammetry of these compounds in the range 1 V to -1V reveals a reversible one-electron wave, assigned to adding one electron to the π*(HATN). Chelation of a single $Re(CO)_3Br$ unit stabilises the reduction potential for the HATNs by about 0.48 V.

A comparison between the redox potentials of HATN-2Me-1ReA HATN-2Br-1ReS HATN-2Br-1ReA HATN-4Br2Me-1ReA and HATN-4Br2Me-2ReS and the already recorded values for HATN-6Me-1Re was made. Reversible ligand centred reduction processes attributed to $HATN/HATN^-$ are observed at -0.37, -0.40, -0.48, -0.41 and 0.02 V (vs. Fc/Fc^+) for HATN-2Me-1ReA, HATN-2Br-1ReS, HATN-4Br2Me-1ReA and HATN-4Br2Me-2ReS respectively. Comparison with the HATN-6Me-1Re (-0.48 V) showed a similar reduction potential.

The reduction potentials are all very close and with no obvious trend (Table 5). The addition of another rhenium to the core also shifts the first reduction potential anodically to 0.02 V, a shift of ~0.4 V.

Table 5 HATN-1Re first reduction potentials (vs. Fc/Fc^+ in DCM)

	$HATN/HATN^-$
HATN-2Me-1ReA	-0.37
HATN-2Br-1ReS	-0.40
HATN-4Br2Me-1ReA	-0.41
HATN-4Br2Me-2ReS	0.02

Cyclic voltammetry is a useful tool for estimating the suitability of a complex as a solar cell dye. The HOMO potential must be more positive than the redox mediator to ensure favourable regeneration kinetics of the oxidised dye by the redox mediator. The LUMO

potential must be more negative than the conduction band of the semiconductor (TiO_2) to obtain efficient electron injection into the conduction band. The LUMO can be estimated from the reduction onset potential (E^{red}_{onset}) while the HOMO level can be calculated using the band-gap found from UV measurements (see Appendix D for calculations). These energy levels have been estimated from solution state cyclic voltammetry (CV) and are summarised in (Table 6).

Table 6 Summary of the energy levels obtained from cyclic voltammetry.

HATN	E_{onset},red (V vs Fc/Fc^+)	λ (nm)	E_{gap}[a] (eV)	HOMO[b] (V)
HATN-2Me-1ReA	-0.3301	730	1.703	1.3729
HATN-2Br -1ReS	-0.1981	710	1.751	1.5529
HATN-4Br2Me-1ReA	-0.2049	720	1.726	1.5211
HATN-4Br2Me-2ReS	0.0833	770	1.614	1.6973

[a] Band gap (eV) = $\frac{1243}{\lambda_{onset}(nm)}$

[b] HOMO (eV) = LUMO (V) + band gap (eV)

Now we have these fundamental results we can predict what is likely to occur for their possible application in dye-sensitised solar cells. The HOMO and LUMO results were used to form a HOMO-LUMO diagram for the HATN complexes. The addition of the I^-/I_3^- redox couple HOMO level is shown as well as the conduction band of TiO_2. When a dye gets excited the electron should move from the LUMO of the complex into the TiO_2. However, this is not possible as the TiO_2 conduction band is too high. HATN-1Re and HATN-2Re reduction potentials are too positive for this to occur.

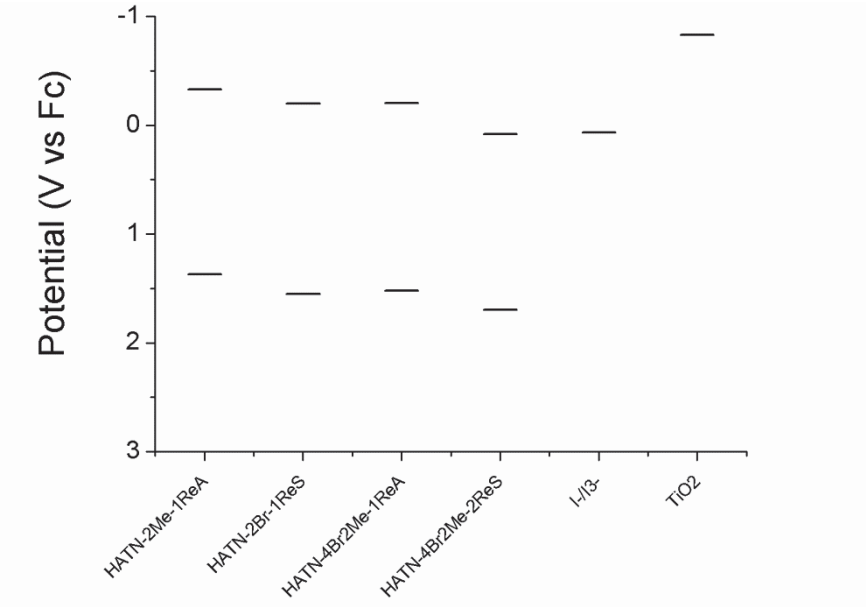

Figure 25 HOMO LUMO levels of selected HATN-1Re complexes

5.5 Copper(I) HATN complexes

The photophysical properties of seven copper HATN complexes (Figure 27) synthesised in Chapter 4 were investigated here. As previously mentioned in Chapter 4 they displayed a colour change dependent on the solvent polarity, an unusual property which has not been observed for any of the copper(I) HATNs reported in the literature.

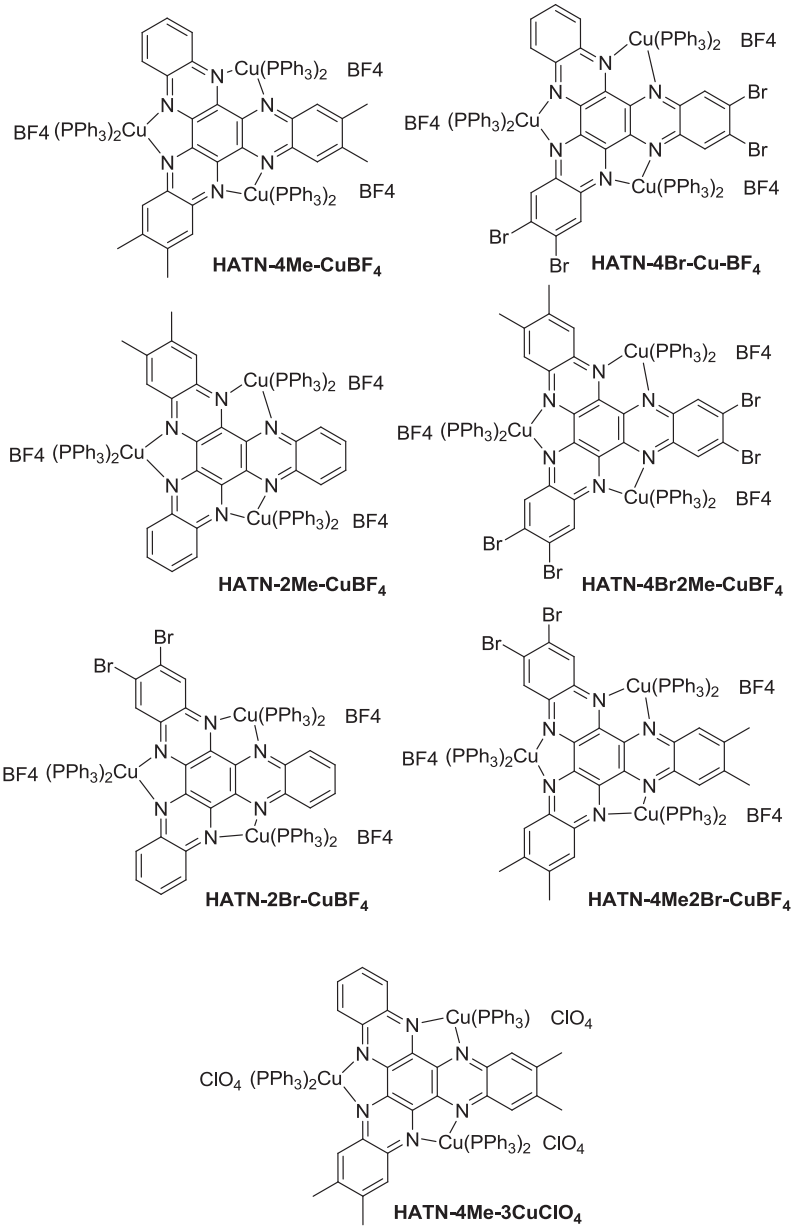

Figure 26 Six copper HATN-3CuBF$_4$ complexes synthesised in Chapter 4 as well as the HATN-4Me-3CuClO$_4$ analogue.

Electronic absorbance and resonance Raman (rR) spectra were recorded in chloroform and electrochemical data in dichloromethane solutions. FT-IR and FT-Raman data were recorded as pure solids. Instrumental details and specific conditions are given in the Appendix D.

Computational models of the HATN complexes were employed to aid the assignment of the electronic absorbance and vibrational spectra, using a DFT/B3LYP calculation with 6-31G (d) for all atoms. The time-dependent calculations were carried out in chloroform, THF, and acetonitrile solvent field using the PCM method. All calculations were performed using the Gaussian09/GaussView5 packages.

The electronic accuracy of the models was measured by comparison of the calculated vibrational frequencies to the IR and FT-Raman data (example Figure 13); the output frequencies were scaled by 0.96. This gave a range of MAD values of 8 cm^{-1} (HATN-4Me2Br-3$CuBF_4$ to 32 cm^{-1} (HATN-4Br-3$CuBF_4$) in the Raman spectra and 9 cm^{-1} (HATN-4Me2Br-3$CuBF_4$) to 16 cm^{-1} (HATN-4Br-3$CuBF_4$) in the IR spectra (See Appendix D for details of the calculations).

5.5.1 Electronic absorbance spectra

The six HATN-3CuBF$_4$ and HATN-4Me-3CuClO$_4$ complexes had electronic spectra displaying up to three absorption peaks in the 300-800 nm region. The lowest energy transition varied between solvents (chloroform/acetonitrile) but was very broad for both. It ranged between 500-700 nm when chloroform was used as the solvent and 450-600 nm when acetonitrile was used as the solvent. This was followed by two or three absorption peaks in the 300-500 nm range. These peaks were all MLCT in character as determined using TD-DFT calculations (see Appendix D).

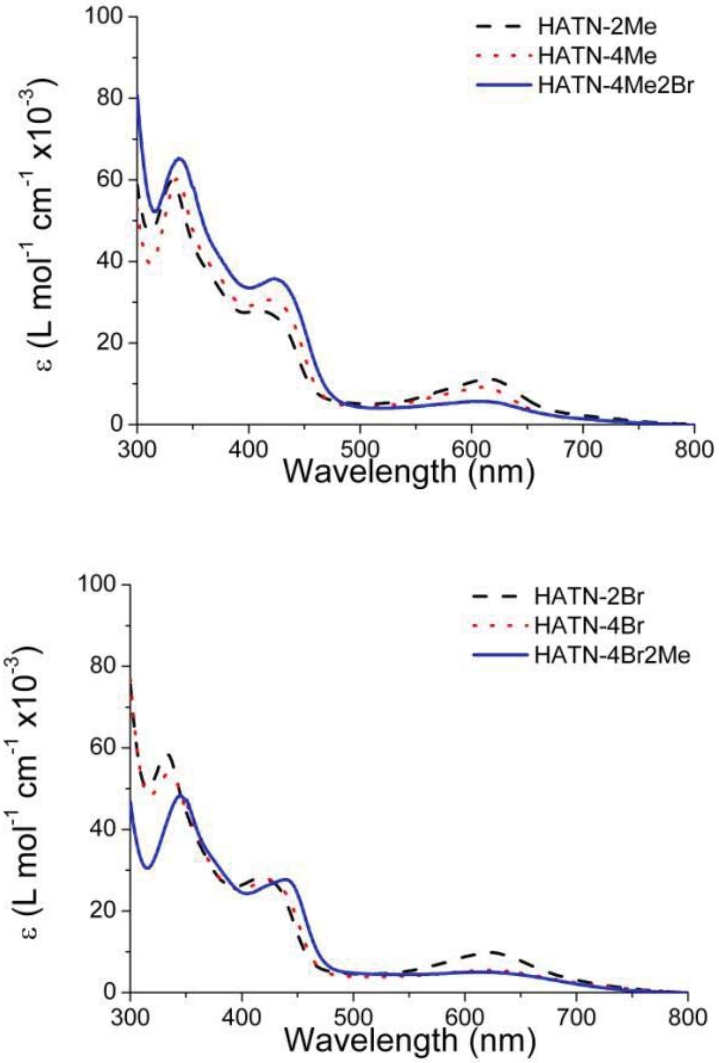

Figure 27 Electronic absorbance spectra of, top: HATN-2Me-3CuBF$_4$ HATN-4Me-3CuBF$_4$ and HATN-4Me2Br-3CuBF$_4$ Bottom: HATN-2Br-3CuBF$_4$ HATN-4Br-3CuBF$_4$ and HATN-4Br2Me-3CuBF$_4$ All spectra were measured in CHCl$_3$.

Table 7 λ_{max} (nm) and absorption coefficients ($\varepsilon/10^3$ $Lmol^{-1}cm^{-1}$) of selected HATN-3CuBF$_4$ complexes in chloroform solution.

HATN	λ (nm) / nm (ε / 10^3 L $mol^{-1}cm^{-1}$)
HATN-2Me-3CuBF$_4$	332 (59.8), 408 (28.0), 616 (11.2)
HATN-4Me-3CuBF$_4$	336 (60.2), 416 (30.6), 611 (9.2)
HATN-4Me2Br-3CuBF$_4$	337 (65.3), 423 (35.8), 611 (5.7)
HATN-2Br-3CuBF$_4$	332 (58.8), 419 (28.1), 623 (9.8)
HATN-4Br-3CuBF$_4$	334.5 (53.6), 423 (27.9), 617 (5.5)
HATN-4Br2Me-3CuBF$_4$	346 (48.2), 439 (27.7), 620 (5.0)
HATN-4Me-3CuClO$_4$	340 (63.6), 419 (31.2), 611 (9.4)

The presence of these three copper centres around HATN results in a delocalisation of charge with the MLCT peaks having a range of only 12 nm (611-623 nm) in chloroform (Figure 27, Table 7). Nevertheless, as expected, HATN-4Me-3CuBF$_4$ with its electron donating methyl substituents has a MLCT band at higher energy (611 nm) than the bromo analogue, HATN-4Br-3CuBF$_4$, at 617 nm. It is also worth noting that it is not possible to have A and S isomers of the copper complexes as all coordination sites are always fully occupied by copper. With three metals occupying all coordinating sites it would be expected that a difference in the substituents would have less of an effect than the rhenium HATN complexes due to the fact that each pyrazine ring will now be attached to two copper atoms spreading out the electron density and reducing the influence of nearby functional groups.

When the absorption spectrum of HATN-4Me-3CuBF$_4$ is compared with HATN-4Me-3CuClO$_4$ in Figure 28, it can be seen that they are almost identical. The crystal structure obtained for HATN-4Me-3CuClO$_4$ showed that one of the copper atoms had only one triphenylphosphine coordinated. If it formed this species in solution it would be expected to display a slightly different spectrum from that of HATN-4Me-3CuBF$_4$

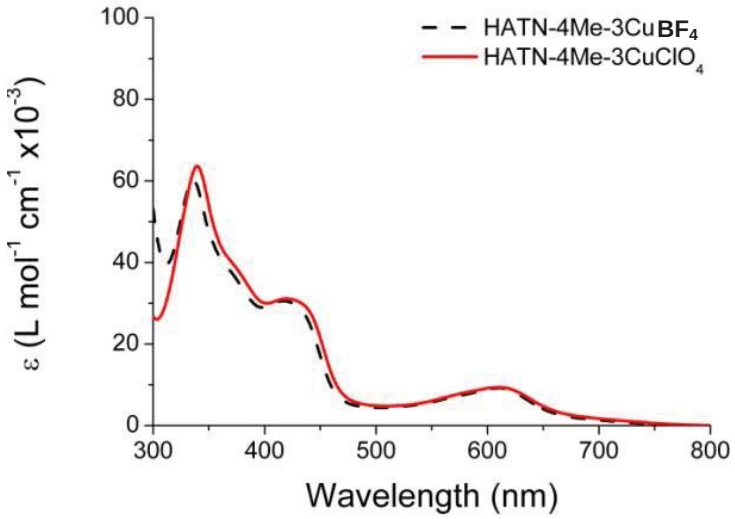

Figure 28 The electronic absorbance spectra measured in $CHCl_3$ of HATN-4Me-3CuBF$_4$ and HATN-4Me-3CuClO$_4$.

Based on the reasonably close match of the TD-DFT UV/Vis simulated spectra using the standard HATN-3CuBF$_4$ model (Figure 29) to the experimental results, it can be assumed the HATN-3CuBF$_4$ complexes all have the HATN-3CuBF$_4$ structure in chloroform solution, where each copper has two triphenylphosphines. There is, however, an error associated with the calculated results so it is possible that the similarity in the absorption spectra of HATN-4Me-3CuBF$_4$ and HATN-4Me-3CuClO$_4$ may perhaps occur if the former compound loses a triphenylphosphine and then both complexes produce the same cationic species [HATN-4Me-3Cu]$^{3+}$. In the solid state structure of HATN-4Me-3CuClO$_4$ one of the ClO_4^- groups is bound weakly to a copper centre, but in $CHCl_3$ solution this ClO_4^- possibly becomes more ionic.

In the literature it has been reported that HATN-6Me forms a 'normal' copper complex with two triphenylphosphines per copper(I) attached, and one of the BF_4^- counter ions weakly associated to Cu(I) centres but in solution the association was not retained.[10,11] This example provided further evidence about, in this case, the nature of the BF_4^- attached to a copper(I) centre. In this case the complex behaves as predicted in $CHCl_3$, with the observations matching up with the TD-DFT calculations. Also no dissociation of triphenylphosphine was needed or invoked.

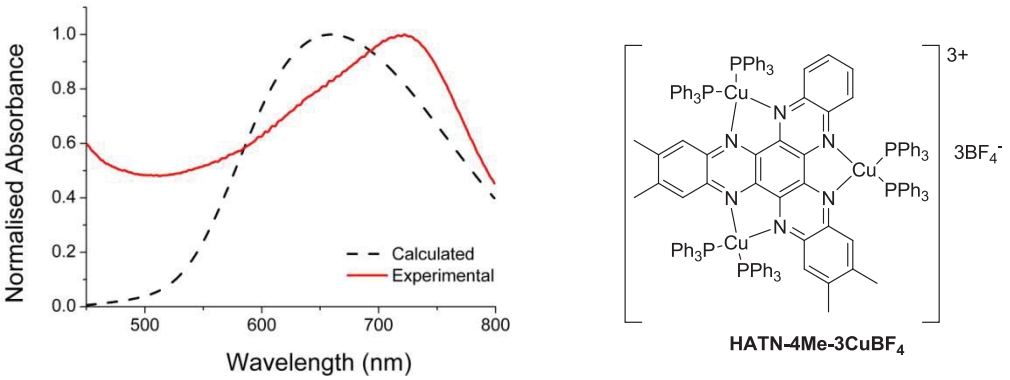

Figure 29 Left: Comparison between experimental and calculated results for HATN-4Me-3CuBF$_4$. Right: The standard structure for HATN-4Me-3CuBF$_4$.

It was found that many orbitals are involved in the MLCT transitions of these complexes but all consist mainly of the HOMO→LUMO transitions, with the electron density in the HOMO orbital centred on two copper atoms while in the LUMO the electron density is evenly spread throughout the HATN ligand (see Figure 30). Negligible shifts are seen between the complexes containing similar groups (e.g. 5 nm for HATN-2Me-3CuBF$_4$ to HATN-4Me-3CuBF$_4$ and 5 nm for HATN-2Br-3CuBF$_4$ and HATN-4Br-3CuBF$_4$).

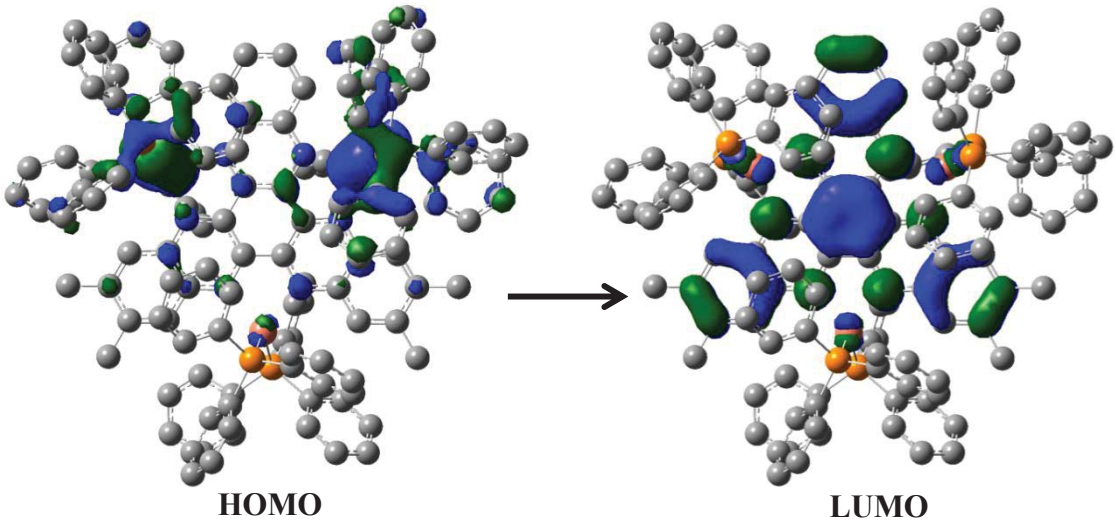

Figure 30 HOMO and LUMO orbitals for HATN-4Me-3CuBF$_4$ Hydrogen atoms are omitted for clarity.

5.5.2 Comparison of the electronic absorbance spectra in chloroform and acetonitrile

A colour change was observed when the HATN-4Me-3CuBF$_4$ complex was dissolved in acetonitrile. In MeCN the complex was red, in chloroform it was green. Once the MeCN has been removed the equilibria swings back to the green form again. This observation is validated in the absorption spectra (Figure 31). It is difficult to identify the MLCT peak positions in acetonitrile as they have broadened into the higher energy transitions but it is possible to see that they are blue-shifted in their peak position (In $CHCl_3$ the absorption band is at ~600 nm and in MeCN it is ~500 nm). The absorption bands in acetonitrile also consist of two distinct bands at ~400 nm, while a broad band appears in the chloroform solvent. The absorption coefficients are lower (ca. half or less) in acetonitrile compared to chloroform as a solvent. The spectrum in MeCN is a closer match to the free ligand than to the copper complex in $CHCl_3$ suggesting the possibility perhaps of some dissociation of the HATN ligand from the copper, but more importantly perhaps of another HATN species containing a lower amount of Cu(I). This will be further developed in Section 5.5.2.2.

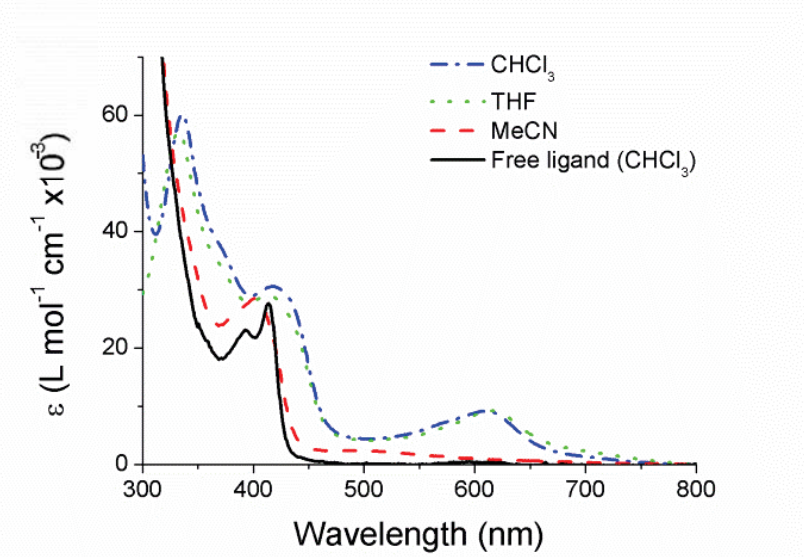

Figure 31 Electronic absorbance spectra of HATN-4Me-3CuBF$_4$ in various solvents

Table 8 λ_{max} (nm) and absorption coefficients of HATN-3CuBF$_4$ ($\varepsilon/10^3$ L mol^{-1} cm^{-1}) complexes in various solvents

	MeCN	THF	$CHCl_3$
HATN-4Me-3CuBF$_4$	450-599 (2.6-1.0)	617 (9.3)	616 (11.2)
HATN-4Br-3CuBF$_4$	450-601 (2.9-1.0)	622 (7.6)	611 (9.2)
HATN-4Me2Br-3CuBF$_4$	450-593 (2.5-1.0)	619 (6.1)	611 (5.7)
HATN-2Br-3CuBF$_4$	450-580 (2.5-1.0)	629 (7.7)	623 (9.8)
HATN-2Me-3CuBF$_4$	450-616 (3.8-1.0)	629 (8.2)	617 (5.5)
HATN-4Br2Me-3CuBF$_4$	450-595 (3.8-1.0)	612 (3.7)	620 (5.0)
HATN-4Me-3CuClO$_4$	450-661 (2.2-1.0)	612 (10.8)	611 (9.4)

The absorption spectra in MeCN solution of the HATN-4Me copper complexes with the tetrafluoroborate and perchlorate anions are shown in Figure 32. The spectra are very similar with their peaks appearing at the same wavelength. The absorbance values for the perchlorate complex are slightly lower than that for the tetrafluoroborate complex, and the peak around 400 nm is resolved into two peaks for the perchlorate anion complex.

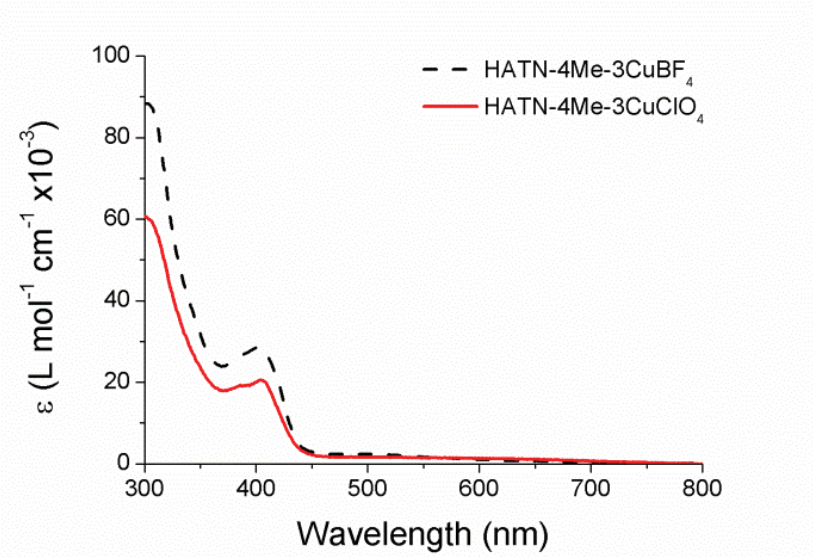

Figure 32 Electronic absorbance spectra of HATN-4Me-3CuBF$_4$ and HATN-4Me-3CuClO$_4$ in MeCN

Three plausible explanations for the shift were considered: i) change in the copper oxidation state from I to II, ii) a solvatochromic shift, and iii) dissociation of copper or triphenylphosphine occurring in acetonitrile solvent.

As green copper compounds containing aromatic nitrogen containing ligands are typically associated with copper(II) compounds,[25] electron spin resonance (ESR) measurements were performed to identify any unpaired electron associated with copper(II). However, no signal was observed (see Figure 35), therefore the possibility of an oxidation was ruled out.

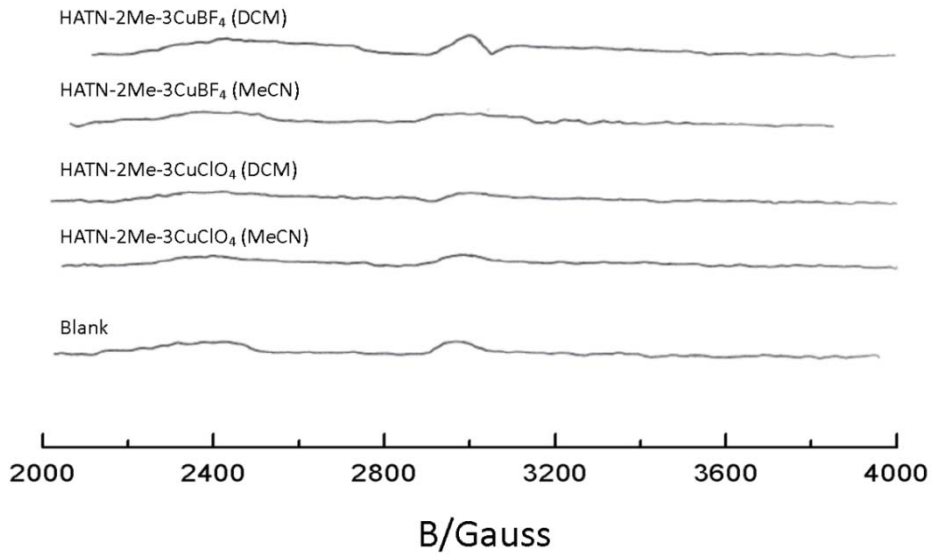

Figure 33 X-band EPR spectra of HATN-2Me-3CuBF$_4$ and HATN-2Me-3CuClO$_4$ in frozen DCM and MeCN at -150 ˚C. Receiver gain 6.3 x 10^3, modulation amplitude 4 x 1.

5.5.2.1 Solvatochromism

The two remaining possibilities are solvatochromism and complex dissociation. Copper(I) complexes of the type $[Cu_2X_2L_2]_n$ (X = halogen, L=N,N'-bis[3-(methylthio)propyl]pyromellitic diimide)) have shown solvatochromism by a halogen-π charge-transfer interaction rather than a coordination of the solvent to the copper(I) site.[26] However there appears to be little known about this phenomenon when triphenylphosphine is coordinated to the copper(I) centre.

For the complex [Ni(phen)(dithiolate)] a blue-shift of 94 nm has been observed between the solvent DMSO and 1,4-doxane respectively.[27] This has been associated with the considerable directional change of the electron density within a molecule (1,10-phenanthroline to 1,2-trifluoromethylethene-1,2-dithiolate) with the solvent interacting with the dipole. Such a feature is not available in the HATN complexes so a shift of over 100 nm seems unlikely to be associated with this type of solvatochromism. In summary there appears to be no evidence for any of the two types of solvatochromism for the HATN complexes.

5.5.2.2 Complex dissociation

Given the crystal structure of the HATN-4Me-3$CuClO_4$ showed that a triphenylphosphine was labile enough to detach from one copper it may be possible that a similar occurrence is happening in solution for HATN-4Me-3$CuBF_4$. If dissociation is occurring three possible species may be produced assuming that only one metal centre is affected at a time. The ligand deficient copper centre may only have one phosphine or one phosphine and a coordinating anion or one phosphine and a coordinating solvent (see Figure 34). As the HATNs are asymmetric this also leads to the possibility of these alterations occurring in both the asymmetric and symmetric positions on the HATN ligands, doubling the options available.

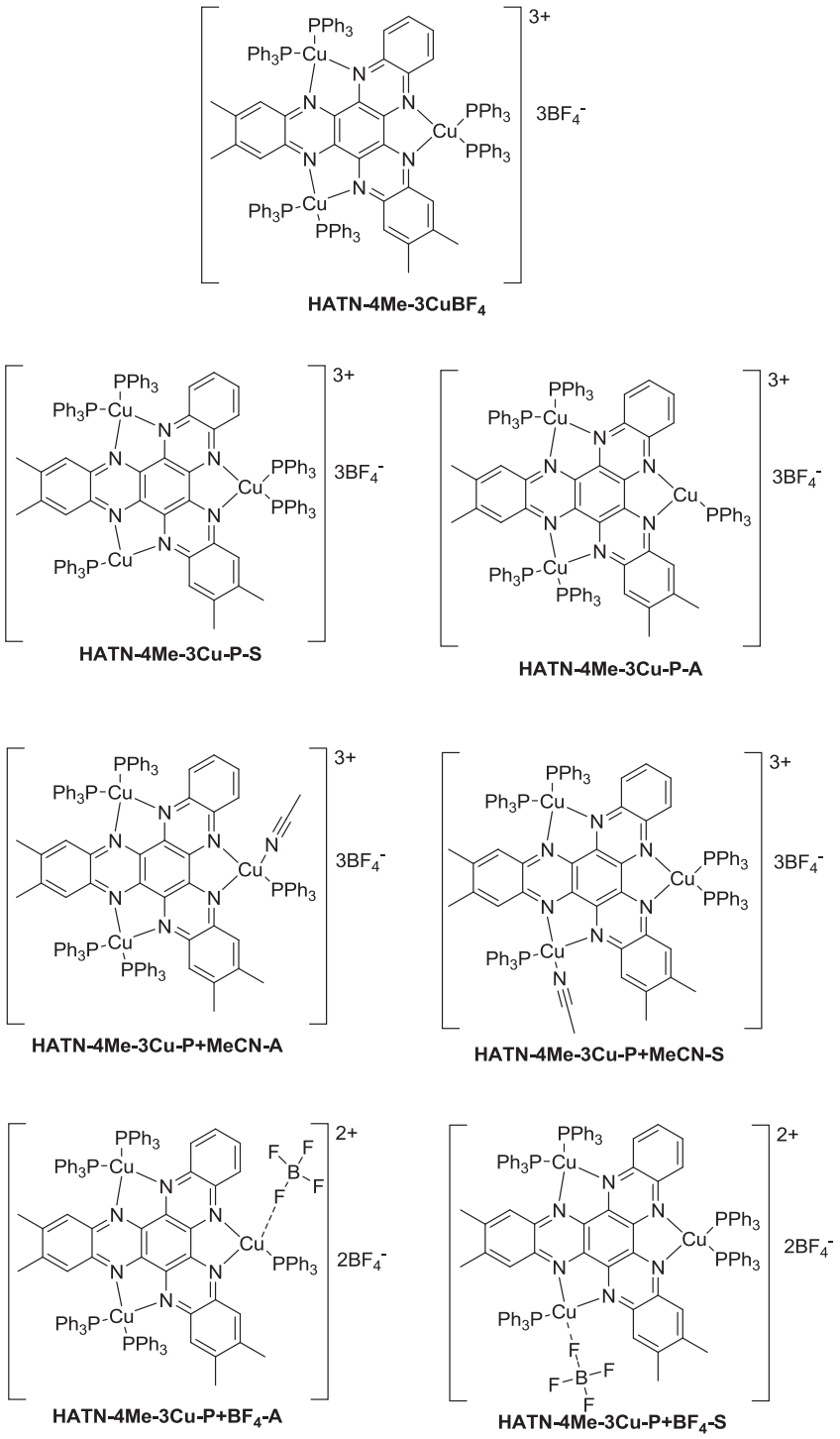

Figure 34 Possible states that the HATN-4Me-3CuBF$_4$ complex is in equilibrium with while in acetonitrile.

To determine if one species was more likely than the other TD-DFT calculations were performed for each species shown in Figure 34 and compared with the experimental data. These showed that the species were all expected to have absorption bands in the

610-635 nm range (Figure 35, left), and these were similar to the experimental value of 611 nm for HATN-4Me-3CuBF$_4$ in CHCl$_3$ (Figure 28).

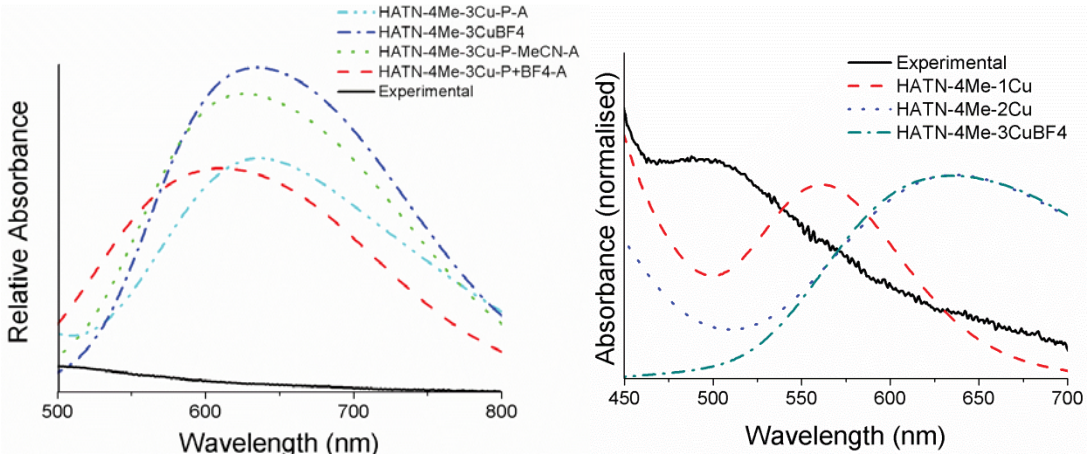

Figure 35 Left: Calculated MLCT bands for HATN-4Me-3CuBF$_4$ and its possible dissociation products in MeCN solution. Right:Calculated MLCT bands for HATN-4Me-1Cu, HATN-4Me-2Cu and HATN-4Me-3CuBF$_4$.

The more likely scenario is copper dissociation. A series of calculations was done for the HATN-4Me ligand attached to one [Cu(PPh$_3$)$_2$] unit giving HATN-4Me-1Cu, and to two [Cu(PPh$_3$)$_2$] units giving HATN-4Me-2Cu. It was found that the two and three copper centres have a similar absorbance at 637 nm but the one copper centre on HATN shifts the MLCT band to 562 nm which is closer to the experimental value making this the more likely compound, in a potentially complicated series of equilibria, to account for the shift (Figure 35, right). However, more work will be required to confirm or deny the proposal. TD-DFT calculations on the single copper HATN species with one triphenylphosphine, or one triphenylphosphine and one acetonitrile, or two HATNs attached to one copper centre, as well as FT-IR, FT-Raman and resonance Raman spectroscopies to see if there are any significant shifts in the vibration number associated with the copper nitrogen bond lability need to be performed.

5.6 Vibrational spectroscopy

FT-IR and Raman spectroscopy were used to study the vibrational behaviour of the complexes; all the spectra were dominated by the aromatic vibrational modes, thereby showing little difference between each complex.

The observed and calculated Raman spectra correlate well, with a mean absolute deviation of 18 cm^{-1} for the 1000-1600 cm^{-1} region for HATN-4Me-3CuBF$_4$ and 14 cm^{-1} for HATN-2Me-3CuBF$_4$. These values show that the calculations are accurate enough to draw information from (Appendix D). The representative FT-Raman spectra for these two complexes are shown below (Figure 36). The Raman spectra of HATN-4Me-3CuBF$_4$ and HATN-2Me-3CuBF$_4$ display typical normal modes for the HATN-3Cu-BF$_4$ complexes and are shown in Figure 37. These reveal that some of the vibrations, notably ca. 1400 cm^{-1} result in a significant perturbation of the central ring, which compresses while the other pyrazine rings expand, and vice versa. The peaks at ca. 1515 cm^{-1} and 1580 cm^{-1} have only small central and pyrazine ring contributions and consist predominantly of outer-ring vibrations. All spectra are similar due to the HATN core and only slight differences due to functional groups are found. (The vibrations are shown with PH_3 instead of PPh_3 as it allows the vibration arrows to be visible, the spectra of both are very similar as the shifts in this range are dominated by HATN, see Appendix D).

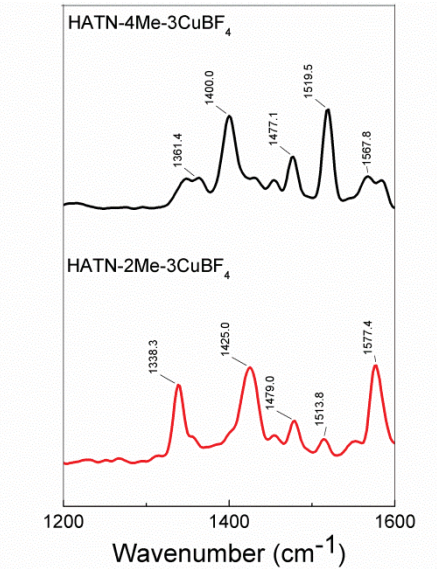

Figure 36 FT-Raman spectra of HATN-3Cu compounds.

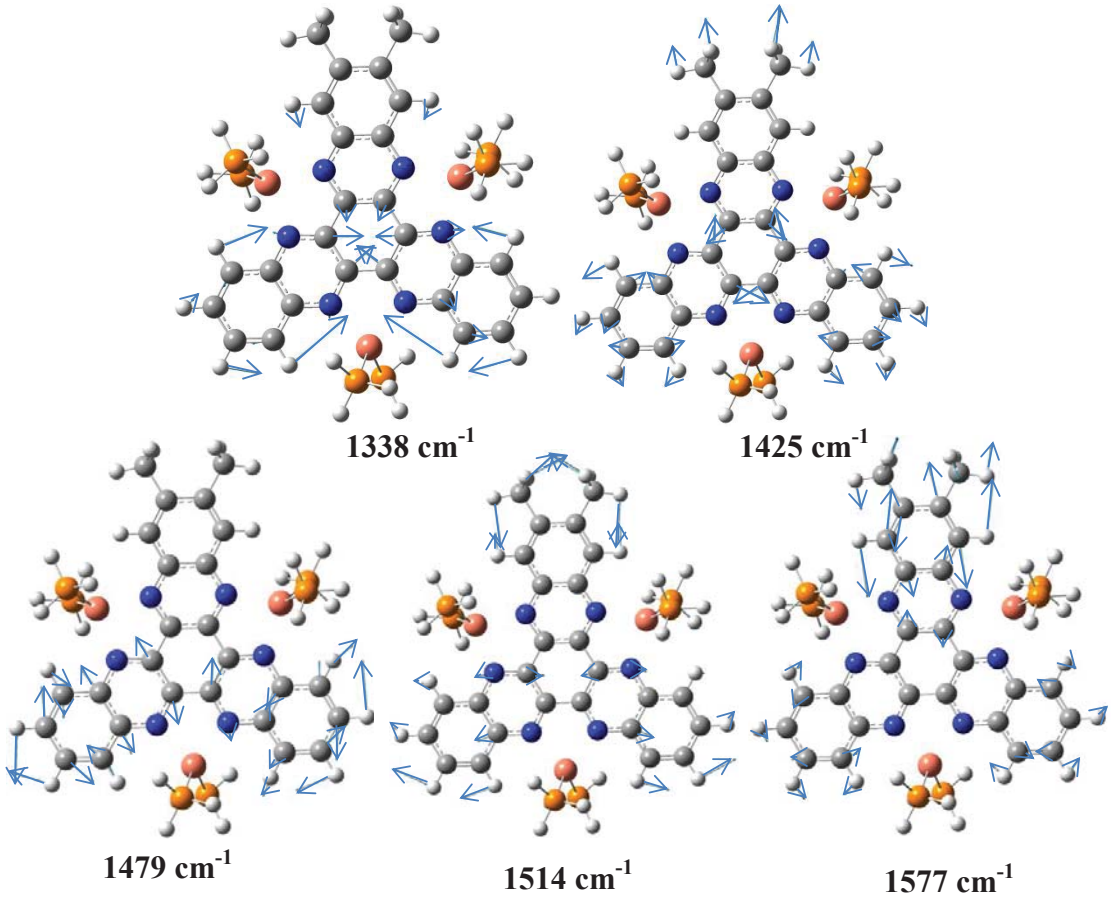

Figure 37 Raman frequency diagrams for HATN-2Me-3CuBF$_4$ (blue arrows indicate vibration direction). Calculation done on the PH$_3$ analogue of HATN-2Me-3CuBF$_4$.

The IR data (see Appendix D) are dominated by a broad set of peaks between 900-1100 cm^{-1}. There are only two other vibration peaks observed one at 750 cm^{-1} and the other at 694 cm^{-1} of which the 694 cm^{-1} does not change with the different ligands attached and is due to phenyl hydrogen wagging. The peak at 750 cm^{-1} is due to out of plane H-wagging on the phenyl groups while the higher numbered transitions (900-1100 cm^{-1}) in the broad peak are due to symmetric HATN distortions.

5.6.1 Resonance Raman Spectra

The electronic absorption spectrum of HATN-2Me-3CuBF$_4$ is dominated by two strong absorption peaks (~600 and 420 nm) and these are probed by exciting the complexes with lasers at 532 and 413 nm corresponding to the MLCT and π-π* absorption bands respectively (see Figure 38).

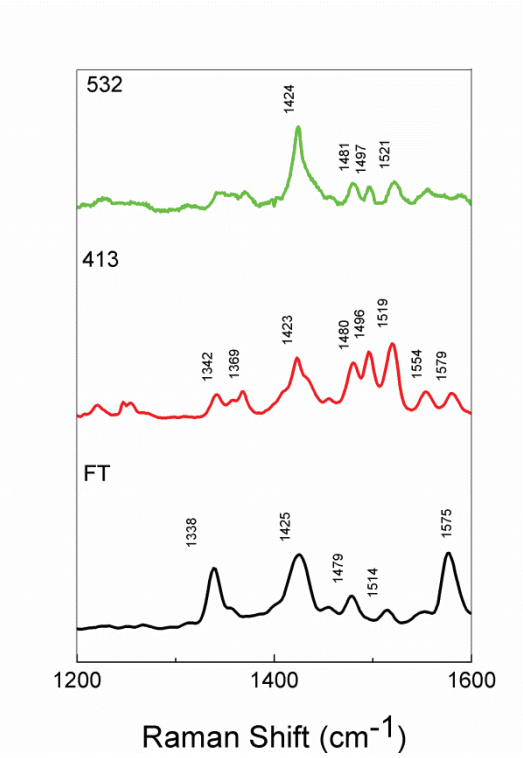

Figure 38 rR enhancements for HATN-2Me-3CuBF$_4$.

The notable Raman bands in the non-resonant spectrum lie at 1338, 1425, 1479, 1514 and 1575 cm^{-1}, while the spectrum with 413 nm excitation (Figure 38) shows enhancement of the vibrational modes at 1369, 1496, and 1521 and 1554 cm^{-1} as well as those peaks seen in the FT-Raman spectrum. The 532 nm excitation produces very similar results to the FT-Raman with only one extra peak at 1497 cm^{-1} being present. All these vibration frequencies have central ring perturbations to a varying degree with the peak at 1425 cm^{-1} being one of the strongest (Figure 39, the same peaks as FT-Raman were not reproduced and these can be seen in Figure 37). The peak at 1521 cm^{-1} has outer ring distortions while they all have H-wagging.

As the excitation wavelength is tuned to the red (413 nm), differing relative intensity patterns emerge such as the peaks between 1150-1160 cm^{-1}.

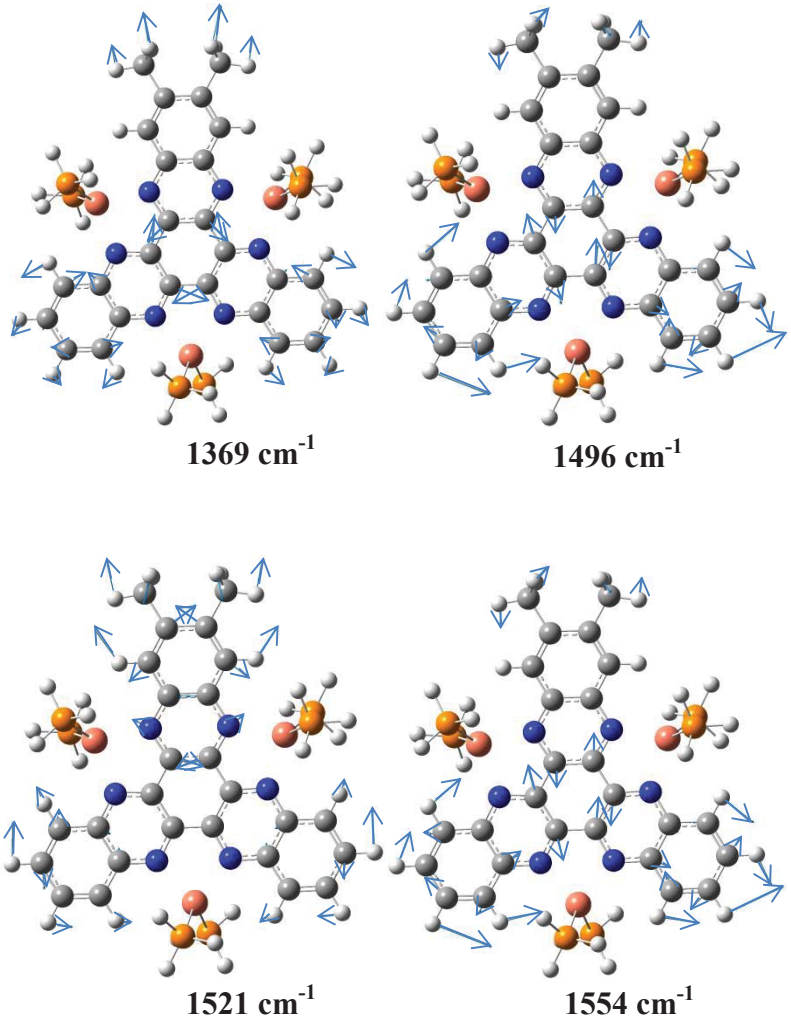

Figure 39 Raman frequency diagrams for rR enhancements using 413 nm excitation (blue arrows indicate stretching direction). The calculation was done on HATN-2Me-3Cu(PH_3)$_2$.

From the TD-DFT calculation it is evident that the dominant acceptor MO in one of the MLCT transitions is the LUMO. The LUMO has a very distinctive bonding/anti-bonding character in which the central ring is strongly bonded while the three attached pyrazine rings being anti-bonded with population of the orbital. If one examines the normal modes, it is clear that 1425 cm^{-1} strongly mimics the bonding changes that occur with the transition to the LUMO orbital. It compresses the central ring while stretching the pyrazines. Additionally, there are many modes that will to some degree reflect these structural changes resulting from LUMO population. The resonance peaks are mostly

influenced by outer ring distortions. (The vibrations are shown with PH_3 instead of PPh_3 groups attached to copper as it makes the shifts visible and the spectra of both are very similar as the shifts in this range are dominated by HATN, see Appendix D).

5.7 Conclusions

The electrochemical, electronic and vibrational behaviours of the HATN-1Re and HATN-2Re complexes were used to assess the coordination behaviour and physical properties of the complexes.

UV/Vis absorption spectra were employed to gain understanding of the hetero-HATN-1Re orbitals showing MLCT transitions in the range of 500-600 nm. This was similar to what was observed with the homo-substituted HATN rhenium complexes. The position of the rhenium atom in the hetero-HATN had little effect on the MLCT band. This suggests that the electron density introduced into the ligand upon excitation is similar for all isomers of hetero-HATN complexes. The addition of a second rhenium onto the ring red-shifts the MLCT band by ~100 nm.

The HATN-1Re vibrational spectra (Raman, r-Raman and IR) were found to consist of mainly outer ring distortions, with their IR spectra having solution resolved CO bands showing the presence of two types of CO positions (in plane and out of plane) confirming the rhenium HATN complexes are the facial isomers. This can be extended to include the HATN-2Re complexes. These vibrations also show that the electron density is located at the rings closest to the rhenium, regardless of functional groups. The Raman spectra show delocalised distortions within the HATN core which are similar for all compounds as the rings closest to the rhenium atoms are the most effected.

The ligand based first reduction potentials of five complexes (HATN-2Me-1ReA, HATN-2Br-1ReS, HATN-4Br2Me-1ReA, HATN-4Br2Me-2ReS) were measured by electrochemistry. It was found that all reduction potentials are similar with no obvious trend. The addition of a second rhenium atom also shifts the reduction potential anodically with HATN-4Br2Me-2ReS having a reduction potential of 0.02 V, a shift of ~+0.4 V from the similar mono-rhenium complex.

The electronic and vibrational behaviours of the HATN-3CuBF$_4$ complexes were used to assess the coordination behaviour and physical properties of the complexes. The Raman spectra of the HATN-3CuBF$_4$ complexes are similar due to the HATN core but there are small differences in their vibration frequencies due to the functional groups in the complexes.

UV/Vis spectra were employed to gain understanding of the HATN-3CuBF$_4$ orbitals showing MLCT transitions in the range of 550-650 nm in $CHCl_3$. These were successfully compared with calculated values of HATN-3CuBF$_4$. However, in MeCN the MLCT band was shifted to ca. 450 nm (the peak was hidden by other transitions near 450 nm). The structure of the HATN complexes in acetonitrile had not been described in literature. The colour change was found not to be attributed to a change in the copper oxidation state and is unlikely to be solvatochromism. The change in MLCT wavelength is most likely to be copper dissociation as this would account for both a lowering in absorption intensity and a blue-shift on changing the solvent from $CHCl_3$ to MeCN. Further work such as vibrational studies in acetonitrile and electrochemistry might help explain this phenomenon.

The FT-IR and FT-Raman data of each of the copper complexes are very similar due to the HATN core accounting for the majority of the vibrations. They displayed central ring perturbations which were enhanced at 532 and 413 nm excitation.

5.8 References

1 Roy, S.; Kubiak, C. P. *Dalton Transactions* **2010**, *39*, 10937.

2 Ghumaan, S.; Sarkar, B.; Patil, M. P.; Fiedler, J.; Sunoj, R. B.; Kaim, W.; Lahiri, G. K. *Polyhedron* **2007**, *26*, 3409.

3 Patra, S.; Sarkar, B.; Ghumaan, S.; Fiedler, J.; Kaim, W.; Lahiri, G. K. *Dalton Transactions* **2004**, 754.

4 Stufkens, D. J.; Vlček Jr, A. *Coordination Chemistry Reviews* **1998**, *177*, 127.

5 Hawecker, J.; Lehn, J.-M.; Ziessel, R. *Journal of the Chemical Society, Chemical Communications* **1984**, 328.

6 Sun, S.-S.; Tran, D. T.; Odongo, O. S.; Lees, A. J. *Inorganic Chemistry* **2001**, *41*, 132.

7 Lakowicz, J. R.; Castellano, F. N.; Gryczynski, I.; Gryczynski, Z.; Dattelbaum, J. D. *Journal of Photochemistry and Photobiology A: Chemistry* **1999**, *122*, 95.

8 Fraser, M. G.; Clark, C. A.; Horvath, R.; Lind, S. J.; Blackman, A. G.; Sun, X.-Z.; George, M. W.; Gordon, K. C. *Inorganic Chemistry* **2011**, *50*, 6093.

9 Krahmer, J.; Beckhaus, R.; Saak, W.; Haase, D. *Zeitschrift für anorganische und allgemeine Chemie* **2008**, *634*, 1696.

10 Roy, S.; Sarkar, B.; Duboc, C.; Fiedler, J.; Sarper, O.; Lissner, F.; Mobin, S. M.; Lahiri, G. K.; Kaim, W. *Chemistry – A European Journal* **2009**, *15*, 6932.

11 Lind, S. J.; Walsh, T. J.; Blackman, A. G.; Polson, M. I. J.; Irwin, G. I. S.; Gordon, K. C. *The Journal of Physical Chemistry A* **2009**, *113*, 3566.

12 Suppan, P. *Journal of Photochemistry and Photobiology A: Chemistry* **1990**, *50*, 293.

13 Coolidge, A. S.; James, H. M.; Present, R. D. *The Journal of Chemical Physics* **1936**, *4*, 193.

14 Dias, H. V. R.; Diyabalanage, H. V. K.; Rawashdeh-Omary, M. A.; Franzman, M. A.; Omary, M. A. *Journal of the American Chemical Society* **2003**, *125*, 12072.

15 Smith, E.; Dent, G. *Modern Raman spectrosopy: a practical approach*; John Wiley and Sons Ltd: England, 2005.

16 Petry, R.; Schmitt, M.; Popp, J. *ChemPhysChem* **2003**, *4*, 14.

17 Placzek, G. *Handbuch der radiologie. Rayleigh-streuung und Raman-effekt*; Academische Verlag: Leipzig, 1934; Vol. 6.

18 McCreery, R. L. *Raman spectroscopy for chemical analysis. A series of monographs of analytical chemisty and its applications*; Wiley Interscience: New York, 2000; Vol. 157.

19 Skoog, D. A.; Holler, F. J.; Crouch, S. R. *Principles of Instrumental Analysis*; 6th ed.; Thomson Brooks/Cole: Belmont, 2007.

20 Schrader, B. *Infrared and Raman spectroscopy: methods and application*; VCH: Weinheim, 1995.

21 Khanna, R. K.; Stranz, D. D.; Donn, B. *The Journal of Chemical Physics* **1981**, *74*, 2108.

22 Siriwardane, U. (2012). "Chapter 4. Molecular Symmetry ". from http://www.chem.latech.edu/~upali/chem481/chem481c4.html.

23 Frisch, M. J. G. W. T., B.; Schlegel, H.B.; Scuseria, G. E.; Robb, M. A.; Cheeseman, J. R.; Scalmani, G.; Barone, V.; Pattersson; A.1 ed ed.; Gaussian, Inc: Wallingford CT: 2009.

24 Dennington, R. K., T.; Millam, J.; *Semichem Inc.: Sawnee Mission KS*, 2009; Vol. Version 5 ed.

25 Pettinari, C.; Marchetti, F.; Polimante, R.; Cingolani, A.; Portalone, G.; Colapietro, M. *Inorganica Chimica Acta* **1996**, *249*, 215.

26 Park, G.; Yang, H.; Kim, T. H.; Kim, J. *Inorganic Chemistry* **2010**, *50*, 961.

27 Chen, C.-T.; Lin, T.-Y. J.; Chen, C.-H.; Lin, K.-J. *Journal of the Chinese Chemical Society* **2000**, *47*, 197.

6.0 Conclusion and final remarks

This project had two main objectives:

i) To create a general method of synthesis for hetero-substituted hexaazatrinapthalene (hetero-HATN) compounds and to use this method to undertake the synthesis of a 'set' of HATNs with varying combinations of functional groups such as bromo, methyl and hydrogen.

ii) To study the coordination behaviours of hetero-HATNs with a selection of transition metals. To carry out physical measurements on the HATN ligands as well as their corresponding complexes using UV/Vis, Raman and IR spectroscopies and electrochemistry.

To this end, two synthetic methods were established to produce hetero-HATNs(see Figure 1). Both methods used rhodizonic acid (RDA) as a starting material from which one or two diaminobenzene (DAB) derivatives could be added (route i and route ii respectively) followed by the oxidation of the hydroxyl groups allowing the addition of the final two or one diaminobenzene derivatives. Both routes are necessary as this allows the addition of one or two diaminobenzene derivatives with sensitive functional groups into the HATN as desired. Another two methods were investigated, the first using tetrahydroxy-p-quinone and the second hexaketocyclohexane but these pathways do not allow the control RDA affords. Route i was used to synthesise HATN-4Me, HATN-4Br, HATN-2Me, HATN-2Br, HATN-4Me2Br and HATN-4Br2Me and Route ii for HATN-4Me1CN and HATN-1CN. The inclusion of bromo functionalities is important as this can enable future reactions of the hetero-substituted HATNs. An example of this is Sonogashira coupling or Suzuki reaction.

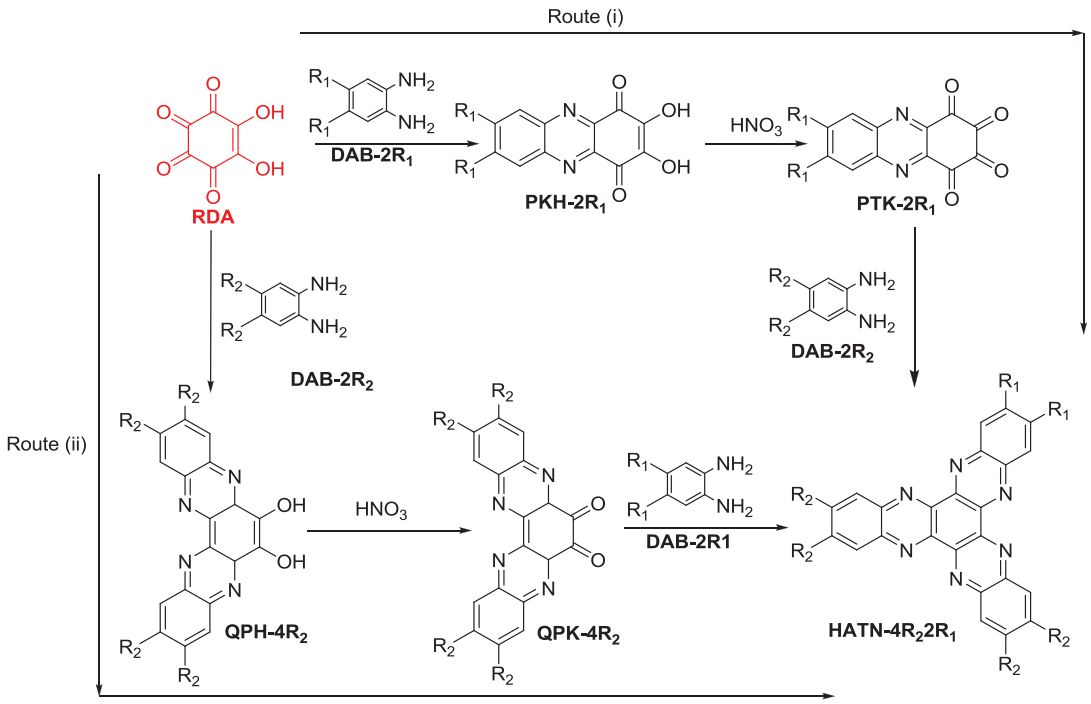

Figure 1 Synthetic pathways for the synthesis of hetero-HATNs.

The crystal structures for the 6,7-dimethyl-2,3-dihydroxy-phenazine-1,4-dione and the 6,7-dimethyl-1,2,3,4-phenazinetetrone were obtained showing the environment of germinal diols and diones. The crystal structure of HATN-4Me was also obtained showing its planar aromatic structure.

UV/Vis spectroscopy was carried out for the six ligands (HATN-4Me, HATN-4Br, HATN-2Me, HATN-4Br2Me, HATN-2Br, HATN-4Me2Br) showing they had very little absorbance in the visible range. IR and Raman spectra displayed standard vibrations. Electrochemistry was done for the HATN compounds and found they all had approximately the same HOMO value (0.9V). This data was used to show that these ligands did not have ideal HOMO and LUMO energy levels for standard dye-sensitised-solar cells. However, they could be suited to hetero-junction solar cells as an n-transporter.

Six ligands (HATN-4Me, HATN-4Br, HATN-2Me, HATN-4Br2Me, HATN-2Br, and HATN-4Me2Br) were tested for use in Field Effect Transistors (FET). It was found that

only two, HATN-4Me and HATN-4Br, had a FET-like response. These results showed that HATN-4Br had an electron mobility of 8.13 $x10^{-4}$ $cm^2V^{-1}s^{-1}$ while HATN-4Me had an electron mobility of 5.38 $x10^{-5}$ $cm^2V^{-1}s^{-1}$. This shows that the electron withdrawing group increased the electron mobility in these devices. Both had high resistances of 107 MΩ and 1.23 GΩ, respectively. The solution processed FETs also had high resistances ranging between 740 kΩ and 54 MΩ and did not exhibit FET behaviour. This means they are not suitable for FET devices but could be useful as organic resistors or possibly semi-conductors.

The electrochemical, electronic and vibrational behaviours of the HATN-1Re and HATN-2Re complexes were used to assess the coordination behaviour and physical properties of the complexes.

UV/Vis absorption spectra were employed to gain understanding of the hetero-HATN-1Re orbitals showing MLCT transitions in the range of 500-600 nm. This was similar to what was observed with the homo-substituted HATN rhenium complexes. The position of the rhenium atom in the hetero-HATN had little effect on the MLCT band. This suggests that the electron density introduced into the ligand upon excitation is similar for all isomers of hetero-HATN complexes. The addition of a second rhenium onto the ring red-shifts the MLCT band by ~100 nm.

The HATN-1Re vibrational spectra (Raman and IR) were found to consist of mainly outer ring distortions, with their IR spectra having solution resolved CO bands showing the presence of two types of CO positions (in plane and out of plane) confirming the rhenium HATN complexes are the facial isomers. This can be extended to include the HATN-2Re complexes. These vibrations also show that the electron density is located at the rings closest to the rhenium, regardless of functional groups. The Raman spectra show delocalised distortions within the HATN core which are similar for all compounds as the rings closest to the rhenium atoms are the most effected.

The ligand based first reduction potentials of five complexes (HATN-2Me-1ReA, HATN-2Br-1ReS, HATN-4Br2Me-1ReA, HATN-4Br2Me-2ReS) were measured by electrochemistry. It was found that the HATN-1Re complexes all had similar reduction potentials with no obvious trend. The addition of a second rhenium atom also shifts the reduction potential anodically with HATN-4Br2Me-2ReS having a reduction potential of 0.02 V, a shift of ~+0.4 V from the similar mono-rhenium complex.

Palladium chemistry was briefly investigated by studying the coordination of $[PdCl_2(benzonitrile)_2]$ with HATN-4Me. The S isomer of palladium was formed in a higher ratio than the A isomer, even though statistically the opposite is expected. From this observation it is reasonable to expect that hetero-HATNs seem to favour S isomer formation and this could extend to other metals. The palladium complex was successfully synthesised but separation of the isomers could not be achieved.

The copper complexes were prepared by the addition of in a 3:1 ratio with each of the HATN ligands (HATN-4Me, HATN-4Br, HATN-2Me, HATN-4Br2Me, HATN-2Br, HATN-4Me2Br) and $[Cu(MeCN)_2(PPh_3)_2]BF_4$ to give general the stoichiometry of HATN-3{$[Cu(PPh_3)_2]BF_4$}. HATN-4Me was also successfully coordinated to $[Cu(MeCN)_2(P(PPh_3)_2]ClO_4$ and crystallography showed that the perchlorate anion dislodged a triphenylphosphine entity to take its place to form [HATN-4Me-$(Cu(PPh_3)_2)_2$-$Cu(PPh_3)ClO_4$]$2ClO_4$.

The HATN copper complexes showed very broad absorptions for their MLCT band with a change of only 12 nm between the variously substituted HATNs. This data along with calculations were used to gain understanding of HATN-3$CuBF_4$ orbitals in chloroform. However, in acetonitrile the MLCT band was shifted to ca. 450 nm. The structure of HATN complexes in acetonitrile had not been described in literature. The colour change was found not to be attributed to a change in the copper oxidation state and is unlikely to be solvatochromism. It is unlikely that dissociation of the phosphine with/without coordination of the anion or solvent could account for the shift. The change in MLCT wavelength is likely due to be copper dissociation by loss of two

copper centres as this would account for both a lowering in absorption intensity and a blue-shift on changing the solvent from $CHCl_3$ to MeCN.

Future studies would involve the addition of other functional groups to the HATN core. This could be done by using the bromo functionality to build on an already complete hetero-substituted HATN or by adding the functional groups in during hetero-substituted HATN synthesis. Due to the lack of solubility of HATNs adding in solubilising groups such as alkyl chains could improve this behaviour.

The synthesis of multi-rhenium HATN complexes would be done as well as a study of their physical properties. This could be extended to mixed metal complexes where rhenium and palladium or rhenium and manganese or rhenium and copper(II) HATN compounds could be synthesised. The synthesis of multi-metal HATNs would also lead on to the study of metal communication.

To gain further understanding of the HATN copper complexes in acetonitrile, their vibrational measurements could be carried out in that solvent. This could aid the understanding of the species involved in this solution and check that dissociation of copper is a valid conclusion to arrive at. The preparation of the 1:1 HATN copper complexes in acetonitrile would also be attempted.

In conclusion, it was found that the hetero-HATNs can be made by following one of two routes using rhodizonic acid. They are able to react with a range of transition metals including rhenium, palladium and copper. The hetero-HATN rhenium complexes show delocalised behaviour in their MLCT band.

Chapter 7

Synthesis

7.0 Abbreviations used in Chapter 7

HATN	5,6,11,12,17,18-hexaazatrinaphthalene
PKH	2,3-dihydroxy-phenazine-1,2-tetrone
PTK	1,2,3,4-phenazinetetrone
RDA	Rhodizonic acid
QPK	Quinoxalineo[2,3-a]phenazine-6,7-dione
MP	Melting point
NMR	Nuclear magnetic resonance
HRMS	High resolution mass spectrometry
AcOH	Acetic acid
ESI-MS	Electrospray ionisation mass spectrometry
$CDCl_3$	Deuterated chloroform
Tol	Toluene
MeCN	Acetonitrile
MeOH	Methanol

7.1 General

All reagents (unless otherwise stated) were purchased from standard chemical suppliers and were used without further purification. Dry degassed DCM was prepared by distilling AR grade off CaH_2 under a N_2 atmosphere. Dry MeOH was prepared by refluxing in Mg turnings and iodine followed by distillation. Dry toluene, ether, and THF were prepared by passing argon-degassed solvent through activated alumina columns.

Chromatography was performed with 230-400 mesh silica gel 60 (SDS) using lab grade reagents which had been distilled. The silica gel slurry was compacted with the specified solvent system of hexanes/ EtOAc or CH_2Cl_2 / MeOH. The compound was then loaded onto the column and eluted with the specified solvent under positive pressure.

NMR data were recorded on a Bruker Avance 400, a Bruker Avance 500, and a Bruker Avance 700 spectrometers. Chemical shifts are relative to TMS or the residual protium in deuterated solvents ($CDCl_3$, 7.26 ppm; DMSO-d_6 2.50 ppm) when TMS is not present. ^{13}C NMR chemical shifts are relative to $CDCl_3$ (77.0 ppm). All NMR data was collected at 25 ˚C.

Melting Point (MP) determinations were performed on a Cambridge Instruments Kofler hot-stage (calibration standards employed).

MALDI-TOF MS were performed on a Micromass ProteomeWorks M@LDI-Reflectron mass spectrometer, fitted with a 337 nm nitrogen UV laser. Electrospray mass spectra were recorded on a Micromass ZMD spectrometer run in positive ion mode.

High resolution MALDI-TOF mass spectra were recorded on a Bruker Daltonics Autoflex spectrometer at Waikato University.

Elemental analyses were provided by the Campbell Microanalytical Laboratory, University of Otago.

7.2 Synthesis

7.2.1 Chapter 2 compounds

PTK-2Me

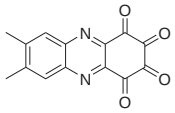

7,8-dimethyl-2,3-dihydroxy-phenazine-1,2-tetrone (PKH-2Me) was made by altering a literature procedure.[1] Sufficient fuming HNO_3 was added to 6,7-dimethyl-1,2,3,4-tetrahydroxyphenazine (PTH-2Me) to cover the solid material (300 mg, 1.10 mmol) and left to sit until vapours ceased being formed. Dioxane (15 mL) was then added and the solvent was removed under reduced pressure to give a precipitate which was filtered to give faint yellow crystals.

Yield: 190 mg (85%). MP 172 ˚C. ^{1}H NMR (400 MHz, DMSO): 8.15 (s, 2H, Ar-*H*) 2.57 (s, 6H, Me-*H*). ^{13}C NMR (100 MHz, DMSO): 191.6, 145.8, 145.4, 142.1, 129.2, 96.6, 20.6. HRMS: 273.15 $[M+H]^{+}$.

PKH-2Br

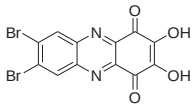

4,5-dibromo-1,2-diaminobenzene (235 mg, 0.884 mmol) in 10% AcOH (120 mL) was added drop-wise to a stirred solution of rhodizonic acid (RDA) (200 mg, 0.907 mmol) in 100 mL of H_2O. Upon completion of the addition the mixture was stirred for a further 1.5 h and the product was filtered to give an orange solid.

Yield: 211 mg (74%). MP 250 ˚C. ^{1}H NMR (500 MHz, DMSO): 8.73 (s, 2H, Ar-*H*). ^{13}C NMR (125 MHz, $CDCl_3$): 177.5, 145.9, 144.9, 141.8, 134.5, 128.9. Anal. Calcd. For $C_{12}H_2N_6Br_2O_4 \cdot 2H_2O$; C, 33.21; H, 1.39; N, 6.56 %. Found C, 33.16; H, 1.41; N, 6.65 %. HRMS: 400.96 $[M+H]^{+}$.

PTK-2Br

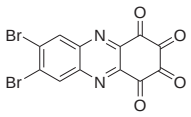

Sufficient fuming HNO_3 was added to 6,7-dibromo-2,3-dihydroxyphenazine-1,2-dione PKH-2Br to cover the solid material (260 mg, 0.650 mmol) and left to sit until vapours ceased being formed. H_2O was then added and the precipitate which was filtered to give a yellow solid as the product.

Yield: 217.4 mg (81%). MP 166 ˚C, ^{1}H NMR (400 MHz, DMSO): 8.86 (s, 2H, Ar-*H*). ^{13}C NMR (125 MHz, DMSO): 190.8, 146.8, 142.3, 134.8, 130.5, 96.7. HRMS: 402.89 $[M+3H]^{+}$. $C_{12}H_4N_6Br_2O_4 \cdot 1.5H_2O$; C, 33.75; H, 1.65; N, 6.56 %. Found C, 33.83; H, 1.46; N, 6.76 %.

QPK-4Me

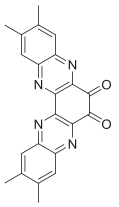

RDA (100 mg, 0.467 mmol) in degassed H_2O (25 mL) was heated to 100 ˚C. 4,5-dimethyl-1,2-diaminobenzene (95.4 mg, 0.700 mmol) was dissolved in degassed 10% AcOH (100 mL) and added to RDA via a dropping funnel over 30 mins. The mixture was left to stir a further 1.5 h, then filtered and the dark solid had fuming nitric acid added to cover it. H_2O was added to dilute the mixture and the precipitated yellow solid collected by filtration. The mixture was recrystallised in dioxane.

Yield: 50.2 mg (39%). MP > 250 ˚C. ^{1}H NMR (400 MHz, $CDCl_3$): 8.16 (s, 2H, Ar-*H*), 8.11 (s, 2H, Ar-*H*) 2.61 (s, 6H, C-H_3), 2.59 (s, 6H, C-H_3). ^{13}C NMR (125 MHz, $CDCl_3$): 178.1, 147.0, 146.2, 144.8, 143.7, 142.5, 142.0, 130.0, 129.5, 21.0, 20.7.

HATN-4Me1CN

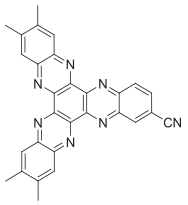

4-cyano-1,2-diaminobenzene (100 mg, 0.751 mmol) dissolved in minimum amount of 10% acetic acid in chloroform was added to 2,3-10,11-tetramethyl-quinoxalino[2,3-a]phenazine-6,7-dione (QPK-4Me) in minimum amount of DMSO and left to sonicate for four hours. The solution was filtered and the precipitate was collected. The solid was sonicated in chloroform and collected by filtration to yield the product as a yellow solid.

Yield: 227.2 mg (65 %). MP > 250 ˚C. ^{1}H NMR (500 MHz, $CDCl_3$): 8.99 (s, 1H, Ar-*H*), 8.70 (d, 1H, *J*=8.4 Hz, Ar-*H*), 8.49 (s, 1H, Ar-*H*), 8.48 (s, 1H, Ar-*H*), 8.45 (s, 2H, Ar-*H*), 8.30 (d, 1H, *J*=8.2 Hz, Ar-*H*), 2.78 (s, 12H, C-H_3). ^{13}C NMR (175 MHz, $CDCl_3$): 145.6, 145.2, 144.5, 144.4, 144.2, 144.0, 143.9, 143.5, 143.4, 143.4, 143.2, 143.1, 143.0, 142.6, 142.1, 141.7, 136.5, 132.1, 131.8, 131.7, 130.6, 129.3, 129.3, 117.8, 115.0, 20.9, 20.9, 20.8, 20.8. MALDI: 467.7 $[M+2H]^{+}$. Anal. Calcd. For $C_{29}H_{19}N_7 \cdot 2H_2O$; C, 69.45; H, 4.62; N, 19.55 %. Found C, 69.46; H, 4.26; N, 19.51 %. FT-R (cm^{-1}): 735, 1363, 1400, 1452, 1477, 1517, 1561, 1616, 2229. FT-IR (cm^{-1}): 839, 876, 1022, 1088, 1209, 1362, 1450, 1481, 1514, 1630, 2231.

HATN-1CN

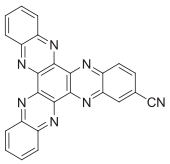

HATN-1CN was synthesised by analogy to the procedure for HATN-4Me1CN except quinoxalino[2,3-a]phenazine-6,7-dione (QPK) was used in place of QPK-4Me. The product was a yellow-green solid. The solid was sonicated in chloroform and collected by filtration to yield the product as a yellow solid.

Yield: 199.8 mg (68 %). MP > 250 ˚C. ^{1}H NMR (700 MHz, $CDCl_3$): 9.08 (d, 1H, *J*=1.6 Hz, Ar-*H*), 8.80 (d, 1H, *J*=8.2 Hz, Ar-*H*), 8.71 (m, 4H, Ar-*H*), 8.15 (dd, 1H, *J*=8.5 Hz, *J*=1.8 Hz, Ar-*H*), 8.09 (m, 4H, Ar-*H*). ^{13}C NMR (175 MHz, $CDCl_3$):145.6, 145.2, 144.4, 143.9, 143.9, 143.9, 143.7, 143.6, 142.7, 142.3, 136.6, 133.0, 132.9, 132.7, 132.7, 132.2, 132.2, 130.7, 117.7, 115.5. HRMS: 410.25 $[M+H]^+$. Anal. Calcd. For $C_{25}H_{11}N_7 \cdot 2H_2O$; C, 67.41; H, 3.39; N, 22.01 %. Found C, 67.05; H, 3.13; N, 21.95 %. FT-R (cm^{-1}): 808, 1363, 1402, 1520, 1364, 1479, 1565. FT-IR (cm^{-1}): 758, 839, 1080, 1134, 1363, 1493, 2233.

HATN-4Me

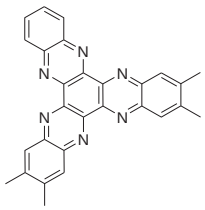

4,5-dimethyl-1,2-diaminobenzene (52 mg, 0.38 mmol) was dissolved in minimum amount of 10% acetic acid in chloroform and added to 1,2,3,4-phenazinetetrone (36 mg, 0.15 mmol) in minimum amount of DMSO and left to sonicate for four hours. The solid was sonicated in chloroform and collected by filtration to yield a yellow-green solid. The solid was recrystallized in a chloroform/ether mixture.

Yield: 42.3 mg (64%). MP > 250 ˚C. ^{1}H NMR (500 MHz, $CDCl_3$): 8.67 (dd, 2H, *J*=8.3 Hz, *J*=6.5 Hz, Ar-*H*), 8.41 (s, 4H, Ar-*H*), 8.02 (dd, 2H, *J*=3.4 Hz, *J*=6.61 Hz, *Ar*-H), 2.64 (s, 12H, C-*H*$_3$). ^{13}C NMR (125 MHz, $CDCl_3$): 143.7, 143.6, 143.4, 143.4,142.9, 142.7, 142.6, 142.5, 131.9, 130.6, 129.3, 129.3, 20.8, 20.8. HRMS: 442.36 $[M+2H]^+$. Anal. Calcd. For $C_{28}H_{20}N_6 \cdot 0.5H_2O$; C, 74.82; H, 4.71; N, 18.70 %. Found C, 74.68; H, 4.44; N, 18.58 %. FT-R (cm^{-1}): 1364, 1400, 1477, 1518. FT-IR (cm^{-1}): 762, 870, 1003, 1022, 1085, 1134, 1214, 1363, 1450, 1477, 1490, 1631.

HATN-4Br

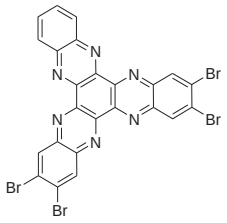

HATN-4Br was synthesised by analogy to the procedure for HATN-4Me except 4,5-dibromo-1,2-diaminobenzene was used in place of 1,2-diaminobenzene. The product was a yellow-green solid. The solid was recrystallized in a chloroform/ether mixture.

Yield: 79.8 mg (76%). MP > 250 ˚C. ^{1}H NMR (500 MHz, $CDCl_3$): 9.03 (s, 2H, Ar-*H*), 9.01 (s, 2H, Ar-*H*) 8.65 (m, 2H, Ar-*H*) 8.01 (m, 2H, Ar-*H*). HRMS: 702.00 $[M+2H]^+$. Anal. Calcd. For $C_{24}H_8Br_4N_6 \cdot 2.5H_2O$; C, 38.69; H, 1.76; N, 11.28 %. Found C, 38.63; H, 1.39; N, 10.84 %. FT-R (cm^{-1}): 1390, 1440, 1520, 1553. FT-IR (cm^{-1}): 761, 881, 943, 1085, 1134, 1174, 1352, 1394, 1444, 1483, 1518, 1720.

HATN-2Me

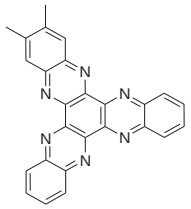

HATN-2Me was synthesised by analogy to the procedure for HATN-4Me except 1,2-diaminobenzene was used in place of 4,5-dimethyl-1,2-diaminobenzene and 6,7-dimethyl-1,2,3,4-phenazinetetrone was used in place of 1,2,3,4-phenazinetetrone. The product was a yellow-green solid. The solid was recrystallized in a chloroform/ether mixture.

Yield: 15.5 mg (25 %). MP > 250 ˚C. ^{1}H NMR (500 MHz, $CDCl_3$): 8.68 (m, 4H, *J*=8.3 Hz, Ar-*H*), 8.43 (s, 2H, Ar-*H*), 8.03 (m, 4H, Ar-*H*), 2.67 (s, 6H, C*H*$_3$). ^{13}C NMR (125 MHz, $CDCl_3$): 143.8, 143.6, 143.4, 142.8, 132.1, 132.0, 130.6, 130.6, 129.3, 20.8. HRMS: 414.36 $[M+2H]^+$. Anal. Calcd. For $C_{26}H_{16}N_6 \cdot 0.5CHCl_3$; C, 67.41; H, 3.52; N, 17.80 %. Found C, 67.15; H, 3.58; N, 17.87 %. FT-R (cm^{-1}): 1364, 1402, 1476, 1521, 1563. FT-IR (cm^{-1}): 755, 862, 1083, 1134, 1214, 1361, 1452, 1492, 1518, 1630.

HATN-4Br2Me

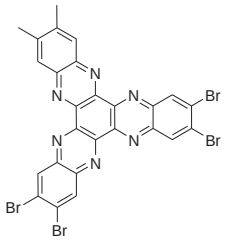

HATN-4Br2Me was synthesised by analogy to the procedure for HATN-4Me except 3,4-dibromo-1,2-diaminobenzene was used in place of 4,5-dimethyl-diaminobenzene and 6,7-dimethyl-1,2,3,4-phenazinetetrone was used in place of 1,2,3,4-phenazinetetrone. The product was a yellow-green solid. The solid was recrystallized in a chloroform/ether mixture.

Yield: 51.3 mg (47 %). MP > 250 ˚C. ^{1}H NMR (500 MHz, $CDCl_3$): 8.99 (s, 2H, Ar-*H*), 8.96 (s, 2H, Ar-*H*), 8.38 (s, 2H, Ar-*H*), 2.66 (s, 6H, C*H*$_3$). HRMS: 729.09 $[M+H]^+$. Anal. Calcd. For $C_{26}H_{12}Br_4N_6 \cdot 1.25CHCl_3 \cdot 0.5DMSO$; C, 37.77; H, 1.79; N, 9.19 %. Found C, 37.66; H, 2.27; N, 9.03 %. FT-R (cm^{-1}): 1390, 1439, 1477, 1515, 1555. FT-IR (cm^{-1}): 881, 874, 941, 1092, 1180, 1356, 1443, 1477.

HATN-2Br

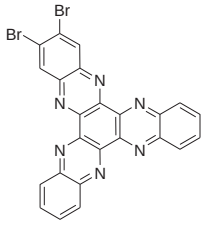

HATN-2Br was synthesised by analogy to the procedure for HATN-4Me except 1,2-diaminobenzene was used in place of 4,5-dimethyl-diaminobenzene and 6,7-dibromo-1,2,3,4-phenazinetetrone was used in place of 1,2,3,4-phenazinetetrone. The product was a yellow-green solid. The solid was recrystallized in a chloroform/ether mixture.

Yield: 20.3 mg (25 %). MP > 250 ˚C. ^{1}H NMR (500 MHz, $CDCl_3$): 9.03 (s, 2H, Ar-*H*), 8.67 (m, 4H, Ar-*H*), 8.06 (m, 4H, Ar-*H*). ^{13}C NMR (175 MHz, $CDCl_3$): 144.4, 143.7, 143.6, 143.6, 142.9, 142.4, 134.3, 132.7, 132.6, 130.7, 130.6, 129.7. HRMS: 543.55 $[M+2H]^+$. Anal. Calcd. For $C_{24}H_{10}Br_2N_6 \cdot 3H_2O$; C, 48.35; H, 2.70; N, 14.10 %. Found C, 48.33; H, 2.22; N, 13.59 %. FT-R (cm^{-1}): 1363, 1398, 1438, 1469, 1519, 1564. FT-IR (cm^{-1}): 760, 884, 935, 972, 1082, 1133, 1178, 1342, 1362, 1401, 1438, 1489, 1715.

HATN-4Me2Br

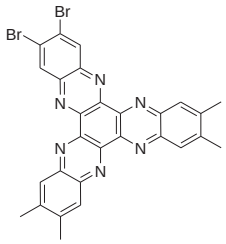

HATN-4Me2Br was synthesised by analogy to the procedure for HATN-4Me except 4,5-dimethyl-1,2-diaminobenzene was used in place of 4,5-dimethyl-diaminobenzene and 6,7-dimethyl-1,2,3,4-phenazinetetrone was used in place of 1,2,3,4-phenazinetetrone. The product was a yellow-green solid. The solid was recrystallized in a chloroform/ether mixture.

Yield: 40.4 mg (45 %). MP > 250 ˚C.^{1}H NMR (500 MHz, $CDCl_3$): 8.98 (s, 2H, Ar-*H*), 8.40 (s, 2H, Ar-*H*), 8.37 (s, 2H, Ar-*H*), 2.65 (s, 12H, C*H*$_3$). ^{13}C NMR (175 MHz, $CDCl_3$): 144.5, 144.2, 143.8, 142.9, 142.9, 142.6, 142.2, 141.9, 134.2, 129.3, 129.1, 20.9, 20.8. HRMS: 600.27 $[M+2H]^+$. Anal. Calcd. For $C_{28}H_{18}Br_2N_6 \cdot 1.25H_2O$; C, 54.17; H, 3.33; N, 13.54 %. Found C, 54.05; H, 3.17; N, 13.35 %. FT-R (cm^{-1}): 1363, 1392, 1450, 1474, 1520, 1558. FT-IR (cm^{-1}): 732, 871, 921, 960, 1001, 1023, 1091, 1181, 1206, 1361, 1441, 1484, 1513, 1628, 1714.

HATN-4Me1COOH

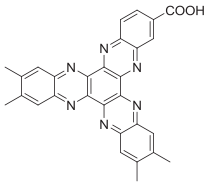

HATN-4Me1COOH was synthesised by analogy to the procedure for HATN-4Me except 6-carboxy-1,2,3,4-phenazinetetrone[1] was used in place of 1,2,3,4-phenazinetetrone. The solid was sonicated in chloroform and collected by filtration to yield a yellow-green solid.

Yield: 56.5 mg (35 %). MP > 250 ˚C. ^{1}H NMR (500 MHz, $CDCl_3$): 10.20 (s, 1H, COO-*H*) 9.44 (s, 2H, Ar-*H*), 8.72 (s, 2H, Ar-*H*), 8.61 (s, 2H, Ar-*H*), 8.48(s, 2H, Ar-*H*), 8.48 (s, 2H, Ar-*H*), 8.47(s, 2H, Ar-*H*), 8.46 (s, 2H, Ar-*H*) 2.99 (s, 12H, C*H*$_3$). MALDI: 486.1 $[MH]^+$ Anal. Calcd. For $C_{29}H_{20}N_6O_2 \cdot 1.25H_2O$; C, 68.70; H, 4.47; N, 16.58 %. Found C, 68.44; H, 4.41; N, 16.26 %. FT-IR (cm^{-1}): 752, 876, 1005, 1088, 1132, 1161, 1217, 1362, 1450, 1483, 1514, 1720.

HATN-1COOH

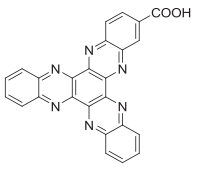

HATN-1COOH was synthesised by analogy to the procedure for HATN-4Me except 1,2-diaminobenzene was used in place of 4,5-dimethyl-1,2-diaminobenzene and 6-carboxy-1,2,3,4-phenazinetetrone was used in place of 1,2,3,4-phenazinetetrone. The solid was sonicated in chloroform and collected by filtration to yield a yellow-green solid.

Yield: 30.0 mg (21 %). MP > 250 ˚C.^{1}H NMR (500 MHz, $CDCl_3$): 8.95 (s, 1H, Ar-*H*), 8.61 (d, 1H, Ar-*H*), 8.54 (m, 6H, Ar-*H*), 8.12 (m, 4H, Ar-*H*). MALDI: 430.0 $[M+2H]^+$. Anal. Calcd. For $C_{25}H_{12}N_6O_2 \cdot 0.75H_2O$; C, 67.95; H, 3.08; N, 19.02 %. Found C, 68.11; H, 3.03; N, 19.21 %. FT-IR (cm^{-1}): 758, 952, 1020, 1076, 1128, 1139, 1161, 1362, 1490, 1722.

7.2.2 Chapter 4 compounds

HATN-2Me-2ReS and HATN-2Me-1ReA

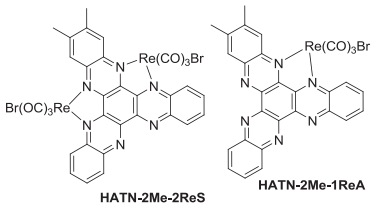

Rheniumpentacarbonyl bromide (34.8 mg, 0.086 mmol) is added to HATN-2Me (35.8 mg, 0.0867 mmol) in 15 mL dry toluene (Tol) and left to stir under Ar overnight. The solvent is then removed under reduced pressure. The compounds were then re-dissolved in toluene and purified by chromatography (CH_2Cl_2/MeOH). The di-rhenium compounds elute first. The mono-rhenium isomers separate into two close bands and elute after the di-rhenium compounds. Consecutive columns are required for purification of all rhenium complexes. The solid was recrystallized in a chloroform/ether mixture.

HATN-2Me-2ReS

Dark green solid. Yield: 8.4 mg (13%). R_f = 0.83(95:5 CH_2Cl_2 / MeOH). MP > 250 ˚C. ^{1}H NMR (400 MHz, 25˚C, $CDCl_3$): 8.98 (dd, 2H, *J*=8.71 Hz, *J*=1.05 Hz, Ar-*H*), 8.89 (s, 2H, Ar-*H*), 8.87 (dd, 2H, *J*=8.31 Hz, *J*=1.51 Hz, Ar-*H*), 8.33 (m, 4H, Ar-H), 2.86 (s, 6H, C*H*$_3$). Anal. Calcd. For $C_{32}H_{16}Br_2N_6O_6Re_2 \cdot 1.5CHCl_3 \cdot 0.75Tol$: C, 34.20; H, 1.74; N, 6.18 %. Found C, 34.30; H, 2.25; N, 6.56 %. HRMS: 952.43 $[M\text{-}2Br]^+$. FT-R (cm^{-1}): 1342, 1429, 1475, 1520, 1577. FT-IR (ν_{co}, cm^{-1}): 2021 1909(b).

HATN-2Me-1ReA

Dark red solid. Yield: 7.2 mg (11%). R_f = 0.33 (95:5 CH_2Cl_2 / MeOH). MP > 250 ˚C ^{1}H NMR (400 MHz, $CDCl_3$): 9.09 (dd, 1H, *J*=8.6 Hz, *J*=1.05 Hz, Ar-*H*), 8.83 (dd, 1H, *J*=8.5 Hz, *J*=1.45 Hz, Ar-*H*), 8.82 (s, 1H, Ar-*H*), 8.71 (m, 2H, Ar-*H*), 8.58 (s, 1H, Ar-*H*), 8.24 (m, 2H, Ar-*H*), 8.10 (m, 2H, Ar-*H*),2.79(s, 3H, C*H*$_3$), 2.72 (s, 3H, C*H*$_3$). Anal. Calcd. For $C_{29}H_{16}BrN_6O_3Re \cdot 2.75H_2O$: C, 42.89; H, 2.67; N, 10.35 %. Found C, 42.93; H, 2.49; N, 9.98 %. HRMS: 683.24 $[M\text{-}Br]^+$. FT-R (cm^{-1}): 1348, 1413, 1473, 1520, 1570. FT-IR (ν_{co}, cm^{-1}): 2023 1907(b).

HATN-2Br-1ReS and HATN-2Br-1ReA

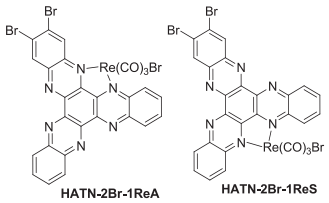

HATN-2Br-1ReS and HATN-2Br-1ReA were synthesised by analogy to the procedure for HATN-2Me-1ReA and HATN-2Me-2ReS except HATN-2Br was used in place of HATN-2Me.

HATN-2Br-1ReS

Dark red solid. Yield: 7.1 mg (11 %). R_f = 0.78 (95:5 CH_2Cl_2 / MeOH). MP >250 ˚C. ^{1}H NMR (400 MHz, $CDCl_3$): δ 9.07 (s, 2H, Ar-*H*), 9.05 (dd, 2H, *J*=8.62 Hz, *J*=1.01 Hz, Ar-*H*), 8.82 (dd, 2H, *J*=8.62 Hz, *J*=1.01 Hz, Ar-*H*), 8.29 (m, 4H, Ar-*H*). Anal. Calcd. For $C_{27}H_{10}Br_3N_6O_3Re{\cdot}0.75CHCl_3{\cdot}0.5Tol$: C, 35.06; H, 1.41; N, 7.73 %. Found C, 34.76; H, 1.88; N, 8.20 %. HRMS: 813.16 $[M\text{-}Br]^+$. FT-R (cm^{-1}): 1334, 1419, 1518, 1570. FT-IR (ν_{co}, cm^{-1}): 2025, 1915(b).

HATN-2Br-1ReA

Dark red solid. Yield: 5.2 mg (7 %). R_f = 0.56 (95:5 CH_2Cl_2 / MeOH). MP > 250 ˚C. ^{1}H NMR (500 MHz, $CDCl_3$): δ 9.27 (s, 1H, Ar-*H*), 9.19 (s, 1H, Ar-*H*), 9.12 (m, 2H, Ar-*H*), 9.00 (dd, 1H, *J*=8.90 Hz, *J*=0.90 Hz, Ar-*H*), 8.85 (dd, 1H, *J*=8.90 Hz, *J*=1.19 Hz, Ar-*H*), 8.47 (m, 2H, Ar-*H*), 8.36 (m, 2H, Ar-*H*). Anal. Calcd. For $C_{27}H_{10}Br_3N_6O_3Re{\cdot}1.5CHCl_3$: C, 31.95; H, 1.08; N, 7.84 %. Found C, 31.53; H, 1.44; N, 7.86 %. HRMS: 813.19 $[M\text{-}Br]^+$. FT-R (cm^{-1}): 1336, 1358, 1412, 1516, 1564. FT-IR (ν_{co}, cm^{-1}): 2029, 1919(b).

HATN-4Me2Br-1ReS and HATN-4Me2Br-2ReA

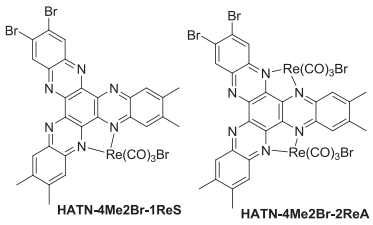

HATN-4Me2Br-1ReS and HATN-4Me2Br-2ReA were synthesised by analogy to the procedure for HATN-2Me-1ReA and HATN-2Me-2ReS except HATN-4Me2Br was used in place of HATN-2Me.

HATN-4Me2Br-1ReS

Dark red solid. Yield: 8.9 mg (13 %). R_f = 0.82 (95:5 CH_2Cl_2 / MeOH). MP > 250 ˚C. ^{1}H NMR (400 MHz, $CDCl_3$): δ 9.03 (s, 2H, Ar-*H*), 8.85 (s, 1H, Ar-*H*), 8.84 (s, 1H, Ar-*H*), 8.54 (s, 2H, Ar-*H*), 2.79 (s, 6H, C*H*$_3$), 2.71 (s, 6H, C*H*$_3$). Anal. Calcd. For $C_{31}H_{18}Br_3N_6O_3Re \cdot 0.5CHCl_3 \cdot 0.5H_2O$: C, 37.03; H, 1.97; N, 8.23 %. Found C, 37.40; H, 2.08; N, 7.75 %. HRMS: 869.28 $[M\text{-}Br]^+$. FT-R (cm^{-1}): 1350, 1404, 1467, 1510, 1566. FT-IR (ν_{co}, cm^{-1}): 2021 1903(b).

HATN-4Me2Br-2ReA

Dark green solid. Yield: 11.0 mg (17 %). R_f = 0.88 (95:5 CH_2Cl_2 / MeOH). MP > 250 ˚C. ^{1}H NMR (400 MHz, $CDCl_3$): δ 9.35 (s, 1H, Ar-*H*), 9.16 (s, 1H, Ar-*H*), 8.96 (s, 1H, Ar-*H*), 8.91 (s, 1H, Ar-*H*), 8.85 (s, 1H, Ar-*H*), 8.84 (s, 1H, Ar-*H*), 8.57 (s, 1H, Ar-*H*), 2.83 (s, 6H, C*H*$_3$), 2.82 (s, 3H, C*H*$_3$), 2.74 (s, 3H, C*H*$_3$). Anal. Calcd. For $C_{34}H_{18}Br_4N_6O_6Re_2 \cdot 2H_2O$: C, 30.60; H, 1.66; N, 6.30 %. Found C, 30.61; H, 1.91; N, 6.24 %. HRMS: 1140.38 $[M\text{- }2Br]^+$. FT-IR (ν_{co}, cm^{-1}): 2019 1911(b).

HATN-4Me-1ReS and HATN-4Me-2ReA

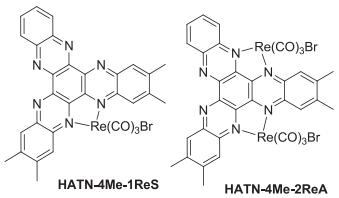

HATN-4Me-1ReS and HATN-4Me-2ReA were synthesised by analogy to the procedure for HATN-2Me-1ReA and HATN-2Me-2ReS except HATN-4Me was used in place of HATN-2Me.

HATN-4Me-1ReS

Dark red solid. Yield: 18.2 mg (28 %). R_f = 0.47 (95:5 CH_2Cl_2 / MeOH). MP > 250 ˚C. ^{1}H NMR (400 MHz, $CDCl_3$): δ 8.87 (s, 2H, Ar-*H*), 8.72 (m, 2H, Ar-*H*), 8.58 (s, 2H, Ar-*H*), 8.10 (m, 2H, Ar-*H*), 2.80 (s, 6H, C*H*$_3$), 2.72 (s, 6H, C*H*$_3$). Anal. Calcd. For $C_{31}H_{20}BrN_6O_3Re{\cdot}0.5CHCl_3{\cdot}0.5Tol$: C, 46.90; H, 2.75; N, 9.38 %. Found C, 46.94; H, 3.33; N, 9.64 %. HRMS: 790.28 $[M]^+$. FT-R (cm^{-1}): 1356, 1413, 1473, 1516, 1568. FT-IR (ν_{co}, cm^{-1}): 2021 1896(b).

HATN-4Me-2ReA

Dark green solid. Yield: 14.1 mg (22 %). R_f = 0.82 (95:5 CH_2Cl_2 / MeOH). MP > 250 ˚C. ^{1}H NMR (400 MHz, $CDCl_3$): δ 9.08 (d, 1H, 8.32, Ar-*H*), 8.82 (s, 1H, Ar-*H*), 8.81 (d, 1H, 8.32 Ar-*H*), 8.56 (s, 1H, Ar-*H*), 8.45 (s, 2H, Ar-*H*), 8.20 (m, 2H, Ar-*H*), 2.78 (s, 3H, C*H*$_3$), 2.71 (s, 3H, C*H*$_3$), 2.68 (s, 6H, C*H*$_3$). Anal. Calcd. For $C_{34}H_{20}Br_2N_6O_6Re_2$: C, 35.80; H, 1.77; N, 7.37 %. Found C, 35.76; H, 1.90; N, 7.03 %. HRMS: 790.34 $[M\text{-}Re(CO)_3Br]^+$. FT-R (cm^{-1}): 1350, 1433, 1475, 1518, 1577. FT-IR (ν_{co}, cm^{-1}): 2021 1913(b).

HATN-4Br-1ReS

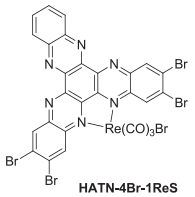

HATN-4Br-1ReS

HATN-4Br-1ReS was synthesised by analogy to the procedure for HATN-2Me-1ReA and HATN-2Me-2ReS except HATN-4Br was used in place of HATN-2Me.

HATN-4Br-1ReS

Dark red solid. Yield: 10.0 mg (15 %) R_f = 0.88 (95:5 CH_2Cl_2 / MeOH). MP > 250 ˚C. ^{1}H NMR (400 MHz, $CDCl_3$): 9.05 (s, 2H, Ar-*H*), 8.71 (s, 2H, Ar-*H*), 8.71 (m, 2H, Ar-

H), 8.09 (m, 2H, Ar-*H*). Anal. Calcd. For $C_{27}H_8Br_5N_6O_3Re \cdot 3CHCl_3 \cdot 1Tol$: C, 29.62; H, 1.28; N, 5.60%. Found C, 30.08; H, 1.52; N, 5.54 %. HRMS: 970.54 $[M]^+$. FT-R (cm^{-1}): 1356, 1400, 1439, 1525, 1572, 1626. FT-IR (ν_{co}, cm^{-1}): 2023 1919(b).

HATN-4Br2Me-2ReS and HATN-4Br2Me-1ReA

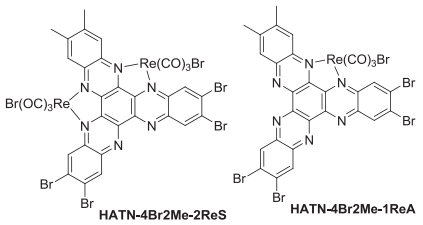

HATN-4Br2Me-1ReS and HATN-4Br2Me-1ReA were synthesised by analogy to the procedure for HATN-2Me -1ReA and HATN-2Me-2ReS except HATN-4Br2Me was used in place of HATN-2Me.

HATN-4Br2Me-2ReS

Dark green solid. Yield: 6.3 mg (9 %). R_f = 0.90 (95:5 CH_2Cl_2 / MeOH). MP > 250 ˚C. ^{1}H NMR (400 MHz, $CDCl_3$): 9.34 (s, 2H, Ar-*H*), 9.14 (s, 2H, Ar-*H*), 8.90 (s, 2H, Ar-*H*), 2.83 (s, 6H, C*H*$_3$). Anal. Calcd. For $C_{32}H_{12}Br_6N_6O_6Re_2 \cdot 1.5H_2O$: C, 26.41; H, 1.04; N, 5.77 %. Found C, 26.32; H, 1.08; N, 5.32 %. HRMS: 999.15 $[M\text{-}Re(CO)_3\text{-}2Br]^+$. FT-R ($cm^{-1}$): 1350, 1406, 1467, 1512, 1566. FT-IR (ν_{co}, cm^{-1}): 2021 1914(b).

HATN-4Br2Me-1ReA

Dark red solid. Yield: 11.0 mg (18 %). R_f = 0.88(95:5 CH_2Cl_2 / MeOH). MP > 250 ˚C. ^{1}H NMR (400 MHz, $CDCl_3$): 9.36 (s, 1H, Ar-*H*), 9.13 (s, 1H, Ar-*H*), 9.05 (s, 1H, Ar-*H*), 9.03 (s, 1H, Ar-*H*), 8.80 (s, 1H, Ar-*H*), 8.56 (s, 1H, Ar-*H*), 2.80 (s, 3H, C*H*$_3$) 2.73 (s, 3H, C*H*$_3$). Anal. Calcd. For $C_{29}H_{12}Br_5N_6O_3Re \cdot 1.5CHCl_3 \cdot 0.5Tol$: C, 31.33; H, 1.35; N, 6.45 %. Found C, 31.29; H, 1.74; N, 6.21 %. HRMS: 998.99 $[M\text{-}Br]^+$. FT-R (cm^{-1}): 1606, 1641. FT-IR (ν_{co}, cm^{-1}): 2023 1917(b).

HATN-4Br2Me-CuBF$_4$

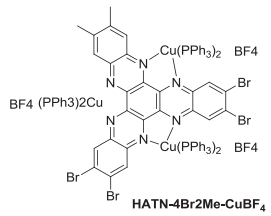

HATN-4Br2Me (25.4 mg, 0.0349 mmol) and $[Cu(MeCN)_2(PPh_3)_2]BF_4$ (57.9 mg, 0.0765 mmol) was stirred in diethylether for 48 h under argon. The mixture was then filtered to provide a green solid as the product. This was purified by crystallisation from methanol.

Yield: 961 mg (75 %). Anal. Calcd. For $C_{134}H_{102}B_3Br_4Cu_3F_{12}N_6P_6 \cdot 2MeCN_2$: C, 55.96; H, 3.76; N, 3.73 %. Found C, 56.01; H, 4.28; N, 3.76 %. FT-IR (cm^{-1}): 674, 748, 1055 (b). FT-R (cm^{-1}): 1072, 1169, 1412, 1466, 1504, 1591, 1643.

HATN-2Br-CuBF$_4$

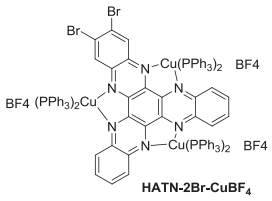

HATN-2Br-$CuBF_4$ was synthesised by analogy to the procedure for HATN-4Br2Me-$CuBF_4$ except HATN-2Br was used in place of HATN-4Br2Me.

Yield: 896 mg (70%). Anal. Calcd. For $C_{132}H_{100}B_3Br_2Cu_3F_{12}N_6P_6 \cdot H_2O$: C, 61.33; H, 3.98; N, 3.25 %. Found C, 61.19; H, 3.99; N, 2.81 %. FT-IR (cm^{-1}): 696, 748, 1052 (b). FT-R (cm^{-1}): 1074, 1407, 1500, 1647. ESI-MS: 1129.5 $[M\text{-}2\{Cu(PPh_3)_2\}\text{-}3BF_4]^+$.

HATN-4Me2Br-CuBF$_4$

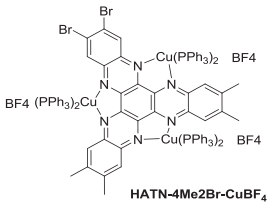

HATN-4Me2Br-CuBF$_4$ was synthesised by analogy to the procedure for HATN-4Br2Me-CuBF$_4$ except HATN-4Me2Br was used in place of HATN-4Br2Me.

Yield: 915 mg (72%). Anal. Calcd. For $C_{136}H_{108}B_3Br_2Cu_3F_{12}N_6P_6 \cdot 0.5CHCl_3$: C, 61.11; H,4.08; N, 3.31 %. Found C, 60.94; H, 4.06; N, 3.35 %. FT-IR (cm^{-1}): 693, 752, 1056(b). FT-R (cm^{-1}): 1074, 1417, 1500, 1579, 1612, 1643. ESI-MS: 1185.5 [M-2{Cu(PPh$_3$)$_2$}-3BF$_4$]$^+$.

HATN-4Me-CuBF$_4$

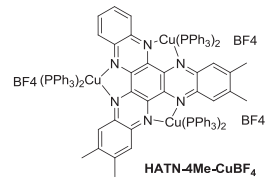

HATN-4Me-CuBF$_4$ was synthesised by analogy to the procedure for HATN-4Br2Me-CuBF$_4$ except HATN-4Me was used in place of HATN-4Br2Me.

Yield: 860 mg (85 %). Anal. Calcd. For $C_{136}H_{110}B_3Cu_3F_{12}N_6P_6$: C, 66.26; H, 4.50; N, 3.41 %. Found C, 66.02; H, 4.56; N, 3.37 %. FT-IR (cm^{-1}): 693, 749, 1053(b). FT-R (cm^{-1}): 1361, 1400, 1477, 1519. ESI-MS: 1028.0 [(M-2{Cu(PPh$_3$)$_2$}-3BF$_4$]$^+$.

HATN-4Me-CuClO$_4$

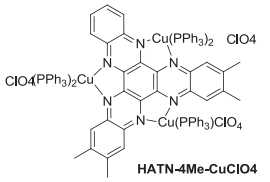

HATN-4Me (13.6 mg, 0.0309 mmol) and $[Cu(MeCN)(PPh_3)_2]ClO_4$ (72.0 mg, 0.0936 mmol) was stirred in diethylether for 48 h under argon. The mixture was then filtered to provide a green solid as the product. This was purified by crystallisation in methanol.

Yield: 520 mg (75%). Anal. Calcd. For $C_{118}H_{95}Cl_3Cu_3N_6O_{12}P_5 \cdot 2CHCl_3 \cdot 1.5MeCN$; C, 58.13; H, 4.00; N, 3.89 %. Found C, 58.21; H, 3.74; N, 4.22 %.

HATN-4Br-CuBF₄

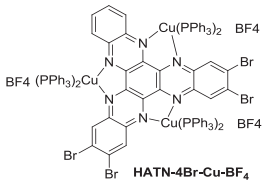

HATN-4Br-$CuBF_4$ was synthesised by analogy to the procedure for HATN-4Br2Me-$CuBF_4$ except HATN-4Br was used in place of HATN-4Br2Me.

Yield: 951 mg (76 %). Anal. Calcd. For $C_{132}H_{98}B_3Br_4Cu_3F_{12}N_6P_6 \cdot 0.75CHCl_3$: C, 56.65; H, 3.54; N, 2.99 %. Found C, 56.50; H, 4.04; N, 3.42 %. FT-IR (cm^{-1}): 694, 748, 1052(b). FT-R (cm^{-1}): 1074, 1407, 1500, 1647.

HATN-2Me-CuBF₄

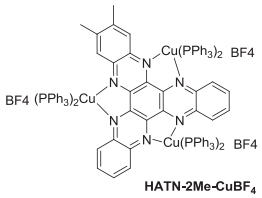

HATN-2Me-$CuBF_4$ was synthesised by analogy to the procedure for HATN-4Br2Me-$CuBF_4$ except HATN-2Me was used in place of HATN-4Br2Me.

Yield: 851 mg (78 %). Anal. Calcd. For $C_{134}H_{106}B_3Cu_3F_{12}N_6P_6 \cdot 2H_2O$: C, 65.07; H, 4.48; N, 3.40 %. Found C, 65.07; H, 4.04; N, 3.38 %. FT-IR (cm^{-1}): 696, 750, 1052(b). FT-R (cm^{-1}): 1338, 1425, 1479, 1514, 1577. ESI-MS: 1001.0 $[M\text{-}2\{Cu(PPh_3)_2\}\text{-}3BF_4]^+$.

HATN-4Me-1PdS and HATN-4Me-1PdA

An orange solution of 171 mg (0.45 mmol) of $(PhCN)_2PdCl_2$ in 15 mL chloroform was slowly added to a stirred, yellow-green solution of 200 mg (0.45 mmol) of HATN-4Me in 20 mL of chloroform. A deep orange colour immediately formed and the solution was stirred for 20 min. The volume was reduced under vacuum to 10 mL. Addition of diethyl ether afforded an orange microcrystalline solid that was collected by filtration, washed with diethyl ether, and dried in air.

HATN-4Me-1PdS

^{1}H NMR (400MHz, 25°C, $CDCl_3$): 9.5(m, 1H, Ar-*H*), 9.3(s, 1H, Ar-*H*), 8.7 (m, 1H, Ar-*H*), 8.5(s, 1H, Ar-*H*), 8.4(s, 2H, Ar-*H*), 8.2(m, 2H, Ar-*H*), 2.7(s, 12H, C*H*$_3$)

HATN-4Me-1PdA

^{1}H NMR (400MHz, 25°C, $CDCl_3$): 9.3(s, 2H, Ar-*H*), 8.7(m, 2H, Ar-*H*), 8.55(s, 2H, Ar-*H*), 8.1 (m, 1H, Ar-*H*), 2.7(s, 12H, C*H*$_3$)

7.3 References

1 Skujins, S. W., G. *Tetrahedron* **1969**, *25*, 3935.